Experimental and Theoretical Study of Resonance Raman Spectroscopy in Ground and Excited Electronic States

©2020

Matthew S. Barclay

Submitted to the graduate degree program in the Department of Chemistry and the Graduate Faculty of the University of Kansas in partial fulfillment of the requirements for the degree of Doctor of Philosophy.

Christopher G. Elles, Chairperson

Marco Caricato, Chairperson

Committee members

Carey K. Johnson

Ward H. Thompson

Brian B. Laird

Craig P. Marshall

Date defended: _____ December 13, 2019

The Dissertation Committee for Matthew S. Barclay certifies
that this is the approved version of the following dissertation:

Experimental and Theoretical Study of Resonance Raman Spectroscopy
in Ground and Excited Electronic States

Christopher G. Elles, Chairperson

Marco Caricato, Chairperson

Date approved: December 19, 2019

ii

Abstract

Spectroscopy is a powerful tool for the identification, study, and selective control of molecular processes. Raman scattering is particularly useful in observing the vibrational properties of molecules, and identifying compounds based on structure. While the experimental measurements provide structural information on the vibrational transitions, the detailed interpretation of Raman spectra for complex molecules requires assignment of the observed Raman bands to specific vibrational motions. As a result, experimental spectra are often compared with calculated vibrational frequencies and Raman intensities. Therefore, it is necessary that the simulated spectra correctly reproduce the experimental Raman spectra. Although simulations of Raman spectra generally have good agreement with experiment, additional work is required to understand the effects of intramolecular electronic and nuclear structure on the Raman intensities of molecules with extended π conjugation.

Conjugated thiophene derivatives have a variety of interesting optical and electronic properties, which makes them ideal targets for studies of charge-transport processes. Additionally, the delocalized π electron distribution gives these compounds relatively large scattering cross-sections, making them excellent model compounds for Raman spectroscopic studies. In particular, time-resolved techniques are able to measure transient Raman spectra in electronically excited states, allowing for the direct observation of structural dynamics following optical excitation, which is instrumental in understanding the charge separation processes in these molecules. Due to small excited-state population, transient Raman measurements typically rely on electronic resonance enhancement, which increases the Raman transition intensities for specific vibrational modes by up to several orders of magnitude. This mode-specific enhancement occurs for vibrations with large displacements along the potential energy surfaces of the higher-lying electronic states, therefore, detailed information can be obtained about the structure of higher-lying states based on which

vibrations have enhanced Raman scattering intensity. Although resonance-enhanced excited-state Raman measurements are often used to increase signal, the role of the resonant electronic transition has been largely overlooked. By combining experimental measurements and theoretical simulations of excited-state Raman spectra, it is possible to gain a more comprehensive understanding of the structure of the higher-lying electronic states.

In this dissertation, we measured resonance-enhanced Raman spectra in excited singlet and triplet electronic states for a set of conjugated thiophene derivatives, and compared the experiments with calculated Raman intensities for the excited states. Using relatively inexpensive computational methods, we were able to assign the experimental Raman bands to specific vibrational motions by considering the resonance enhancement condition in detail. Additionally, it was found that the experimental resonance Raman intensities can be qualitatively reproduced by calculations of the energy gradient of the higher-lying electronic state along vibrational displacements, particularly for vibrations that have relatively large resonance enhancements. We also investigated the effect of inter-ring torsion on the Raman intensities of aryl-substituted benzene and thiophene compounds in the ground state, for which density functional theory calculations tend to overestimate the delocalization of the π electron distribution between aryl rings. In addition to providing a benchmark for the accuracy of theoretical methods, the combination of experimental and simulated Raman spectra provided more detailed insight into the electronic and structural properties of the conjugated thiophene molecules than could be obtained by either approach alone. Finally, we studied the excited-state dynamics of 2,5-diphenylthiophene (DPT) following photoexcitation. We found that, by examining the potential energy gradients of higher-lying electronic states, it was possible to characterize vibrational coherences observed in the excited-state absorption spectrum, ultimately providing a more complete interpretation of the excited-state dynamics of this model compound.

Acknowledgements

My foremost and deepest thanks go to my two advisors, Dr. Christopher Elles and Dr. Marco Caricato, whose insightful planning, careful guidance, and exceptionally collaborative spirits were paramount in the successful completion of this doctoral research project. More importantly, their scientific curiosity, personal mentorship, and seemingly infinite patience all worked to provide an intellectual environment that was ideal for stimulating my professional development, and, ultimately, allowing me to grow well beyond my limitations. I count myself impossibly lucky to have had this rare opportunity to learn so much from each of them, and absolutely none of it would have been possible without their cooperation.

I also owe a great deal of my success to all the current and former members of both of my research groups: Dr. Tim Quincy, who taught me nearly everything I know about FSRS, Drs. Tal Aharon, Chris Otolski, and Alessandro Biancardi, who were always available to help whenever I had questions or scientific curiosities, and Sijin Ren, Amy Jystad, Kristen Burns, Ty Balduf, David Stierwalt, Kaihua Zhang, Dan Johnson, PJ Srivastava, Ryan Lampton, and Katherine Vander Laan, who continue to provide stimulating discussions, intellectual perspectives, and support as I near the end of this great chapter in life. I am eternally grateful to KU as well, whose financial support and collaborative environment allowed me to pursue my passion for both computational and experimental fields of physical chemistry.

Finally, I dearly wish to thank my family. First, to my brother Michael, whose experienced advice and kinship as a physical chemist provided an inestimable foundation for my personal and professional growth, the true value of which continues to reveal itself with each passing day. Of course, I am also immeasurably thankful to my mother, Deborah, whose brilliant mind and unending support would always help me to persevere and strive to surpass my limits, and my father, Scott, whose intellectual discussions and considered perspectives helped remind me to think about

problems from every angle.

Contents

5 Probing Dynamics in Higher-Lying Electronic States with Resonance-Enhanced Femtosecond Stimulated Raman Spectroscopy 46

6 Femtosecond Stimulated Raman Scattering from Triplet Electronic States: Experimental and Theoretical Study of Resonance Enhancements 71

10 Summary and Future Directions   157

References   164

List of Figures

xiii

List of Tables

Chapter 1

Introduction

Developments in the field of photochemistry, particularly over recent decades, have become instrumental in the characterization of materials,[1] as well as the determination of the physical and chemical properties of compounds.[2] Through spectroscopic techniques, light-matter interactions provide detailed information about the electronic and structural characteristics of the systems of interest. Time-resolved electronic and vibrational spectroscopies are particularly useful for studying the behavior of molecules following photoexcitation. Understanding the dynamical evolution of compounds in photoexcited states can lead to the optical control of photochemical and photophysical processes, where desired molecular dynamics are induced through vibrational[3–5] or electronic excitation[6] and yield reaction products[7,8] that would otherwise be unattainable. However, while the experimental measurements provide an accurate observation of the excited-state dynamics, it is necessary to complement experiments with accurate theoretical calculations of excited-state properties in order to interpret the results and identify the specific electronic states and nuclear motions that are observed. Characterizing the electronic and vibrational properties of the material using both experimental and theoretical techniques gives valuable insight into how the nuclei will respond to changes in the electronic state, and ultimately lead to a better understanding of how photoexcitation induces the dynamics of the compounds.

In this dissertation, I focus on Raman spectroscopy, which is an indispensable tool in the identification and structural characterization of materials.[9–12] This vibrational technique involves the inelastic scattering of light due to its interaction with a molecule, which undergoes a transition between two vibrational states. The difference in energy between the incident and scattered light is related to the frequencies of the vibrational transitions, and, therefore, provides information on the

molecular structure of the compound. In order to efficiently determine the structure from Raman spectra, the experimental measurements are often analyzed alongside simulations of these spectra that utilize electronic structure methods.[13,14] Thus, it is important that the simulated spectra provide an accurate representation of the experiment, and many studies have been performed to benchmark the accuracy of Raman intensities calculated using various computational methods.[15–20] Nevertheless, many of these benchmark studies have focused on relatively small molecules (e.g. H_2O, NH_3, C_2H_6, etc.) in the ground electronic state,[15,16,20] and, although the simulated Raman spectra are generally in good agreement with experiment, the calculations still show some discrepancies in the ground state, particularly for larger compounds with π conjugated structure (e.g. adenine, thymine, or 4-aminobenzonitrile),[13,17,21] and additional work is necessary.

Additionally, the development of ultrafast laser pulses allows for the measurement of transient Raman spectra in electronically excited states of molecules, using the femtosecond stimulated Raman spectroscopy (FSRS) technique. The FSRS measurement, which is given in detail in Chapter 3 and has been thoroughly described in the literature,[22–24] involves an initial, actinic laser pump pulse that photoexcites the molecule into an excited electronic state, after which a second, Raman pump pulse interacts with the sample and, simultaneously, a probe pulse which stimulates Raman scattering into the different vibrational energy levels of the excited electronic state. Thus, the ultrafast temporal resolution of FSRS allows for the measurement of the vibrational transitions of the molecule as it evolves along the excited-state potential energy surface (PES), providing a direct observation of molecular dynamics following optical excitation. However, the observed Raman scattering intensity is limited by the excited-state population that is produced by the actinic laser pulse. As a result, the majority of FSRS experiments use a Raman pump excitation energy that is resonant with an electronic transition in order to take advantage of resonance enhancement, where the Raman scattering intensities are increased by multiple orders of magnitude, allowing for an observable signal in the experiment.[24]

Although the resonance-enhanced FSRS measurements provide a powerful means of observing excited-state vibrational dynamics, it is necessary to identify the specific vibrational motions

that correspond to the experimental Raman bands in order to obtain a meaningful interpretation of the results. The excited-state vibrational frequencies can be calculated using electronic structure methods, but accurate experimental band assignments also require a comparison with calculations of excited-state Raman intensities. Unfortunately, analytical methods for the simulation of excited-state Raman intensities are currently unavailable in electronic structure software packages. Furthermore, the resonance enhancement is vibrational mode-specific, and Raman transitions with the largest enhancement have significant nuclear displacements along the PES of the resonant higher-lying electronic state.[25–27] Therefore, accurate simulations of excited-state resonance Raman spectra require careful consideration of the resonant electronic transitions, as well as the vibrational modes that are most likely to be enhanced through that resonance condition. One of the primary goals of our work is to compare resonance-enhanced FSRS spectra with relatively inexpensive simulations of excited-state Raman spectra in order to develop methods for accurately analyzing the FSRS measurements and, ultimately, interpret the experimental observations.

We focus our analysis on a series of conjugated organic molecules, with particular emphasis on compounds containing aryl-substituted thiophene and benzene. The molecular polarizability in these molecules is highly sensitive to the delocalized π electron distribution between aromatic rings,[28] therefore, Raman spectroscopy, which measures the change in polarizability as a function of vibrational motion,[29,30] is instrumental in identifying the structures of these compounds and how that structure affects the physical applications.[31–33] Due to their conjugated structure, these aromatic derivatives also have a variety of optical and electronic applications as photoactive sub-units of molecular photochromic switches,[7,8,34] organic photovoltaics,[35–37] and the monomers of conductive polymers.[38–40] These compounds experience rapid intersystem crossing (ISC) following photoexcitation, and have relatively long-lived lifetimes of the triplet electronic states, which is important for charge-separation and transport in conductive organic materials.[38,41–43] Therefore, in the particular application of charge transport, the performance of these aryl-substituted compounds is directly related to their behavior in the excited state, and they have been the target of numerous studies of transient electronic[44–47] and vibrational[48–51] dynamics. In addition to their interesting

applications, the photophysical dynamics of these molecules in the excited state are reliable and fairly well-understood, making them ideal model compounds for our analysis.

Previous studies characterizing the excited-state properties of the thiophene-based compounds have shown that this class of molecules follows a consistent trend after photoexcitation at roughly 310 nm. The initial laser pulse causes a $S_1 \leftarrow S_0$ transition through $\pi \rightarrow \pi^*$ excitation, then the molecule undergoes structural relaxation *via* planarization of the aryl-substituted framework and vibrational cooling on the order of a few ps.[47] The S_1 state of these compounds undergoes ISC directly into the triplet state (T_1), which eventually decays back to the ground electronic state. Because the excited-state dynamics are relatively straightforward, we can tune the time delay between the actinic and Raman pump pulses to measure Raman spectra of the vibrationally relaxed S_1 or T_1 states, which is convenient for comparison with simulations of Raman spectra at the excited-state equilibrium geometries. Additionally, the transient absorption (TA) spectra for the singlet and triplet excited states are energetically well-separated. This separation allows for the selective resonance enhancement of FSRS spectra in either the S_1 or T_1 state, which is particularly beneficial in molecules with ISC rates fast enough that there is a simultaneous population of T_1 and S_1 states.

In this work, we utilize a combination of experimental time-resolved spectroscopic techniques and theoretical calculations of excited-state properties in order to accurately assign and interpret the resonance-enhanced FSRS spectra of conjugated thiophene derivatives, as well as to obtain a more comprehensive description of their electronic and structural properties. Motivated by these goals, we begin with a comparison of resonance-enhanced FSRS spectra with off-resonant excited-state Raman spectra, in order to assign the experimental Raman bands to vibrational modes (Chapter 4).[52] From the results of this work, we compared the FSRS spectra with simulations of excited-state resonance Raman spectra, and further investigated the factors that led to the resonance enhancement conditions in both the singlet and triplet states of the thiophene derivatives (Chapters 5-6).[53,54] We have also studied the dependence of the Raman spectra on the molecular orientations of these molecules in the ground state (Chapters 7-8), which sheds additional light on the dis-

crepancies between calculated and experimental Raman intensities that are observed in the excited state due to delocalized π conjugation.[55,56] We applied the knowledge gained from these studies to the excited-state dynamics of a di-phenyl substituted thiophene, which provided a detailed interpretation of low-frequency vibrational coherences observed in the experiment (Chapter 9).

Chapter 4 details our work to accurately assign FSRS spectra to calculated excited-state vibrational modes. We utilized numerical calculations of off-resonant excited-state Raman spectra to assign the resonance-enhanced FSRS bands to the calculated modes based on symmetry considerations, as well as the resonance enhancement condition for electronic transitions from a (π, π^*) state. We benchmarked the band assignments for a series of conjugated thiophene molecules in both the S_1 and T_1 states, supported by comparisons between molecules in the benchmark series with similar structure, such as 2-phenylthiophene (PT), 2-methyl-5-phenylthiophene (MPT), and 2,5-diphenylthiophene (DPT).

The vibrational assignments are further supported by simulations of the resonance-enhanced Raman spectra.This work is shown in Chapter 5, where we explored the resonance enhancements of the S_1 state of DPT in more detail. The FSRS spectrum was measured at different Raman excitation wavelengths across the profile of the excited-state absorption (ESA) band, and compared with simulations of resonance Raman spectra for $S_N \leftarrow S_1$ transitions that may be resonant with the Raman excitation frequency. Since the simulated resonance Raman spectra are predicted for individual $S_N \leftarrow S_1$ transitions, it is possible to identify the resonant electronic state that has the largest contribution to the resonance-enhanced FSRS spectrum, which provides valuable insight into the interpretation of the experimental FSRS spectrum of the S_1 state.

However, the resonance enhancements in the triplet electronic states of the aryl-substituted thiophenes are more complicated. Chapter 6 focuses on the enhancements due to the resonance condition in the T_1 state of PT. Similar to our study of the S_1 state of DPT, we performed FSRS measurements at different Raman excitation energies along the profile of the triplet ESA band, and compared the experimental spectra to simulated resonance Raman spectra. Contrary to the singlet excited state of DPT, for which the TA spectrum and calculated $S_N \leftarrow S_1$ oscillator strengths

consistently show one dominant electronic transition, the triplet absorption spectrum for PT, in both the calculations and the TA measurement, have contributions from multiple $T_N \leftarrow T_1$ transitions. Therefore, the simulated Raman spectra still provide important information for the interpretation of the FSRS measurements, and the experiments are useful in benchmarking the accuracy of the calculations.

In Chapter 7, we benchmark Raman intensities in the ground state calculated with a set of density functionals and the second-order Møller-Plesset perturbation theory (MP2) method with experimental measurements of spontaneous Raman spectra for a series of substituted benzene and thiophene compounds. Although the simulated Raman spectra are generally in good agreement with experiment, the calculations tend to overestimate the relative Raman intensities of higher-frequency vibrations (1400-1600 cm^{-1}) compared to those of lower-frequency bands, particularly in molecules with multiple aryl rings such as biphenyl (BP), PT, MPT, and DPT.

This overestimation of calculated Raman intensities in high-frequency bands was investigated further by examining the effects of anharmonicity and ring-ring torsion on the Raman spectrum, which is presented in Chapter 8. In this study, we compared the ground-state experimental Raman spectra of BP, PT, and 2,2-bithiophene (BT) with anharmonic corrections to the calculated Raman intensities, as well as the calculated Raman spectra at different inter-ring dihedral angles. This work provides important information on how the Raman intensities are affected by changes in the π conjugation due to ring-ring torsion, which offers insight into the cause of the discrepancies between calculated relative intensities and experiment.

In addition to the detailed analysis and interpretation of the ground- and excited-state Raman spectra, it was demonstrated in Chapters 5-8 that our comparisons between calculated and experimental results give a more comprehensive understanding of the characteristics and physical properties of the electronic transitions of the conjugated molecules. As a result, this insight becomes very useful when interpreting excited-state dynamics. In Chapter 9, we present a study of the excited-state dynamics in DPT immediately following $S_1 \leftarrow S_0$ photoexcitation. The TA spectrum of DPT shows regular low-frequency oscillations (<200 cm^{-1}) in the differential absorption at multiple

probe wavelengths, which are attributed to vibrational coherences in the S_1 state of DPT that alter the Franck-Condon overlap in transitions to other S_N states. Typically, vibrational coherences can be identified through the time-resolved vibrational coherence spectroscopy (VCS),[57–61] where a Fourier transform is applied to the time-dependent oscillations to obtain the vibrational Raman spectrum in the frequency domain.[62–65] However, the vibrational coherences observed in DPT are more difficult to assign based on calculated S_1 normal mode frequencies alone. Nevertheless, our extensive work characterizing the resonance-enhancement condition for the excited-state Raman spectrum in DPT provides important insights into the $S_N \leftarrow S_1$ transitions. Thus, it is possible to use the detailed information gained from our analysis of the PES gradients along S_1 and the higher-lying S_N states to obtain a complete physical picture of the initial excited-state dynamics in the molecule studied.

Our work has emphasized the value of studying complex physical and chemical processes from both experimental and theoretical approaches. Through our measurements and calculations of excited-state Raman spectroscopy, we demonstrate methods of interpreting complicated FSRS spectra using relatively inexpensive calculations, which gives a comprehensive picture of the excited-state dynamics. Even in the ground-state Raman spectra, our investigations from both theoretical and experimental perspectives reveal structure-dependent effects on Raman intensities that are not fully understood. Our efforts not only provide a significant step forward in the efficient analysis and detailed interpretation of the FSRS technique, but also shed light on the excited-state properties of conjugated thiophenes. The information gained at every step of our investigations contributes to a much more complete understanding of Raman spectroscopy and conjugated molecules in general, and, ultimately, highlights the importance of combining experimental and theoretical methods.

Chapter 2

Theory

2.1 Theory of Raman Scattering

When monochromatic radiation is incident on a material sample, the light-matter interaction produces scattered radiation through both inelastic and elastic processes, depending on whether or not the light exchanges energy with individual molecules. The light scattered from a bulk sample consists of a number of different frequency components that relate to how the molecules retain and store that energy. The inelastic scattering of the incident light carries detailed information about the structure of the material, an effect first recognized by C. V. Raman in 1927,[66] hence, it is known as Raman scattering, while the elastic scattering process is referred to as Rayleigh scattering. Shortly after, the classical theory of polarizability was developed by Placzek in 1934,[67] which included the contributions from Kramers, Heisenberg, and Dirac,[68] and outlined the generation of Rayleigh and Raman scattering as a response to the oscillating electric dipole induced in a molecule by an incident electric field of light.

From classical electrodynamics, the scattered intensity radiated by an induced dipole as a response to incident radiation of frequency ν_p is given as $I(\theta)$,[29,30]

$$I(\theta) = \frac{\pi^2 c \tilde{\nu}_p^4 \, |\mu_{ind}(\nu_s)|^2 \, \sin^2(\theta)}{2 \, \varepsilon_0} \tag{2.1}$$

where $\tilde{\nu}_p$ is the frequency (in cm^{-1}) of the incident radiation, $|\mu_{ind}(\nu_s)|$ is the amplitude of the induced dipole that oscillates at a frequency of ν_s, and θ is the angle between the dipole and the direction of propagation of the light. Considering the incident field as a perturbation to the

molecular dipole moment, the induced dipole moment can be written as a sum of time-dependent induced dipole moments (omitting the dependence on v_s for brevity),

$$\vec{\mu}_{ind} = \vec{\mu}_{ind}^{(1)} + \vec{\mu}_{ind}^{(2)} + \vec{\mu}_{ind}^{(3)} + ... \tag{2.2}$$

where $\vec{\mu}_{ind}^{(1)} \gg \vec{\mu}_{ind}^{(2)} \gg \vec{\mu}_{ind}^{(3)}$ and so on in a swiftly converging series. In relation to the perturbation from the incident electric field of the light wave, $\vec{E}_p$, the terms in Equation 2.2 are defined as,[29]

$$\vec{\mu}_{ind}^{(1)} = \boldsymbol{\alpha} \cdot \vec{E}_p \tag{2.3}$$

$$\vec{\mu}_{ind}^{(2)} = \frac{1}{2}\boldsymbol{\beta} \cdot \vec{E}_p \cdot \vec{E}_p \tag{2.4}$$

$$\vec{\mu}_{ind}^{(3)} = \frac{1}{6}\boldsymbol{\gamma} \cdot \vec{E}_p \cdot \vec{E}_p \cdot \vec{E}_p \tag{2.5}$$

where $\boldsymbol{\alpha}$, $\boldsymbol{\beta}$, and $\boldsymbol{\gamma}$ are the tensors for the molecular polarizability, hyperpolarizability, and second hyperpolarizability, respectively. Focusing on the largest term, $\vec{\mu}_{ind}^{(1)}(v_s)$, which is linear in $\vec{E}_p$, there can be two components: one that is associated with Rayleigh scattering, $\vec{\mu}_{ind}^{(1)}(v_p)$, and one associated with Raman scattering, $\vec{\mu}_{ind}^{(1)}(v_p \pm v_k)$, where v_k is a molecular vibrational frequency. Equation 2.1 shows that the scattered intensity at a particular frequency is related to the amplitude, $|\mu_{ind}(v_s)|$, at that frequency. Therefore, we can rewrite Equation 2.3 for Rayleigh and Raman scattering,

$$\vec{\mu}_{ind}(v_p) = \boldsymbol{\alpha}^{Ray} \cdot \vec{E}_p(v_p) \tag{2.6}$$

$$\vec{\mu}_{ind}(v_p \pm v_k) = \boldsymbol{\alpha}^{Ram} \cdot \vec{E}_p(v_p) \tag{2.7}$$

where $\boldsymbol{\alpha}^{Ray}$ is the equilibrium polarizability tensor and $\boldsymbol{\alpha}^{Ram}$ is the polarizability tensor associated with v_k, in that it relates the field, $\vec{E}_p$, which oscillates at a frequency of v_p, to an induced oscillation of the dipole at a frequency of $v_s = v_p \pm v_k$. Since $\boldsymbol{\alpha}$ is, in general, related to the nuclear motions of the molecule, we can derive an expression for the tensor elements, $\alpha_{\rho\sigma}$ (where ρ and σ are Cartesian axes), through a Taylor series expansion of the polarizability with respect to the mass-

weighted normal displacement coordinate, q_k, of each vibrational mode k,

$$\alpha_{\rho\sigma} = (\alpha_{\rho\sigma})_0 + \sum_k \left(\frac{\partial \alpha_{\rho\sigma}}{\partial q_k}\right)_0 q_k + \frac{1}{2} \sum_{k,l} \left(\frac{\partial^2 \alpha_{\rho\sigma}}{\partial q_k \partial q_l}\right)_0 q_k q_l + ... \qquad (2.8)$$

where the subscript 0 indicates that the terms are evaluated at the equilibrium molecular geometry. Neglecting the terms that are 2nd order and higher in q_k in Equation 2.8, and focusing on a single normal mode, the polarizability tensor can be approximated as,[29]

$$\boldsymbol{\alpha} \simeq \boldsymbol{\alpha}_0 + \left(\frac{\partial \boldsymbol{\alpha}}{\partial q_k}\right)_0 q_k \qquad (2.9)$$

in which we define,

$$\boldsymbol{\alpha}^{Ray} = \boldsymbol{\alpha}_0 \qquad (2.10)$$

$$\boldsymbol{\alpha}_k^{Ram} = \left(\frac{\partial \boldsymbol{\alpha}}{\partial q_k}\right)_0 \qquad (2.11)$$

Although this classical approach is sufficient for bulk material properties,[69] it is necessary to include a quantum mechanical treatment of the polarizability in order to extract detailed information about the molecular properties, such as the transitions between vibronic energy levels that are involved in the Raman scattering process.

2.2 Quantum Mechanical Theory of Raman Scattering

From a quantum mechanical perspective, the oscillating dipole that produces Raman-scattered light is defined as the time-dependent induced transition dipole, $(\vec{\mu}_{ind})_{fi}$, between an initial vibrational state $|v_i\rangle$ and a final state $|v_f\rangle$. As a result, we can rewrite Equation 2.3 in Dirac notation,

$$\begin{aligned} \langle(\vec{\mu}_{ind})_{fi}\rangle &= \langle v_f| \boldsymbol{\alpha} \cdot \vec{E}_p |v_i\rangle \\ &\approx \langle v_f| \boldsymbol{\alpha} |v_i\rangle \cdot \vec{E}_p \qquad (2.12) \\ &\approx \boldsymbol{\alpha}_{fi} \cdot \vec{E}_p \end{aligned}$$

where $\boldsymbol{\alpha}_{fi}$ is the transition polarizability, and $\vec{E}_p$ is the incident electromagnetic field, which is approximated to be constant within the whole molecule. In this semi-classical approach, it is assumed that the wavelength of the incident light is significantly larger than the size of the molecule. This is valid for our work, which utilizes dilute samples of relatively small (<100 nm) conjugated thiophene derivatives, and the incident radiation is within the range of optical frequencies (300-800 nm). Therefore, we use a classical treatment of the electric field, rather than full quantum-mechanical treatment of both $\vec{E}_p$ and the molecule. In general, the transition polarizability between the initial and final vibronic states $|i\rangle$ and $|f\rangle$ can be derived from second-order time-dependent perturbation theory in a sum-over-states approach,[29,67]

$$\boldsymbol{\alpha}_{fi} = \frac{1}{\hbar} \sum_n \left(\frac{\langle f| \hat{\mu} |n\rangle \langle n| \hat{\mu} |i\rangle}{\omega_{ni} - \omega_p - i\Gamma_n} + \frac{\langle f| \hat{\mu} |n\rangle \langle n| \hat{\mu} |i\rangle}{\omega_{fn} + \omega_p + i\Gamma_n} \right) \tag{2.13}$$

where $|n\rangle$ are all possible intermediate states, Γ_n are phenomenological broadening terms related to the dephasing of each intermediate state, $\hat{\mu}$ is the electric dipole operator, and ω_{ni} and ω_{fn} are transition frequencies.

Due to the difficulty of calculating the vibronic states in Equation 2.13, we can separate the nuclear and electronic parts of the transition polarizability and expand it as a Taylor series of the electronic polarizability, similar to the classical case in Equation 2.8,

$$\boldsymbol{\alpha}_{fi} = \boldsymbol{\alpha}_0 \langle v_f | v_i \rangle + \sum_k \left(\frac{\partial \boldsymbol{\alpha}}{\partial q_k} \right)_0 \langle v_f | q_k | v_i \rangle + ... \tag{2.14}$$

where the subscript 0 again indicates values at the equilibrium geometry, which corresponds to zero displacement along a vibration. Neglecting higher-order terms in the expansion, and assuming harmonic normal modes and static conditions ($\omega_p = 0$), Equation 2.14 reduces to a single term that describes the fundamental Raman transition for each mode k.[29,30] Under these assumptions, the transition polarizability is proportional to the electronic polarizability derivative with respect to q_k,

$$\boldsymbol{\alpha}_{fi}^k \propto \sqrt{\frac{\hbar}{4\pi\nu_k}} \left(\frac{\partial \boldsymbol{\alpha}}{\partial q_k} \right)_0. \tag{2.15}$$

In order to relate the transition polarizability back to the Raman scattering intensity from Equation 2.1, we follow the steps outlined by Neugebauer *et al.*, which describe the polarizability derivative as a function of the intrinsic Raman activity of the molecule, S_k.[30] The Raman activity is defined along the molecule-fixed axes, $(x', y',$ and $z')$. However, the components of the polarizability tensor depend on the space-fixed coordinate system of the laboratory frame of reference, $(x, y,$ and $z)$, therefore we can transform the coordinate system using direction cosines,

$$\alpha_{\rho\sigma,fi} = \sum_{\rho'\sigma'} \alpha_{\rho'\sigma',fi} \cos(\rho\rho')\cos(\sigma\sigma') \tag{2.16}$$

where $\rho,\sigma = x,y,z$ and $\rho',\sigma' = x',y',z'$. Considering an experimental setup in which the incident beam of light propagates along the z-axis of the laboratory reference and has an electric field that is linearly polarized along the y-axis, and the scattered light is observed along the x-axis ($\theta = \pi/2$), the expectation value of the time-dependent induced transition dipole simplifies to,[30]

$$\langle(\vec{\mu}_{ind})_{fi}\rangle^2 = \langle(\mu_{ind,y})_{fi}\rangle^2 + \langle(\mu_{ind,z})_{fi}\rangle^2$$
$$= \left(\langle\alpha_{yy,fi}\rangle^2 + \langle\alpha_{zy,fi}\rangle^2\right)|\vec{E}_p|^2 \tag{2.17}$$

where the scattered light that results from the $\langle(\mu_{ind,y})_{fi}\rangle$ and $\langle(\mu_{ind,z})_{fi}\rangle$ terms has an electric field polarized along the y- and z-axes, respectively. Thus, the combination of the two components in Equation 2.17 describes the unpolarized expectation value of the induced transition dipole. We note that, for the unpolarized case, Equation 2.17 also holds for $\theta = 0, \pi$. For a sample of N_i molecules in the initial vibrational state, where we assume an isotropic distribution of molecular orientations (thus, classically averaging the cosine terms in Equation 2.16), we can define the unpolarized Raman activity as a function of the polarizability derivative terms,[29,30]

$$\langle\alpha_{yy,fi}\rangle^2 + \langle\alpha_{zy,fi}\rangle^2 = N_i \frac{45a_k'^2 + 7\gamma_k'^2}{45} = N_i \frac{S_k}{45} \tag{2.18}$$

$$a_k' = \frac{1}{3}\left[(\alpha_{xx}')_k + (\alpha_{yy}')_k + (\alpha_{zz}')_k\right] \tag{2.19}$$

12

$$\gamma_k'^2 = \frac{1}{2} \Big\{ \big[(\alpha_{xx}')_k - (\alpha_{yy}')_k \big]^2 + \big[(\alpha_{yy}')_k - (\alpha_{zz}')_k \big]^2$$
$$+ \big[(\alpha_{zz}')_k - (\alpha_{xx}')_k \big]^2 + 6 \big[(\alpha_{xy}')_k^2 + (\alpha_{yz}')_k^2 + (\alpha_{zx}')_k^2 \big] \Big\} \tag{2.20}$$

and, for the kth vibration, the elements of the polarizability derivative are given as:

$$(\alpha_{\rho\sigma}')_k = \left(\frac{\partial \alpha_{\rho\sigma}}{\partial q_k} \right)_0 . \tag{2.21}$$

where a_k' is the average isotropic polarizability, and γ_k' is defined as the anisotropy. Thus, the Stokes Raman scattering intensity, $I_k(\theta)$, is primarily a function of $(\boldsymbol{\alpha}')_k$ and the frequency of the scattered light, $(\tilde{v}_p - \tilde{v}_k)$,

$$I_k(\pi/2) \propto \frac{(\tilde{v}_p - \tilde{v}_k)^4}{1 - \exp[-hc\tilde{v}_k/k_BT]} \left(\frac{1}{\tilde{v}_k} \right) S_k \tag{2.22}$$

where the exponential term in the denominator accounts for the Boltzmann population summed over all levels of mode k.

2.3 Time-Dependent Theory of Resonance Raman Scattering

In this section, we summarize the main equations for the time-dependent theory of resonance Raman scattering for completeness, however, a more detailed theoretical formulation can be found in Chapter 6. In the previous section, we restricted the treatment of Raman scattering to static conditions ($\omega_p = 0$) under the assumption that the static case provides an accurate description of the experiment when the incident field is off-resonance. However, when the incident excitation field is at or near resonance with an electronic transition ($\omega_p \approx \omega_{ni}$), the Raman activity increases substantially, and the transition polarizability is no longer simply described by Equation 2.15. The enhancement of the Raman signal is a result of the small denominator in the first term of Equation 2.13, as ω_p approaches ω_{ni}. The second term in Equation 2.13 is negligible under resonance or near-resonance conditions.[29]

Assuming that the Born-Oppenheimer approximation holds, and in the limit of weak vibronic

coupling,[25,29,70,71] the expression for the transition polarizability under resonance conditions in Equation 2.13 reduces to a sum over the intermediate vibrational states, $|v_n\rangle$, of a single, resonant electronic state, $|N\rangle$. In the time-dependent formalism for resonance Raman scattering, the denominator in the first term of Equation 2.13 is converted from the frequency domain to the time domain through a Fourier transform,[27,29,72,73]

$$\alpha_{fi} \approx \frac{i}{\hbar} \sum_{v_n} \int_0^\infty \langle v_f | \vec{\mu}_{IN} | v_n \rangle \langle v_n | \vec{\mu}_{NI} | v_i \rangle e^{-i(\omega_n - \omega_i - \omega_p - i\Gamma_n)t} dt \qquad (2.23)$$

where $\langle v_f |$ and $|v_i\rangle$ are both within the initial electronic state $|I\rangle$, $\vec{\mu}_{NI}$ is the electronic transition dipole between the initial and intermediate electronic states, and ω_n and ω_i are the energies of the intermediate and initial vibronic states, respectively. The sum over vibrational states $|v_n\rangle$ gives a time-dependent wavepacket, $|v_i(t)\rangle$, that evolves according to the Hamiltonian, $\hat{H}_N$,[25,27,29,31] describing nuclear motion in the intermediate electronic state, $|N\rangle$. Thus, we recast Equation 2.23 as the time-integrated overlap of the wavepacket in the resonant state $|v_i(t)\rangle = e^{-i\hat{H}_N t/\hbar} |v_i\rangle$ with the vibrational wavefunction of the final state $\langle v_f |$,[53]

$$\alpha_{fi} \approx \frac{i}{\hbar} \int_0^\infty |\vec{\mu}_{NI}|^2 \langle v_f | e^{-i\hat{H}_N t/\hbar} | v_i \rangle e^{i(\omega_i + \omega_p + i\Gamma_n)t} dt . \qquad (2.24)$$

An implicit assumption in Equation 2.24 is that the electronic transition dipole follows the Condon approximation, which gives only the A term in the Albrecht description of Raman scattering.[29,74,75] The other Albrecht scattering terms (B, C, and D) include Herzberg-Teller (HT) vibronic coupling between electronic states. The vibronic coupling terms arise from a perturbative expansion of the transition dipole in the nuclear coordinates of intermediate electronic state $|N\rangle$,[29,31]

$$\vec{\mu}_{NI} = \left(\vec{\mu}_{NI} \right)_0 + \sum_j \left(\frac{\partial \vec{\mu}_{NI}}{\partial q_j^{(N)}} \right)_0 q_j^{(N)} + ... \qquad (2.25)$$

The derivative of the electronic transition dipole with respect to the nuclear coordinates $q_j^{(N)}$ of the

j^{th} mode,[29]

$$\left(\frac{\partial \vec{\mu}_{NI}}{\partial q_j^{(N)}}\right)_0 = \frac{1}{\hbar}\left\{\sum_{M\neq I}(\vec{\mu}_{NM})_0 \frac{\langle M|\left(\frac{\partial \hat{H}_{elec}}{\partial q_j^{(N)}}\right)|I\rangle}{\omega_I - \omega_M} + \sum_{M\neq N}\frac{\langle N|\left(\frac{\partial \hat{H}_{elec}}{\partial q_j^{(N)}}\right)|M\rangle}{\omega_N - \omega_M}(\vec{\mu}_{MI})_0\right\} \quad (2.26)$$

provides the vibronic coupling of electronic states $|N\rangle$ and $|I\rangle$ to other electronic states $\{|M\rangle\}$ through the perturbation of the electronic Hamiltonian ($\hat{H}_{elec}$), where ω_I, ω_N, and ω_M, are the energies of the corresponding electronic states. Substituting the expansion for $\vec{\mu}_{NI}$ and truncating Equation 2.25 at first order yields:

$$\begin{aligned}
\boldsymbol{\alpha}_{fi} \approx \frac{i}{\hbar}\int_0^\infty dt\, e^{i(\omega_i + \omega_p + i\Gamma_n)t}\bigg\{ & \left|(\vec{\mu}_{NI})_0\right|^2 \langle v_f|e^{-i\hat{H}_N t/\hbar}|v_i\rangle \\
& + \sum_j (\vec{\mu}_{IN})_0\left(\frac{\partial \vec{\mu}_{NI}}{\partial q_j^{(N)}}\right)_0 \langle v_f|e^{-i\hat{H}_N t/\hbar}q_j^{(N)}|v_i\rangle \\
& + \sum_j \left(\frac{\partial \vec{\mu}_{IN}}{\partial q_j^{(N)}}\right)_0 (\vec{\mu}_{NI})_0 \langle v_f|q_j^{(N)}e^{-i\hat{H}_N t/\hbar}|v_i\rangle \\
& + \sum_j\sum_l \left(\frac{\partial \vec{\mu}_{IN}}{\partial q_j^{(N)}}\right)_0\left(\frac{\partial \vec{\mu}_{NI}}{\partial q_l^{(N)}}\right)_0 \langle v_f|q_j^{(N)}e^{-i\hat{H}_N t/\hbar}q_l^{(N)}|v_i\rangle\bigg\}.
\end{aligned} \quad (2.27)$$

The first term on the right-hand side is the Albrecht A term from Equation 2.24. Together, the second and third terms on the right-hand side are the Albrecht B and C terms, where the B term includes coupling between intermediate state $|N\rangle$ and all other electronic states, and the C term includes coupling of the initial electronic state to the other electronic states. Similarly, the final term in Equation 2.27 accounts for D term scattering, which incorporates contributions from other electronic states coupled to $|N\rangle$ and $|I\rangle$ simultaneously. As in Equation 2.26, the B, C, and D terms scale with the inverse of the energy separation between coupled electronic states. It is worth noting that the calculated polarizability derivative from Equation 2.15 implicitly contains some degree of vibronic coupling for transitions in which only one vibrational quantum number changes.[29]

2.4 Gradient Approximation to the TD-RR Formalism

Due to the difficulty of evaluating Equations 2.24 and 2.27, a popular approach is the semi-classical "gradient approximation" to the TD-RR formalism.[53,71,72] In this approach, which is described in more detail in Chapter 6, the time-dependent overlap integral $\langle v_f | v_i(t) \rangle$ is simplified by approximating the initial wavefunction $|v_i(t)\rangle$ with a Gaussian function at $t = 0$, which then propagates in time on the intermediate state potential (V_N) according to the Hamiltonian of the intermediate electronic state. Substituting a Gaussian wavefunction into Equation 2.24, and using classical equations of motion to define the early time-evolution of the wavepacket based on the potential energy gradient of state N, $\frac{\partial V_N}{\partial q_k}$, we obtain the simplified version of the time-dependent overlap integral,[53,72]

$$\alpha_{fi}^k \approx -\frac{i}{\hbar} |\vec{\mu}_{NI}|^2 \left(\frac{\partial V_N}{\partial q_k} \right) \int_0^\infty \exp \left\{ i(\omega_i + \omega_p - \omega_{NI} + i\Gamma_n)t - \left(\frac{\partial V_N}{\partial q_k} \right)^2 \frac{t^2}{4\omega_k} \right\} t \, dt \qquad (2.28)$$

where ω_{NI} is the vertical transition energy between electronic states N and I. The spectral lineshape information contained within the integral in Equation 2.28 can be computationally expensive to evaluate. Nevertheless, the amplitude of the transition polarizability is proportional to the energy gradient and the square modulus of the electronic transition dipole, and the resonance-enhanced Raman scattering intensity of mode k can be obtained as,[53,54,76]

$$I_k \propto F(\tilde{v}_p, \tilde{v}_k) |\vec{\mu}_{NI}|^4 \left(\frac{\partial V_N}{\partial q_k} \right)^2 \qquad (2.29)$$

where $F(\tilde{v}_p, \tilde{v}_k)$ contains the dependence of the resonance-enhanced intensity on the frequencies of the incident and scattered light,

$$F(\tilde{v}_p, \tilde{v}_k) = \frac{\tilde{v}_p(\tilde{v}_p - \tilde{v}_k)^3}{1 - \exp[-hc\tilde{v}_k/k_B T]} \left(\frac{1}{\tilde{v}_k} \right). \qquad (2.30)$$

We note that the frequency dependence differs from that in Equation 2.22 due to the resonance condition. As detailed in the literature,[29,70,72,77] the second term in Equation 2.13 becomes rel-

atively insignificant on-resonance, which alters the dependence on the frequency of the incident light from $(\tilde{\nu}_p - \tilde{\nu}_k)^4$ to $\tilde{\nu}_p(\tilde{\nu}_p - \tilde{\nu}_k)^3$. Although Equation 2.29 neglects the time-dependent integral in Equation 2.28, it allows for the determination of resonance-enhanced Raman intensities from relatively inexpensive calculations of electronic transition dipoles and resonant-state potential energy gradients, which is particularly advantageous for simulating resonance Raman spectra in electronically excited states.

Chapter 3

Methods

3.1   Computational Methods

As outlined in Chapter 2, the calculation of Raman intensities both off- and on-resonance is determined by the transition polarizability, $\boldsymbol{\alpha}_{fi}^{k}$. In the off-resonance case, $\boldsymbol{\alpha}_{fi}^{k}$ is related to the polarizability derivative from Equation 2.15.[67] Therefore, the off-resonance Raman intensities are calculated using Equation 2.22, where the Raman activity, S_k, is a function of the derivative of the electronic polarizability with respect to mass-weighted vibrational displacement coordinates.[29,30,52] Although analytical polarizability derivatives have been implemented in various programs for ground electronic states, they are currently unavailable for excited states. Accordingly, we calculate the polarizability derivatives in electronically excited states numerically by stepping along the mass-weighted vibrational displacement coordinates of the calculated normal modes. The numerical derivative may contain errors due to the choice of step size of the vibrational displacements of each mode. A large step size is susceptible to errors due to anharmonicity, while the change in polarizability from very small displacements cannot be distinguished from computational noise. To find a good compromise between these two factors, we optimized the step size for the vibrational displacements based on comparisons with analytical calculations of Raman spectra for several small molecules (H_2, H_2O, CH_4, NH_3, methanol, and 2,2-dichloropropane) and theoretical methods. We included both wavefunction and density functional based methods (HF and B3LYP, respectively), and used the 6-31G* and aug-cc-pVDZ basis sets. The percent error between the numerical and analytical Raman activity was determined for each vibration in all molecules, and these errors were averaged to obtain the total average percent error at each step size. Figure 3.1,

which comes from the Supporting Information for Ref. #52. After fitting the errors in Figure 3.1 to a high-order (20th) polynomial, the step size with the minimum average error was determined to be at 7.408 x10^{-4} times the normalized displacement coordinate. As detailed in later chapters,
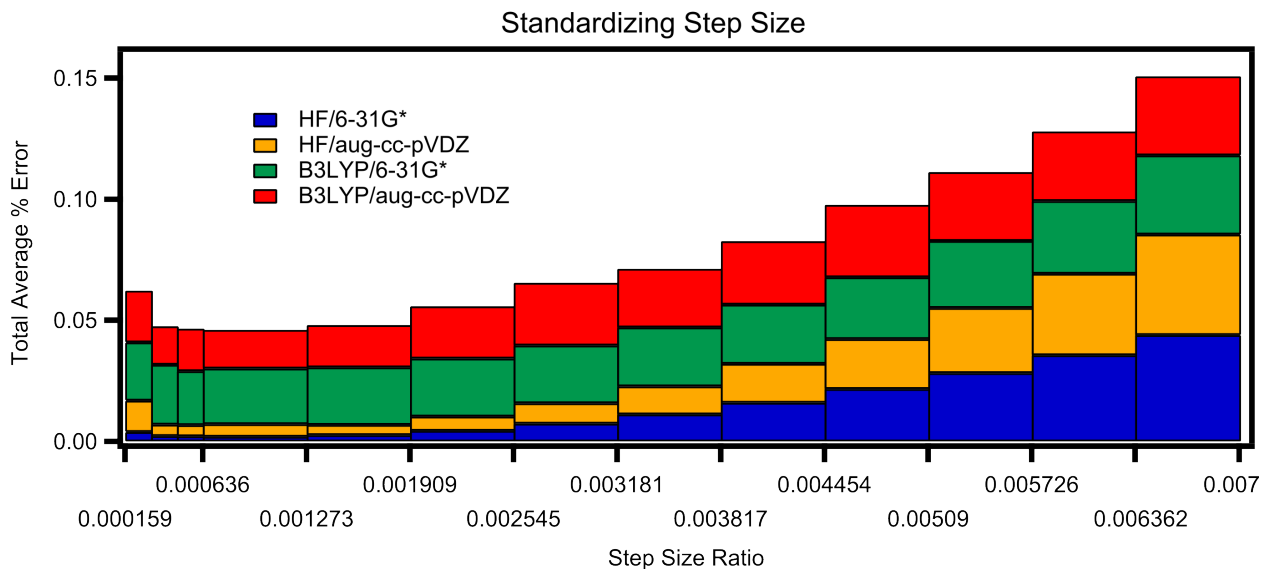
Figure 3.1: Standardization of the step size of the numerical polarizability derivative. The step size ratio is defined as a fraction of the unitless normal mode displacement of mass-weighted coordinates. The percent errors are averaged over each of the vibrations in the molecules at each level of theory to obtain the colored bars, and those values are averaged over methods at each step size to obtain the total average percent error.

the numerical derivative of polarizability was used primarily for time-dependent density functional theory (TD-DFT) methods and equation of motion coupled cluster theory with single and double excitations (EOM-CCSD), however, the derivative can be applied to any method for which the polarizabilities and normal modes are available.

Simulations of resonance-enhanced Raman spectra are calculated using Equation 2.27, which relies on the time-dependent theory of resonance Raman scattering (TD-RR) to define the time-dependent wavepacket $|v_i(t)\rangle = e^{-i\hat{H}_N t/\hbar}|v_i\rangle$.[25,27,29,31,72] Although the time-evolution of this wavepacket depends on the topology of the potential energy surface (PES) of the resonant electronic state, $|N\rangle$, the Raman intensity observed for a particular mode is calculated from the overlap of $|v_i(t)\rangle$ with the vibrational wavefunction, $\langle v_f|$, in $|I\rangle$, as well as the transition dipole, $\vec{\mu}_{NI}$, between $|N\rangle$ and the initial electronic state, $|I\rangle$. A direct implementation of Equation 2.27 has been described in

detail by Baiardi *et al.*,[31] where the calculation of only the first term, which contains no implicit vibronic coupling, corresponds to the Franck-Condon (FC) approximation, and the calculation of the first three terms of Equation 2.27 is referred to as the "FCHT" approach to denote the inclusion of Herzberg-Teller coupling. This approach, which is currently implemented in Gaussian,[78] uses the extrapolation of a harmonic potential expanded around the minimum-energy geometry of $|N\rangle$ in order to obtain the vibrational wavefunctions at the Franck-Condon geometry. Although the FCHT approach works well for ground-state resonance Raman spectra with resonant excitation to relatively low-lying electronic states,[31,76,79] FSRS measurements of electronically excited systems tend to be resonant with transitions to higher-lying states, where the density of states is larger and the PES of the states are more anharmonic. Thus, we also simulate resonance Raman spectra using Equation 2.29, which incorporates the gradient approximation to the TD-RR formalism.[53,54,72] As a result, the resonance-enhanced Raman intensities are obtained by calculating $\vec{\mu}_{NI}$ and the potential energy gradient in the resonant state, $\left(\frac{\partial V_N}{\partial q_k}\right)$, along the nuclear displacement coordinates of the vibrational modes of $|I\rangle$, where V_N is the potential energy of $|N\rangle$. The energy gradients are calculated numerically, using the same step size optimized for the polarizability derivatives. The transition dipoles between excited electronic states are obtained using Gaussian[78] for EOM-CCSD, and Dalton[80–83] for TD-DFT methods.

3.2 Experimental Methods

3.2.1 Overview

The photophysical dynamics and kinetics in this dissertation are observed using time-resolved transient spectroscopy techniques that incorporate an actinic pump pulse, a continuum probe pulse, and, in the case of transient Raman spectroscopy, a Raman pump pulse. Transient electronic absorption (TA) spectra are obtained by creating excited-state population with the actinic pump pulse and then measuring the absorption and stimulated emission using the probe pulse, varying the time delay between pulses to observe the kinetics following photo-excitation. We obtain resonance-

enhanced Raman spectra of transient electronic states in the molecules of interest by utilizing the time-resolved vibrational technique of resonant femtosecond stimulated Raman spectroscopy (R-FSRS).[22–24,84] By varying the delay between the actinic pump and the Raman pump and tuning the Raman pump excitation wavelength, we selectively probe the resonance Raman scattering in the excited singlet or triplet state of each of the compounds measured. As a result, information on the electronic transitions and excited-state dynamics observed in the TA spectra are complementary to the R-FSRS experiment. The experimental details are discussed within each chapter, therefore, Sections 3.2.2 and 3.2.3 will focus primarily on the technical aspect involved in the experimental analysis.

3.2.2   Transient Absorption Spectroscopy

The TA measurements utilize the modified outputs of an amplified Ti:sapphire laser (Coherent, Legend Elite) which produces 35 fs pulses at 800 nm with 1 kHz repetition rate. The tunable actinic pump pulses are generated by splitting the 800 nm fundamental and passing part of it into a commercial optical parametric amplifier (OPA) with two stages of frequency conversion that can produce pulses in the range 260-2600 nm, however, since our experiments focus on substituted thiophene compounds, we utilize actinic excitation wavelengths between 300 and 400 nm. The actinic pulse is then compressed via a fused-silica prism pair to a duration of $\sim$100 fs, as estimated from the full width at half maximum (FWHM) of cross-correlation measurements of two-photon absorption in glass. We generate fs probe pulses by focusing the other part of the 800 nm laser output into a translating CaF_2 window to produce broadband white-light (WL) pulses spanning 340-750 nm. Both pulses overlap in the sample, a flowing liquid jet with pathlength of 300 μm, before being dispersed by a grating (300 line/mm) onto a 2068 pixel linear CCD array (Hamamatsu, S11156-2048). A synchronized optical chopper is used to block every other pump pulse, allowing for time-resolved measurement of differential absorption, ΔA,

$$\Delta A(t) = -\log\left(\frac{I_{ON}}{I_{OFF}}\right) \tag{3.1}$$

where I_{OFF} is the intensity of light transmitted at each probe wavelength when the pump beam is blocked, and I_{ON} is the intensity observed when both the pump and probe beams are incident on the sample. To eliminate anisotropic effects, TA spectra are measured with the polarization of the pump and probe pulses set to be at "magic angle" (54.7°) with respect to each other. We account for cross-phase modulation effects[85,86] by plotting the peak intensity of the cross-correlation signal against probe wavelength, and fitting the signal to a fifth-order polynomial. The fit is then used to offset the time-dependence of the ΔA signal measured at each wavelength.

3.2.3 Resonant Femtosecond Stimulated Raman Spectroscopy (R-FSRS)

The R-FSRS technique utilizes an actinic pump pulse followed by a picosecond Raman pump pulse that is temporally overlapped with a WL probe pulse in order to produce stimulated Raman scattering with high spectral resolution (<30 cm^{-1}). We generate our actinic pump and probe pulses as described in Section 3.2.2, but, to maximize transient Raman signal, we set the polarization of all three pulses to be parallel to each other, and they intersect at a small angle in a flow cell with 1 mm thick CaF$_2$ windows and 0.5 mm pathlength. The Raman pump is generated by passing a third portion of the 800 nm fundamental into an additional commercial OPA, which provides tunable near-IR pulses that are subsequently passed through a 25 mm long β-barium borate (BBO) crystal to produce Raman pump pulses with high spectral resolution (<0.5 nm) via spectral compression of the second harmonic.[87–89] The Raman pump is then passed through a 4f spectral filter,[87] using a set-up that is described in detail in the dissertation of Dr. Timothy Quincy,[90] to produce pulses that have $\sim$1 ps duration and <30 cm^{-1} bandwidth. We account for background signals obtained from different combinations of the three pulses by chopping the actinic pump pulse at 500 Hz (as in Section 3.2.2) and the Raman pump pulse at 250 Hz. The R-FSRS signal is measured as a differential Raman gain, $\Delta Gain$, which we calculate using the combinations of pump and probe signals,

$$\Delta Gain = \left(\frac{I_{ON-ON}}{I_{ON-OFF}} \right) - \left(\frac{I_{OFF-ON}}{I_{OFF-OFF}} \right) \tag{3.2}$$

where $I_{OFF-OFF}$ is the signal measured when both actinic and Raman pumps are blocked, I_{OFF-ON} is measured with only the actinic pump blocked, I_{ON-OFF} is with only the Raman pump blocked, and I_{ON-ON} is with all beams present. Thus, the $\Delta Gain$ is calculated as the difference between the excited-state Raman gain and the ground-state Raman gain.

In order to isolate the R-FSRS signal from excited-state transient absorption, excited-state depletion, and ground-state stimulated Raman scattering signals, we perform baseline subtractions and solvent corrections. This steps for this procedure are displayed in Figure 3.2, which comes from the Supporting Information for Ref. #54, where the measurement of the Raman spectrum of the T_1 triplet state of 2-phenylthiophene (PT) is used as an example. As illustrated in Figure 3.2(a), the baseline corrections to the excited-state Raman gain, $\left(\frac{I_{ON-ON}}{I_{ON-OFF}}\right)$, and ground-state Raman gain, $\left(\frac{I_{OFF-ON}}{I_{OFF-OFF}}\right)$, are obtained by fitting each to a 15th order polynomial, masking the signals of known solvent bands. After subtracting the fits from the Raman gain signals, we obtain the baseline-corrected Raman spectra in Figure 3.2(b). Based on the Raman intensities of the solvent bands, we account for the attenuation of the Raman pump pulse due to resonant excitation of the T_1 state by scaling the ground-state Raman gain signal to match the intensities of the solvent Raman bands. The final R-FSRS signal is then obtained by subtracting the scaled ground-state Raman Gain from the excited-state Raman Gain spectrum, as shown in Figure 3.2(c).
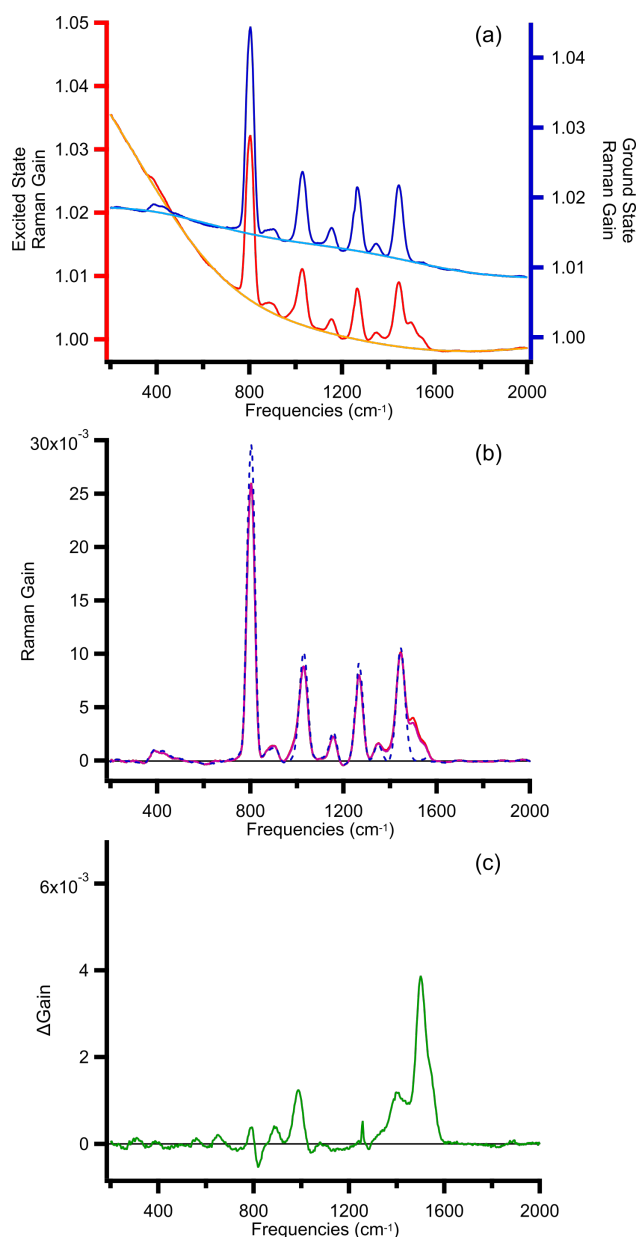
Figure 3.2: Sample procedure for the isolation of FSRS spectrum from background signals. (a) Excited-state Raman gain (red) and ground-state Raman gain (blue) signals for a solution of PT in cyclohexane at 365 nm Raman pump excitation. The baseline fits (orange, light blue) are subtracted from the Raman gain curves to obtain the baseline-corrected spectra. (b) The baseline-corrected ground-state Raman spectrum (dashed blue) is scaled by 0.877 (purple) to match the intensity of the 801 cm^{-1} cyclohexane band in the baseline-corrected excited-state Raman spectrum (red). The scaled Raman spectrum is then subtracted from the excited-state Raman spectrum to produce the ΔGain signal. (c) The baselined and solvent-corrected FSRS of the T$_1$ state of PT at 365 nm Raman excitation.

Chapter 4

Accurate Assignments of Excited-State Resonance Raman Spectra: A Benchmark Study Combining Experiment and Theory

(This work was published as Ref. #52. Supporting information is available online.)

4.1 Introduction

Femtosecond stimulated Raman scattering (FSRS) is a sensitive method for probing excited-state dynamics.[24,84] The technique reveals the structural evolution of a molecule by monitoring changes in the vibrational spectrum as a function of time following optical excitation. Correctly interpreting the excited-state dynamics therefore requires accurate assignments of the bands in the transient Raman spectrum. While some assignments are possible based on simple chemical intuition or comparison with known ground-state spectra, many assignments require at least some level of comparison with excited-state calculations. In general, the excited-state vibrational frequencies are relatively easy to calculate, but the Raman intensities are more difficult to obtain due to the need to calculate changes of the excited-state polarizability tensor along each of the normal mode coordinates. The intensities are important for comparison with experiment, because the frequencies alone may not provide enough information in regions of the spectrum with a relatively high density of states. An important and often overlooked complication is that experimental FSRS measurements often rely on mode-specific resonance enhancement effects in order to compensate for the small population of molecules in the excited state,[24,84,91] or to selectively probe a sin-

gle species in the transient spectrum.[34] Resonance enhancement effects are difficult to include in excited-state Raman calculations, because of challenges in treating higher-lying electronic states that are responsible for the resonant condition.

This chapter examines the assignment of excited-state Raman bands by comparing off-resonance calculations with experimental resonance-enhanced FSRS spectra for a series of π-conjugated molecules. The resonance enhancements are vibrational mode-dependent, leading to relative intensities in the experimental spectra that can be very different from the off-resonance calculations.[25,26,92] We show that a comparison across the entire series of benchmark compounds facilitates the assignment of the experimental transitions, even though a direct comparison of the calculated off-resonance intensities with the experimental spectrum for only a single molecule can be misleading and could result in incorrect assignments. The vibrational frequencies depend on the structure of the molecule, but modes with similar nuclear motions are enhanced for all of the molecules in the series because resonant excitation into the excited-state absorption bands causes a similar change of the π-conjugated structure for each molecule.

Our calculations neglect the resonance condition in an attempt to find a balance between accuracy and computational efficiency. More sophisticated methods that explicitly treat the resonance enhancement by directly simulating the third-order polarization response of an excited molecule are computationally expensive and would be prohibitive for calculating the spectra for a series of relatively large compounds.[23,93–99] Instead, our off-resonance calculations take advantage of efficient analytical second derivatives of the energy that are now available for time-dependent density functional theory (TDDFT) in order to calculate the excited-state polarizability.[100–103] Specifically, we calculate the excited-state Raman activities using single numerical differentiation of the (analytical) static polarizability tensor along each of the excited-state normal mode coordinates.[30] This method gives excited-state Raman spectra with DFT accuracy at relatively low computational cost. Earlier attempts to calculate Raman spectra from the excited-state polarizability required numerical differentiation of the electric dipole moment with respect to the electric field, in addition to the normal mode displacements.[104–106]

The series of compounds in our benchmark study consists of aryl-substituted thiophenes that are representative π-conjugated systems. Thiophene derivatives have been the subject of previous transient absorption[45–47] and FSRS studies[48–50,107] because of their importance as building blocks for photoactive polymers and molecular switches. Conjugated thiophenes also undergo rapid intersystem crossing (ISC), which is an important property for charge separation and transport in conductive organic materials.[38,41–43] The ISC rates depend on the structure of the compound, and range from tens to hundreds of picoseconds.[47] We compare the calculated and experimental Raman spectra for both singlet and triplet excited states of each molecule in order to evaluate resonance enhancement effects in the different spin states. In general, we find that the calculated off-resonance intensities are in better agreement with resonance-enhanced experimental spectra for triplet states compared with singlet states. Comparing trends in the calculated and experimental spectra across the entire series of molecules allows us to make accurate assignments for both the singlet and triplet states using relatively low-cost off-resonance excited-state calculations, provided the electronic resonance condition is taken into consideration.

4.2   Methods

The series of aryl-substituted thiophene derivatives includes 2,5-diphenyl-thiophene (DPT), 2-phenyl-thiophene (PT), 2-methyl-5-phenyl-thiophene (MPT), 2,4-dimethyl-5-phenyl-thiophene (DMPT), 2,5-terthiophene (TT), 2,2'-bithiophene (2,2'-BT), 2,3'-bithiophene (2,3'-BT), and 3,4'-dihexyl-2,2'-bithiophene (DHBT). All compounds were obtained commercially and used as received by dissolving in cyclohexane (1-10 mM).

Transient absorption and stimulated Raman measurements use the modified output of an amplified Ti:Sapphire laser (Coherent Legend Elite). An optical parametric amplifier (OPA) and two stages of nonlinear frequency conversion provide ~80 fs actinic pulses at 310 nm that are attenuated to 0.5-0.9 μJ at the sample. The frequency-doubled output of a second OPA passes through a 25 mm long BBO crystal to produce ps-duration Raman pump pulses via second harmonic generation (SHG), followed by a $4f$ spectral filter for additional spectral narrowing and rectification.[87,108]

The resulting Raman pump pulses are tunable over the range 350–650 nm, with bandwidths of $\sim$15-30 cm^{-1} and pulse energies up to 1 μJ. The fs broadband probe pulses come from continuum generation in a circularly translating CaF$_2$ substrate. After the sample, a spectrograph disperses the probe light onto a linear CCD array detector with 2048 pixels. We use an adapted version of the scanning multichannel technique developed by Challa *et al.*[109] in order to reduce systematic noise from the variable pixel response of the CCD array. Specifically, we obtain FSRS spectra by averaging measurements at five different grating angles in the spectrograph with approximately 20 cm^{-1} shift between individual spectra. The baseline subtraction method is described in the supplemental information (SI). We record off-resonant ground-state Raman spectra using a commercial Raman spectrometer (StellarNet) with 785 nm laser source and 4 cm^{-1} resolution. We remove solvent bands from the ground- and excited-state Raman spectra by subtraction. The experimental procedures are described in more detail elsewhere.[53]

We calculate off-resonance Raman spectra by applying the polarizability derivative approach of Neugebauer *et al.*[30]. In the case of the excited-state Raman calculations, we first obtain the S$_1$ or T$_1$ minimum energy geometry and normal mode coordinates analytically using TDDFT with the B3LYP functional[110–112] and aug-cc-pVDZ basis set.[113] The Raman activities are then obtained by taking numerical derivatives of the excited-state static polarizability tensor with respect to displacements along the normal mode coordinates. We determine the optimum step size for the normal mode displacements based on comparison with analytical ground-state Raman calculations for several small molecules and various levels of theory (Figure S1 in the SI). Numerical differentiation at the standardized step size gives Raman activities that are nearly identical to the analytical results for S$_0$. We use the same step size for the excited-state calculations. A recent benchmarking study by Staniszewska *et al.*[114] motivates our choice of B3LYP/aug-cc-pVDZ. All calculations were performed using a development version of the GAUSSIAN suite of programs.[78]

4.3 Results and Discussion

4.3.1 Transient Absorption Spectroscopy and Excited-State Dynamics

Figure 4.1 shows the transient electronic absorption spectra for the series of aryl-substituted thiophene derivatives following $\pi \rightarrow \pi^*$ excitation with an actinic pulse near 310 nm. The transient spectrum of each compound is characterized by strong excited-state absorption (ESA) and stimulated emission (SE) bands of the singlet S_1 excited state at short time delays. Although not shown here, the spectra evolve on a timescale of a few ps due to structural relaxation and vibrational cooling, including planarization of the molecule in response to the increased double-bond character of the inter-ring C–C bonds in the $\pi\pi^*$ state.[47] All of the molecules eventually undergo intersystem crossing (ISC) to a triplet excited state, T_1, at longer delay times. The intersystem crossing times (τ_{ISC}) vary from 22 to 267 ps, depending on the structure of the molecule, and are summarized in Table 4.1. The triplet states are relatively long-lived (> 1 ns), and have ESA bands at shorter wavelengths compared with the singlet excited states.

The relatively fast $S_1 \rightarrow T_1$ relaxation times are a result of strong spin-orbit coupling of the thiophene sulfur atom, with non-planar geometries accelerating the ISC.[47] Accordingly, the ISC rate increases for molecules with more than one sulfur atom, and for molecules that have steric interactions that destabilize the planar geometry of the S_1 excited state. The three-ring compounds DPT and TT have the longest τ_{ISC} due to increasing conjugation that favors a more planar structure in the excited state.[115]

In order to measure the stimulated Raman spectra of the singlet and triplet excited states, we tune the Raman pump wavelength close to the maximum of the respective ESA band (red and green arrows in Figure 4.1), and adjust the delay between actinic pump and Raman probe pulses accordingly. The S_1 spectra are measured at delays ranging from 5 to 30 ps to allow vibrational relaxation and cooling in the singlet state, but before ISC begins to populate the triplet state. The T_1 spectra are obtained at delays that are about four times longer than the ISC time of each molecule to ensure significant conversion to the triplet state. Table 4.1 gives the experimental time delays
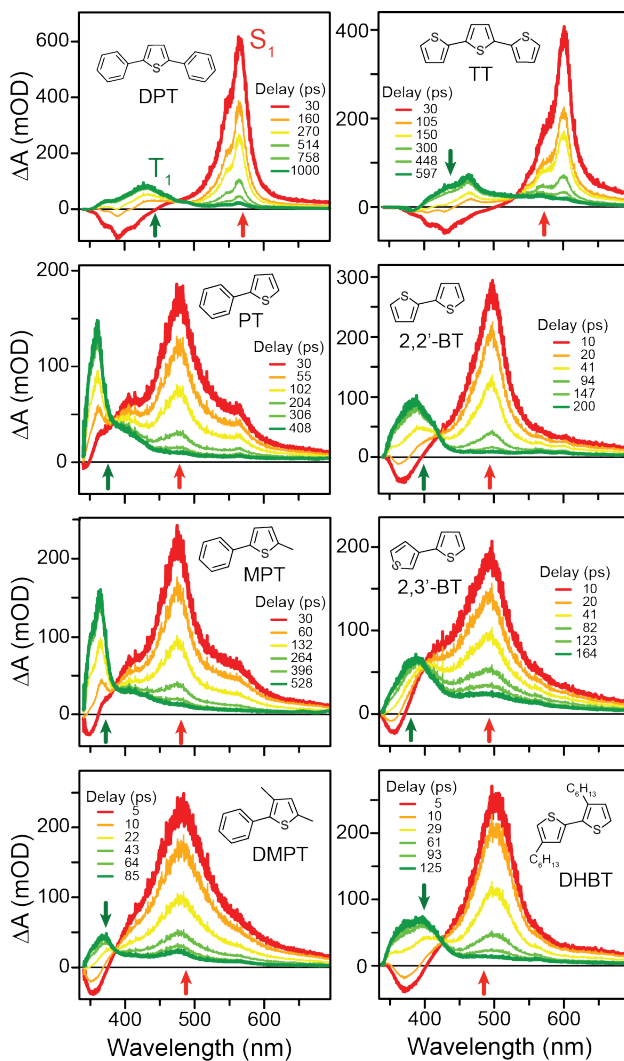
Figure 4.1: Transient absorption spectra showing the evolution from S_1 (red) to T_1 (green) excited states for the series of aryl-substituted thiophene derivatives. Red and green arrows indicate the Raman pump wavelengths for stimulated resonance Raman measurements of the singlet and triplet excited states, respectively.

Table 4.1: Intersystem crossing lifetimes and FSRS delay times[a]

	τ_{ISC}	S_1 delay	T_1 delay
DPT	267	30	1000
PT	102	30	410
MPT	132	30	530
DMPT	22	5	85
TT	149	50	595
2,2'-BT	41	10	200
2,3'-BT	37	10	165
DHBT	29	5	125

[a] All times in ps.

for the singlet and triplet FSRS measurements.

4.3.2 Ground-State Raman Spectroscopy

Before examining the excited-state Raman spectra, we compare the calculated and experimental spectra for the ground electronic state of each molecule in Figure 4.2. The S_0 spectra are off-resonant for both experiment and theory. Comparing the calculated ground-state spectra with experiment provides an important reference point for estimating the accuracy of the DFT calculations. The accuracy in the ground state is the best that can be expected for the excited-state calculations based on inherent limitations of the method and basis set (B3LYP/aug-cc-pVDZ). To facilitate the comparison between ground and excited states, the ground state calculations use the same numerical differentiation along the normal mode coordinates that we use for the excited states below, even though analytical derivatives are available for the ground state. The numerical derivatives give Raman activities that differ from the analytical derivative results by <0.05%.

As expected, the calculated vibrational frequencies overestimate the experimental values, therefore we apply an empirical frequency scaling factor. A scaling factor of 0.976 gives the best agreement across the entire series of molecules (see below), consistent with the commonly accepted value of 0.970 for this level of theory and basis set.[116] We also broaden each transition in the calculated spectrum with a 15 cm^{-1} Gaussian in order to simulate the experimental line widths in

Figure 4.2.

The ground-state calculations generally are in good agreement with the experimental Raman spectra for S_0. In most cases, the calculations reproduce the experimental frequencies within $\sim$20 cm^{-1} and the intensities within an order of magnitude, which is typical for DFT.[14,117,118] For example, the calculations accurately reproduce the dominant C=C ethylenic stretches in the frequency range $\sim$1400-1700 cm^{-1}. The only discrepancies in this region are for DHBT, DMPT, and MPT, each of which has one or two bands with slightly higher relative intensity in the experiments than predicted by theory. We note that these three are the only alkyl substituted compounds, and that the orientations of the methyl and hexyl side groups might affect the calculated spectra. Although the conformational dependence is important, it is beyond the scope of this work.

The S_0 calculations also slightly underestimate the relative intensities of some of the lower-frequency modes. Figure 4.2 shows the low-frequency region of the calculated spectra on an expanded scale in order to facilitate the comparison in this region. Although the relative intensities are underestimated by up to an order of magnitude, the calculated frequencies are in very good agreement with experiment. The most notable discrepancy is the relatively strong experimental band just below 1000 cm^{-1} for the phenyl-substituted thiophenes MPT, PT, and DPT, where the experimental intensities more closely match the spectra on the 10x expanded scale. Previously reported computational and experimental spectra for the S_0 state of DPT also have an approximately tenfold difference in the relative intensity of the $\sim$1000 cm^{-1} band, consistent with our observation.[118]

4.3.3 Resonance Raman Spectroscopy of T_1

We examine the calculated and experimental Raman spectra of the triplet excited states in Figure 4.3. As is the case for the S_0 spectra, the T_1 calculations use the numerical differentiation procedure, even though T_1 is the lowest triplet state and therefore can be treated as a ground state to obtain analytical derivatives of the polarizability. All of the spectra from the off-resonant T_1 calculations are dominated by a single, strong band near 1500-1550 cm^{-1}, with much weaker transitions
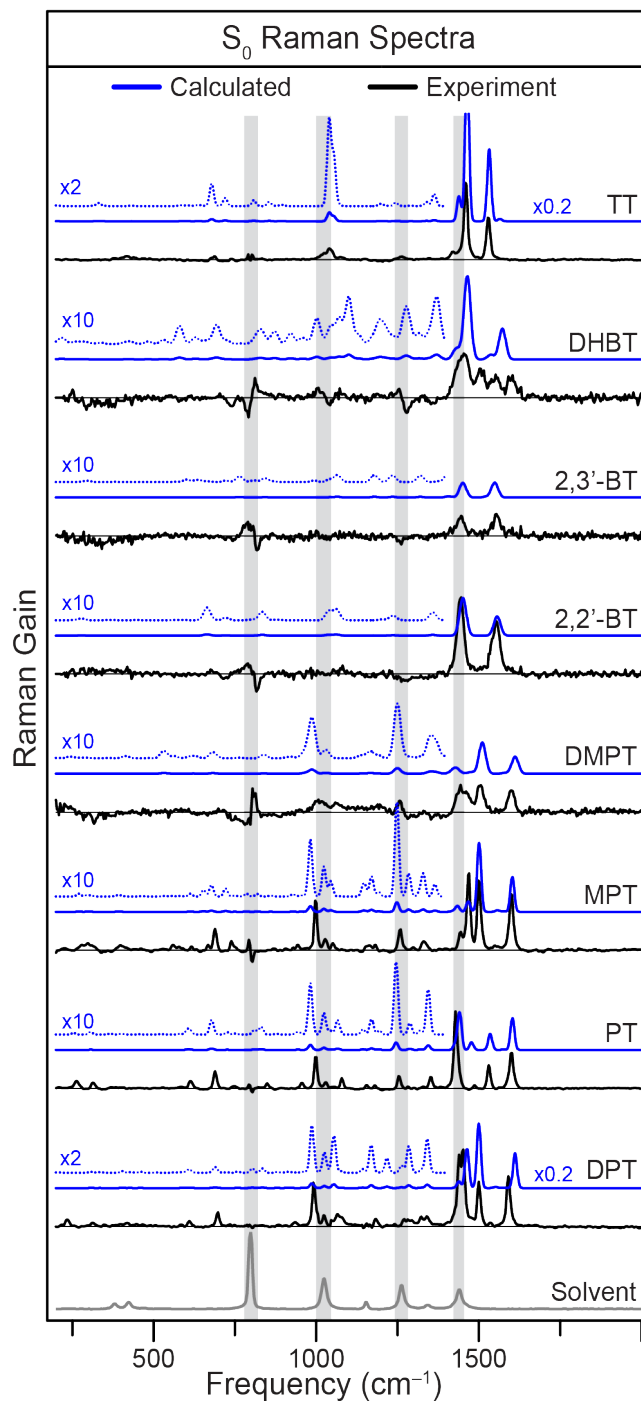
Figure 4.2: Raman spectra of the ground electronic states. Calculated spectra (blue lines) are shown on a common intensity scale, except TT and DPT are reduced by a factor of 5. The the low-frequency region of each spectrum is also shown on an expanded scale (dotted blue lines, 10x). Experimental spectra in cyclohexane solution (black lines) are measured off-resonance using either spontaneous Raman at 785 nm (TT, MPT, PT, DPT) or stimulated Raman at 370 nm (DHBT, 2,3'-BT, 2,2'-BT, DMPT). The solvent spectrum is shown for reference, and to indicate where there may be subtraction errors in the experimental spectra.

at lower frequencies. We obtain the best agreement with the experimental frequencies by using a scaling factor of 0.964, as discussed in more detail below. We apply 25 cm^{-1} Gaussian broadening to the calculated transitions in the figure in order to match the experimental resolution.

Unlike the S_0 spectra, the experimental T_1 spectra are obtained with Raman pump wavelengths that are resonant with an excited-state (triplet-triplet) absorption band. Despite the resonance condition, the calculated spectra are generally in good agreement with experiment, including the most prominent transitions in the ethylenic stretching region, ∼1400-1700 cm^{-1}. The bithiophene compounds (DHBT and BT) and terthiophene (TT) have only a single, strong band in this region, whereas the spectra of all four phenyl-substituted thiophenes have an additional shoulder. The shoulders appear as distinct transitions in the calculated spectra of MPT and PT.

Compared with the ethylenic stretching modes, many of the weaker transitions in the lower-frequency regions of the experimental T_1 spectra are more difficult to distinguish from noise. However, there are several transitions that are reproduced by the calculations, such as the pair of peaks representing the phenyl stretching modes near 894 cm^{-1} and 986 cm^{-1} for DMPT, MPT, and PT. In a few cases, the experimental bands are much stronger than the calculations predict. For example, the prominent bands near 343 cm^{-1} in the experimental spectra of TT and DHBT are significantly stronger than any of the calculated modes in that region.

The significantly higher experimental intensities of the low-frequency bands is probably due to the resonance condition. Analogous with ground-state resonance Raman spectroscopy,[26,92] we expect an additional enhancement for vibrational modes that have a large displacement in the upper triplet states relative to the minimum-energy structure of T_1.[38] Resonance enhancement also explains the emergence of the broad Raman features near 650–750 cm^{-1} in the experimental spectra of DMPT, MPT, and PT, as well as the relative increase in the intensity of the experimental bands of DPT near 340, 541, and 1134 cm^{-1}. Overall, the generally good agreement between the off-resonant calculations and the resonant experimental stimulated Raman spectra suggest that the resonance condition does not significantly affect the triplet spectra, with the exception of a few specific low-frequency modes.
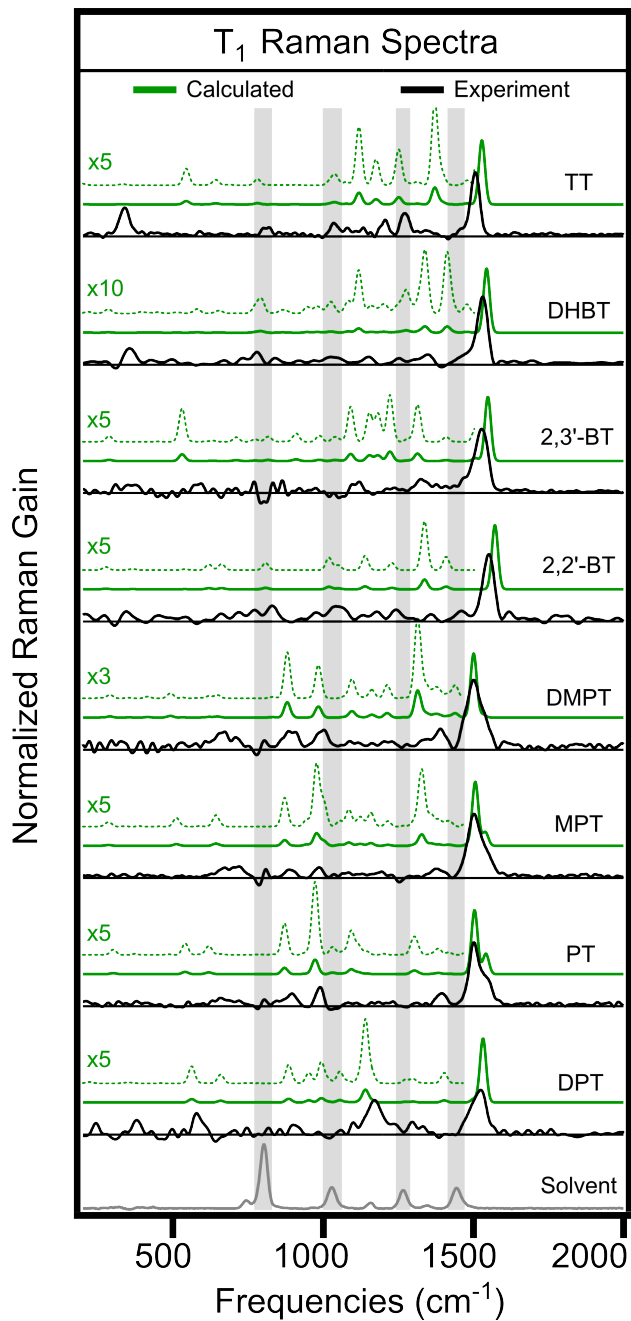
Figure 4.3: Raman spectra of the triplet states. Calculated spectra (green lines) are normalized to the most intense peak of each molecule, with the low-frequency region of each spectrum also shown on an expanded scale (dotted green lines). Experimental spectra (black) are measured in resonance with the T_1-T_n absorption band of each compound, and are also normalized to the most intense peak of each spectrum. The solvent spectrum is shown for reference, and to indicate where there may be subtraction errors in the experimental spectra.

4.3.4   Resonance Raman Spectroscopy of S_1

The Raman spectra of the singlet excited states are the main focus of this work. Figure 4.4 shows the experimental and calculated spectra for the S_1 state of each molecule. The calculated spectra include 25 cm^{-1} Gaussian broadening, and a frequency scaling factor of 0.977. As before, all of the strongest bands in the calculated off-resonance spectra are in the ethylenic range, 1400–1700 cm^{-1}, with the lower-frequency transitions having much lower intensity. In sharp contrast with the S_0 and T_1 results, however, some of the low-frequency modes are among the *strongest* bands in the experimental spectra of the S_1 excited states.

The stark discrepancy between the relative intensities in the experimental and calculated spectra indicates that the resonance condition plays a significant role for the S_1 excited states. Based on the time-dependent formalism for resonance Raman spectroscopy,[26,92] the resonance enhancement of a given vibrational mode depends on the relative displacement of the higher-lying excited-state potential energy surface along the normal mode coordinate of the lower-lying electronic state. In the case of the singlet excited-state FSRS spectra, the resonance enhancement comes from the displacement of the molecule in the S_n excited states relative to the initial S_1 state. We examine this resonance condition in more detail elsewhere,[53] but we note that all of the compounds in this study have similar ESA bands due to secondary π excitation from S_1. Therefore, we predict the strongest enhancements for vibrational modes that are most sensitive to changes in the occupancy of conjugated π and π^* orbitals.

Some of the most notable resonance enhancements in the experimental S_1 Raman spectra include the bands in the range 650–700 cm^{-1} for TT, 2,2'-BT, MPT, PT, and DPT, and near 333 cm^{-1} for DHBT, 2,3'-BT, and DMPT. These are the strongest bands in each of the experimental spectra, even though the off-resonant calculations show only very weak transitions below ~1400 cm^{-1}. Despite neglecting the resonance condition in the calculations, we can still use the calculated spectra to help assign the experimental transitions based on the frequencies. However, we show below that it is also important to consider the specific nuclear motions associated with each vibration in order to determine which transitions gain intensity from the resonance condition. Fig-

36
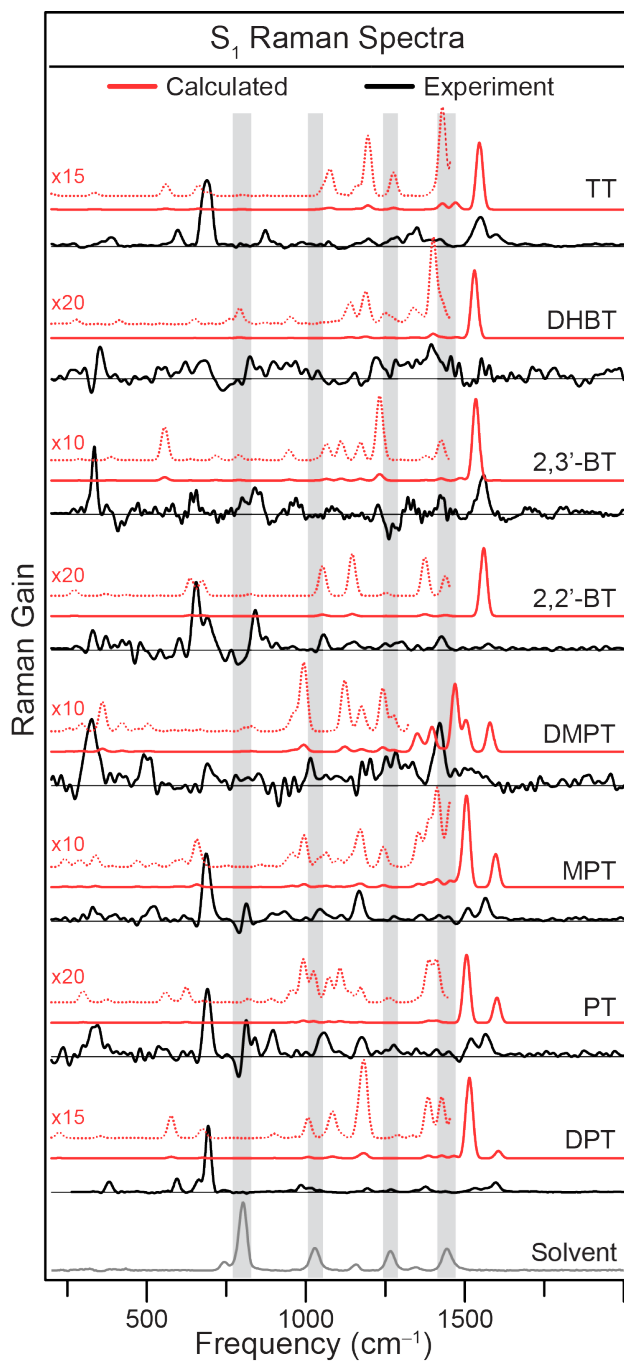
Figure 4.4: Raman spectra of the S_1 excited states. Calculated spectra (red lines) are normalized to the most intense peak of each molecule, with the low-frequency region of each spectrum also shown on an expanded scale (dotted red lines). Experimental spectra (black lines) are measured in resonance with the strong S_1-S_n absorption band of each compound, and are also normalized to the most intense peak of each spectrum. The solvent spectrum is shown for reference, and to indicate where there may be subtraction errors in the experimental spectra.

37

ure 4.4 shows each of the calculated spectra on an expanded scale below $\sim$1450 cm^{-1} to facilitate the comparison.

4.3.5   Resonance Raman Band Assignments for S_1

As a first step in assigning the S_1 transitions, we evaluate the accuracy of the calculated frequencies by considering the empirical scaling factors in more detail. The scaling factors reported above for the S_0, T_1, and S_1 states were obtained by comparing the most prominent experimentally observed transitions with the calculated frequencies for all of the molecules. Rather than making the assignments and frequency comparisons by inspection alone, we compare the calculated vibrational motions across the series of molecules in order to refine our initial assignments, as described in the example below. Table 4.2 lists the assigned transitions. The resulting calibration curves in Figure 4.5 include a total of 30–40 transitions for each state, and give scaling factors for all three states (0.976 $\pm$ 0.001 for S_0, 0.964 $\pm$ 0.003 for T_1, and 0.977 $\pm$ 0.003 for S_1) that are in close agreement with the commonly accepted value of 0.970 for ground-state calculations using B3LYP/aug-cc-pVDZ.[116]

Table 4.2: Vibrational Band Assignments[a]

Molecule	S_0			T_1			S_1		
	Mode	Calc.	Exp.	Mode	Calc.	Exp.	Mode	Calc.	Exp.
TT	ν_{54}	1532	1528	ν_{55}	1528	1506	ν_{55}	1546	1547
	ν_{52}	1464	1459	ν_{47}	1251	1272	ν_{52}	1430	1417
	ν_{50}	1439	1417	ν_{45}	1176	1207	ν_{45}	1196	1197
	ν_{25}	720	741	ν_{38}	1037	1034	ν_{32}	847	873
	ν_{23}	679	678	ν_{30}	781	810	ν_{25}	695	693
				ν_6	331	339	ν_{17}	560	597
							ν_{10}	336	388
DHBT	ν_{118}	1465	1454	ν_{120}	1544	1531	ν_{120}	1531	1562
				ν_{98}	1337	1348	ν_{103}	1400	1394
				ν_{51}	787	780	ν_{41}	652	685
				ν_{26}	287	355	ν_{31}	414	354
2,3'-BT	ν_{36}	1549	1554	ν_{36}	1548	1528	ν_{36}	1535	1560
	ν_{34}	1451	1446	ν_{33}	1314	1326	ν_{34}	1426	1422
				ν_{28}	1091	1108	ν_{28}	1111	1082
				ν_7	384	349	ν_{20}	826	839
							ν_{15}	636	645
							ν_7	387	334
2,2'-BT	ν_{36}	1557	1550	ν_{36}	1572	1551	ν_{36}	1560	1575
	ν_{34}	1451	1446	ν_{27}	1050	1043	ν_{35}	1439	1427
				ν_7	365	335	ν_{29}	1146	1152
							ν_{26}	1056	1056
							ν_{20}	826	841
							ν_{16}	674	690

Molecule	S$_0$ Mode	S$_0$ Calc.	S$_0$ Exp.	T$_1$ Mode	T$_1$ Calc.	T$_1$ Exp.	S$_1$ Mode	S$_1$ Calc.	S$_1$ Exp.
							v_{14}	637	656
DMPT	v_{57}	1611	1601	v_{56}	1501	1502	v_{54}	1469	1420
	v_{54}	1511	1507	v_{50}	1386	1392	v_{43}	1276	1282
	v_{49}	1427	1448	v_{34}	983	999	v_{22}	667	690
	v_{42}	1249	1255	v_{28}	881	894	v_{16}	504	496
	v_{36}	1030	1059				v_{14}	422	326
	v_{32}	987	1007						
MPT	v_{50}	1603	1599	v_{49}	1506	1501	v_{50}	1597	1564
	v_{47}	1501	1499	v_{44}	1384	1379	v_{49}	1506	1511
	v_{46}	1468	1470	v_{31}	978	986	v_{42}	1368	1363
	v_{38}	1248	1260	v_{24}	872	889	v_{36}	1160	1167
	v_{29}	982	997				v_{32}	1041	1044
	v_{17}	677	689				v_{20}	670	688
	v_{16}	654	667				v_{13}	524	522
	v_{15}	613	616				v_{10}	391	330
	v_{9}	389	399						
PT	v_{43}	1604	1599	v_{42}	1504	1501	v_{43}	1601	1566
	v_{41}	1535	1530	v_{39}	1384	1394	v_{42}	1506	1521
	v_{39}	1441	1429	v_{28}	975	989	v_{35}	1265	1277
	v_{37}	1344	1351	v_{22}	871	895	v_{32}	1138	1176
	v_{34}	1245	1253				v_{29}	1056	1056
	v_{26}	982	997				v_{23}	891	897
	v_{14}	678	689				v_{17}	679	690
	v_{11}	604	612				v_{11}	558	537
	v_{10}	583	583				v_{7}	374	343
	v_{5}	307	315						
	v_{4}	254	264						
DPT	v_{68}	1611	1591	v_{68}	1532	1490	v_{69}	1606	1598
	v_{64}	1500	1500	v_{52}	1141	1134	v_{67}	1519	1532
	v_{62}	1464	1446	v_{18}	562	539	v_{59}	1384	1377
	v_{45}	1056	1067	v_{10}	350	340	v_{53}	1186	1193
	v_{41}	988	991				v_{40}	969	984
	v_{23}	687	698				v_{25}	675	693
	v_{19}	609	610				v_{18}	577	594
	v_{18}	589	585				v_{10}	353	382
	v_{10}	335	351						
	v_{9}	309	313						

a) Calculated frequencies have been multiplied by a scaling factor of 0.976 for S$_0$, 0.964 for T$_1$, and 0.977 for S$_1$.

The strong correlation between experimental and theoretical frequencies suggests that, on average, the calculations accurately reproduce the excited-state vibrations within ∼20-30 cm^{-1} after applying the empirical scaling factor. Thus, relatively isolated vibrations are easy to assign based on frequencies alone. More congested regions of the spectrum require closer inspection and careful consideration of resonance enhancement effects. For example, Figure 4.6 shows the 450-900 cm^{-1} region of the S$_1$ spectrum for MPT, PT, and DPT. In contrast with the single, strong experimental
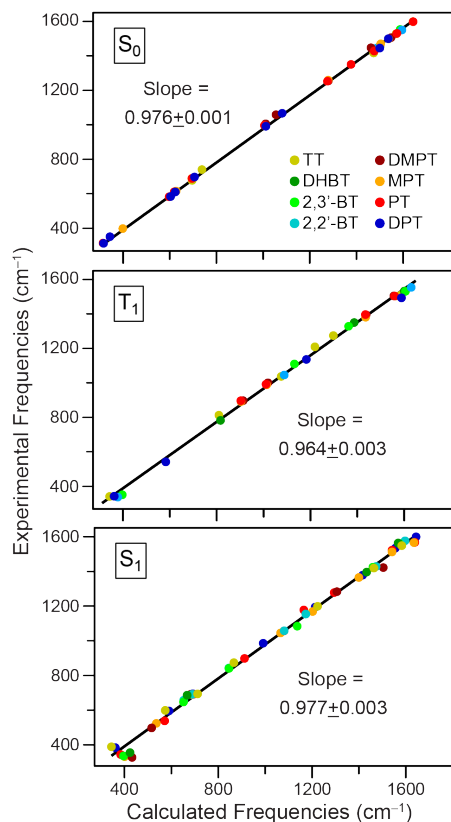
Figure 4.5: Calibration curves comparing the frequencies of the most prominent experimental bands with the calculated frequencies of the assigned transitions for S_0, T_1, and S_1. The slopes of the best-fit lines give the frequency scaling factors.

bands near $690\ \mathrm{cm}^{-1}$, the strongest calculated transitions of the three molecules vary by almost 100 cm^{-1}. Although it is tempting to assign the experimental transitions based on the most prominent bands in the calculated spectra, the variation of the calculated frequencies compared with the relatively invariant experimental values suggests that mode-specific resonance enhancement effects are important. In order to make the assignments, we exploit the fact that only transitions to the totally symmetric vibrational modes of a molecule are enhanced by resonant excitation.[29,118] Transitions to non-totally symmetric modes will not contribute to strongly resonance-enhanced FSRS spectra like those considered here. Furthermore, resonance enhancement effects are most pronounced for vibrational modes that are Franck-Condon active in the resonant (upper) electronic state.

The S_1 state of DPT has fifteen calculated vibrations in the range 500-800 cm^{-1}. Twelve of those vibrations are non-totally symmetric modes that can be neglected using symmetry arguments

40
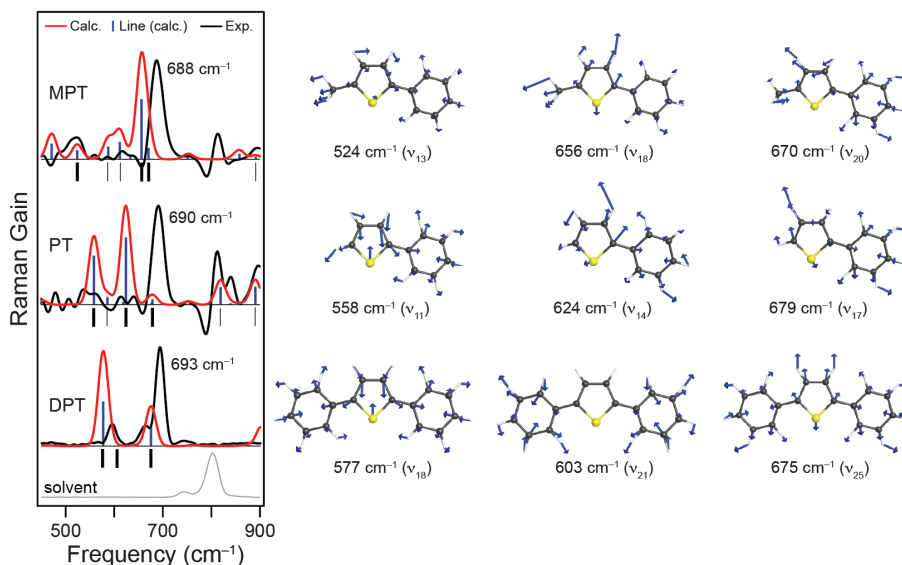
Figure 4.6: Comparison of the experimental (black) and calculated (red) S_1 spectra of MPT, PT, and DPT. Black bars under the spectra indicate which of the calculated modes are totally symmetric (a' in PT and MPT; a_1 in DPT). The images on the right-hand side show vibrational displacement vectors for selected transitions that are indicated by bold black bars below the spectra.

from above.[29] The transition energies of the three totally symmetric (a_1) vibrations of DPT are indicated by vertical black bars immediately below the experimental and calculated spectra in Figure 4.6. The nuclear displacement vectors on the right side of the figure show that the calculated vibrations at 577 cm^{-1} (ν_{18}) and 675 cm^{-1} (ν_{25}) are combinations of in-phase phenyl ring distortions with the symmetric C–S–C bending and stretching modes of the thiophene ring, respectively. The phenyl motions are similar to the 6a vibration in Wilson's notation for substituted benzene compounds,[119] which typically has strong Raman activity. In contrast, the third a_1 vibration at 603 cm^{-1} involves a phenyl ring distortion that is similar to the 6b vibration in Wilson's notation.[119] The 6b vibration typically has very weak Raman activity, consistent with our calculated spectrum for DPT.

In addition to the larger off-resonance Raman activities, modes ν_{18} and ν_{25} are more likely to be Franck-Condon active under π excitation than the more localized motion of the 603 cm^{-1} mode (ν_{21}). We expect π excitation to be delocalized across the entire molecule, therefore the delocalized modes are more likely to gain intensity in the resonance enhanced FSRS spectrum. Thus, we identify the experimental FSRS bands at 594 cm^{-1} and 693 cm^{-1} as ν_{18} and ν_{25}, respectively,

41

based on symmetry and resonance enhancement considerations. The different relative intensities of the transitions to v_{18} and v_{25} in the experimental and calculated S_1 spectra are probably a result of stronger resonance enhancement of the higher-frequency mode. A stronger enhancement of v_{25} suggests that the upper state in the S_1–S_n transition may have a larger displacement along the C–S–C stretching coordinate compared with C–S–C bending. We tentatively assign the weak shoulder near 670 cm^{-1} in the experimental spectrum of DPT as an overtone or combination mode, based on the intensity dependence as a function of excitation wavelength, described elsewhere.[53]

The band assignments are not as obvious for the lower-symmetry molecules PT and MPT, because fewer transitions can be excluded based on symmetry alone. Nevertheless, we determine that the strongest experimental transitions in the 500-800 cm^{-1} region are not the same as the strongest transitions in the calculated off-resonant spectra for these two molecules. Specifically, we assign the dominant experimental bands of PT and MPT as the relatively weak calculated transitions at 679 cm^{-1} (v_{17}) and 670 cm^{-1} (v_{20}), respectively, based on the strong correlation between experimental and calculated frequencies, as well as the similar nuclear motions compared with the v_{25} mode of DPT.

The motions of the assigned vibrations for all three molecules, illustrated on the far right side of Figure 4.6, have similar phenyl deformation (6a in Wilson's notation) and delocalized character that is likely to be Franck-Condon active. In contrast, the strongest transition in the calculated spectrum of MPT (v_{18}, 656 cm^{-1}) is primarily localized on the thiophene ring, and includes significant displacement of the methyl group. Although the 656 cm^{-1} mode has more intensity in the off-resonance spectrum, the π conjugated electronic resonance is not likely to give a strong enhancement in this methyl rocking mode.

In the case of PT, the strongest calculated transition (v_{14}) is more than 65 cm^{-1} below the experimental band, compared with only 11 cm^{-1} for the assigned mode, v_{17}. Furthermore, v_{14} has an asymmetric distortion of the phenyl ring that is less likely to be Franck-Condon active than the symmetric 6a-type distortion of the assigned mode. The next closest totally symmetric (a') vibration in the calculated spectrum is the mode at 586 cm^{-1}, which has a 6b-type phenyl

distortion (not represented in the figure) that is similar to the very weak 603 cm^{-1} mode in DPT. Neither of the 6b-type modes contribute to the FSRS spectra.

The other band with notable intensity in this region of the spectrum for PT is the calculated transition to ν_{11} at 558 cm^{-1}. This mode is a combination of C–S–C bend and phenyl ring deformation that is similar to the 577 cm^{-1} (ν_{18}) mode in DPT and 524 cm^{-1} (ν_{13}) mode in MPT. All three of these calculated modes align well with weak transitions in the experimental spectra. Although the experimental bands associated with these assignments are consistently weaker than the higher frequency modes assigned above, these additional features support our overall assignment of the vibrations in the FSRS spectrum. The similar relative intensities of the two experimental bands for all three molecules show that resonance enhancement effects are conserved for vibrations with the same types of motion.

Finally, we note that the assignment of the 690 cm^{-1} experimental band in PT as ν_{17} rather than ν_{14} indicates that the π resonance condition favors the localized C–S stretching motion involving the unsubstituted carbon (C$_5$) rather than the phenyl-substituted carbon (C$_2$). Interestingly, the aryl-substituted C–S stretching motion has been implicated in the rapid ISC of phenyl- and thienyl-substituted thiophenes.[43,107] subtle distinction between modes ν_{14} and ν_{17} of PT highlights the importance of accurately assigning transitions in experimental FSRS spectra. Mode ν_{14} should be a better probe of the PT deactivation coordinate (C$_2$–S stretching) compared with ν_{17}. In fact, while a shift of the former vibration to lower frequency would indicate weakening of the C$_2$–S bond, a concomitant shift to higher frequency would be expected for ν_{17} due to strengthening of the C$_5$–S bond.

Our calculations here consider only the minimum energy geometry of the S$_1$ state of each molecule, however transient FSRS calculations have the potential to use these spectroscopic signatures to distinguish motions along the reaction coordinate.[102] In fact, our assignments for MPT are consistent with the recently reported dynamics of that molecule, where the intense band near 690 cm^{-1} was observed to shift slightly to higher energy following the initial excitation. Notably, the shift to higher energy is consistent with the expected strengthening of the methyl-substituted C–S

bond, based on the prominent motion along that bond for mode ν_{20}, rather than the weakening of the phenyl-substituted C–S bond for ν_{18}. The shift to higher energy therefore provides additional evidence that ν_{20} is the observed FSRS band, rather than ν_{18}, even though the latter has the stronger calculated off-resonance intensity. Without considering resonance enhancements across all three compounds, it would be tempting to make incorrect assignments of the intense Raman bands of PT or MPT based on the calculated intensities alone.

4.4   Conclusions

A key result of this work is that accurate excited-state resonance-enhanced Raman assignments are possible using relatively low-cost off-resonant calculations, provided the effects of the electronic resonance condition are taken into consideration. Importantly, the assignments are made possible by comparing the spectra for several molecules with similar structure. Transitions in the 500-800 cm^{-1} region of the S$_1$ spectra of DPT, PT, and MPT provide a representative example for making assignments based on symmetry and resonance enhancement considerations across multiple compounds.

Most FSRS measurements rely on an electronic resonance condition to obtain increased Raman scattering signals, but there have not been any systematic studies examining how the resonance condition affects the assignment of experimental spectra before now. Our benchmark study shows that off-resonance calculations can be deceiving, and highlights the importance of mode-specific resonance enhancement effects. While we have compared the experimental and theoretical Raman spectra for a series of aryl-substituted thiophene molecules, we expect similar results for other sets of structurally related compounds having similar excited-state absorption spectra.

We are currently working on a procedure to simulate excited-state resonance Raman enhancements directly using the gradient approximation.[72] After identifying the resonant S$_n$ states responsible for the excited-state absorption, this approach would obtain the mode-specific resonance enhancements by calculating the gradients of the relevant excited-state potential energy curves along the S$_1$ normal mode coordinates. A comprehensive understanding of resonance enhance-

ment effects will provide more detailed insight on the structural evolution of molecules in excited electronic states by allowing more precise tracking of the nuclear motions using FSRS spectra.

Chapter 5

Probing Dynamics in Higher-Lying Electronic States with Resonance-Enhanced Femtosecond Stimulated Raman Spectroscopy

(Adapted from Ref. #53. Supporting information is available online.)

5.1 Introduction

Femtosecond stimulated Raman scattering (FSRS) is a time-resolved technique for probing the structural dynamics of molecules in electronically excited states.[22–24,120,121] Vibrational frequency shifts reveal changes in molecular structure and bonding as a molecule evolves along an excited-state potential energy surface. By measuring the time evolution with vibrational resolution, the technique provides more detailed structural information about the excited-state dynamics than is usually available from transient electronic absorption measurements alone.[24] Transient Raman measurements often take advantage of a tunable Raman excitation wavelength to target specific electronic resonances. Matching a specific resonance in the transient electronic absorption spectrum allows one to selectively probe a specific intermediate or product species due to enhanced Raman scattering.[34,41,51,122–126] While the resonance condition serves the important purpose of increasing the Raman signal in transient measurements, both for species selectivity and simply to improve signal-to-noise, the influence on mode-dependent Raman intensities has been largely ignored.

The resonance condition has long been recognized in ground-state Raman spectroscopy as a

way to probe the Franck-Condon region of an electronically excited state.[25,72–74] The vibrational frequencies still report on the ground electronic state, but mode-dependent enhancements of the vibrational intensities reflect the relative displacement of the upper potential energy surface along each of the ground-state vibrational coordinates. Therefore, tuning the Raman excitation wavelength into resonance with a specific electronic transition reveals detailed information about the upper state through the excitation-wavelength dependent Raman gain profiles of the different vibrational modes. Modes with the largest displacement in the upper state give the largest relative Raman scattering enhancements, thus reporting on the initial dynamics of the molecule moving out of the Franck-Condon region of the upper state. Such detailed information about the upper electronic state has not been explored in FSRS measurements, where the focus of most experiments remains on the time-evolving dynamics of the lower state.

Considering the upper electronic state in FSRS measurements is important in two contexts. On one hand, the relative intensities in the transient Raman spectrum depend on the identity of the resonant electronic state. We previously showed for a series of thiophene derivatives that the calculated off-resonance Raman activities do not adequately represent the experimental intensities, and that the correct assignment of FSRS bands requires careful consideration of the resonance condition.[52] Neglecting mode-specific resonance enhancement effects can result in erroneous assignments that could affect the interpretation of the transient dynamics. On the other hand, resonance-enhanced FSRS measurements also provide novel information about the higher-lying potential energy surface, analogous to ground-state resonance Raman spectroscopy.

In this chapter, we examine mode-specific resonance enhancements in the excited-state Raman spectrum of a non-reactive model compound, 2,5-diphenylthiophene (DPT), in order to show that it is feasible to extract information about the upper potential energy surface from FSRS measurements. Specifically, we measure the excitation-wavelength dependence of the excited-state resonance Raman spectrum of DPT in the relaxed (*i.e.* thermally equilibrated) S_1 state. The excitation-wavelength dependence of the excited-state Raman spectrum reveals strong enhancement of several vibrational modes related to the secondary excitation of the conjugated π elec-

tronic structure. We compare the experimental results with calculated excited-state Raman spectra for resonant and off-resonant excitation from the relaxed S_1 state. The resonant calculations consider both the S_1-S_n electronic transition strengths and the relative displacements of the upper (S_n) potential energy surfaces in order to simulate resonance Raman spectra for each of the higher-lying states. The experimental results provide a stringent test of the computational approach, and indicate important limitations based on the level of theory and basis set, whereas the calculated spectra facilitate the interpretation of the experimental spectra. This work provides a foundation for making better assignments of resonance-enhanced excited-state Raman spectra, as well as extracting novel information about higher-lying excited states from FSRS measurements.

5.2 Theory

We briefly summarize key results from the time-dependent formalism for resonance Raman scattering theory in order to illustrate our approach to calculating resonance-enhanced FSRS spectra. More detailed theoretical descriptions of resonance Raman scattering are available in Chapter 2, as well as in the literature.[27,29,30,73,74,92,127,128] The time-dependent formalism for resonance Raman scattering[71,72] provides an intuitive picture to relate the geometry change in an upper state with the mode-dependent resonance Raman intensities. From Equation 2.13, which gives the general, sum-over-states approach to the transition polarizability tensor, α_{fi}, we assume that the Raman excitation frequency, ω_p, is resonant with a single transition from the initial state i to an upper electronic state n, ω_{ni}. Thus, when $\omega_p \approx \omega_{ni}$, the summation reduces to include only the vibrational levels, $|v_n\rangle$, of the resonant state. Very briefly, after converting the frequencies in Equation 2.13 to energies ($E_{v_i} = \hbar\omega_{v_i}$, etc.) and replacing the denominator with a formally equivalent half Fourier transform,

$$\frac{1}{(E_{v_n} - E_{v_i} - E_p - i\hbar\Gamma_{v_n})} = \frac{i}{\hbar} \int_0^\infty e^{-i(E_{v_n} - E_{v_i} - E_p - i\hbar\Gamma_{v_n})t/\hbar} dt \tag{5.1}$$

the transition polarizability can be recast in terms of a time-dependent wave packet that propagates on the upper electronic state, $|v_i(t)\rangle = e^{-i\hat{H}_n t/\hbar}|v_i\rangle$.[29] The resulting expression for the polarizability term is essentially the time-integrated Franck-Condon overlap between the wavepacket $|v_i(t)\rangle$ and the vibrational wavefunction of the final state, $|v_f\rangle$,[27,72,73]

$$\alpha_{fi} \approx \frac{i}{\hbar}|\mu_{ni}|^2 \int_0^\infty \langle v_f|v_i(t)\rangle \, e^{i(E_{v_i}+E_p)t/\hbar - \Gamma_n t} dt \tag{5.2}$$

where μ_{ni} is the electronic transition dipole. Thus, the intermediate states in the Raman scattering process are replaced by the time-dependent wave packet, which represents the propagation of the initial (ground-state) vibrational wavefunction on the potential energy surface of the upper electronic state. As before, the damping term $e^{-\Gamma_n t}$ accounts for dephasing.

The expression further simplifies by using a Gaussian function to approximate the $t = 0$ wavepacket along each vibrational coordinate q_k, which then evolves in time according to Newton's equation, $F_{q_k} = -\frac{\partial V_n}{\partial q_k}$. The subscript n indicates that the motion follows the potential of the upper state, whereas the vibrational coordinates q_k are the normal modes of the lower electronic state. This description of the time-dependent overlap integral using classical dynamics gives the transition polarizability for each vibration k,[71,72]

$$\alpha_{fi}^k \approx -\frac{i}{\hbar}\frac{|\mu_{ni}|^2}{(2\omega_k)^{1/2}}\left(\frac{\partial V_n}{\partial q_k}\right)\int_0^\infty e^{i(E_{v_i}+E_p-E_n)t/\hbar - \Gamma_n t} e^{-\left(\frac{\partial V_n}{\partial q_k}\right)^2 t^2/4\omega_k} t\,dt \tag{5.3}$$

where ω_k is the frequency of normal mode k in the lower electronic state, E_n is the vertical electronic transition energy, and the integral is the excitation profile as a function of Raman excitation energy E_p. Finally, the intensity for a resonance Raman transition to the fundamental vibration of mode k is proportional to the square of the polarizability term,

$$I_k \propto E_p E_s^3 |\alpha_{fi}^k|^2 \approx E_p E_s^3 \frac{|\mu_{ni}|^4}{2\omega_k}\left(\frac{\partial V_n}{\partial q_k}\right)^2 \tag{5.4}$$

for incident and scattered photon energies E_p and E_s, respectively.

Equation 5.4 introduces the crucial concept that the transition polarizability, and therefore the

Raman intensity of a given mode k, depends on the slope of the resonant (upper) electronic state along that vibrational coordinate. This result provides a foundation for calculating excited-state resonance Raman spectra based on the electronic transition strength, $|\mu_{ni}|^2$, and the gradients of the upper-state potential, $\partial V_n / \partial q_k$. The frequencies are determined by the normal modes of the lower electronic state, while the relative intensities depend on the slope of the upper-state potential energy surface along each of those vibrational coordinates. For the excited-state resonance Raman spectra shown below, $|v_i\rangle$ represents the ground vibrational level of the first electronically excited state S_1, and the resonant states $|v_n\rangle$ are the vibrational levels of a single higher-lying electronic state S_n. The experimental Raman excitation wavelengths are resonant with a single excited-state absorption band, and are sufficiently far from the stimulated emission band to exclude any contributions from resonance with the ground electronic state. While the gradient approximation makes several significant assumptions, this approach provides a valuable starting point for comparison with the experimental resonance-enhanced FSRS spectra.

5.3 Experimental and Computational Methods

The experimental setup used to obtain the FSRS spectra has been described in detail in Chapter 3 and elsewhere.[53,90] The sample consists of a 1.0 mM solution of 2,5-diphenylthiophene (TCI America) in cyclohexane (spectroscopic grade, Fisher). Irradiating the sample with $\sim$0.8 μJ actinic pump pulses gives a maximum transient absorption of approximately 200 mOD at 560 nm. We measure the ground-state Raman spectrum of DPT (15 mM in cyclohexane) using a commercial Raman spectrometer (StellarNet) with 785 nm cw pump laser and 4 cm^{-1} resolution.

We use a development version of the GAUSSIAN software package[78] for all calculations, except where indicated. First, we calculate off-resonant Raman spectra for both the ground and first excited electronic states using time-dependent density functional theory (TD-DFT) with B3LYP/aug-cc-pVDZ. We obtain the mode-dependent Raman activities by numerical differentiation of the polarizability tensor along each of the normal mode coordinates at the optimized geometry of each state.[30] Our excited-state calculations use analytical polarizabilities for S_1.[53,78] Using this method,

we previously compared the calculated off-resonance excited-state Raman intensities with experimental resonance-enhanced FSRS spectra for a series of eight aryl-substituted thiophene derivatives, including DPT.[53] Our earlier work shows good agreement between the calculated and experimental frequencies, even though the resonance condition significantly alters the intensities of the experimental spectra.

In order to account for the resonance condition explicitly, we simulate the excited-state Raman spectrum of DPT based on the time-dependent formalism described above. In short, we calculate the $S_n \leftarrow S_1$ transition moments and the gradients of the S_n potential energy surfaces at the S_1 optimized geometry for states up to $n = 20$. For the resonance Raman calculations, we use both TD-DFT and equation of motion coupled-cluster theory with single and double excitations (EOM-CCSD) to obtain the excited states.[129] We obtain the TD-DFT electronic transition moments from the double residues of the quadratic response functions using the Dalton software package,[80–83] and calculate EOM-CCSD transition moments using the unrelaxed transition density approximation.[130] The TD-DFT calculations are more efficient, but the EOM-CCSD calculations should provide a more accurate representation of the excited states. Due to the computational cost of the EOM-CCSD calculations, we only calculate gradients for a few vibrational modes. Additional details are provided below.

5.4 Results

5.4.1 Excited-State Dynamics

Figure 5.1 shows the evolution of the transient electronic absorption spectrum of DPT following excitation at 310 nm. At early delay times, the transient spectrum has a strong excited-state absorption band centered near 565 nm and a weaker stimulated emission band near 390 nm. We observe quantum beating in the excited-state absorption band within the first few ps (not shown), and the band narrows slightly on a $\sim$15 ps time scale due to structural relaxation and vibrational cooling in the S_1 excited state. Integrating the singlet absorption band at 1 ps after excitation gives an

experimental oscillator strength of $\sim$0.3 for the S_n-S_1 transition. Both the excited-state absorption and stimulated emission bands decay with a single exponential time constant of 270 ± 7 ps due to intersystem crossing (ISC) to a long-lived triplet state. A weaker triplet-triplet absorption band near 430 nm appears on the same timescale as the decay of S_1, similar to previous measurements of two- and three-ring aryl-substituted thiophene derivatives in solution.[44,47,48,53,118]

Transient stimulated Raman (FSRS) measurements track the structural dynamics of DPT in more detail by following the evolution of the excited-state vibrational spectrum. In Figure 5.2, we show the transient FSRS spectrum of DPT following actinic excitation at 310 nm. The Raman excitation wavelength of 620 nm is on the low-energy tail of the S_1 excited-state absorption band. All of the FSRS bands decay to the baseline on a similar timescale as the ISC observed in the transient electronic absorption spectrum, and therefore are assigned as S_1 vibrations.[53] We do not readily observe triplet bands because the Raman pump wavelength is off-resonant of the T_1 absorption band.

The most dominant features in the transient Raman spectrum include a pair of delocalized ring deformation modes in the 600-700 cm^{-1} range, phenyl and thiophene distortion modes near 988 and 1191 cm^{-1}, and a pair of ethylenic stretching modes in the 1500-1600 cm^{-1} region that are characteristic of π-conjugated molecules.[53] The assignments are discussed in more detail below. Notably, the relative intensities of the 1529 and 1596 cm^{-1} vibrations change within the first few ps following excitation, as highlighted in the lower panel of Figure 5.2. Bragg and coworkers[48] recently showed that the relative intensities of the analogous in-phase and out-of-phase ethylenic stretching modes of quaterthiophene track the evolution of the molecule to a more planar structure in the excited state. Similarly, a change in the relative intensities of the two modes in DPT indicates rapid planarization on a timescale of 0.8 ± 0.2 ps, due to the quinoidal character of the (π, π^*) excited state. We note that there is a slight increase in the intensity of the transient electronic absorption signal on this timescale as well, although the transient electronic spectrum does not provide the same level of insight about the structural evolution of the molecule that is available from the Raman measurement.
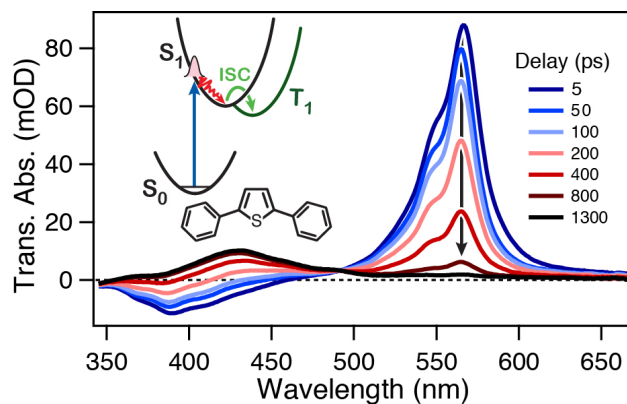
Figure 5.1: Evolution of the transient electronic absorption spectrum of DPT following 310 nm excitation. Inset shows the structure of the molecule and a schematic energy level diagram.
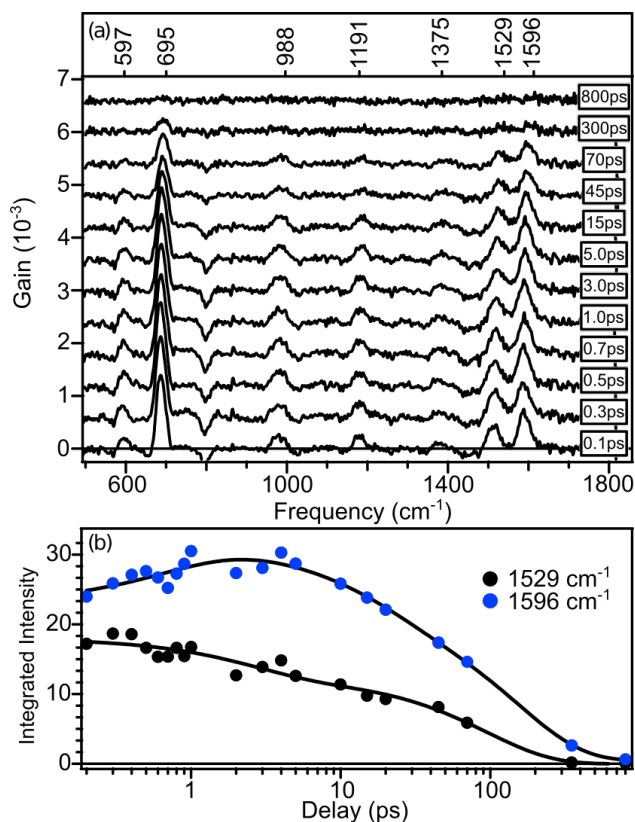
Figure 5.2: Evolution of the FSRS spectrum of DPT following excitation at 310 nm. The Raman pump wavelength is 620 nm. The negative signal at 800 cm^{-1} is an artifact from subtraction of the solvent signal. Panel (b) shows the integrated intensities of the 1529 and 1596 cm^{-1} bands as a function of time. Solid lines are fits to the data using a sum of two exponentials.

5.4.2 Ground- and Excited-State Raman Spectroscopy

While the evolution of the FSRS spectrum reveals information about the structural dynamics on S_1, the primary focus of this chapter is using the mode-specific resonance Raman enhancements to probe the higher-lying excited states, S_n. In order to separate the effects of the time-evolving wavepacket on S_1, we measure the wavelength-dependent transient Raman spectrum of DPT at a fixed delay of 30 ps following the initial excitation. This delay allows the molecule to relax and dissipate excess vibrational energy to the solvent. In other words, the 30 ps delay allows us to probe DPT at the minimum-energy geometry of the S_1 potential energy surface, and therefore simplifies the comparison of the experimental and computational spectra.

Before making a direct comparison between experiment and theory for the excited-state Raman spectrum, we first compare the experimental and computational Raman spectra for the ground state of DPT in Figure 5.3. The ground-state calculation provides a reference for the best level of agreement that can be expected for a given computational method and basis set, because both the experimental and computational spectra are off-resonant for the ground state of DPT. One complication in simulating the ground-state spectrum of DPT is the conformational flexibility due to rotation of the phenyl rings. DPT has a non-planar optimized ground-state geometry, with roughly 20° dihedral angle between the central thiophene and each of the phenyl rings. The relative orientation of the two phenyl rings results in two nearly iso-energetic structures with C_S and C_2 symmetry, separated by a torsional barrier smaller than $k_B T$ at room temperature. Even the fully planar (C_{2v}) structure is accessible at room temperature. Figure 5.3 shows the calculated Raman spectrum of the lower-energy C_2 species; however, the spectra for the C_S and C_{2v} structures are nearly identical. The spectra for all three species are available in the supporting information (SI), along with a table of vibrational frequencies for the ground state of DPT.

The calculated ground-state frequencies (B3LYP/aug-cc-pVDZ) are within $\sim$20 cm^{-1} of the experimental values. The calculated intensities are also in reasonably good agreement with the experimental spectrum, although the calculations underestimate the relative intensities of some of the lower frequency bands by up to an order of magnitude. This systematic underestimation of
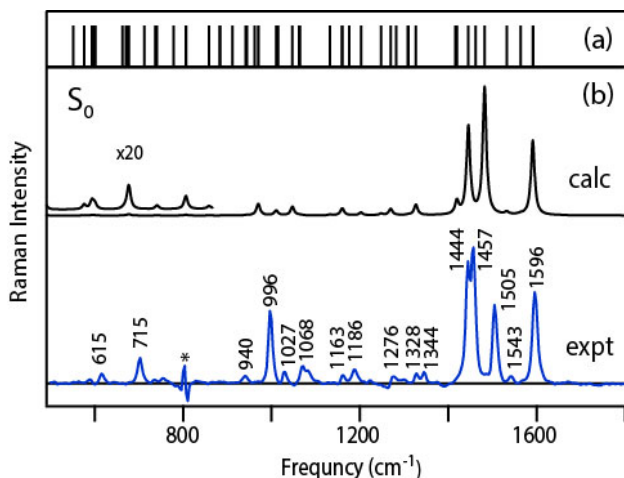
Figure 5.3: Calculated (B3LYP/aug-cc-pVDZ) and experimental off-resonance ground-state Raman spectra of DPT. Calculated spectrum includes $10\ \mathrm{cm}^{-1}$ Lorentzian broadening, and is also shown on an expanded scale below $900\ \mathrm{cm}^{-1}$. For reference, the top panel (a) shows all of the calculated vibrational frequencies after applying an empirical frequency scaling factor of 0.970.[116]

the low-frequency modes is consistent with our previous results across a series of aryl-substituted thiophenes.[53] The most notable discrepancy for DPT is the phenyl ring breathing mode near 996 cm^{-1}, which is stronger than predicted by theory, as is also apparent in earlier work by Castro $et\ al.$[118] We are currently exploring the reason for this systematic underestimation of the low-frequency intensities, and early indications suggest that including anharmonic effects accounts for some, but not all, of the discrepancy. Nevertheless, the calculated off-resonance Raman spectrum provides a good representation of the experimental ground-state spectrum of DPT.

In contrast with the ground-state, the calculated off-resonance Raman spectrum for the excited state of DPT does not adequately reproduce the experimental FSRS spectrum, as shown in Figure 5.4. The figure compares the experimental FSRS spectrum at 600 nm Raman pump wavelength with the calculated off-resonance Raman spectrum at the optimized S_1 geometry.[53] Although the 600 nm Raman pump wavelength is only on the tail of the excited-state absorption band, we observe mode-specific resonance enhancement effects compared with the off-resonance calculation. Most notably, the low-frequency mode near 695 cm^{-1} is the strongest band in the experimental spectrum, even though the off-resonance calculation predicts relatively weak scattering at low frequencies. The discrepancy is much more significant than in the ground-state spectrum. Fur-

thermore, the off-resonance calculations predict the wrong relative intensities of the two phenyl deformation modes (ν_{18} and ν_{25}), and also of the two ethylenic stretching modes (ν_{67} and ν_{69}). The mode-specific enhancements are even more pronounced when the Raman excitation wavelength approaches the maximum of the excited-state absorption band (see below), which is a clear sign of resonance-enhancement.
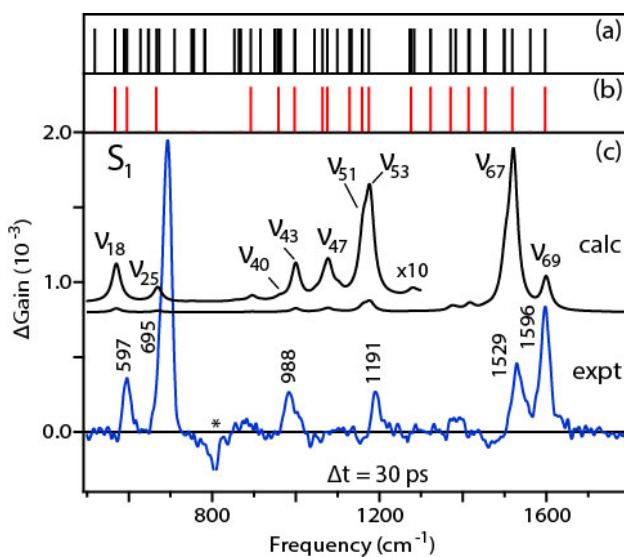
Figure 5.4: Calculated (B3LYP/aug-cc-pVDZ) and experimental excited-state Raman spectra of DPT. The calculated off-resonance spectrum includes 25 cm^{-1} Lorentzian broadening, and is also shown on an expanded scale below 1300 cm^{-1} to emphasize the low intensity bands in this region. The experimental FSRS spectrum is measured at a time delay of 30 ps using 600 nm Raman excitation wavelength, and the asterisk indicates an artifact from subtraction of the solvent background. For reference, the top two panels show (a) all of the calculated vibrational frequencies, and (b) only the totally symmetric vibrations. The calculated frequencies include an empirical scaling factor of 0.970.[116]

Even though the calculated off-resonance spectrum does not accurately reproduce the experimental intensities due to mode-specific enhancements, the calculated frequencies provide a foundation for assigning vibrations in the excited-state Raman spectrum.[53] The top panel of Figure 5.4 shows the full set of calculated vibrational frequencies for the optimized S_1 excited state using B3LYP/aug-cc-pVDZ.[53] The optimized structure is planar, with C_{2v} symmetry. In the absence of Herzberg-Teller coupling, only totally symmetric (and degenerate) vibrations are symmetry-allowed in resonance Raman,[29] therefore the second panel shows only the subset of a_1-symmetry modes for the DPT excited state. This narrower collection of states provides the basis for our as-

signment of the experimental spectrum. For example, the experimental bands at 1529 and 1596 cm^{-1} are relatively easy to assign as delocalized ethylenic stretching modes v_{67} and v_{69}, respectively, because these are the only two totally symmetric modes in this frequency range. The delocalized character of the two vibrations and the strong coupling with the conjugated π backbone of the molecule explain the strong intensities in both the on- and off-resonant spectra.

We assign other experimental bands in comparison with the calculated frequencies, but also considering which motions are likely to be enhanced by the resonance condition.[53] The S_1 excited-state absorption band represents excitation of π electrons, therefore we anticipate the largest enhancements for modes that are sensitive to changes of the π bonding framework, as these modes should have the largest displacement between S_1 and the upper electronic state. For example, we assign the most intense Raman band at 695 cm^{-1} as v_{25}, which is a totally symmetric vibration that includes symmetric phenyl ring distortion and thiophene C-S-C stretching motions. This delocalized mode has large displacement along the π-conjugated framework of DPT, consistent with a strong resonance enhancement under π-excitation. Similarly, the 597 cm^{-1} vibration is assigned as v_{18}, a delocalized phenyl ring distortion and thiophene C-S-C bending mode that is also sensitive to π excitation.

Although the above assignments are supported by the appearance of the corresponding bands in the calculated off-resonance spectrum, we reiterate that assignments should not be made based on intensity alone. We previously showed that the calculated off-resonance intensities can be deceiving if the resonance enhancement effects are not carefully considered.[53] This cautionary point is highlighted by our assignment of the experimental band of DPT at 988 cm^{-1} as v_{40}, rather than v_{43}. Based on intensity alone, it would be tempting to assign the experimental FSRS band as the more intense v_{43} from the calculated spectrum, but the primarily C-H bending motion associated with that mode is not expected to have the same degree of resonance enhancement as the in-plane C-C-C bending and ring deformation of v_{40}. Instead, the shoulder at roughly 1025 cm^{-1} is tentatively assigned as C-H bending and weak phenyl ring distortion associated with v_{43}. Similarly, the experimental band at 1191 cm^{-1} could be assigned as either v_{51} or v_{53}

based on calculated frequencies and intensities alone, but we assign this band as ν_{53} based on the more delocalized C=C and C-S stretching character of the latter, which is likely to have stronger resonance enhancement. Table 1 shows the experimental and calculated vibrational frequencies and assignments for several transitions. All of these modes are expected to have strong resonance enhancement related to the distortion of the molecular structure upon secondary excitation of π electrons from the S_1 state of DPT. The assignments are further supported by calculated resonance enhancements that we discuss below.

Table 5.1: Assignment of Experimental Excited-State Raman Bands

Vibration	Calc. Frequency $(cm^{-1})^a$	Exp. Frequency (cm^{-1})	Relative Gain^b	Motion^c
ν_{18}	572	597	29.5	C-S-C bend and phenyl def.
ν_{25}	669	695	13.5	C-S-C sym. str. and phenyl def.
ν_{40}	962	988	15.9	C-C-C bend/phenyl def.
ν_{43}	1000	1025	–	C-H bend and phenyl def.
$\nu_{10} + \nu_{25}$	–	1048	–	–
ν_{51}	1163	–	–	C-H bend
ν_{53}	1178	1191	6.4	C-H bend and thiophene def.
$\nu_{18} + \nu_{25}$	–	1267	>100	–
$2\nu_{25}$	–	1375	14.9	–
ν_{67}	1509	1529	4.1	delocalized C=C str.
ν_{69}	1596	1596	5.1	delocalized C=C str.
$\nu_{18} + 2\nu_{25}$	–	1899	–	–
$3\nu_{25}$	–	1986	–	–

^{a} B3LYP/aug-cc-pVDZ with empirical scaling factor of 0.970.[116] ^{b} Ratio of integrated band intensities for 565 and 600 nm Raman excitation wavelengths. ^{c} See Figure 1 in the SI for images of the displacement vectors.

5.4.3   Resonance Raman Excitation Profiles

We examine the relative enhancements of the excited-state resonance Raman bands in more detail by tuning the Raman excitation wavelength across the S_1 absorption band. Figure 5.5 shows the experimental Raman spectrum at eight different pump wavelengths ranging from 560 to 600 nm. We limit the Raman pump wavelength to the low-frequency side of the absorption band to prevent

dispersive peak shapes, as described in the literature,[51,124,131] and to avoid becoming resonant with the stimulated emission band below $\sim$500 nm.
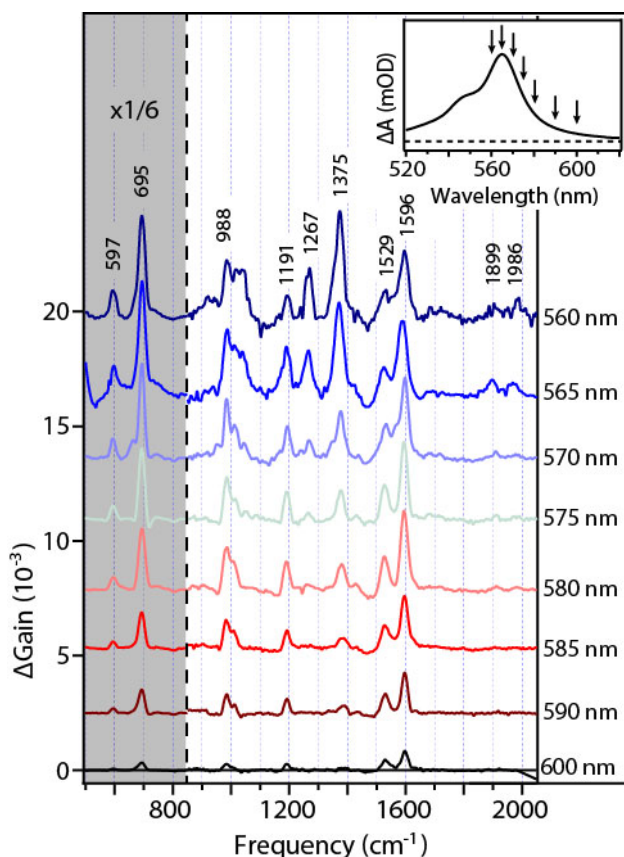
Figure 5.5: Excited-state resonance Raman spectra at $t = 30$ ps delay for eight different Raman excitation wavelengths. Spectra are scaled by 1/6 intensity below 825 cm^{-1} to facilitate comparison of these high-intensity transitions with other regions of the spectrum. Inset shows the Raman excitation wavelengths in reference to the excited-state absorption spectrum.

In order to better highlight the mode dependence of the resonance enhancement effect, Figure 5.6 shows the excitation profiles for eight of the most dominant FSRS bands. The excitation profiles show the variation of the frequency-integrated band intensities as a function of Raman excitation wavelength. We use integrated band intensities to account for small variations in frequency resolution due to changing experimental parameters at the different excitation wavelengths. By normalizing the integrated intensity of each band to the value obtained at 600 nm, the figure shows the relative enhancements as a function of decreasing wavelength. For reference, the figure also includes the intensity profile of the S_1 excited-state absorption band, which increases by a

factor of 9.0 from 600 to 565 nm.
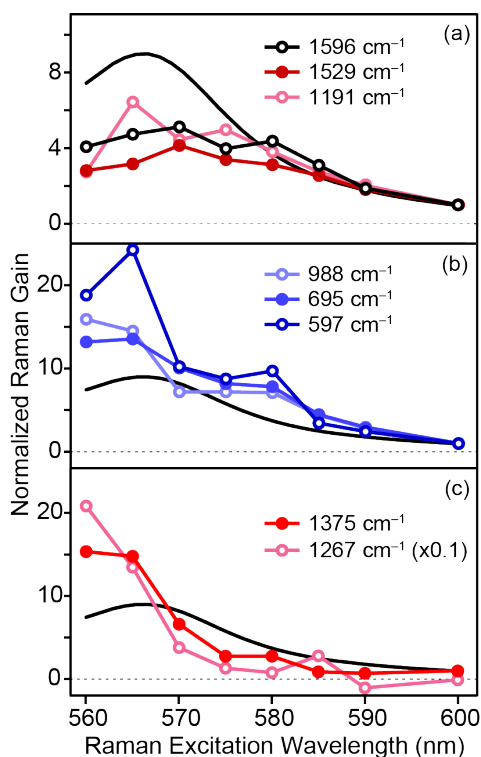
Figure 5.6: Excitation profiles for several excited-state Raman bands, normalized to the value at 600 nm. For reference, solid black lines are the excited-state absorption spectrum. The three panels show (a) modes with modest gain profiles, (b) modes with stronger resonance enhancement, and (c) overtone and combination modes.

We group the excitation profiles into three different categories based on the relative increase of the Raman gain between 600 and 565 nm. The first group includes the bands at 1191, 1529, and 1596 cm^{-1}, which have modest gain across the spectrum, increasing slightly less than the S_1 absorption band increases over the same range, and centered at a Raman excitation wavelength between 565 and 575 nm, which is slightly red-shifted from the peak of the excited-state absorption band. The second group includes bands that increase more rapidly than the excited-state absorption profile, including those at 597, 695, and 988 cm^{-1}. These two categories have gain profiles that generally follow the intensity of the excited-state absorption band at the Raman excitation wavelength, with the main difference being whether the bands have significant off-resonance intensity or not. Bands with off-resonance intensity are already fairly strong for 600 nm Raman excitation, and therefore tend to have more modest gain profiles, while bands that have lower intensity in the

off-resonance spectrum increase more rapidly when moving on-resonance.

Finally, a third group of gain profiles includes the bands at 1267 and 1375 cm^{-1}. Notably, these bands are indistinguishable from noise in the early resonance regime, but gain significant intensity as the Raman pump wavelength approaches the S$_1$ absorption maximum. The delayed onset of the excitation profile for these bands is consistent with the expected behavior for overtone and combination modes in a resonance Raman spectrum, having essentially no intensity off-resonance, but becoming quite strong when the resonance condition is fully realized.[27,29,132] Thus, we assign the 1267 and 1375 cm^{-1} bands as the $\nu_{18} + \nu_{25}$ combination and $2\nu_{25}$ overtone modes, respectively. Two features also emerge at 1899 and 1986 cm^{-1} that we assign as transitions to the $\nu_{18} + 2\nu_{25}$ combination and $3\nu_{25}$ overtone modes. A band near 1048 cm^{-1} has similar behavior, consistent with the $\nu_{10} + \nu_{25}$ combination mode, based on our previous assignment of the ν_{10} fundamental at 382 cm^{-1}.[53] Strong overtone and combination modes are a signature of large geometry changes in the resonant (upper) electronic state, therefore the prominent progression in ν_{25} points to a very large displacement and correspondingly intense Franck-Condon activity along the thiophene symmetric C-S-C stretching coordinate for S$_n \leftarrow$ S$_1$ excitation of DPT.

5.4.4 Calculated Excited-State Resonance Raman Spectra

For comparison with experiment, we simulate the excited-state resonance Raman spectrum of DPT using either TD-DFT or EOM-CCSD, and the time-dependent formalism described above. In short, we find the optimized S$_1$ geometry and then use Equation 5.4 to calculate resonance Raman intensities from the S$_n$-S$_1$ transition strengths and S$_n$ gradients for states up to $n = 20$. We obtain the gradients numerically by calculating the energies at small positive and negative displacements along each of the S$_1$ normal mode coordinates relative to the S$_1$ equilibrium geometry. All of the calculated frequencies, transition strengths, and gradients are listed in the SI.

Figure 5.7 shows the results from TD-DFT with B3LYP/aug-cc-pDVZ. The top panel of the figure compares the experimental transient absorption spectrum with the calculated S$_n \leftarrow$ S$_1$ transitions, including a simulated excited-state absorption spectrum with 0.25 eV Gaussian broadening.

We estimate an experimental oscillator strength of $f \approx 0.3$, but only two of the calculated transitions have $f > 0.01$, and both are at much longer wavelength. Nevertheless, the lower panel of the figure compares the experimental FSRS spectrum at an excitation wavelength of 570 nm with the simulated excited-state resonance Raman spectra for each of the higher-lying states with $f > 0.004$. The simulated Raman spectra include 25 cm^{-1} Lorentzian broadening, and we divide the spectrum for each state by the oscillator strength ($f \propto E_p |\mu_{ni}|^2$) to allow comparison among states with very different transition strengths.

The simulated spectra in the lower panel of Figure 5.7 highlight the important role of geometry changes in the upper states in determining the relative resonance Raman scattering intensities. Each of the electronic states gives a distinct resonance Raman spectrum, but most have a relatively large gradient in the ethylenic stretching modes at 1509 and 1596 cm^{-1} due to excitation of conjugated π electrons for each of the $S_n \leftarrow S_1$ transitions. In contrast with the calculated off-resonance spectrum in Figure 5.4, several of the states also have noticeable intensity in the lower frequency thiophene distortion modes below $\sim$700 cm^{-1}, although none are as intense as the associated experimental bands (note the different intensity scaling factors for the experimental and computational spectra below 850 cm^{-1}). A few of the states also correctly predict that there are some Raman bands with intensity in the intermediate frequency range (not including overtone and combination modes, which are excluded from our simulation), but none of the calculated states matches both the experimental FSRS spectrum and the electronic transition strength. Most of the electronic transitions have either very low oscillator strength (<0.01) or much longer wavelength than the experimental band at 560 nm. The generally poor agreement with the experimental spectra suggests that TD-DFT does not accurately reproduce the higher-lying electronic states of DPT. This result is not unexpected, because TD-DFT is a single reference method that neglects double excitation and other effects that are likely to play a role in states that are accessible by sequential two-photon excitation.[133,134]

The top panel of Figure 5.8 compares the experimental transient absorption spectrum with the calculated $S_n \leftarrow S_1$ transitions and simulated S_1 absorption spectrum from EOM-CCSD/6-
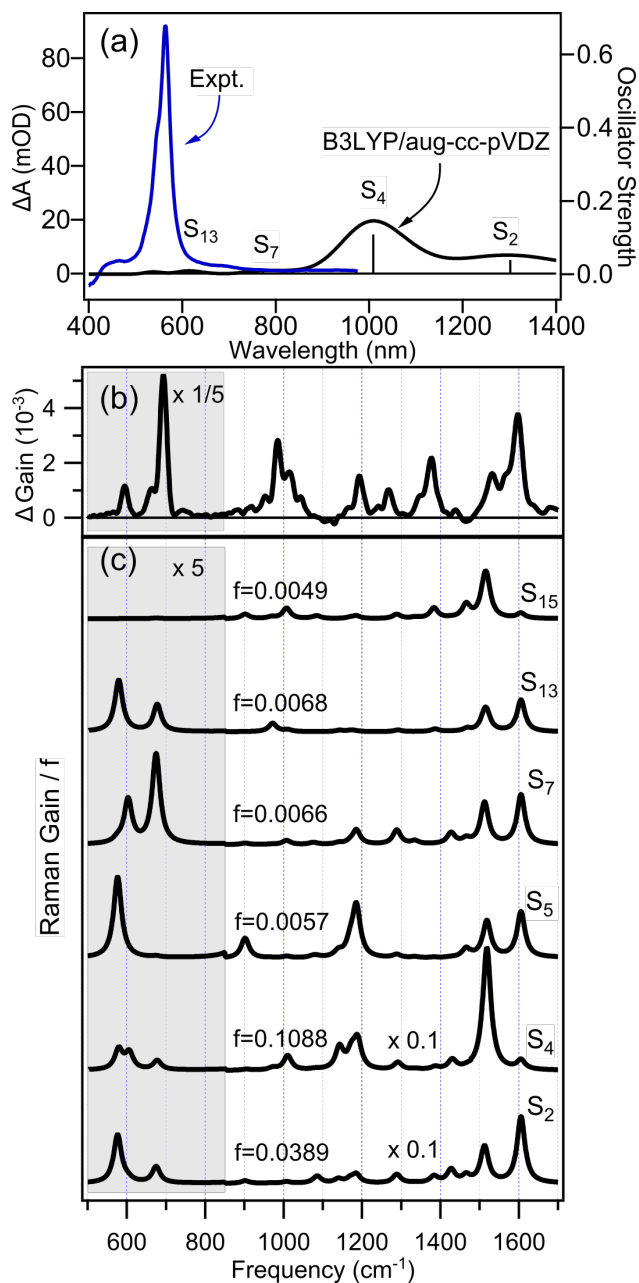
Figure 5.7: Comparison of experimental spectra at $t = 30$ ps with calculated spectra from TD-DFT (B3LYP/aug-cc-pVDZ). Panel (a) shows transient absorption spectrum and calculated $S_n \leftarrow S_1$ electronic transitions, including a simulated spectrum with 0.25 eV Gaussian broadening. The lower panel compares (b) experimental FSRS spectrum at 570 nm Raman excitation wavelength, with (c) the simulated resonance Raman spectra for calculated transitions with $f > 0.004$. Simulated Raman spectra include 25 cm^{-1} Lorentzian broadening, and have been divided by f to facilitate comparison for states with low S_n-S_1 transition strength.

31G*. The higher-level EOM-CCSD calculations are computationally more expensive than TD-DFT, but explicitly treat double excitations. We use a relatively small basis set for the EOM-

CCSD calculations because the S_1 geometry optimization and vibrational frequency calculations are computationally expensive. Even with the smaller basis set, the calculated electronic transitions from EOM-CCSD are in better agreement than TD-DFT with the experimental transient absorption spectrum. Specifically, the $S_5 \leftarrow S_1$ transition has the correct oscillator strength, and is within 0.64 eV of the experimental wavelength. State S_5 has up to $\sim$25% double excitation character in the EOM-CCSD calculation, which might explain the absence of a similar transition from TD-DFT. For reference, EOM-CCSD underestimates the S_1-S_0 transition energy by $\sim$0.3 eV at both the S_0 and S_1 optimized geometries, compared with the experimental ground-state absorption and excited-state stimulated emission spectra, respectively.

The lower panel of Figure 5.8 shows the simulated resonance Raman spectra using EOM-CCSD/6-31G* for all of the electronic states with $f > 0.004$. Although EOM-CCSD is too expensive for a complete vibrational analysis, we simulate two key regions of the Raman spectrum by calculating S_n gradients along seven of the S_1 normal mode coordinates (see SI). Some of these modes are responsible for the strongest transitions in the experimental spectrum, while others are not as prominent. Several of the simulated resonance Raman spectra have features that resemble the experimental FSRS spectrum, but the best agreement is for state S_5, which also has the largest oscillator strength. The simulated spectrum for S_5 correctly predicts the relative Raman intensities in both the high- and low-frequency regions of the experimental spectrum, including most notably the relatively strong transition near 700 cm^{-1}. The $S_4 \leftarrow S_1$ transition, which has the second largest oscillator strength and is relatively close in energy ($\sim$0.5 eV) to S_5, also has some favorable features. Additionally, while the resonance Raman intensities calculated for S_5 predict a relatively weak ν_{67} band compared to experiment, the spectrum simulated for S_4 predicts a relatively strong intensity for ν_{67}. Considering both the electronic transition strengths and the simulated resonance Raman spectra, S_5 provides the best individual representation of the upper electronic state in the experimental transient absorption spectrum of DPT.

The electron density difference maps in panels (a) and (b) of Figure 5.9 show the electronic structure changes associated with transitions to S_4 and S_5 from the EOM-CCSD calculation, re-
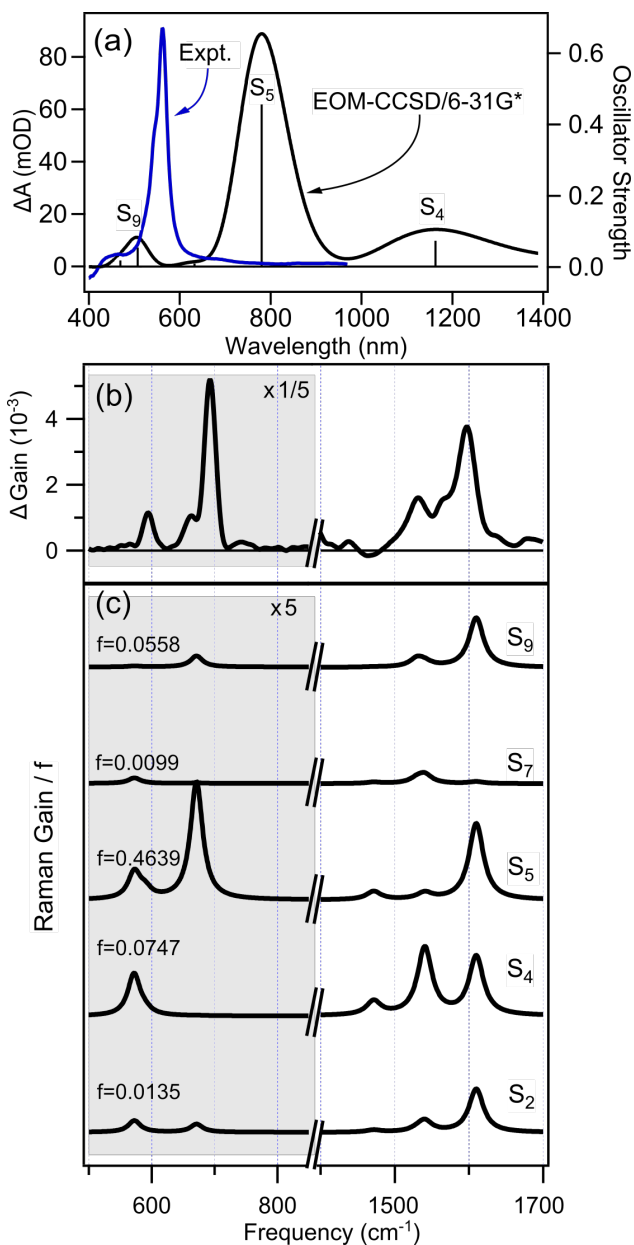
Figure 5.8: Comparison of experimental transient absorption and FSRS spectra with the simulated spectra from EOM-CCSD/6-31G*. See Figure 5.7 caption for details. The simulated Raman spectra in (c) include only seven vibrations due to computational cost. The calculated S_1 frequencies and S_n gradients are listed in the SI, and include an empirical scaling factor of 0.944.[116]

spectively. The electron density alternates along the long axis of the molecule due to the change in π bonding pattern, along with a reduction of electron density in non-bonding sulfur orbitals. The net change in electron density is responsible for the displacement of the upper potential energy surface relative to S_1, but the gradients provide a more intuitive picture by projecting those structural

changes onto the S_1 normal modes.
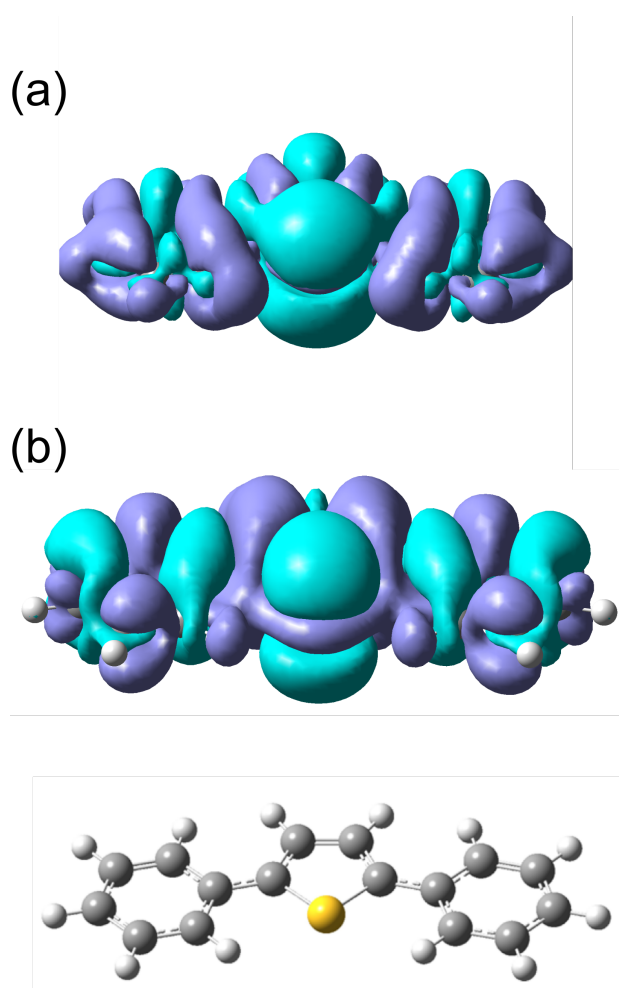
Figure 5.9: Electron density difference maps for the (a) $S_4 \leftarrow S_1$ and (b) $S_5 \leftarrow S_1$ transitions calculated with EOM-CCSD/6-31G*. Blue indicates a decrease in density and purple indicates an increase. The ball-and-stick model shows the orientation of the molecule for visual reference.

Although we are limited to a relatively small basis set for the S_1 geometry optimization and frequency calculations using EOM-CCSD, we examine the basis set dependence using the optimized geometries from lower-level calculations. Specifically, we simulate the excited-state absorption and resonance Raman spectra using a larger aug-cc-pVDZ basis set at the optimized S_1 geometries and normal mode displacements obtained from B3LYP/aug-cc-pVDZ and EOM-CCSD/6-31G* (Figures S4 and S5 in the SI). Comparing the full EOM-CCSD/6-31G* results with EOM-CCSD/aug-cc-pVDZ calculations at the lower-level optimized geometries indicates that the calculated $S_n \leftarrow S_1$ electronic transitions depend on the basis set, but are relatively insensitive to

small changes of the nuclear geometry. In contrast, the calculated resonance Raman spectra (Figure S5) are sensitive to small geometry changes, even for the same basis set. Resonance Raman calculations using a lower-level optimized geometry not only suffer from using normal modes that are obtained at a different level of theory, but also from non-zero gradients of S_1 due to the different geometry.

5.5 Discussion

Mode-specific resonance enhancements in the experimental FSRS spectrum of DPT probe the upper electronic state in the $S_n \leftarrow S_1$ transient absorption. The strong resonance enhancement of ν_{25}, including a prominent progression of overtone and combination bands involving this mode, indicates that the primary motion in S_n is initially along a delocalized thiophene C-S-C symmetric stretching and phenyl deformation coordinate, with additional contributions from the ring distortion and ethylenic stretching motions identified in Table 6.1. While some of these motions could be predicted *a priori* based on the change in π bonding between the two states (as in Figure 5.9), or even from the vibronic structure of the experimental excited-state absorption spectrum (Figure 5.1), the relative Raman intensities provide a more quantitative picture of the upper-state potential energy surface by mapping the initial dynamics onto the S_1 normal modes.

There are many examples where resonance Raman spectroscopy probes the ultrafast dynamics of a molecule excited above S_1.[48,123,125,135,136] In the present case, however, we use the transient FSRS spectrum to probe the upper-state dynamics after excitation from the relaxed S_1 geometry, rather than the equilibrium ground-state geometry. Not only is it possible to access different electronic states using sequential excitation, but also the geometry change between S_0 and S_1 allows access to new regions of the upper potential energy surfaces. In the case of DPT, secondary excitation simply induces a structural distortion due to changes in the conjugated π bonding configuration. In more reactive molecules, a similar measurement could reveal new reaction pathways that are not accessible directly from S_0. For example, we have shown elsewhere that the sequential two-photon excitation of a photochromic molecular switch leads to a different reaction efficiency

than single photon excitation from the ground-state geometry.[7,8]

The dynamics of higher-lying excited states are extremely difficult to probe using other methods, because strong coupling and a high density of states above S_1 leads to rapid non-adiabatic dynamics. As Kasha's rule predicts, molecules typically relax back to S_1 within $\sim$200 fs or less.[137,138] This rapid electronic relaxation does not leave much time for the system to evolve on the upper surfaces, therefore the initial, impulsive motions out of the Franck-Condon region are likely to determine the efficacy of reaction channels that are accessible from the higher-lying states. Given the very short lifetimes, transient electronic absorption measurements do not usually have sufficient time resolution to observe wave packet motions in the higher-lying states of a polyatomic molecule.[8] However, resonance Raman inherently probes the motion out of the Franck-Condon region of the upper state following $S_n \leftarrow S_1$ excitation, and thus provides a direct window on the ultrafast dynamics within the first few tens of fs following secondary excitation, including structural information based on the vibrational motions involved.

Our work also shows that experimental resonance-enhanced FSRS measurements can provide a valuable benchmark for comparison with excited-state calculations. For example, there has been growing interest in calculating accurate excited-state absorption spectra of conjugated polymers and related compounds, in order to better understand the nature of the electronic transition.[134] Comparison of the calculated and experimental excited-state resonance Raman spectra could provide an important reference point for assessing the quality of calculated transient absorption spectra. Higher-lying electronic states are particularly challenging to calculate because of strong electronic coupling and the rapidly increasing density of states above S_1. The situation is even more complicated for transitions between two excited states, due to additional contributions from states with double (or higher) excitation character. Although it can be difficult to evaluate the quality of excited-state calculations based on electronic transition energies and oscillator strengths alone, a comparison of the experimental Raman intensities with the calculated gradients is a more sensitive test of the calculated upper-state potential energy surface.

In the case of DPT, poor agreement between the simulated spectra and experiment reveals sig-

nificant short-comings in the TD-DFT calculations for predicting the upper electronic states, possibly due to multiple excitation character for transitions originating from the $S_1((\pi, \pi^*))$ state. The EOM-CCSD calculations are more promising, although further evaluation is necessary to confirm that the better agreement with experiment is not fortuitous. The theoretical treatment in this case is simplified by making several key approximations. For example, we neglect any contributions from Herzberg-Teller coupling or Duschinsky rotation, which often complicate even ground-state Raman measurements. In addition, Raman de-enhancement effects due to competing contributions from different upper states could be significant for higher-lying states due to the rapidly increasing density of states above S_1.[139–141] Fortunately, DPT has many favorable characteristics that simplify the comparison between experiment and theory, including an isolated excited-state absorption band and sufficiently long excited-state lifetime to allow relaxation into the thermally equilibrated S_1 state following the initial excitation. This work represents a proof of concept measurement to show that we are able to probe the upper states in a simple case of the relaxed S_1 geometry. Similar measurements for a reactive system with shorter excited-state lifetime are forthcoming.

5.6   Conclusions

Although most FSRS studies do not explicitly consider the resonance condition, experimental resonance Raman spectra are sensitive to the upper electronic state. Using a tunable Raman excitation wavelength, we have investigated the mode-specific resonance enhancements for DPT in order to probe the higher-lying excited state. The Raman gain profiles indicate that the resonant upper electronic state (S_n) is primarily displaced along delocalized coordinates with significant C-S-C bending and symmetric stretching due to secondary excitation of the conjugated π electrons. Simulated spectra based on the time-dependent formalism for resonance Raman scattering reproduce the basic details of the excited-state spectra, depending on the level of theory. Although limited to only a few vibrations, the simulated resonance Raman spectrum using EOM-CCSD/6-31G* provides a more accurate representation of the experimental spectrum than TD-DFT. The agreement of our simulated spectra in spite of a simplified theoretical formalism emphasizes the significance of

the resonant electronic state in reproducing the observed mode-specific resonance enhancements. This work highlights the ability of resonance-enhanced FSRS measurements to provide new information about higher-lying electronically excited states.

Chapter 6

Femtosecond Stimulated Raman Scattering from Triplet Electronic States: Experimental and Theoretical Study of Resonance Enhancements

(This work was published as Ref. #54. Supporting information is available online.)

6.1 Introduction

Femtosecond stimulated Raman scattering (FSRS) is a time-resolved technique that provides detailed information about the structural evolution of molecules.[22–24,84] By monitoring changes in the vibrational spectrum following photo-excitation, the dynamics of the molecular structure and bonding are observed as the system evolves along the excited- and/or ground-state potential energy surfaces. FSRS measurements often tune the Raman excitation wavelength to match an electronic transition of a target molecule in order to give a resonance enhancement of the transient Raman signal. Resonance with a specific electronic state increases the Raman transition strength of some modes by up to several orders of magnitude, depending on the character of the resonant electronic state.[25–27] Thus, tuning to a particular resonance in the transient absorption spectrum allows for the selective measurement of Raman transitions from a particular species along the reaction path, while also significantly improving the signal-to-noise ratio.[34,41,51,107,123–126]

However, mode-specific resonance enhancements complicate the interpretation of FSRS spectra, particularly the assignment of the observed Raman bands to specific vibrational modes of the molecule in an excited state.[25,26,92] Although some assignments are possible based on simple

chemical intuition and comparison with vibrational frequencies from the ground electronic state, calculated frequencies and intensities are important for making accurate assignments in the excited state, particularly in regions of the spectrum with a high density of vibrational states. The excited-state vibrational frequencies are relatively easy to compute, but the Raman intensities are more challenging because they require the evaluation of changes in the excited-state polarizability tensor along each of the vibrational coordinates.[29,30,52,105,106,142]

Using a series of conjugated thiophene derivatives for benchmark comparison, we showed that it is possible to assign resonance-enhanced FSRS bands for a series of structurally similar molecules by calculating the off-resonant excited-state Raman spectra, and carefully considering which vibrational modes are most likely to be enhanced by the electronic resonance.[52] Vibrations with the strongest scattering signals have significant nuclear displacement along the potential energy surface of the resonant higher-lying excited state relative to the initial state upon $S_N \leftarrow S_1$ or $T_N \leftarrow T_1$ excitation with the Raman pump pulse. In a second contribution, we examined the resonance condition explicitly using a gradient approximation of the time-dependent resonance Raman (TD-RR) theory to simulate the experimental FSRS spectrum of the S_1 state of 2,5-diphenylthiophene (DPT).[53] The simulated spectrum qualitatively reproduced the mode-specific resonance enhancements by matching the gradients in a specific excited state (S_N) to the assigned vibrations of S_1.

In contrast with the S_1 spectra, where the resonance enhancement is strongly mode-dependent, the calculated off-resonance Raman spectra of the triplet states are in close agreement with the experimental FSRS spectra for the T_1 states of DPT and other aryl thiophenes in our benchmark series.[52] A similarly weak wavelength dependence of the resonance Raman spectrum has been observed for triplet states of other conjugated organic systems,[38,143,144] suggesting that triplet states may be less sensitive to mode-dependent resonance enhancement compared with the singlet states of the same molecules. In this chapter, we explore the weak wavelength dependence of the triplet Raman spectrum of the model compound 2-phenylthiophene (PT) in more detail. Comparing experimental FSRS spectra at different Raman excitation energies with theoretical simulations of the

72

on- and off- resonance spectra, we determine that the weaker mode-dependence of the T_1 Raman intensities compared with S_1 is a result of contributions from overlapping electronic transitions and increased homogeneous broadening of resonant T_N states, possibly due to non-adiabatic coupling within the triplet manifold.

This chapter is organized as follows. We briefly recount the relevant aspects of the time-dependent theory for resonance Raman scattering in Section 2, then summarize our experimental and theoretical approaches in Section 3. We compare the experimental and calculated electronic absorption spectra for the triplet state of PT in Section 4.1, and assign the vibrational bands of the FSRS spectrum with off-resonant calculations of the T_1 Raman spectrum in Section 4.2. In Sections 4.3 and 4.4, we examine the excitation wavelength dependence of the T_1 FSRS spectrum and then compare it to simulations of resonance Raman spectra obtained using two methods: an extrapolation of harmonic potentials, and the gradient approximation of TD-RR theory. Finally, we discuss the results in Section 5, and summarize our main conclusions in Section 6.

6.2 Theory

In order to motivate the different computational approaches used in the following sections, we begin with a brief summary of Raman scattering theory. More extensive descriptions of Raman and resonance Raman (RR) scattering are available in the literature.[27,29,30,72–74,92,127,128]

The intensity of a Raman transition from an initial vibrational state $|v_i\rangle$ to a final state $|v_f\rangle$ is proportional to the square of the transition polarizability tensor,

$$I \propto \omega_p(\omega_p - \omega_{fi})^3 \, |\alpha_{fi}|^2 \tag{6.1}$$

where ω_p is the incident photon frequency and ω_{fi} is the frequency of the vibrational transition. As introduced by Kramers, Heisenberg, and Dirac,[68] and also in the Placzek formulation of second-order time dependent perturbation theory,[67] the generic expression for the transition polarizability

between any two initial and final states $|i\rangle$ and $|f\rangle$ can be written as a sum over states,

$$\alpha_{fi} = \frac{1}{\hbar} \sum_n \left(\frac{\langle f| \hat{\mu} |n\rangle \langle n| \hat{\mu} |i\rangle}{\omega_{ni} - \omega_p - i\Gamma_n} + \frac{\langle f| \hat{\mu} |n\rangle \langle n| \hat{\mu} |i\rangle}{\omega_{nf} + \omega_p + i\Gamma_n} \right) \tag{6.2}$$

where $\{|n\rangle\}$ are all possible intermediate vibronic states, Γ_n are phenomenological broadening terms related to the dephasing of each intermediate state, $\hat{\mu}$ is the electric dipole operator, and ω_{ni} and ω_{nf} are the transition frequencies.

Due to the difficulty of evaluating the full sum-over-states expression in Equation 6.2, the transition polarizability can instead be recast in terms of a Taylor series expansion of the full electronic polarizability (α) with respect to the mass-weighted displacement of each vibrational coordinate, q_k,

$$\alpha_{fi} = \alpha_0 \langle v_f|v_i\rangle + \sum_k \left(\frac{\partial \alpha}{\partial q_k} \right)_0 \langle v_f| q_k |v_i\rangle + ... \tag{6.3}$$

where the subscript 0 indicates values at zero displacement of a vibration. Neglecting higher-order terms in the expansion, and assuming harmonic normal modes and an off-resonance electronic condition ($\omega_p = 0$), the transition polarizability for the fundamental of each vibrational mode k is proportional to the electronic polarizability derivative with respect to q_k,[29,30]

$$\alpha_{fi}^k \propto \sqrt{\frac{\hbar}{2\omega_k}} \left(\frac{\partial \alpha}{\partial q_k} \right)_0 \tag{6.4}$$

where ω_k is the vibrational frequency of the mode.

The Raman activity increases substantially when the incident pump field is at or near resonance with an electronic transition, in which case the transition polarizability is no longer simply described by Equation 6.4. The enhancement of the Raman signal is a result of the small denominator in the first term of Equation 6.2 as ω_p approaches ω_{ni}. Thus, the expression for the transition polarizability in Equation 6.2 reduces to a sum over intermediate vibrational states, $|v_n\rangle$, assuming that the Born-Oppenheimer approximation holds and in the limit of weak vibronic coupling.[25,29,71,74] For resonance with a single electronic state, the sum includes only vibrational levels

of the resonant electronic state, $|N\rangle$. The second term in Equation 6.2 is negligible under resonance or near-resonance conditions.[29]

In the time-dependent formalism for resonance Raman scattering, the denominator in the first term of Equation 6.2 is converted from the frequency domain to the time domain through a Fourier transform,[27,29,72,73]

$$\alpha_{fi} \approx \frac{i}{\hbar} \sum_{v_n} \int_0^\infty \langle v_f | \mu_{IN} | v_n \rangle \langle v_n | \mu_{NI} | v_i \rangle \, e^{-i(\omega_n - \omega_i - \omega_p - i\Gamma_n)t} dt \tag{6.5}$$

where $\langle v_f |$ and $|v_i\rangle$ are both within the initial electronic state $|I\rangle$, μ_{NI} is the electronic transition dipole between the initial and intermediate electronic states, and ω_n and ω_i are the frequencies of the intermediate and initial vibronic states, respectively. The sum over states $|v_n\rangle$ gives a time-dependent wavepacket that evolves according to the Hamiltonian, $\hat{H}_N$,[25,27,29,31] describing nuclear motion in the intermediate electronic state, $|N\rangle$. Thus, we recast Equation 6.5 as the time-integrated overlap of the wavepacket in the resonant state $|v_i(t)\rangle = e^{-i\hat{H}_N t/\hbar} |v_i\rangle$ with the vibrational wavefunction of the final state $\langle v_f|$,[53]

$$\alpha_{fi} \approx \frac{i}{\hbar} \int_0^\infty |\mu_{NI}|^2 \langle v_f | e^{-i\hat{H}_N t/\hbar} |v_i\rangle \, e^{i(\omega_i + \omega_p + i\Gamma_n)t} dt \ . \tag{6.6}$$

An implicit assumption in Equation 6.6 is that the electronic transition dipole follows the Condon approximation, which gives only the A term in the Albrecht description of Raman scattering.[29,74,75] The other Albrecht scattering terms (B, C, and D) are a result of Herzberg-Teller (HT) vibronic coupling between electronic states. The vibronic coupling terms arise from a perturbative expansion of the transition dipole in the nuclear coordinates of intermediate electronic state $|N\rangle$,[29,31]

$$\mu_{NI} = (\mu_{NI})_0 + \sum_j \left(\frac{\partial \mu_{NI}}{\partial q_j^{(N)}} \right)_0 q_j^{(N)} + \dots \tag{6.7}$$

The derivative of the electronic transition dipole with respect to the nuclear coordinates $q_j^{(N)}$ gives the vibronic coupling of electronic states $|N\rangle$ and $|I\rangle$ with all other states $\{|M\rangle\}$ as a perturbation

of the electronic Hamiltonian, $\hat{H}_{elec}$.[29]

$$\left(\frac{\partial \mu_{NI}}{\partial q_j^{(N)}}\right)_0 = \frac{1}{\hbar}\left\{\sum_{M \neq I}(\mu_{NM})_0\frac{\langle M|\frac{\partial \hat{H}_{elec}}{\partial q_j^{(N)}}|I\rangle}{\omega_I - \omega_M} + \sum_{M \neq N}\frac{\langle N|\frac{\partial \hat{H}_{elec}}{\partial q_j^{(N)}}|M\rangle}{\omega_N - \omega_M}(\mu_{MI})_0\right\} \qquad (6.8)$$

Substituting the expansion for μ_{NI} and truncating Equation 6.7 at first order yields a more complete form of the transition polarizability,

$$\begin{aligned}
\alpha_{fi} \approx \frac{i}{\hbar}\int_0^\infty dt\, e^{i(\omega_i + \omega_p + i\Gamma_n)t}\Big\{& \left|(\mu_{NI})_0\right|^2\langle v_f|e^{-i\hat{H}_N t/\hbar}|v_i\rangle \\
& + \sum_j (\mu_{IN})_0\left(\frac{\partial \mu_{NI}}{\partial q_j^{(N)}}\right)_0\langle v_f|e^{-i\hat{H}_N t/\hbar}q_j^{(N)}|v_i\rangle \\
& + \sum_j \left(\frac{\partial \mu_{IN}}{\partial q_j^{(N)}}\right)_0(\mu_{NI})_0\langle v_f|q_j^{(N)}e^{-i\hat{H}_N t/\hbar}|v_i\rangle \\
& + \sum_j\sum_l \left(\frac{\partial \mu_{IN}}{\partial q_j^{(N)}}\right)_0\left(\frac{\partial \mu_{NI}}{\partial q_l^{(N)}}\right)_0\langle v_f|q_j^{(N)}e^{-i\hat{H}_N t/\hbar}q_l^{(N)}|v_i\rangle\Big\}.
\end{aligned} \qquad (6.9)$$

The first term on the right-hand side is the Albrecht A term from Equation 6.6. Together, the second and third terms on the right-hand side are the Albrecht B and C terms, where the B term includes coupling between intermediate state $|N\rangle$ and all other electronic states, and the C term includes coupling of the initial electronic state to the other electronic states. Similarly, the final term in Equation 6.9 represents D-term scattering, which includes contributions from electronic states coupled to $|N\rangle$ and $|I\rangle$ simultaneously. Equation 6.8 shows that the B, C, and D terms scale with the inverse of the energy separation between the coupled electronic states, and therefore are most important for states nearby in energy. It is worth noting that the calculated polarizability derivative from Equation 6.4 implicitly contains some degree of vibronic coupling for transitions in which only one vibrational quantum number changes.[29]

The implementation of Equation 6.9 using computational methods has been described in detail by Baiardi *et al.*,[31] where the first term, containing no implicit vibronic coupling, corresponds to the Franck-Condon (FC) approximation, and the B-C terms are labeled as FCHT to denote the

inclusion of Herzberg-Teller coupling. This implementation uses the extrapolation of a harmonic potential expanded around the minimum-energy geometry of $|N\rangle$ in order to obtain the vibrational wavefunctions at the Franck-Condon geometry. This approach works well for ground-state resonance Raman spectra with resonant excitation to relatively low-lying electronic states.[31,76,79] However, FSRS measurements of electronically excited systems tend to be resonant with transitions to higher-lying states, where the density of states is larger and the states become more anharmonic.

An alternative to the FC and FCHT approach is the semi-classical "gradient approximation" to the TD-RR formalism,[53,71,72] where the time-dependent overlap integral $\langle v_f | v_i(t) \rangle$ is simplified by approximating the initial wavefunction $|v_i(t)\rangle$ with a Gaussian function at $t = 0$, which then propagates in time on the potential energy surface (PES) of the intermediate electronic state, V_N, according to the Hamiltonian of that state. Although the time-evolution of this wavepacket depends on the topology of the PES of $|N\rangle$, the Raman intensity observed for a particular mode, k, depends on the time-integrated overlap of $|v_i(t)\rangle$ with the vibrational wavefunction $\langle v_f |$ of the final state. Thus, the time-evolution of the wavepacket using classical equations of motion depends, to first order, on the gradient of the upper-state PES along each of the vibrational coordinates of the lower state, $\frac{\partial V_N}{\partial q_k}$. Substituting a Gaussian wavefunction into Equation 6.6 gives the simplified version of the time-dependent overlap integral,[53,72]

$$\alpha_{fi}^k \approx -\frac{i}{\hbar} |\mu_{NI}|^2 \left(\frac{\partial V_N}{\partial q_k} \right) \int_0^\infty e^{i(\omega_i + \omega_p - \omega_{NI} + i\Gamma_n)t} e^{-\left(\frac{\partial V_N}{\partial q_k} \right)^2 \frac{t^2}{4\omega_k}} t \, dt \tag{6.10}$$

where ω_{NI} is the vertical transition energy between electronic states N and I. The final expression for the resonance-enhanced Raman scattering intensity of mode k is proportional to the square of the transition polarizability term, and therefore depends on the square of the gradient of the potential along q_k.[53,76]

$$I_k \propto \omega_p (\omega_p - \omega_k)^3 \, |\alpha_{fi}^k|^2 \approx \omega_p (\omega_p - \omega_k)^3 \frac{|\mu_{NI}|^4}{2\omega_k} \left(\frac{\partial V_N}{\partial q_k} \right)^2 \tag{6.11}$$

Due to computational cost, our calculations using the gradient approximation neglect vibronic

coupling, and therefore include only A-term scattering. However, by numerically calculating the adiabatic PES of the resonant electronic state along the nuclear displacement coordinates of T_1, the resonance Raman spectra obtained with the gradient approximation partially account for the anharmonicity of the potentials of higher-lying electronic states, contrary to the FC and FCHT approaches.

In Section 4, we compare the experimental FSRS spectrum with both the off-resonance calculations and the simulated resonance Raman spectra using the FC/FCHT models (Equation 6.9) and the gradient approximation (Equation 6.11).

6.3   Experimental and Computational Methods

The experimental setup for transient absorption (TA) and FSRS measurements was described previously,[53] therefore we only summarize the main points here. We split the output of an amplified Ti:Sapphire laser (Coherent, Legend Elite HP) into three portions and use nonlinear frequency conversion to generate actinic pump, Raman pump, and Raman probe pulses. A commercial optical parametric amplifier (OPA) with two additional stages of nonlinear frequency conversion produces actinic pump pulses at 300 nm ($\sim$90 fs and $\sim$1.0 μJ at the sample). A second commercial OPA provides tunable near-IR pulses that we subsequently pass through a 25 mm long β-barium borate (BBO) crystal to produce spectrally narrow ($<$0.5 nm) Raman pump pulses ranging from 360-385 nm via spectral-compression of the second harmonic.[87–89] We generate Raman pump pulses at 400 nm by passing a portion of the 800 nm fundamental directly through the long BBO. Passing the narrowband pulses through a $4f$ spectral filter eliminates asymmetry in the temporal profile and further narrows the bandwidth.[87] The resulting Raman pump pulses have $\sim$1 ps duration, 0.3-0.7 μJ per pulse, and $<$30 cm^{-1} bandwidth. Using a focal diameter of $\sim$100 μm at the sample minimizes excited-state population depletion and ensures that the resonant-FSRS signal scales linearly with pulse energy.[145] We generate fs Raman probe pulses by focusing a small portion of the 800 nm laser fundamental into a translating CaF_2 window to produce white-light continuum spanning 340-750 nm.[52,53] We use the full bandwidth of the probe pulses for TA measurements, but only a

narrow range of $\sim$25-30 nm for FSRS. Dispersion of the uncompressed probe pulses over the narrow range of the FSRS measurement is negligible compared with the duration of the pump pulse. All three pulses overlap in the sample with parallel polarization.

After the sample, a 1/8 m imaging spectrograph with 1800 line/mm grating disperses the Raman probe pulses onto a 2068 pixel linear CCD array (Hamamatsu, S11156-2048) with instrument-limited resolution that ranges from $\sim$45 to $\sim$29 cm^{-1} as we tune the excitation wavelength from 360 to 400 nm. We measure the intensity of the transmitted probe light at 1 kHz, chopping the actinic pump pulses at 500 Hz and the Raman pump pulses at 250 Hz for active background subtraction. Averaging 4×10^6 laser pulses per spectrum gives a standard deviation of <10^{-5} in the Raman gain signal. The baseline subtraction method is described in the Supporting Information (SI). The sample consists of a 1.2 mM solution of 2-phenylthiophene (TCI America) in cyclohexane (spectroscopic grade, Fisher).

We calculate electronic absorption and Raman spectra using either unrestricted open-shell time-dependent density functional theory (TD-DFT) with the B3LYP or BHLYP functionals,[110,111] or the equation of motion coupled cluster theory with single and double excitations method (EOM-CCSD).[146–148] B3LYP and BHLYP are global hybrid functionals with 20% and 50% Hartree-Fock (HF) exchange, respectively, that typically give good agreement with experimental ground-state Raman spectra.[114,149] In all cases, we use the aug-cc-pVDZ basis set[113] for a good compromise between accuracy and computational cost for the CCSD calculations. We calculate off-resonant T_1 Raman spectra analytically for DFT and numerically for CCSD.[150–153] We simulate the resonance Raman spectra using both the FC and FCHT approaches (B3LYP only), as well as the gradient approximation (TD-DFT and EOM-CCSD), as described above.

Due to the difficulty in optimizing the geometry of high-lying states, our resonance Raman calculations using the FC and FCHT approaches (without and with HT coupling, respectively)[31] only include the spectrum for resonance with a single upper state T_N having the strongest electronic transition strength. The contribution from T_N is determined following the adiabatic Hessian model, which includes both Duschinsky rotation and the normal mode frequency changes between

79

states.[31] Both the FC and FCHT calculations were carried out with an incident energy equal to the adiabatic transition energy of the resonant state.

For the gradient approximation, we calculated the $T_N \leftarrow T_1$ transition moments for states up to $N = 20$ with either TD-DFT or EOM-CCSD. The gradients of the T_N potential energy surfaces were determined numerically by fitting a second-order polynomial to three points along each of the T_1 normal mode coordinates, including the optimized geometry and ±7.408 x10^{-4} times the normalized displacement. The magnitude of the displacement was optimized in previous work to minimize the errors in calculated Raman activities.[52] All calculations were performed using a development version of the GAUSSIAN software package,[78] and all simulated Raman spectra include 25 cm^{-1} Gaussian broadening.

6.4 Results and Analysis

6.4.1 Excited-State Absorption Spectroscopy

The evolution of the transient absorption (TA) spectrum of PT is displayed in Figure 6.1. After $S_1 \leftarrow S_0$ excitation at 300 nm, the TA spectrum has a strong excited-state absorption band at 475 nm and a stimulated emission band at 340 nm. The 475 nm band is attributed to transitions from the S_1 state, and narrows within the first $\sim$10 ps due to structural relaxation and vibrational cooling.[47,107] The excited molecule undergoes intersystem crossing (ISC) to T_1 with a single-exponential time constant of $\tau_{ISC} = 102 \pm 5$ ps, resulting in the appearance of a series of triplet-triplet absorption bands that includes a strong transition centered near 360 nm and several weaker transitions at longer wavelengths.[47,52,107]

Figure 6.2 compares the experimental absorption spectrum of T_1 at a time delay of 408 ps (4 $\times$ τ_{ISC}), with the calculated spectra of the triplet state from EOM-CCSD, TD-B3LYP, and TD-BHLYP. The figure includes a deconvolution of the experimental triplet absorption spectrum with a sum of five Lorentzian bands. The deconvolution uses the same adjustable bandwidth for all of the transitions. The best fit to the data gives a bandwidth of 0.197 ± 0.001 eV, with relatively
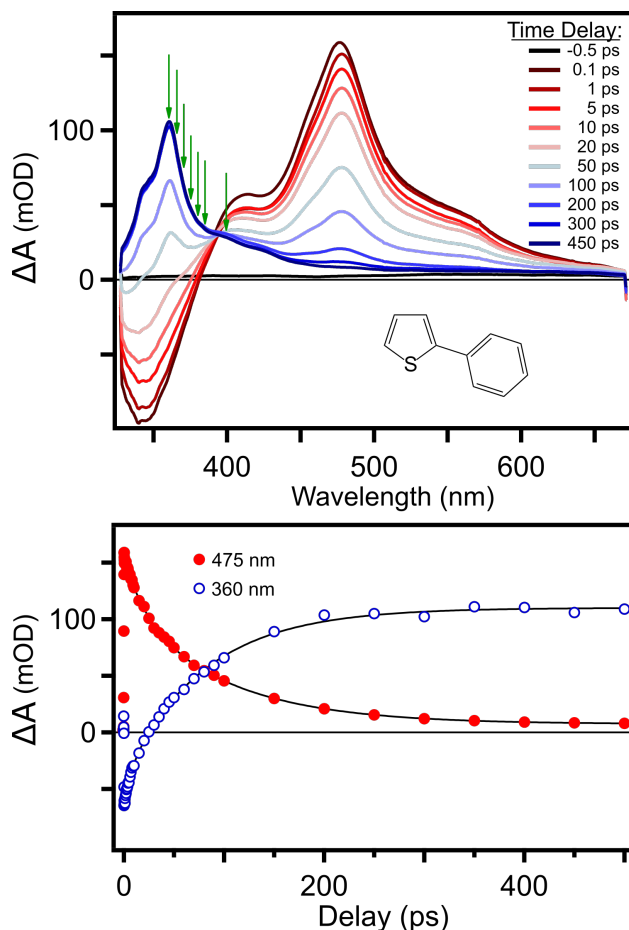
Figure 6.1: Evolution of the transient electronic absorption spectrum of PT following 300 nm excitation. Green arrows in the top panel indicate Raman excitation wavelengths for FSRS measurements (360-400 nm) at 408 ps delay. The lower panel shows the kinetics at 475 and 360 nm to illustrate the simultaneous decay of S_1 and rise of T_1.

small uncertainties in the band positions and amplitudes. Details of the deconvolution are given in Figure S3 of the SI.

For comparison, the simulated spectra in Figure 6.2 have been shifted to align the strongest calculated transitions in each case with the maximum of the TA spectrum. The simulated spectra include Lorentzian broadening with a FWHM of 0.2 eV, consistent with the deconvolution of the experimental spectrum. The three computational methods give slightly different $T_N \leftarrow T_1$ excitation energies, but the qualitative structure of all three calculated spectra are in good agreement with experiment. Each of the calculated spectra has a single, strong transition to T_{12} or T_{13}, depending on the method, as well as several weaker transitions. Although TD-B3LYP requires the smallest
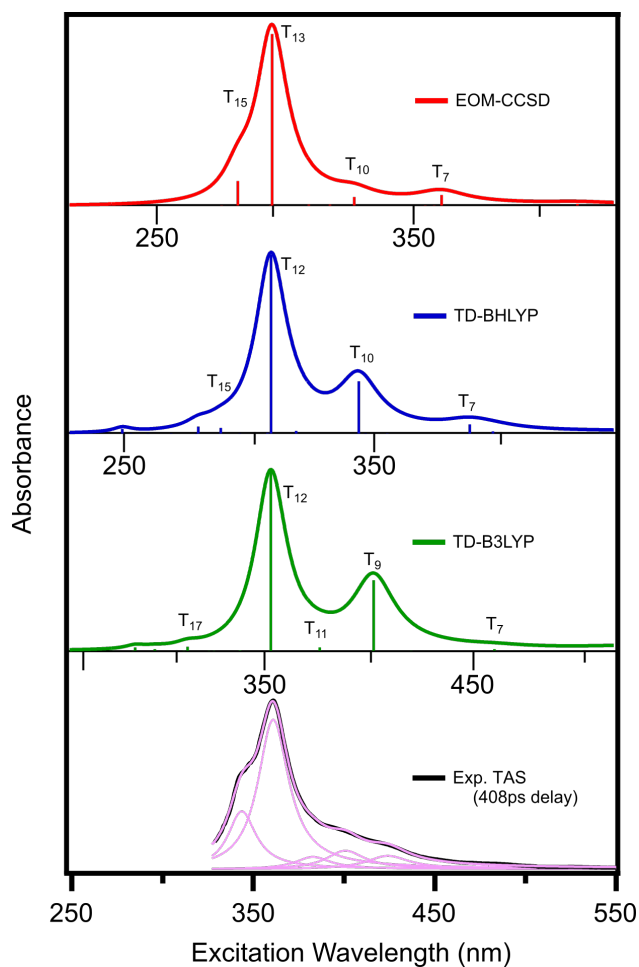
Figure 6.2: Electronic absorption spectra for the T_1 state of PT. Calculated spectra are shifted by 0.720 eV (EOM-CCSD), 0.575 eV (TD-BHLYP), and 0.110 eV (TD-B3LYP) to align the strongest transition with experiment. Simulated spectra use 0.2 eV Lorentzian broadening. Pink lines show a deconvolution of the experimental spectrum with 5 Lorentzian bands.

shift to align the strongest transition with experiment, the other methods reproduce the shape better, particularly EOM-CCSD. The calculations indicate that there are as many as 6 optically accessible states within $\sim$0.4 eV of the state with the strongest transition.

6.4.2 Vibrational Assignments for the T_1 FSRS Spectrum

The experimental FSRS spectrum for the T_1 state of PT is shown in Figure 6.3, along with the calculated off-resonance Raman spectra using B3LYP, BHLYP, and CCSD. A complete list of calculated frequencies and Raman activities is included in Table S2 of the SI. The frequencies of the calculated spectra in Figure 6.3 are multiplied by empirical scaling factors of 0.970,[116] 0.924,[154] and 0.963[116] for B3LYP, BHLYP, and CCSD, respectively. The experimental spectrum was measured with the Raman pump excitation at 365 nm and a delay of 408 ps. The long time delay and resonance with the triplet absorption band ensure that the resonance enhanced FSRS spectrum includes contributions from only the T_1 state.

Using the calculated frequencies as a foundation, we assign the Raman bands by identifying the vibrations most likely to have strong resonance enhancement.[52] We predict the resonance enhancements of the vibrational modes based on two criteria: the mode must be totally symmetric (a') to provide a non-zero contribution to the resonance Raman activity,[29,72] and the PES of the resonant electronic state will have a large gradient along the vibrational displacement coordinate of the T_1 normal mode.[26,27,73,76] We expect that the $T_N \leftarrow T_1$ transitions are most likely π-π^* excitations, and therefore the largest gradients in T_N will be along vibrational modes with significant distortion of the π-conjugated framework of the molecule.[52,53]

The vibrational assignments based on B3LYP are listed in Table 6.1 and the nuclear displacement vectors for the assigned vibrations are represented in Figure 6.4. The majority of assignments are straightforward, as there is only one calculated totally symmetric vibration within $\sim$40 cm^{-1} of the experimental bands. Two noteworthy exceptions are the bands at 1402 cm^{-1} and 1444 cm^{-1}, for which there are three possible assignments: ν_{38}, ν_{39}, and ν_{40}. While the FSRS signals may be attributed to any combination of these C=C stretching and C–H bending vibrations, our calcula-
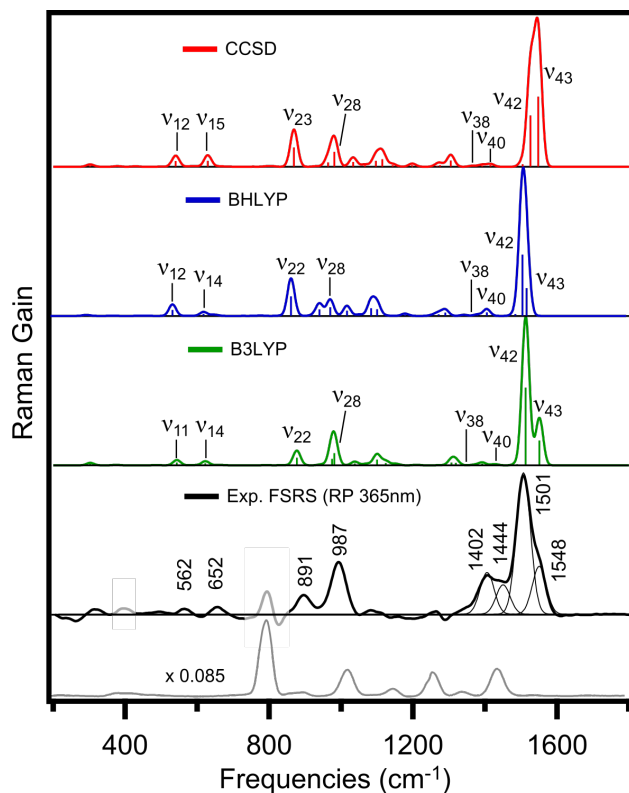
Figure 6.3: Raman spectra for the T_1 state of PT. Calculated off-resonance Raman spectra include 25 cm^{-1} Gaussian broadening and frequency correction factors given in the text. The experimental spectrum was measured with 365 nm Raman excitation and 408 ps delay, with thin black lines showing a deconvolution of the 1350-1600 cm^{-1} region using four Gaussian functions. The cyclohexane solvent spectrum (grey) is included for comparison.

tions of the resonance-enhanced Raman spectra (presented in a later section) predict ν_{38} and ν_{40} to have the strongest resonance enhancements, despite their small amplitudes in the off-resonance spectra. Similarly, the band at 987 cm^{-1} could be assigned as either ν_{27} or ν_{28}, but the calculations are most consistent with the latter. The results for BHLYP and CCSD are similar to B3LYP, and the assignments for all three methods are listed in Table S3 of the SI.

For a more quantitative comparison, Table 6.1 shows the relative intensities of the assigned Raman bands in the experimental and calculated (B3LYP) spectra. The ratios for the calculated intensities are relative to the strongest transition at 1513 cm^{-1}. The relative experimental intensities are obtained by integrating each Raman band and taking the ratio relative to the strongest band at 1501 cm^{-1}. To deconvolute the overlapping high-frequency Raman bands in the experimental FSRS spectrum, we fit the 1350-1600 cm^{-1} region of the spectrum to a sum of four Gaussian

(a) ν_{11} (b) ν_{14} (c) ν_{22} (d) ν_{28} (e) ν_{38} (f) ν_{40} (g) ν_{42} (h) ν_{43}
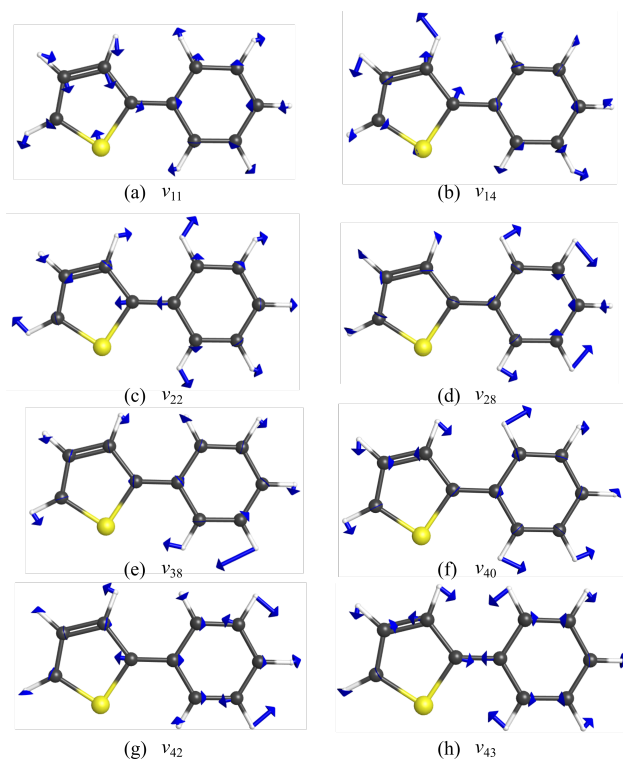
Figure 6.4: Vibrational displacement vectors for assigned vibrations of the T_1 state of PT (B3LYP).

Table 6.1: Assignment of T_1 Raman Transitions

Vibration	Symmetry	Calc. Frequency[a] (cm^{-1})	Calc. Relative Raman Intensity[b]	Exp. Frequency (cm^{-1})	Exp. Relative Raman Intensity[b]	Motion
ν_{11}	a'	544	0.035	562	0.030	C-S-C bend and phenyl dist.
ν_{14}	a'	622	0.027	652	0.071	C-S-C str. and phenyl dist.
ν_{22}	a'	877	0.096	891	0.146	C-C-C bend/ring dist.
ν_{28}	a'	981	0.234	987	0.396	C-C-C bend/phenyl dist.
ν_{38}	a'	1370	0.005	1402	0.295 [c]	bridging C=C str. and C-H bend
ν_{39}	a'	1392	0.019	-	-	bridging C=C str. and C-H bend
ν_{40}	a'	1427	0.007	1444	0.208 [c]	thienyl C=C str. and C-H bend
ν_{42}	a'	1513	1.000	1501	1.000 [c]	C=C str. and phenyl dist.
ν_{43}	a'	1551	0.322	1548	0.339 [c]	C=C str. and ring dist.

[a] B3LYP, includes frequency scaling factor of 0.970. [116] See Table S3 for assignments using BHLYP and CCSD.
[b] Ratio of integrated band intensities relative to the band at 1513 cm^{-1} (calc.) or 1501 cm^{-1} (exp.). The experimental Raman excitation wavelength is 365 nm.
[c] From deconvolution of the 1350-1600 cm^{-1} region of the FSRS spectrum.

functions. We use a single, adjustable FWHM parameter of 46 cm^{-1} to match the experimental line width based on the instrument resolution. The deconvolution, shown in Figure 6.3, reveals at least four bands, including a band at 1548 cm^{-1} that appears as a shoulder of the stronger 1501 cm^{-1} band, and the two bands at 1402 and 1444 cm^{-1}, respectively. See Figure S4 in the SI for a

more detailed description of the deconvolution.

Comparing the spectra in Figure 6.3 and the relative intensities in Table 6.1, we find good agreement between experiment and theory for most of the assigned vibrations. The relative intensities of the experimental bands agree with the calculations to within 10%, except for the bands at 1402 and 1444 cm^{-1}, which are significantly stronger in the experiment. The other computational methods have similar agreement with the experimental FSRS spectrum, and relative intensities that differ from B3LYP by less than 20% in most cases (Table S3). Therefore, all of the simulated off-resonance spectra are in good agreement with the experimental FSRS spectrum, other than the 1402 and 1444 cm^{-1} bands, with B3LYP performing slightly better than the other methods. Good agreement between off-resonance calculations and the resonance-enhanced Raman spectra also has been reported in the literature for the triplet states of a number of other molecules.[38,144,155,156] In contrast, our previous studies of the excited singlet (S$_1$) states of PT, DPT, and other aryl-thiophenes showed significant disagreement in the intensities between the resonance-enhanced FSRS spectra and the calculated off-resonant S$_1$ Raman spectra.[52,53] To the best of our knowledge, the reason for the much weaker mode dependence of the resonance Raman enhancement for the triplet spectra compared with singlet spectra has not been addressed.

6.4.3   Wavelength Dependence of the T$_1$ FSRS Spectrum

In order to explore resonance-enhancement effects in the T$_1$ spectrum of PT, we measure the Raman excitation wavelength dependence by tuning the Raman pump from the maximum absorption at 360 nm to a weaker band in the triplet absorption spectrum at 400 nm in ~5 nm increments (see green arrows in Figure 6.1). The FSRS signal is too weak to observe at longer wavelengths. Figure 6.5 shows the FSRS spectrum at each Raman excitation wavelength. To account for differences in the signal strength due to slight variation of the Raman pump power and beam overlap at the different pump wavelengths, we normalize the transient spectra based on the intensities of the solvent Raman bands at the different excitation wavelengths (Figure S2 of the SI). We use the integrated intensities of the four dominant Raman bands of the pure solvent (801, 1028, 1266, and 1444 cm^{-1}

of cyclohexane) to normalize the spectrum at each excitation wavelength. We also account for the $\omega_p(\omega_p - \omega_k)^3$ frequency dependence of the solvent Raman signal (Equation 6.1) by multiplying each of the normalized spectra with an additional correction factor relative to the value at 400 nm.
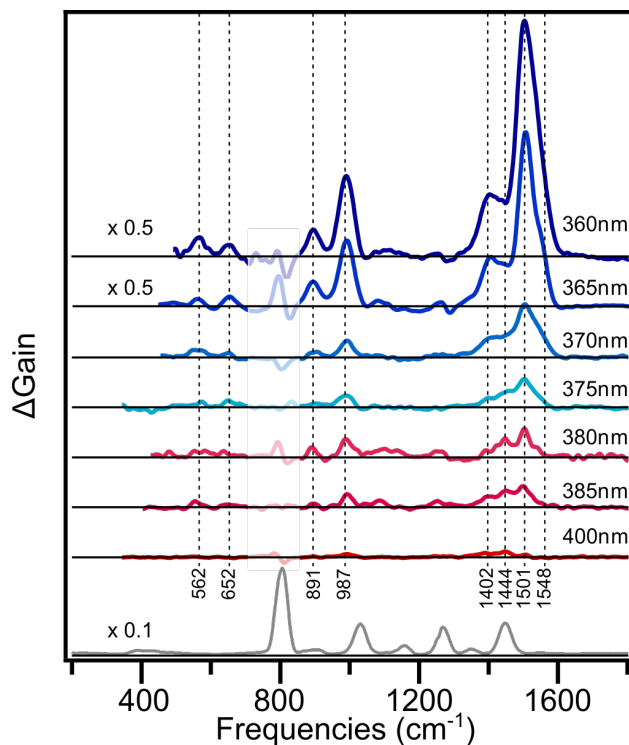
Figure 6.5: Excitation wavelength dependence of FSRS spectrum for the T_1 state of PT. Vertical dashed lines indicate assigned vibrations from Table 6.1. Cyclohexane solvent spectrum (grey) shown for comparison.

The Raman intensities of PT become significantly weaker in Figure 6.5 as the excitation wavelength moves off resonance with the strongest $T_N \leftarrow T_1$ transition at 360 nm. Even at longer wavelengths, all of the bands assigned in Figure 6.3 are resolved, except the 652 and 1548 cm^{-1} bands, which fall below the noise level. We also observe a change in the relative intensities of the high-frequency bands. The 1501 cm^{-1} band, which dominates the spectrum at Raman pump wavelengths $\leq$ 375 nm, becomes weaker in intensity than the 1402 and 1444 cm^{-1} bands at 400 nm excitation.

Figure 6.6 compares the Raman excitation profiles for each of the assigned vibrational bands with the profile of the triplet absorption spectrum. The intensities of the 1402, 1444, 1501, and 1548 cm^{-1} bands are obtained through the same deconvolution procedure at each wavelength as
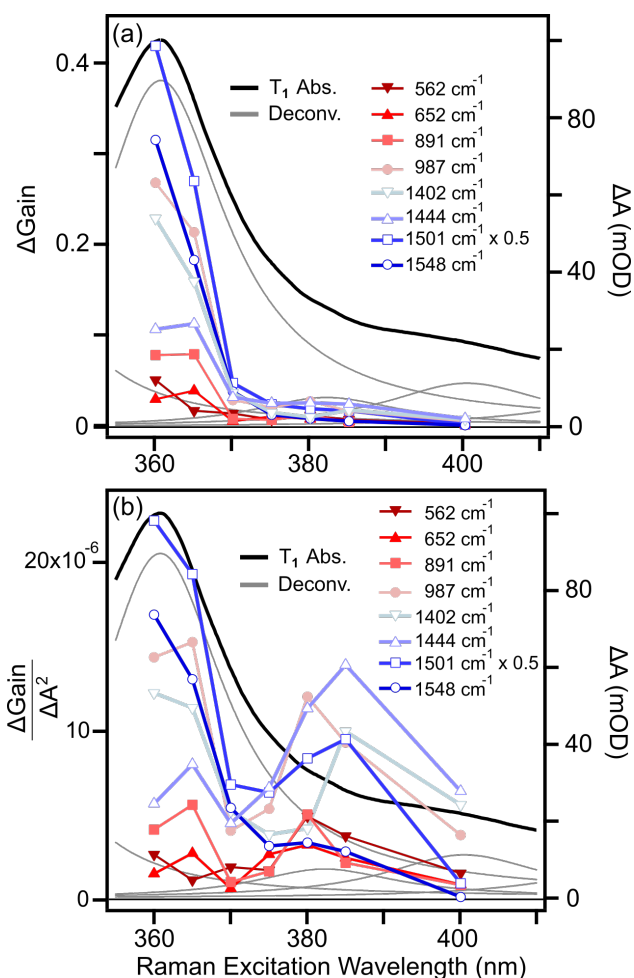
Figure 6.6: Raman excitation profiles for the assigned FSRS bands. The top panel compares integrated intensities of Raman bands with the profile of the triplet absorption spectrum. The lower panel shows the same excitation profiles divided by the square of the triplet absorption $(\Delta A)^2$ at each Raman excitation wavelength to compensate for the strong electronic contribution to the resonance enhancement. The T_1 absorption spectrum (thick black) and Lorentzian deconvolution (grey) from Figure 6.2 are included for comparison.

described above for the FSRS spectrum at 365 nm. The deconvolution at each wavelength is shown in Figure S5 of the SI. The relative behaviors of the mode-specific excitation profiles at longer wavelengths are difficult to distinguish in Figure 6.6(a) due to the strong resonance enhancement, therefore we scale the excitation profiles by dividing the Raman gain at each excitation wavelength by the square of the triplet absorption signal $(\Delta A)^2$ at that wavelength in Figure 6.6(b). The result is similar to dividing the Raman gain by a factor $|\mu_{NI}|^4$ in order to eliminate the mode-independent electronic contribution to the resonance enhancement (see below). Although the $(\Delta A)^2$ term is phenomenological, dividing by this value allows for a better comparison of the relative wavelength dependence of the Raman gain profiles for the individual Raman bands by compensating for the strong electronic resonance enhancement of the experimental FSRS signal.

Figure 6.6(b) shows that the excitation profile of the 1548 cm^{-1} band closely follows the shape of the deconvoluted absorption band at 360 nm, and the profile of the 1444 cm^{-1} band has a maximum near 385 nm that roughly matches the center wavelength of a second transition in the deconvolution of the TA spectrum. The 987, 1402, and 1501 cm^{-1} bands have excitation profiles that follow both electronic transitions, initially dropping in intensity from 360 to 370 nm, increasing at 380-385 nm, then decreasing again at longer wavelengths. In contrast, the 562, 652, and 891 cm^{-1} bands have comparatively little variation in normalized intensity with the Raman excitation wavelength. In order to explore the resonant $T_N \leftarrow T_1$ transitions that contribute to these mode-specific enhancement trends, we simulate the resonance-enhanced excited-state Raman spectrum in the next section.

6.4.4 Simulated Resonance Raman Spectra

First, we simulate the resonance Raman spectrum of the triplet state of PT with the FC and FCHT methods using TD-B3LYP. The calculated spectra are shown in Figure 6.7 for a single electronic state at a frequency resonant with the adiabatic transition energy. It is immediately apparent that the calculations do not accurately reproduce the experimental spectrum, regardless of the inclusion of vibronic coupling. Both the FC and FCHT results are dominated by several strong bands below
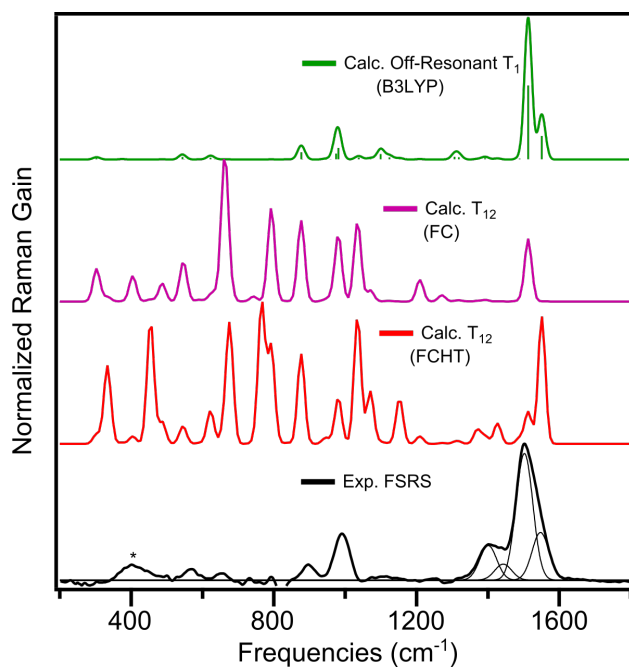
Figure 6.7: Comparison of simulated resonance Raman spectra from FC and FCHT approaches with calculated off-resonance and experimental FSRS spectra. FC/FCHT spectra are calculated for resonance with state T_{12} at the adiabatic transition energy (26470 cm^{-1}). All simulated spectra are from B3LYP and include 0.970 frequency scaling factor and 25 cm^{-1} Gaussian broadening. Asterisk denotes an artifact from the CaF_2 sample window.

1000 cm^{-1}, which contrasts with the experimental FSRS spectrum in the bottom panel of the figure.

Next, we simulate the resonance Raman spectrum using the gradient approximation[71,72,76] with TD-BHLYP, TD-B3LYP, and EOM-CCSD, as shown in Figure 6.8. The calculated Raman intensities have a strong dependence on the electronic absorption strength that makes it difficult to distinguish qualitative features for the weaker $T_N \leftarrow T_1$ transitions. Thus, the simulated resonance Raman spectra in Figure 6.8 are divided by the square of the electronic oscillator strength, f^2, which is proportional to $|\mu_{NI}|^4$ for each transition. This scaling is similar in approach to the phenomenological scaling of the experimental Raman gain profiles in Figure 6.6(b), and reveals the gradients of each excited state T_N along the totally-symmetric (a_1) normal modes of T_1. The figure only shows simulated spectra for the two states with the strongest electronic transitions at each level of theory. Gradient calculations for additional electronic states T_N are shown in Figure S6 of the SI. Due to computational cost, we restrict the EOM-CCSD gradient calculations to include only the vibrations within a limited range of frequencies near the assigned experimental bands.

The simulated resonance Raman spectra from the gradient method have several features that are in good agreement with experiment. For example, many of the vibrations that have intensity in the simulated spectra match the assigned vibrations in Figure 6.3, including the 1501 and 1548 cm^{-1} bands. Notably, the Raman spectra for resonance with the strongest (T_{12} or T_{13}) and second strongest (T_9 or T_{10}) electronic transitions at each level of theory predict significant intensity in ν_{38} and ν_{40}, respectively. The resonance enhancement of ν_{38} and ν_{40} is consistent with the relatively strong experimental FSRS bands at 1402 cm^{-1} and 1444 cm^{-1}. Furthermore, the stronger enhancement of ν_{40} for resonance with T_9/T_{10} compared with T_{12}/T_{13} matches the experimental excitation profile for the 1444 cm^{-1} band in Figure 6.6. We also point out that the Raman intensities of the low-frequency vibrations using the gradient method are much more reasonable than those from the FC/FCHT methods in Figure 6.7.

However, there are also some important discrepancies using the gradient approach that require
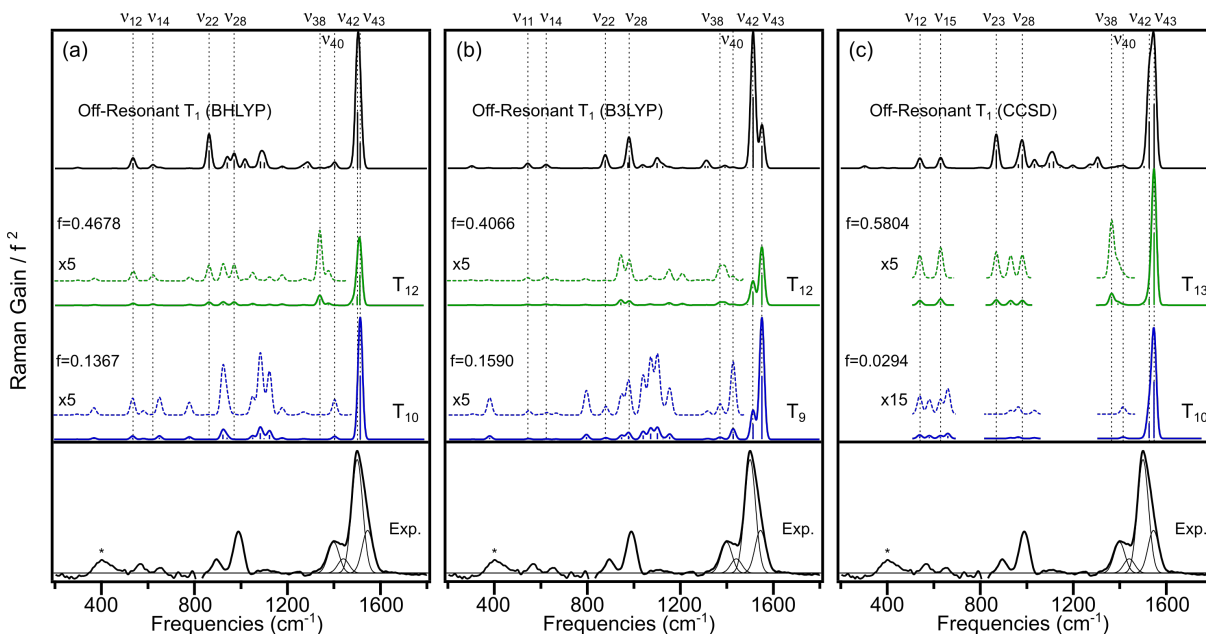
Figure 6.8: Comparison of simulated resonance Raman spectra from the gradient approximation with calculated off-resonance and experimental FSRS spectra. Simulated spectra are shown for resonance with the two strongest electronic transitions only, and include frequency scaling and 25 cm^{-1} Gaussian broadening. Asterisk denotes an artifact from the CaF_2 sample window.

closer investigation, such as the relative intensities of the 1501 and 1548 cm^{-1} Raman bands. The gradient calculations consistently predict stronger enhancement of the 1548 cm^{-1} band, in contrast with the dominant 1501 cm^{-1} band in both the experimental FSRS and calculated off-resonance spectra. To highlight this point, Figure 6.9 compares the high-frequency region of the experimental and simulated resonance Raman spectra. The figure shows the FSRS spectrum measured at 360 nm, and includes only the calculated resonance Raman spectrum for the electronic state with the strongest transition strength (T_{12} or T_{13}) in each computational method. The simulations also predict the wrong relative intensities of these high-frequency modes for resonance with the second strongest transition (T_9 or T_{10}, depending on the level of theory). The enhancement of the higher-frequency mode for both electronic states contrasts the experimental excitation profile, which decreases sharply with increasing wavelength for the 1548 cm^{-1} band. Similarly, the simulated resonance Raman spectra for T_9/T_{10} have much lower intensity in the 987, 1402, and 1501 cm^{-1} bands compared with T_{12}/T_{13}, which does not match the recurrence of the experimental excitation profiles around 380-385 nm.

92

Figure 6.9: High-frequency region of the simulated resonance Raman spectra for the strongest $T_N \leftarrow T_1$ transitions. Assigned vibrations are indicated by vertical dotted lines. Simulated Raman spectra are normalized, and include 25 cm^{-1} Gaussian broadening. Experimental FSRS spectrum at 360 nm Raman pump is shown for comparison, including deconvolution with 4 Gaussian bands.

6.5 Discussion

The simulated Raman spectra using resonance and off-resonance methods agree with different aspects of the experimental FSRS spectrum of 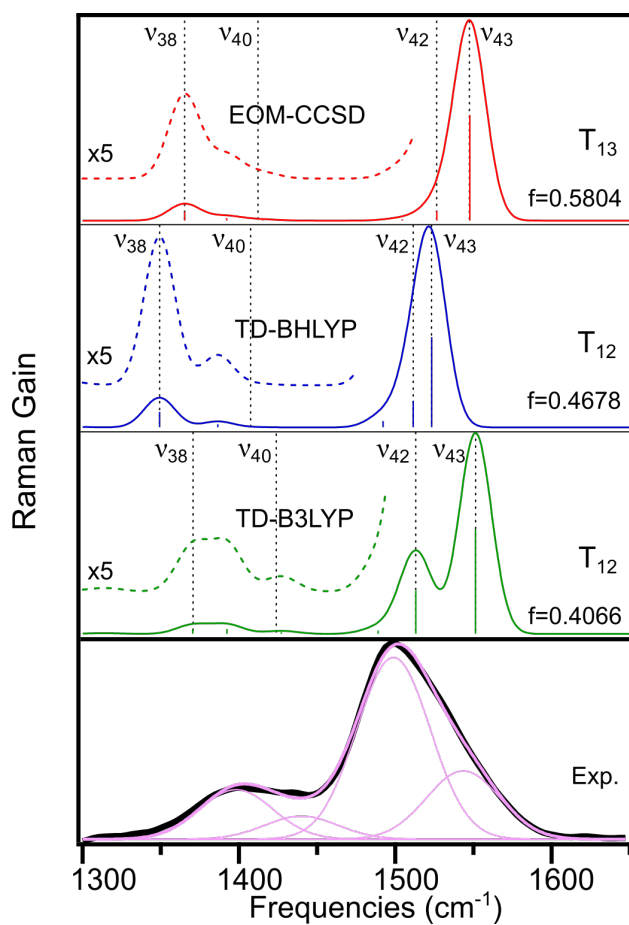the T_1 state of PT, but neither approach fully reproduces the experimental results. Off-resonance calculations generally are in good agreement with the experimental spectrum, with a few notable exceptions where the calculations underestimate the intensities of the experimental bands. Simulated resonance Raman spectra using the FC/FCHT methods and the gradient approximation introduce the effects of electronic resonance, but do not provide a better overall agreement with the experimental spectrum than the off-resonance calculations. The failure of the FC/FCHT methods in reproducing the experiment is likely a consequence of using the harmonic approximation to extrapolate the PES of the higher-lying triplet state from its minimum to the Franck-Condon geometry. On the other hand, simulated resonance Raman spectra using the gradient approximation correctly predict strong enhancements for several of the high-frequency vibrations (>1200 cm^{-1}), and explain the strong 1402 and 1444 cm^{-1} bands that are absent from the off-resonant spectra. However, the gradient approach does not accurately predict the relative intensities for many of the bands in the FSRS spectrum, for example the bands at 1501 and 1548 cm^{-1}, or give the correct excitation profiles for many of the assigned vibrations.

In the limit of energetically well-separated electronic transitions, resonance Raman spectra are dominated by contributions from a single electronic state, as observed in our previous work on the resonance Raman spectrum for the S_1 state of DPT.[53] The experimental FSRS spectrum of DPT has strongly mode-dependent resonance enhancements, and excitation profiles that follow the amplitude of the excited-state absorption spectrum. However, considering that the approach of calculating resonance enhancements for individual excited states is not sufficient to reproduce the observed spectra for the T_1 state of PT, we speculate that in this case it is necessary to consider the combined effect of multiple states simultaneously. This hypothesis is consistent with the deconvolution of the experimental TA spectrum in Figure 6.2, which shows multiple overlapping electronic transitions. The simultaneous signal enhancement from multiple states can be described in terms of additive and non-additive effects. The gradient approximation should be able to cap-

ture the former by summing the properly weighted contributions from each adiabatic state T_N, but not the latter without including non-adiabatic (*i.e.* HT) coupling. In principle, the FCHT method should be able to partially capture both effects, but the reliance on the harmonic approximation severely limits the applicability of that approach in this case, because the harmonic potentials do not accurately represent the interacting electronic states far from their equilibrium geometries.

The role of multiple electronic states in the T_1 spectrum of PT is supported by the mode-specific experimental excitation profiles in Figure 6.6(b). The Raman bands with vibrational frequencies above $\sim$900 cm^{-1} have the greatest intensity for either $\sim$360 or $\sim$380 nm excitation, suggesting resonance enhancement from at least two separate electronic transitions. The lower intensities for these vibrations near $\sim$370-375 nm may indicate a possible resonance de-enhancement due to non-adiabatic coupling between electronic states. As detailed in the literature,[140,157,158] resonance de-enhancement is a result of population transfer between coupled electronic states, and would manifest as a decrease in the Raman excitation profile near the energy of the non-adiabatic curve crossing. Non-adiabatic effects are likely for the triplet states of PT, given the close proximity of several electronic transitions in both the calculated and experimental absorption spectra. However, our simulations do not account for these non-additive de-enhancement effects.

Notably, the resonance Raman calculations using the gradient approximation correctly predict the strong resonance enhancement of the 1402 and 1444 cm^{-1} bands based on specific electronic resonances (T_{12}/T_{13} and T_9/T_{10}, respectively). Although these modes are very weak in the off-resonance calculation, the gradient calculations indicate strong enhancement of the two vibrations in resonance with the two different electronic states. The character of the vibrations may explain both the different intensities in the off-resonant and resonant spectra, as well as the different electronic states responsible for enhancement of the two modes. The displacements in Figure 6.4 show that modes ν_{38} and ν_{40} have more in-plane C–H bending than C=C stretching character. The C–H bending motion is not expected to significantly change the polarizability of the conjugated system, which would explain the relatively weak off-resonance intensity for these vibrations (*cf.* Equation 6.4). In contrast, the calculated gradients along the normal mode coordinates for ν_{38} in T_{12}/T_{13}

and for v_{40} in T_9/T_{10} are larger than the gradients of most other vibrations, which explains the relatively large resonance Raman intensity of the experimental bands (Equation 6.11). The different gradients for the two modes in the two electronic states may reflect the relative degree of delocalization of the C=C stretching excitation. Both vibrations have similar C–H bending character, but the C=C stretching is more localized on the thienyl ring for v_{40}.

In contrast with the excitation profiles of the higher-frequency vibrations, the bands at 562, 652, and 891 cm^{-1} are relatively insensitive to the Raman excitation wavelength. The weak mode-specific enhancements of these FSRS bands may be a result of non-additive homogeneous broadening effects and the overlapping contributions from several electronic transitions. Homogeneous broadening is likely to play a more significant role for low-frequency vibrations, where the vibrational period is comparable to the dephasing time.[159–161] Homogeneous broadening is related to the phenomenological damping term $i\Gamma_n$ in the denominator of Equation 6.2, which represents the dephasing of each vibronic state $|n\rangle$. Typical homogeneous broadening for vibronic transitions of a molecule in the condensed phase is of the order 10^1-10^2 cm^{-1}.[29,76,161] Thus, the denominator $\omega_{ni} - \omega_p - i\Gamma_n$ for each term in the sum-over- states expression of the transition polarizability (Equation 6.2) is of the order 10^4 cm^{-1} for off-resonance transitions ($\omega_{ni} \approx 10^4$, $\omega_p = 0$), or 10^1-10^2 cm^{-1} for resonance terms ($\omega_{ni} - \omega_p \approx 0$) where the denominator is determined by the magnitude of Γ_n. As a result, the contributions to the transition polarizability for resonant electronic transitions are generally $\sim10^2$-10^3 times larger than off-resonant transitions, which gives an enhancement of $\sim10^4$-10^6 in the intensity (Equation 6.1).

The FWHM broadening in the triplet spectrum of PT is 0.197 eV (or ~1590 cm^{-1}). This is more than twice that of the relatively well isolated $S_N \leftarrow S_1$ absorption band of DPT (~0.09 eV).[53] Thus, the deconvolution of the experimental TA spectrum of PT provides an upper limit for the magnitude of homogeneous broadening of $\sim10^3$ cm^{-1}. The additional broadening compared with a more typical value of $\Gamma_n \sim10^1$-10^2 cm^{-1} reduces the maximum amplitude of the resonance enhancement for any individual electronic transition by 1-2 orders of magnitude, and also spreads out the resonance across a wider range of excitation wavelengths. At the same time, the broadening

of nearby transitions leads to contributions from those states as well. For example, the B3LYP calculations predict transitions to T_{11} and T_{14} that are 0.24 eV below and 0.17 eV above the strongest transition to T_{12}, respectively. These differences in energy are comparable to the upper limit of Γ_n from the deconvolution of the experimental spectrum. Therefore, all three of these states could contribute to the Raman spectrum simultaneously.

Vibronic coupling may also play a role in determining the relative intensities in the resonance Raman spectrum of the T_1 state of PT. The off-resonance Raman spectra calculated with Equation 6.3 already include contributions from B-term scattering, because the polarizability derivative implicitly contains some vibronic coupling terms through the dipole derivative with respect to vibrational displacements, as described by Long.[29] Thus, the consistently good agreement between the off-resonance Raman spectra and the experiment could be an indication that vibronic coupling is involved. As mentioned above, the FC and FCHT calculations are not helpful in evaluating this effect due to shortcomings of the harmonic approximation, whereas the gradient approach neglects any explicit vibronic coupling contributions. Although beyond the scope of this work, it would be desirable to extend the gradient approximation to include such non-additive, higher-order effects.

6.6 Conclusions

We report the excitation wavelength dependence of the FSRS spectrum for the T_1 state of PT, and compare the trends we observe to simulated on- and off-resonance Raman spectra using several theoretical approaches. The experimental results provide a rigorous benchmark for the accuracy of the computational techniques, whereas the computational results highlight the difficulties of interpreting FSRS spectra involving more than one resonant or nearly resonant electronic transition. These results also point to important limitations of the FC and FCHT approaches for the calculation of resonance Raman spectra in the presence of broad, overlapping transitions. The more densely packed manifold of the high-lying electronic states makes it difficult to extrapolate the PES from the excited-state minimum to the Franck-Condon geometry using the harmonic approximation.

The mode-specific excitation profiles in the experimental FSRS spectrum may be explained by

homogeneous broadening of the $T_N \leftarrow T_1$ transitions. A Lorentzian deconvolution of the triplet absorption spectrum indicates several overlapping transitions, each with significant homogeneous broadening. Estimates of an upper limit to the Γ_n values, based on the experimental TA spectrum, show that these values are roughly an order of magnitude larger than what is typically observed in resonance Raman measurements. The reasonably large Γ_n values increase the relative importance of the mode-specific resonance enhancement contributions from nearby transitions, which may explain the broad excitation profiles observed for the Raman bands. The significant homogeneous broadening is possibly a result of increased vibronic coupling between the electronic states of the triplet manifold. Thus, the good agreement between the off-resonance Raman calculations and the experimental spectrum may indicate that the contributions from multiple transitions and vibronic coupling effects have an influence on the FSRS spectrum that is comparable to or even larger than the electronic resonance condition. In summary, this work highlights the necessity of considering multiple contributions when extracting information about resonant electronic states in FSRS and helps explain the good agreement of off-resonant calculations with the resonance-enhanced FSRS spectra of the triplet states of PT.

Chapter 7

A Benchmark Study of Ground State Raman Spectra in Conjugated Molecules

(This work was published as Ref. #55. Supporting information is available online.)

7.1 Introduction

Raman spectroscopy is an indispensable tool in the identification and structural characterization of molecules, especially aromatic compounds where electron conjugation effects increase the polarizability of the molecule and give relatively strong Raman scattering cross-sections.[9–12] Conjugated organic polymers and oligomers are particularly good targets for Raman studies due to increased polarizability and sensitivity of the Raman bands to the structure of the conjugated molecular backbone.[28] Electronic conjugation along the molecular backbone of a polymer or oligomer is responsible for efficient charge mobility that makes these compounds valuable components for photovoltaic materials and other applications.[38,40,162,163] Some of the more common conjugated polymers include phenyl and thienyl derivatives, for which the charge-transport properties are sensitive to the orientation between the aromatic rings and their substituents.[31,40,47–49,107,162,164–166] Raman spectroscopy provides valuable information about the structure and the dynamics of these conjugated systems, but requires accurate assignments of the observed vibrational bands.

Computational studies are particularly useful in predicting the Raman spectra and assigning bands to specific vibrational motions.[52] Thus, it is important to know which methods provide the best balance between computational cost and accuracy for the calculation of Raman intensities and vibrational frequencies. Several benchmarking studies have been performed to evaluate the accu-

racy of Raman intensity calculations using density functional theory (DFT) and other electronic structure methods. However, these studies either examined the density functional dependence across a series of small molecules (e.g. H_2O, NH_3, C_2H_6, etc.),[15,16] or for a single medium-size molecule (e.g., adenine or 4-aminobenzonitrile),[13,14,17,20] or they compared a series of medium-size molecules using a single density functional.[33,167] The studies on small molecules showed that the accuracy of Raman intensities calculated with hybrid density functionals is not significantly different from the results at higher levels of theory.[15,16] Other benchmark studies that examine the basis set dependence in conjugated systems (e.g., benzene and α-pinene) concluded that polarization functions and especially diffuse functions are necessary to reproduce accurate Raman intensities, but that the results obtained with DFT show little variation between double- and triple-zeta basis sets.[18,19] These findings are generally supported by similar studies of basis set and functional dependence that include at least one medium-size molecule (e.g., thymine), and typically give the best agreement with experiment using B3LYP and a medium basis set, such as 6-311++G** or aug-cc-pVTZ.[13,14,20,21] Additionally, a benchmark investigation of range-separated functionals on several small molecules and adenine showed that, while B3LYP gives the most accurate vibrational frequencies, the best performance for Raman intensities is obtained with M06-L, M06-HF, and LC-ωPBE.[17]

However, to the best of our knowledge, a systematic examination of the accuracy of Raman spectra calculated using multiple density functionals benchmarked against experiment has not been performed for phenyl and thienyl oligomers. These systems are the building blocks of the most common conducting polymers,[40,162,168] and determining the best level of theory for accurate simulations of their Raman spectra is therefore of great importance. We previously compared experimental ground-state Raman spectra with spectra calculated using B3LYP/aug-cc-pVDZ for a series of aryl-substituted thiophene derivatives.[52,53] The calculated Raman intensities are generally in good agreement with experiment, as expected for this level of theory.[13,14,18-21] However, we observed a discrepancy in the relative Raman intensities for three of the phenyl-containing molecules in our set: 2-phenylthiophene (PT), 2-methyl-5-phenylthiophene (MPT),

and 2,5-diphenylthiophene (DPT). We find that the calculated intensities of the lower-frequency bands in the range 200-1000 cm^{-1} are weaker than the higher-frequency bands (1400-1600 cm^{-1}) compared with the experimental spectra. Similar discrepancies in the relative Raman intensities of high- and low-frequency modes calculated with DFT are observed in the literature, and are most evident in the Raman spectra of substituted benzene derivatives such as toluene,[169] 4-aminobenzonitrile,[13] and thioanisole.[33] To our knowledge, this discrepancy between the high- and low-frequency vibrations of substituted benzenes has not been addressed. Thus, a major goal of this study is to determine whether a more accurate description of the electron conjugation effects can resolve this issue.

In this chapter, we study seven substituted benzene and thiophene compounds, including benzene (Bz), toluene (Tol), 2,2'-bithiophene (BT), biphenyl (BP), 2-phenylthiophene (PT), 2-methyl-5-phenylthiophene (MPT), and 2,5-diphenylthiophene (DPT). We examine the density functional dependence of the Raman spectra using a set of seven functionals at various levels of the "Jacob's Ladder" hierarchy of chemical accuracy,[170] along with second-order Møller-Plesset perturbation theory (MP2), and compare the calculations with experiment. The chapter is organized as follows. We first introduce the computational methods and experimental details in Section 2. In Section 3.1, we compare the experimental and calculated Raman spectra for each molecule. We then analyze the performance of each functional in Section 3.2, comparing the accuracy of the calculated frequencies and the relative intensities across our test set. Finally, we discuss our results and summarize our main conclusions in Section 4.

7.2   Computational and Experimental Methods

We calculate ground-state Raman spectra using a set of density functionals with increasing complexity in the physical description of the electron exchange-correlation.[170] The range of functionals extends from the generalized gradient approximation (GGA) to include meta-GGA (M-GGA), hybrid-GGA (H-GGA), hybrid-meta-GGA (HM-GGA), hybrid-GGA with separation of short- and long-range exchange contribution, and double-hybrid-GGA (DH-GGA).[110,111,171–177]

We also compare the DFT results with MP2.[178–181] The methods are listed in Table 7.1 in ascending order of complexity, along with the percentage of Hartree-Fock (HF) exchange for the hybrid functionals, the basis sets used, and the empirical vibrational frequency scaling factors.[116,182,183]

Table 7.1: Methods used to calculate Raman intensities.

Method	Type	% HF[a]	Basis Set	Freq. Scaling
PBE[171]	GGA		aug-cc-pVTZ	0.993[183]
M06-L[172]	M-GGA		aug-cc-pVTZ	0.965[183]
B3LYP[110,111]	H-GGA	20	aug-cc-pVTZ	0.968[116]
TPSSh[173,174]	HM-GGA	10	aug-cc-pVTZ	0.968[183]
M06-HF[175]	HM-GGA	100	aug-cc-pVTZ	0.932[183]
CAM-B3LYP[176]	H-GGA	19[b], 65[c]	aug-cc-pVTZ	0.954[183]
B2PLYP[177]	DH-GGA	53, 27[d]	aug-cc-pVDZ	0.963[182]
MP2[178–181]	WF[e]		aug-cc-pVDZ	0.959[116]

[a] Percentage of Hartree-Fock exchange contribution.
[b] Short-range.
[c] Long-range.
[d] Percentage of perturbative correlation contribution.
[e] Wave function-based method.

The optimized geometries, vibrational frequencies, and Raman intensities for each molecule were calculated using all of the functionals and MP2. For BT, we optimized both the *cis* and *trans* conformers, and report the calculated Raman spectrum as a Boltzmann-weighted average of the two structures. All other molecules have a single minimum-energy structure. We used the aug-cc-pVTZ basis set[184] with most functionals to provide the diffuse and polarization functions necessary to accurately calculate Raman intensities,[19] but we used aug-cc-pVDZ[113] with B2PLYP and MP2 due to computational cost. The frequencies of the calculated spectra were multiplied by the uniform scaling factors shown in Table 7.1. These commonly used scaling factors were obtained empirically by comparison with the experimental frequencies for sets of diatomic, triatomic, and other small organic molecules.[116,182,183] The calculated Raman intensities, I_n, were obtained as:[29,30]

$$I_n = S_n \frac{(\tilde{v}_p - \tilde{v}_n)^4}{\tilde{v}_n} \left[1 - \exp\left(-\frac{hc\tilde{v}_n}{k_B T} \right) \right] \tag{7.1}$$

where S_n is the calculated static Raman activity (in Å^4/amu), $\tilde{v}_p$ is the Raman excitation frequency

(12,739 cm^{-1} or 785 nm), $\tilde{v}_n$ is the calculated vibrational frequency for the nth band (in cm^{-1}), h is Planck's constant, c is the speed of light, k_B is Boltzmann's constant, and T is the temperature (300 K). The simulated Raman intensities include 15 cm^{-1} Gaussian broadening. All calculations were performed using a development version of the GAUSSIAN software package.[78]

All compounds were obtained commercially and used without further purification. We prepared samples of liquid benzene, liquid toluene, and solutions of BP (0.6 M in cyclohexane), BT (0.3 M in DMSO), PT (0.2 M in cyclohexane), MPT (0.2 M in cyclohexane), and DPT (15 mM in cyclohexane) in a 2 cm diameter glass vial. We measured the ground-state Raman spectra using a commercial spectrometer (StellarNet) with 785 nm cw pump laser and 4 cm^{-1} resolution. Pure liquid samples were irradiated from above in order to avoid contributions to the Raman signal from the glass walls of the vessel. The other samples were irradiated from the side, in which case we subtracted the solvent-only spectra to remove contributions from the solvent and the glass walls.

We tested the effect of solvation on the spectra by comparing the gas and condensed phase vibrational frequencies for three molecules for which gas-phase infrared (IR) data is available in the literature: Bz,[185,186] Tol,[187] and BP[188], and the Raman fractional intensities for the two molecules for which gas-phase Raman spectra are available: Bz,[185,186] and BP.[188] The experimental gas and condensed-phase Raman stick spectra for Bz and BP are reported in Figures S1-S2, the vibrational frequencies are reported in Tables S1-S3, the Raman fractional intensities in Tables S4-S5, and the statistical analysis in Tables S6-S7 in the Supporting Information (SI). These data show that the experimental Raman spectra in gas and condensed phase are indeed very similar. The changes in frequencies are at most 12-16 cm^{-1}, which is much smaller than the shift in frequencies due to the scaling factors for the calculations. The differences in fractional intensities are also relatively small. The statistical analysis of the errors shows that for benzene (Table S6) some methods agree better with the gas phase data than with the condensed phase data (while other methods do not), which is not too surprising given that benzene is a relatively simple molecule. On the other hand, the errors for BP (Table S7) are essentially identical when using the experimental gas or condensed phase data as reference. We also computed the Raman spectra in solution for PT and DPT using the

103

polarizable continuum model of solvation (PCM): [189] the intensities increased by $\sim$80% in solution compared to gas phase, but the relative intensities were essentially unchanged. Therefore, since the solvation effect is overall significantly smaller than the intrinsic errors of each computational method, and the continuum models are not able to reproduce this effect anyway, we only performed gas phase calculations to reduce computational cost.

7.3 Results and Analysis

7.3.1 Simulated and Experimental Raman Spectra

Figure 7.1: Calculated and experimental Raman spectra for Bz. Each spectrum is normalized to the largest band in the observed region.

Figure 7.2: Calculated and experimental Raman spectra for Tol. Each spectrum is normalized to the largest band in the observed region.

We begin our comparison of the experimental and calculated data from a qualitative analysis of the actual Raman spectra, reported in Figures 7.1-7.7 for all systems. In each plot, the spectra are normalized to the strongest transition. For the first three compounds, benzene, toluene, and BP, the most intense band in each experimental spectrum is near 1000 cm^{-1}, corresponding to a phenyl distortion mode, where three alternating C atoms on the ring simultaneously bend inward (mode 12 in Wilson's notation), see Figures 7.1-7.3. While this feature is reproduced correctly by all theoretical methods for benzene, there is not as good agreement for the other two molecules. For toluene, some methods reproduce the qualitative relative intensities of the measured spectrum (e.g., B3LYP), while others predict that the most intense band is at 800 cm^{-1} (e.g., M06-HF),
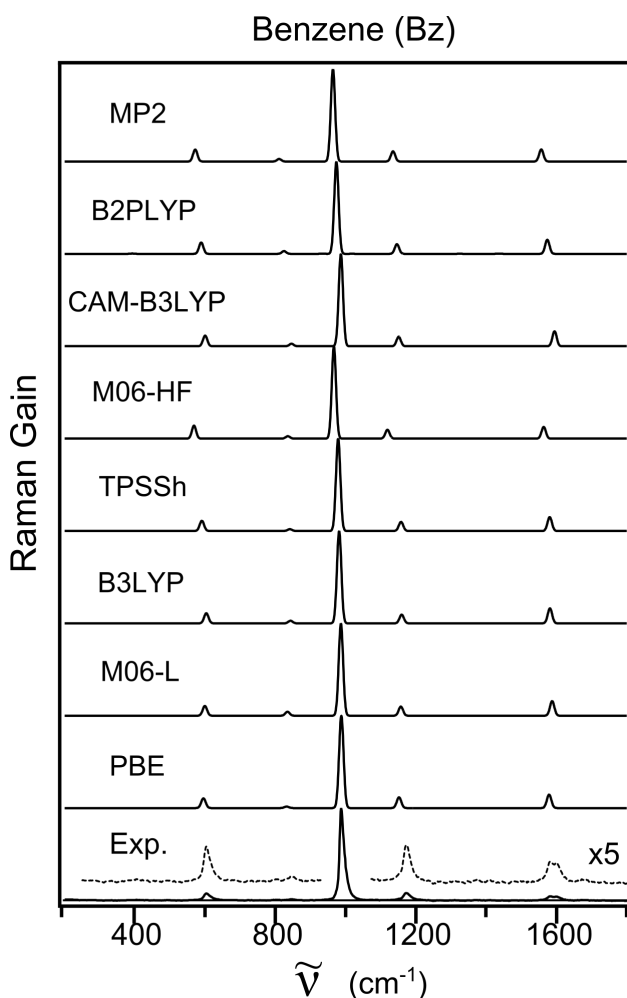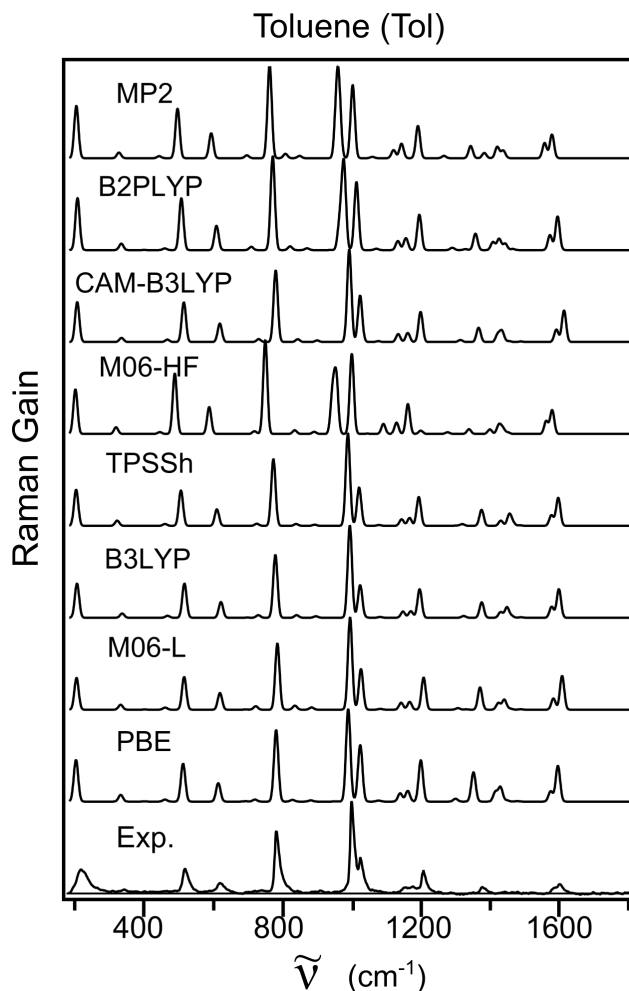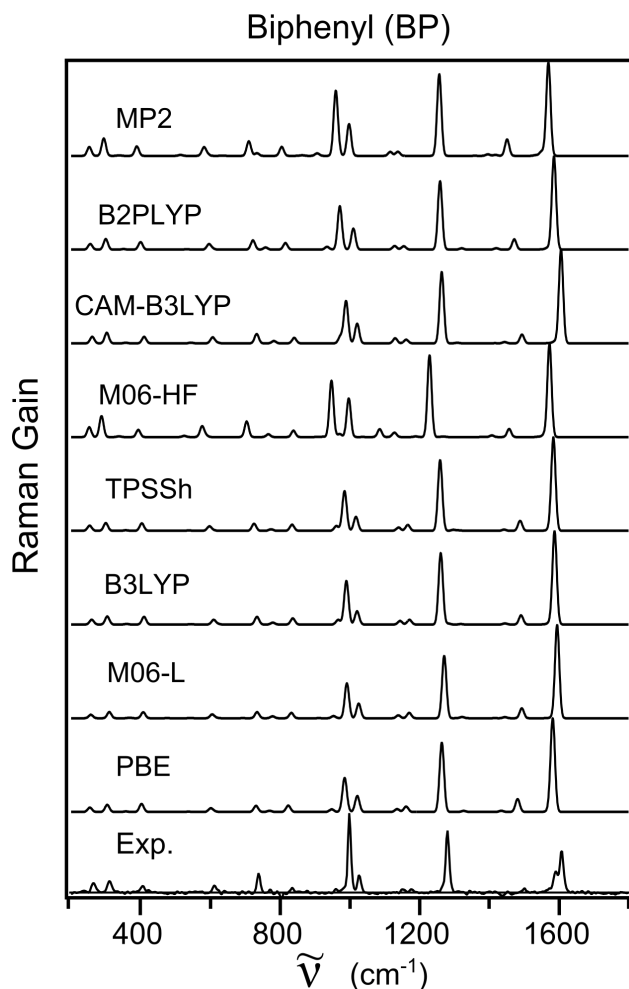
Figure 7.3: Calculated and experimental Raman spectra for BP. Each spectrum is normalized to the largest band in the observed region.

which corresponds to a phenyl-bending and ring-substituent C-C stretching vibrational mode (19a in Wilson's notation). For BP, the calculated spectra are similar across all methods, and they consistently give the wrong relative intensities of the three most intense Raman bands at 999, 1281, and 1608 cm^{-1} compared with experiment. A few additional discrepancies are due to the effect of solvation in the experiments. For instance, in benzene, the signal at $\sim$1600 cm^{-1} is due to a doubly-degenerate vibrational mode in the gas-phase calculations and experiments (i.e., the 9a and 9b ethylenic stretching motions, in Wilson's notation[190,191]). In the solution-phase experiment, these vibrations split into two partially overlapping bands at 1582 and 1605 cm^{-1}, as determined from a Gaussian deconvolution of the spectrum in Figure S3 of the SI. Similarly,

for BP there are also two overlapping bands at $\sim$1600 cm^{-1} in the condensed-phase experiment, while the gas phase calculations and experiment only have one. The four normal modes of BP (D$_2$ point-group symmetry) with frequencies between 1600 and 1700 cm^{-1} are the symmetric and anti-symmetric combinations of the 9a and 9b local modes. The intense $\sim$1600 cm^{-1} band calculated with each method only has contributions from the symmetric combination of the 9a local modes (where the normal mode has *a* symmetry). The calculations give negligible Raman activity in the anti-symmetric combination of 9a (b_3 symmetry), the symmetric combination of 9b (*a*), and the anti-symmetric combination of 9b (b_2). Therefore, we treat the two experimental bands at $\sim$1600 cm^{-1} for Bz and BP as a single one for the comparison with the simulations, see Figure S3 of the SI for the deconvolution details. Despite these differences, the calculated spectra are generally in good agreement with experiment for all levels of theory, and do not differ significantly between methods.

In the thiophene derivatives, the most intense experimental bands are in the ethylenic stretching region (1400-1600 cm^{-1}), see Figures 7.4-7.7. Note that the Raman spectrum of BT has a smaller signal-to-noise ratio due to a weaker Raman scattering cross-section compared to the other thiophene compounds. Additionally, to account for the two conformers of BT that are thermally accessible at room temperature, the calculated Raman spectra in Figure 7.4 are averaged based on the Boltzmann weighting of the two structures determined with each method. All computational methods reproduce the experimental observation that the high-frequency bands are the most intense in this subset of molecules. However, the relative intensities of these bands are often incorrectly predicted; a few significant examples include the MP2 spectrum for PT in Figure 7.5 and DPT in Figure 7.7, and the CAM-B3LYP spectrum for MPT in Figure 7.6. A quick visual inspection of the figures reveals that the relative intensity of the 1000 cm^{-1} band is also consistently underestimated by the calculations with respect to the intensities of the high-frequency bands for all four compounds. In fact, the same trend holds that the calculated intensities of most low-frequency bands are underestimated compared to the high-frequency bands, as we discuss more quantitatively in the next section. Nevertheless, the simulations provide a reasonable description of the experimental
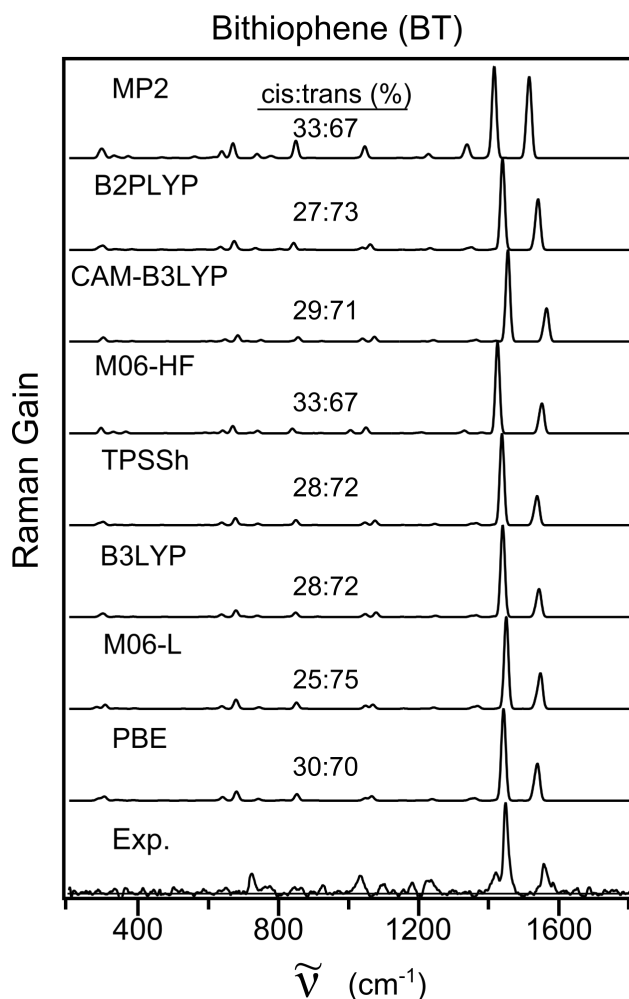
Figure 7.4: Calculated and experimental Raman spectra for BT. The calculated spectra are averaged based on the Boltzmann population factors for the two rotational conformers of BT, and each spectrum is normalized to the largest band in the observed region.

spectra with all methods.

7.3.2 Analysis of the Errors in the Simulated Raman Spectra

We assess the performance of each computational method based on the accuracy of the vibrational frequencies and relative intensities of the calculated Raman bands compared with the experiment. We focus on the strongest bands in each experimental spectrum, which are identified in Table 7.2. A full comparison with the calculated Raman bands at each level of theory is included in Tables S8-S14 in the SI. In the case of overlapping transitions that coalesce into a single band in the

Figure 7.5: Calculated and experimental Raman spectra for PT. Each spectrum is normalized to the largest band in the observed region.

simulated spectra, we report the frequency of the band maximum and the sum of the fractional intensities for the contributing modes. The fractional intensities in the calculated and experimental spectra are defined as:

$$\bar{I}_n = \frac{I_n}{I_{total}} \tag{7.2}$$

where I_n is the integrated intensity of the nth Raman band, see Eq. 8.1, and $I_{total} = \sum_n I_n$ is the integrated intensity of all the Raman bands of a molecule in the region of interest (200-1800 cm^{-1}). In each compound, we consider only the contributions from experimental Raman bands that are clearly above the signal-to-noise ratio, see Tables 7.2 and S8-S14. In all cases, the experimental I_{total} includes 83-98% of the total Raman intensity obtained by integrating over the entire 200-
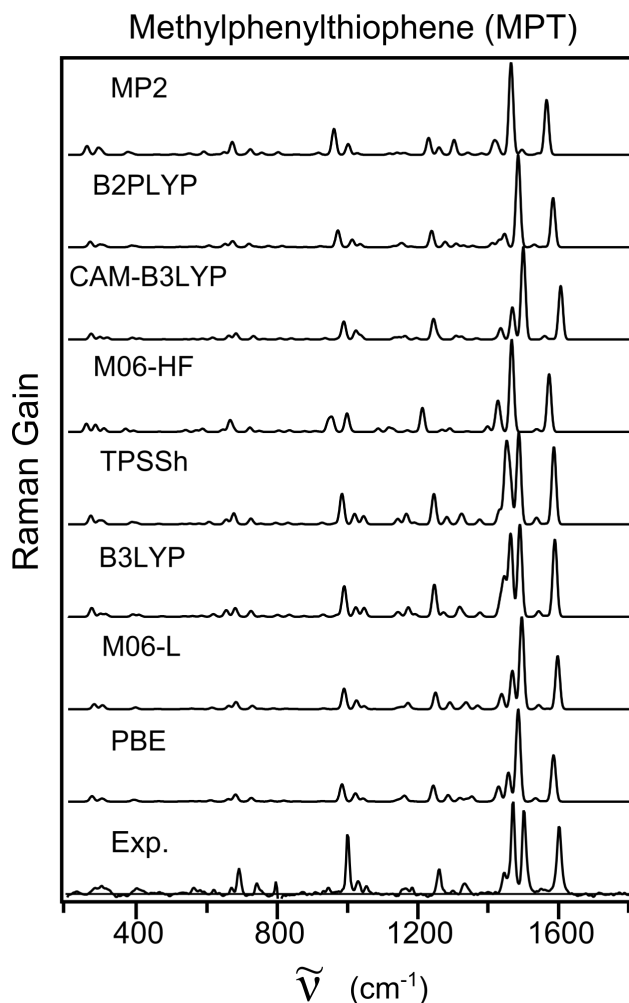
Figure 7.6: Calculated and experimental Raman spectra for MPT. Each spectrum is normalized to the largest band in the observed region.

1800 cm^{-1} region for a given molecule (see Table S15 for details specific to each compound). In cases where there is clearly more than one contribution to an experimental Raman band, we use a Gaussian deconvolution to obtain the individual vibrational bands (Figure S3 of the SI). The experimental bands are then matched with the Raman bands in the simulated spectra, and we obtain the calculated band intensities by summing over all the calculated vibrational transitions that overlap within a simulated band.

Figure 7.8 (a) displays the cumulative errors of the calculated frequencies compared with the experimental frequencies for all of the Raman bands identified in our test set. Each of the eight bars in panel (a) of the figure is obtained by stacking the signed errors for that method normalized by the
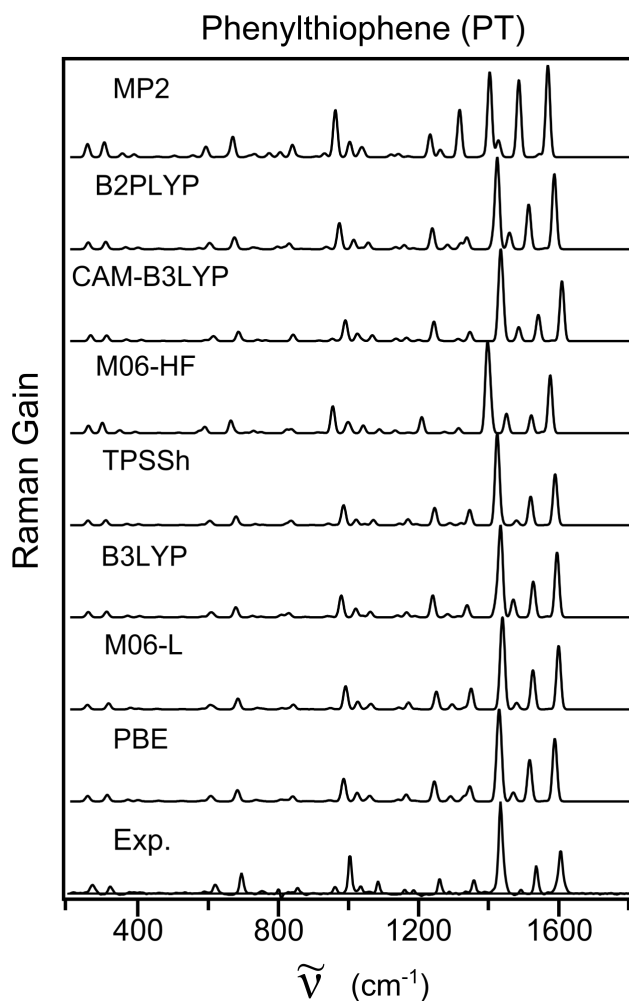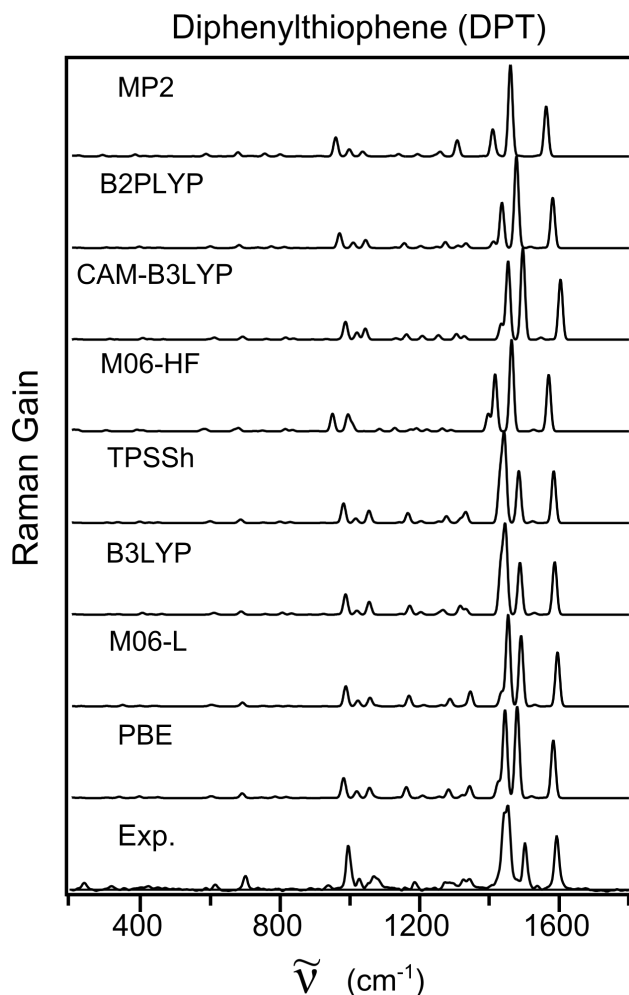
Figure 7.7: Calculated and experimental Raman spectra for DPT. Each spectrum is normalized to the largest band in the observed region.

total number of modes across all molecules (N_{freq}): $(\tilde{v}_n^{calc} - \tilde{v}_n^{exp})/N_{freq}$. Thus, the length of each bar is equal to the mean unsigned error (MUE) of the Raman band positions for a given method. Panel (b) in the figure reports the mean signed errors (MSE), and the standard deviations (σ_{MSE}). The results in Figure 7.8 are summarized in Table 7.3 for each method, including the maximum unsigned error (Max). The errors are evaluated with the empirically scaled frequency values (using the standard vibrational frequency correction factors from Table 7.1). Results for the unscaled frequencies are included in Figure S4 of the SI. Based on the errors in scaled frequencies, M06-L performs best in both accuracy and precision. B3LYP and CAM-B3LYP provide the next best agreement with experiment, but the smaller spread of the errors (σ_{MSE}) in B3LYP indicates slightly

Table 7.2: Experimental Raman band positions ($\tilde{\nu}_n$) and fractional intensities ($\bar{I}_n$).

Bz		Tol		BP		BT		PT		MPT		DPT	
$\tilde{\nu}_n$ (cm^{-1})	$\bar{I}_n$	$\tilde{\nu}_n$ (cm^{-1})	$\bar{I}_n$	$\tilde{\nu}_n$ (cm^{-1})	$\bar{I}_n$	$\tilde{\nu}_n$ (cm^{-1})	$\bar{I}_n$	$\tilde{\nu}_n$ (cm^{-1})	$\bar{I}_n$	$\tilde{\nu}_n$ (cm^{-1})	$\bar{I}_n$	$\tilde{\nu}_n$ (cm^{-1})	$\bar{I}_n$
603	0.082	217	0.166	264	0.040	706	0.092	264	0.038	399	0.025	237	0.020
845	0.015	516	0.093	309	0.049	1019	0.109	314	0.023	667	0.011	612	0.011
987	0.737	618	0.051	405	0.032	1219	0.099	612	0.032	689	0.048	700	0.034
1172	0.094	781	0.205	610	0.026	1410	0.103	689	0.062	740	0.023	993	0.115
1582	0.039	1000	0.218	738	0.058	1441	0.413	1000	0.117	997	0.115	1028	0.025
1605	0.032	1024	0.093	834	0.014	1549	0.185	1079	0.032	1028	0.031	1069	0.065
		1151	0.020	961	0.011			1254	0.042	1260	0.056	1186	0.017
		1175	0.023	999	0.229			1352	0.044	1331	0.032	1283	0.043
		1206	0.065	1027	0.054			1429	0.347	1445	0.053	1336	0.059
		1374	0.022	1151	0.012			1530	0.082	1469	0.206	1440	0.148
		1582	0.015	1175	0.011			1600	0.180	1501	0.191	1454	0.194
		1601	0.029	1281	0.218					1549	0.022	1502	0.118
				1500	0.014					1599	0.189	1593	0.150
				1593	0.233								

Table 7.3: Statistical error analysis of the calculated Raman frequencies (cm^{-1}).

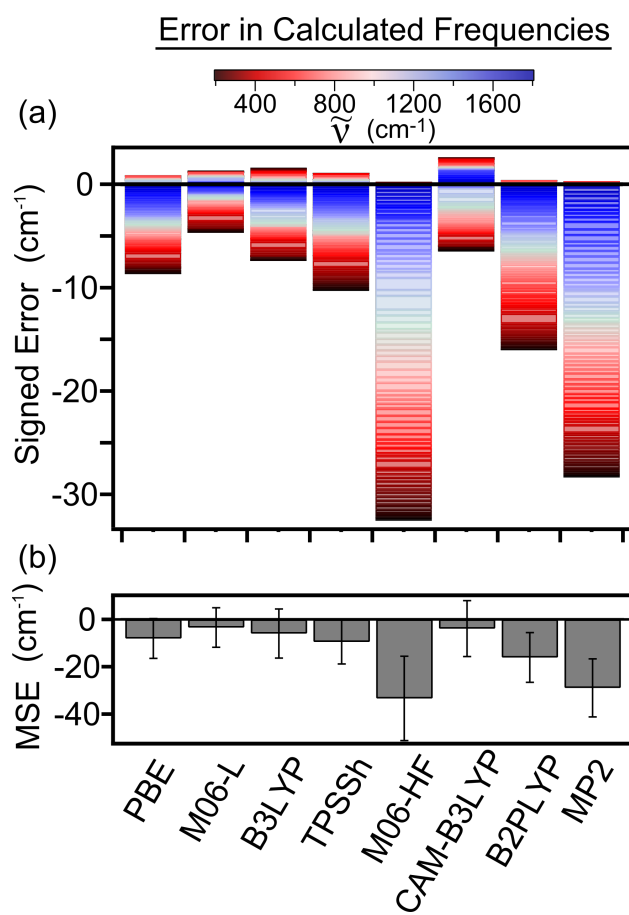| Method	MSE	σ_{MSE}	MUE	Max
PBE	-7.8	8.1	9.3	43.0
M06-L	-3.4	8.1	5.8	45.0
B3LYP	-5.8	10.1	8.8	44.9
TPSSh	-9.3	9.1	11.2	45.8
M06-HF	-32.4	17.3	32.6	101.3
CAM-B3LYP	-3.8	11.5	9.0	43.8
B2PLYP	-15.6	10.2	16.3	70.4
MP2	-28.1	11.9	28.4	55.5

Figure 7.8: Cumulative signed errors normalized by the total number of modes (a) of the calculated Raman frequencies for each method, after empirical scaling. Contributions are color-coded based on vibrational frequency. Mean signed errors (MSE) are shown in panel (b), along with standard deviations (σ_{MSE}) as error bars.

better performance than CAM-B3LYP. The largest errors and standard deviation are observed with M06-HF, MP2, and B2PLYP, and are most evident in Figures 7.2, 7.4, and 7.7 for Tol, BT, and DPT, respectively. These three methods systematically underestimate the Raman shifts by 10-40 cm^{-1}.

Overall, the calculated spectra are in reasonably good agreement with experiment, as the average unsigned error in band position is <40 cm^{-1} for each method, and many of the qualitative aspects of the band positions are reproduced even at the lowest level of theory. However, we observe a systematic discrepancy in the relative Raman intensities across each spectrum. The differences are more apparent in Tol, BP, and BT, although there is a considerable disagreement for the ~1000 cm^{-1} band in each of the phenyl-thiophene derivatives (PT, MPT, and DPT). The calculated Raman spectra for all six of these molecules generally have relative intensities of high-frequency bands (>1200 cm^{-1}) that are larger than those of low-frequency bands, compared to experiment. It is not immediately clear whether the calculations overestimate the intensities of higher frequency bands, underestimate intensities of lower frequency bands, or both.

We examine the accuracy of each method in terms of the fractional intensities $\bar{I}_n$, see Eq. 7.2. Figure 7.9 (a) gives the cumulative signed errors (normalized by the total number of modes) in fractional intensities observed over all Raman bands in each method. The MSE with the standard deviations (σ_{MSE}) are in panel (b). Having defined $\bar{I}_n$ relative to the total integrated intensity of all Raman bands considered, the MSE is equal to zero for each method because both the calculated and experimental fractional intensities, by definition, sum to unity. The majority of the signed errors of low-frequency bands (colored red in Figure 7.9a) are negative, and the errors in high-frequency bands (colored blue in Figure 7.9a) are mostly positive. In other words, the fractional intensities in each method are generally underestimated for Raman bands with frequency <1200 cm^{-1}, and overestimated for vibrations at higher frequency. The results of Figure 7.9 are summarized in Table 7.4.

There is relatively little variation in the MUEs (i.e. length of the colored bars in Figure 9a) between the different functionals. However, taking into consideration both the MUE and the spread of

114
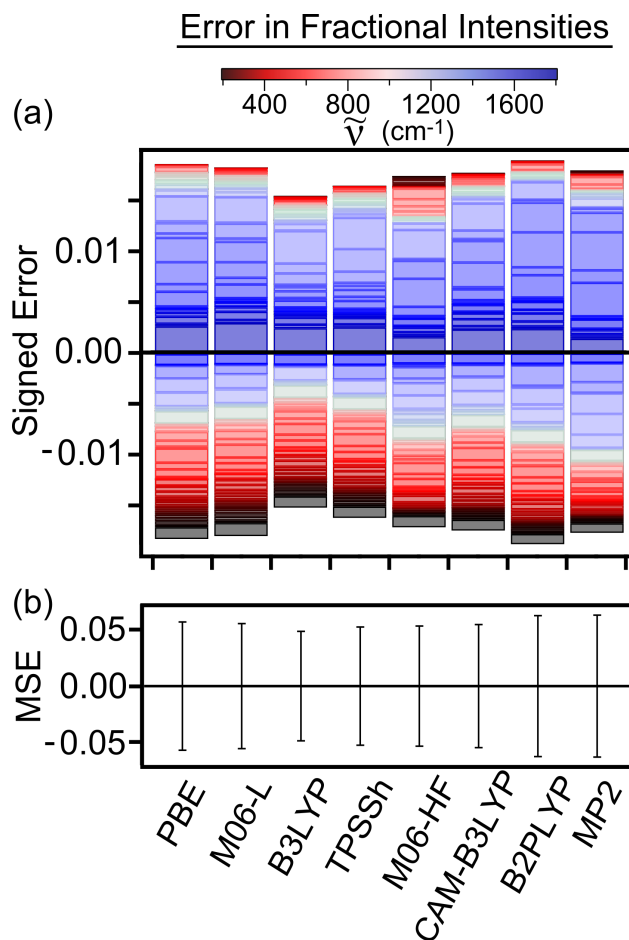
Figure 7.9: Cumulative signed errors normalized by the total number of modes (a) in calculated Raman fractional intensities for each method. Contributions are color-coded based on vibrational frequency. MSEs are shown in panel (b) along with standard deviations (σ_{MSE}) as error bars.

Table 7.4: Statistical error analysis of the calculated fractional Raman intensities.

Method	σ_{MSE}	MUE	Max
PBE	0.0556	0.0353	0.1862
M06-L	0.0541	0.0348	0.2086
B3LYP	0.0470	0.0294	0.2324
TPSSh	0.0510	0.0313	0.2247
M06-HF	0.0521	0.0331	0.2081
CAM-B3LYP	0.0532	0.0337	0.1933
B2PLYP	0.0614	0.0363	0.2509
MP2	0.0619	0.0342	0.2724

the signed errors (σ_{MSE}), the results show that B3LYP gives the best agreement between calculated and experimental fractional intensities. TPSSh provides the next best agreement, and although the MUEs of M06-HF and CAM-B3LYP are nearly identical, the range-separated functional has a smaller σ_{MSE}. The largest errors are observed in B2PLYP, MP2, and PBE, although the latter has a somewhat smaller σ_{MSE}.

We further analyze the trends in intensities between the low and high frequency regions of the spectrum by defining the ratio of fractional intensities, ρ_n:

$$\rho_n = \frac{\bar{I}_n^{calc}}{\bar{I}_n^{exp}} \tag{7.3}$$

where $\bar{I}_n$ is defined in Eq. 7.2. The ρ_n value reveals the level of agreement between the fractional intensities of the calculated and experimental Raman bands. However, in order to simplify the comparison between functionals, we show $\log(\rho_n)$ in Figure 7.10, where $\log(\rho_n) = 0$ indicates perfect agreement between calculated and experimental relative intensities. The figure shows that the fractional Raman intensities are consistently underestimated for the majority of bands with frequencies <1200 cm^{-1}, and the relative intensities of higher frequency transitions are more likely to be overestimated, for each individual compound.

Although we do not necessarily expect a correlation between the relative intensity and the vibrational frequency of a band, Figure 7.10 reveals a clear (and approximately linear) increase of $\log(\rho_n)$ with increasing frequency for all of the compounds and all levels of theory. To highlight the apparent trend, the figure includes linear fits to the data for each compound. For clarity, Figure 7.10 shows only a single fit across all methods. Results of the fits for individual methods are listed in Table S16 of the SI, and show generally the same behavior in slope and correlation across all methods. The fit lines in the figure are only a visual guide, nonetheless, they highlight several outlying bands, particularly in BT, BP, and DPT. Single outliers, like the M06-HF intensity ratio for the 961 cm^{-1} band in BP, and the MP2 value for the 1440 cm^{-1} band in DPT, are shoulder bands in Figures 7.3 and 7.7 that are not well-reproduced by particular methods. However, other bands
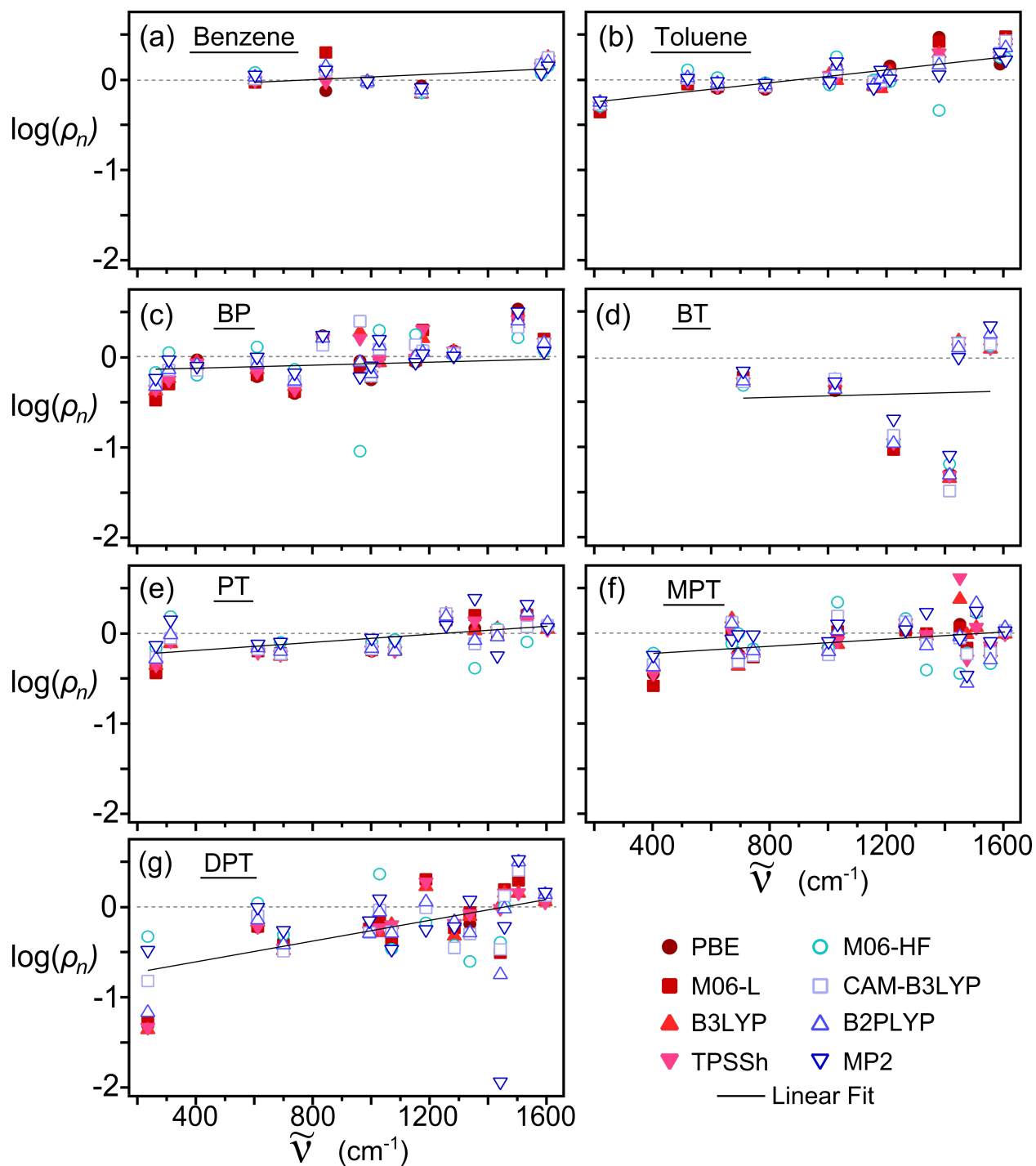
Figure 7.10: Log plot of the ratios of calculated and experimental fractional intensities for (a) Bz, (b) Tol, (c) BP, (d) BT, (e) PT, (f) MPT, and (g) DPT.

117

stand out as consistent outliers across multiple methods, such as the 1219 and 1410 cm^{-1} bands in BT. The 1410 cm^{-1} band appears as the shoulder of a more intense band at 1441 cm^{-1}, assigned as the anti-symmetric and symmetric combinations of an ethylenic stretching mode, respectively. On the other hand, the 1219 cm^{-1} band is mainly a C-H bending mode, and the fractional intensity appears to be consistently underestimated by the calculations with each method.

Previous studies of substituted benzene molecules have observed a conformational dependence between Raman intensities and the orientation of the substituent.[32,33,192] To ensure that the differences between methods for the conjugated compounds in our test set are not affected by differences in the minimum geometries, we also calculated Raman spectra with each method for PT at a fixed torsion angle of $\phi = 27°$ (the optimized angle in B3LYP). The Raman spectra for the fixed torsion are shown in Figure S7 of the SI, and are essentially identical to the spectra calculated at the optimized geometry for each method, as shown in Figure 7.5 (the torsion angles of the optimized geometries with all methods are reported in Table S33).

7.4 Discussion and Conclusions

We have performed DFT and MP2 calculations for the Raman spectra of a set of substituted benzene and thiophene compounds, and benchmarked the accuracy of each method with experimental Raman spectra. For all tested methods, we find generally good agreement with the measurements. The methods that give the most accurate vibrational frequencies are similar to those that give the most accurate Raman intensities. With the available scaling factors, the frequencies calculated with M06-L, B3LYP, and CAM-B3LYP have the lowest MUEs, while the functionals with the lowest σ_{MSE} are M06-L, PBE, and TPSSh. On the other hand, the errors in the average fractional intensities show less variation across methods, but Figure 7.9 and Table 7.4 indicate two functionals that perform slightly better than the rest. The MUEs in the intensities of B3LYP and TPSSh are roughly ~11%-19% and ~5%-14% smaller than the remaining methods, respectively. The σ_{MSE} values are ~10%-24% smaller with B3LYP, and ~2%-17% smaller with TPSSh, than the other methods. The higher accuracy of the relative intensities calculated with hybrid density functionals

may indicate a cancellation of errors related to the amount of exact HF exchange.

However, the better agreement with experiment in the fractional intensities for some of the functionals still does not account for the discrepancy in relative intensities between high- and low-frequency vibrations of a molecule. The trends in Figures 7.9 and 7.10 show that, with the exception of a few outliers in M06-HF and MP2, all methods consistently overestimate the fractional intensities in high-frequency bands and underestimate those of low-frequency transitions. The discrepancy between high and low-frequency intensities is likely due, in part, to the effects of conjugation across aromatic rings, which is tuned by the relative orientation dynamics between the rings.[32,33,192] We will focus on this issue in a separate study.

Although the discrepancies in relative intensities are largely the same across the various methods, the best performance for frequencies and intensities is obtained with the hybrid functionals B3LYP and TPSSh, which, respectively, provide a $\sim$11%-19% and $\sim$5%-14% better agreement between calculated and experimental Raman spectra than the other methods.

Chapter 8

On the Discrepancy between Experimental and Simulated Ground-State Raman Intensities for Conjugated Phenyl and Thiophene Derivatives

(This work was published as Ref. #56. Supporting information will be available online.)

8.1 Introduction

Aromatic organic compounds continue to be the focus of numerous studies of charge-transfer,[162] intermolecular $\pi - \pi$ interactions,[164,193] and ring-ring delocalization.[163] In particular, polymeric chains of phenyl and thienyl derivatives have efficient inter- and intra-molecular charge mobility due to the extended π-conjugated structure,[38,48,49,162] which makes them ideal compounds for organic solar cells.[40,168] The charge-transport properties of these compounds are sensitive to the relative orientation of the aromatic rings and their substituents.[31,164–166,194] As a result, many studies have examined the torsional energy barriers in oligothiophenes,[166,195,196] biphenyl and substituted biphenyl derivatives,[197–201] and the effects of torsion angle on the vibrational properties of substituted benzenes.[202,203] The conjugation in these substituted aryl molecules has a significant effect on the polarizability,[28] therefore Raman spectroscopic techniques have been a powerful tool in characterizing the structures of these compounds and determining their effects on the physical properties of the molecules.[31–33]

Computational studies are particularly useful in assigning the Raman bands observed in experimental spectra,[52] and predicting the structures that correspond to the experiment. Recently, we

benchmarked calculations of ground state Raman spectra using density functional theory (DFT) and second-order Møller-Plesset perturbation theory (MP2) with experiment for a set of substituted benzene and thiophene compounds.[55] Our study indicates that, although the Raman spectra calculated with each method are in fairly good agreement with experiment, all of the calculated spectra tend to overestimate the intensities of higher-frequency Raman bands (>1200 cm^{-1}) relative to those of lower frequency transitions. We found that B3LYP gives the best agreement with the experimental relative intensities ($\sim$5-19% better than the other methods), although there is still a discrepancy between low- and high-frequency Raman intensities.

The overestimation of high-frequency Raman intensities has been reported in the literature, and is most evident in the Raman spectra of substituted benzene derivatives, including toluene,[169] 4-aminobenzonitrile,[13] and thioanisole derivatives.[33,192] Ohno *et al.* observed that the Raman intensities of low-frequency ring-substituent torsion (13-45 cm^{-1}) and out-of-plane bending (86-192 cm^{-1}) modes are particularly sensitive to the orientation of the substituent in analogues of thioanisole.[192] However, to our knowledge, the conformation-dependent effects of ring-ring conjugation on the Raman spectra of di-aryl molecules have not been investigated, nor has the overestimation of calculated relative Raman intensities in high-frequency modes compared with experiment.

In this chapter, we compare the experimental Raman spectra of biphenyl (BP), 2-phenylthiophene (PT), and 2,2'-bithiophene (BT) with calculations that explore the anharmonic corrections to the Raman intensities as well as the torsion angle dependence. The torsional energy barriers are calculated with DFT, and the coupled cluster with single, double, and noniterative triple excitations [CCSD(T)] method. The chapter is organized as follows. We introduce the computational and experimental details in Section 8.2. In Section 8.3.1, we compare the experimental Raman spectra of all three compounds to calculations with and without anharmonic correction, and assign the vibrational bands. We present the torsional dependence of the relative Raman intensities of the molecules in Section 8.3.2, as well as the comparison of DFT and CCSD(T) potential energy surfaces along the inter-ring torsion. Finally, we discuss the results in Section 8.4, and summarize our

main conclusions in Section 8.5.

8.2 Computational and Experimental Methods

We calculated ground-state Raman spectra using the B3LYP functional,[110,111] which was previously shown to provide the most accurate description of relative Raman intensities in BP, PT, and BT.[55] For BT, we optimized both the *cis* and *trans* isomers, and computed Raman intensities as a Boltzmann-weighted average of the two structures. PT and BP have a single minimum-energy structure. All calculations utilize the aug-cc-pVDZ basis set,[113] which provides an effective compromise between accurate Raman intensities and computational cost.[18,19] For BP, PT, and BT, the fractional Raman intensities, defined relative to the total integrated intensity within the range 200-1800 cm^{-1}, calculated using B3LYP/aug-cc-pVDZ differ from those of B3LYP/aug-cc-pVTZ with a mean unsigned discrepancy of <2% for each molecule. Additionally, the dihedral angles of the equilibrium geometries calculated for each molecule differ between basis sets by less than 2°, except for *trans*-BT, for which the dihedral angles calculated using aug-cc-pVDZ and aug-cc-pVTZ are 15.7° and 20.7°, respectively. The harmonic frequencies obtained for the Raman spectra are scaled by 0.970, the empirical vibrational scaling factor that has been determined for this level of theory.[116] The calculated Raman intensities, I_n, were obtained as:[29,30,55]

$$I_n = S_n \frac{(\tilde{v}_p - \tilde{v}_n)^4}{\tilde{v}_n} \left[1 - \exp\left(-\frac{hc\tilde{v}_n}{k_B T} \right) \right] \tag{8.1}$$

where S_n is the calculated static Raman activity (in Å^4/amu), $\tilde{v}_p$ is the Raman excitation frequency (12,739 cm^{-1} or 785 nm), $\tilde{v}_n$ is the calculated vibrational frequency for the nth band (in cm^{-1}), h is Planck's constant, c is the speed of light, k_B is Boltzmann's constant, and T is the temperature (300 K). Fractional intensities are computed as:[55]

$$\bar{I}_n = \frac{I_n}{I_{total}} \tag{8.2}$$

where I_n is the integrated intensity of the nth Raman band, and $I_{total} = \sum_n I_n$ is the integrated intensity of all assigned Raman bands of the molecule in the region of interest (200-1800 cm^{-1}). In order to quantify the agreement in relative intensities, we also define the ratio of fractional intensities, ρ_n:[55]

$$\rho_n = \frac{\bar{I}_n^{calc}}{\bar{I}_n^{exp}} \tag{8.3}$$

where $\bar{I}_n$ is defined in Eq. 8.2.

Perturbative quartic anharmonic corrections to the fundamental, first overtones, and combination bands transitions of the Raman spectra are computed through numerical differentiation of the potential with respect to normal mode vibrational displacement coordinates.[204,205] Comparisons of the anharmonic corrections with experiment in all three compounds, given in Figure S1 of the Supporting Information (SI), show that the the overtones and combination bands have negligible contribution to the calculated Raman spectra. Therefore, the anharmonic spectra in the following figures only show the corrections to the fundamental Raman transitions. Raman spectra at different torsion angles were calculated with B3LYP/aug-cc-pVDZ. We explored the torsional dependence by optimizing the structure around fixed values of the ring-ring dihedral angle. Torsional energies at these geometries are also calculated with CCSD(T). A full table of calculated energies along the dihedral angle is available in Table S1 in the SI (including the CCSD data). The simulated Raman spectra include 15 cm^{-1} Gaussian broadening. All calculations were performed using a development version of the GAUSSIAN software package.[78]

The ground-state Raman spectra were measured using a commercial spectrometer (StellarNet) with 785 nm cw pump laser and 4 cm^{-1} resolution. All three compounds were obtained commercially and solutions of BP (0.6 M in cyclohexane), PT (0.2 M in cyclohexane), and BT (0.3 M in DMSO) were prepared in a 2 cm diameter glass vial. For each sample, we subtract the solvent-only spectrum to remove contributions from the solvent and the glass walls. The solvents used in the experiments are not expected to significantly affect the Raman spectra of the solutes. We verified this in Ref. 55, comparing the error of the calculations with available experimental data in gas phase and in condensed phase for benzene and BP. Additionally, we computed the Raman spec-

tra of each compound in solution using the polarizable continuum model of solvation (PCM),[189] shown in Figure S2 of the SI. Generally, the intensities increased relative to the gas phase, but their relative magnitudes are unchanged. Thus, we neglect solvent effects in the calculations to reduce computational cost. We explored the effect of solute aggregation on the Raman spectra with DFT calculations of stacked dimers of PT. The calculated spectra are included in Figure S3 of the SI, and show little to no change in the relative Raman intensities of the various dimers. Therefore, we do not discuss aggregation effects in the following. We also investigated possible pre-resonance effects by calculating Raman intensities of each molecule in the presence of an incident field of light, which was set to 785 nm as in experiment. The results, given for each molecule in Figure S4 of the SI, show that the incident field generally increases the Raman intensities of individual bands by an average of ∼30-50%, but the differences in relative Raman intensities are negligible. Therefore, the calculations in the chapter were performed in static conditions.

8.3   Results

8.3.1   Band Assignments and Anharmonic Corrections

A comparison of the experimental and calculated Raman spectra for BP is shown in Figure 8.1. We focus on the strongest bands in the experimental spectrum, which are assigned to the harmonic vibrations based on the calculated Raman intensities. Anharmonic corrections to the Raman spectrum are also shown in Figure 8.1. The vibrational displacement vectors for the assigned transitions are included in Figure S5 of the SI. The assignments are also listed in Table 8.1. In Table 8.1, we define in-plane and out-of-plane motions relative to the individual phenyl rings.

   As outlined in our previous study,[55] the harmonic calculations provide generally good agreement in frequencies (accurate to within <40 cm^{-1}) and predict relatively strong intensities in most of the Raman bands observed in the experiment. However, there are discrepancies in the $\bar{I}_n$ values of transitions at frequencies lower than $\sim$800 cm^{-1} and at frequencies higher than $\sim$1400 cm^{-1}. The percent error in $\bar{I}_n$ for each of the Raman bands $>$1400 cm^{-1} is between 95% and 154%. The

Figure 8.1: Ground-state Raman spectra of BP. The Raman transitions calculated with harmonic potentials (top) and anharmonic corrections (middle) are shown with the experimental spectrum (bottom). Experimental band assignments are indicated in the calculated spectra (dotted lines). All results are normalized to the strongest band in each spectrum.

remaining bands have <60% error compared to experiment. The anharmonic corrections to the fundamental transitions, shown in Figure 8.1 and Table 8.1, show better agreement in $\bar{I}_n$ for a majority of bands, with the error reduced by between 6% and 28%. The better agreement is mainly observed for the bands <800 cm^{-1}, although the largest error reduction of 28% occurs in v_{28} (from 43% error in the harmonic $\bar{I}_{28}$ to 15% error in the corrected intensities). While a few bands have worse agreement, such as v_{38}, for which the error increases by 19%, the anharmonic corrections generally provide more accurate fractional intensities. The mean unsigned error (MUE) in $\bar{I}_n$ decreasing from 0.035 in the harmonic calculations to 0.030, which reduces the overall error by 13%.

The Raman spectra of PT are shown in Figure 8.2. As with BP, the strongest experimental bands are assigned, and the vibrational displacements of the assigned bands are included in Figure S6 in the SI. The assignments are listed in Table 8.2, along with the fractional intensities.

The calculated harmonic $\bar{I}_n$ are generally in better agreement with experiment than in BP, with

125

Table 8.1: Assignment of BP Raman Transitions

Vibration	Harm.[a] $\tilde{v}_n$ (cm^{-1})	$\bar{I}_n$	Anharm. $\tilde{v}_n$ (cm^{-1})	$\bar{I}_n$	Exp. $\tilde{v}_n$ (cm^{-1})	$\bar{I}_n$	Motion
v_4	256	0.017	262	0.024	264	0.040	out-of-plane phenyl rocking
v_5	303	0.029	310	0.041	309	0.049	in-phase ring dist.
v_8	404	0.026	407	0.035	405	0.032	out-of-plane phenyl C−C−C bend
v_{12}	603	0.019	619	0.024	610	0.026	antisym. phenyl C−C−C bend
v_{17}	729	0.026	745	0.037	738	0.058	sym. phenyl C−C−C bend
v_{19}	818	0.022	826	0.027	834	0.014	out-of-plane phenyl C−H bend
v_{23}	946	0.010	952	0.008	961	0.011	out-of-plane C−H bend and C−C−C bend
v_{28}	979	0.131	1006	0.195	999	0.229	C−C−C bend/phenyl dist.
v_{30}	1019	0.066	1034	0.060	1027	0.054	outer phenyl C−C−C bend
v_{34}	1135	0.012	1161	0.018	1151	0.012	antisym. in-plane C−H bend
v_{37}	1164	0.015	1186	0.014	1175	0.011	sym. in-plane C−H bend
v_{38}	1259	0.247	1284	0.148	1281	0.218	bridging C−C stretch and C−H bend
v_{46}	1482	0.035	1510	0.038	1500	0.014	bridging C−C stretch and asym. phenyl dist.
v_{48}	1575	0.004	1590	0.004	1589	0.079	antisym. phenyl C=C stretch
v_{49}	1595	0.341	1606	0.325	1608	0.154	bridging C−C stretch and sym. phenyl dist.

[a] B3LYP with empirical scaling factor of 0.970. [116]

Table 8.2: Assignment of PT Raman Transitions

Vibration	Harm.[a] $\tilde{v}_n$ (cm^{-1})	$\bar{I}_n$	Anharm. $\tilde{v}_n$ (cm^{-1})	$\bar{I}_n$	Exp. $\tilde{v}_n$ (cm^{-1})	$\bar{I}_n$	Motion
v_4	252	0.018	256	0.030	264	0.038	out-of-plane thienyl rocking
v_5	305	0.019	312	0.031	314	0.023	in-phase ring dist.
v_{11}	601	0.022	613	0.033	612	0.032	C−S−C bend and phenyl dist.
v_{14}	675	0.035	705	0.049	689	0.062	C−S−C stretch and phenyl dist.
v_{26}	976	0.073	1001	0.113	1000	0.117	C−C−C bend/phenyl dist.
v_{29}	1059	0.024	1080	0.028	1079	0.032	thienyl C−H bend
v_{34}	1238	0.074	1254	0.080	1254	0.042	thienyl C−H bend and bridging C−C stretch
v_{37}	1336	0.041	1352	0.022	1352	0.044	thienyl C=C stretch and thienyl C−H bend
v_{39}	1432	0.355	1444	0.362	1429	0.347	thienyl C=C stretch and delocalized C−H bend
v_{41}	1526	0.120	1535	0.034	1530	0.082	thienyl C=C stretch and bridging C−C stretch
v_{43}	1594	0.220	1606	0.217	1600	0.180	C=C stretch and phenyl dist.

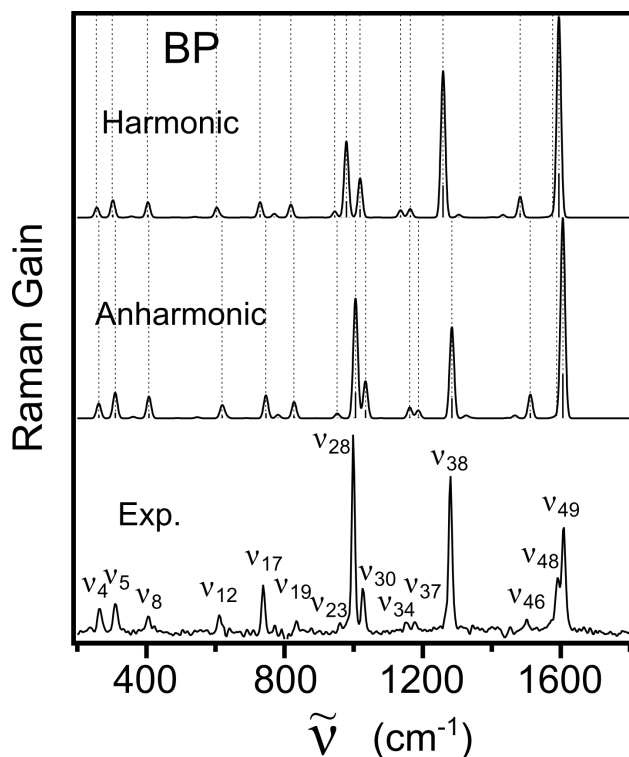[a] B3LYP with empirical scaling factor of 0.970. [116]

Figure 8.2: Ground-state Raman spectra of PT. The Raman transitions calculated with harmonic potentials (top) and anharmonic corrections (middle) are shown with the experimental spectrum (bottom). Experimental band assignments are indicated in the calculated spectra (dotted lines). All results are normalized to the strongest band in each spectrum.

a MUE of 0.021. The percent error for all bands remains within <60%, except for ν_{34}, for which the fractional intensity is overestimated by $\sim$76%. Similar to BP, the anharmonic corrections to the fundamental Raman transitions reduce the overall MUE by 15%, and the largest reduction of errors (between 12% and 34%) occur in the bands below 1100 cm^{-1}. The error is reduced by 34% for ν_{26} in PT (mode 12 in Wilson's notation[190,191]), and is analogous to ν_{28} in BP).

The Raman spectra of BT are given in Figure 8.3, where the calculated spectra include the contributions from both *cis* and *trans* conformations according to Boltzmann weighting factors. Similar to the spectrum of PT, the Raman bands with the largest intensity in BT are in the high-frequency region of both the calculated and experimental spectra (1400 to 1600 cm^{-1}). However, BT has a weaker scattering cross-section than PT, and the experimental spectrum has a noticeably smaller signal-to-noise ratio. As a result, we tentatively assign the strongest Raman bands in the experiment based not only on their position and relative intensities in the calculated spectra, but
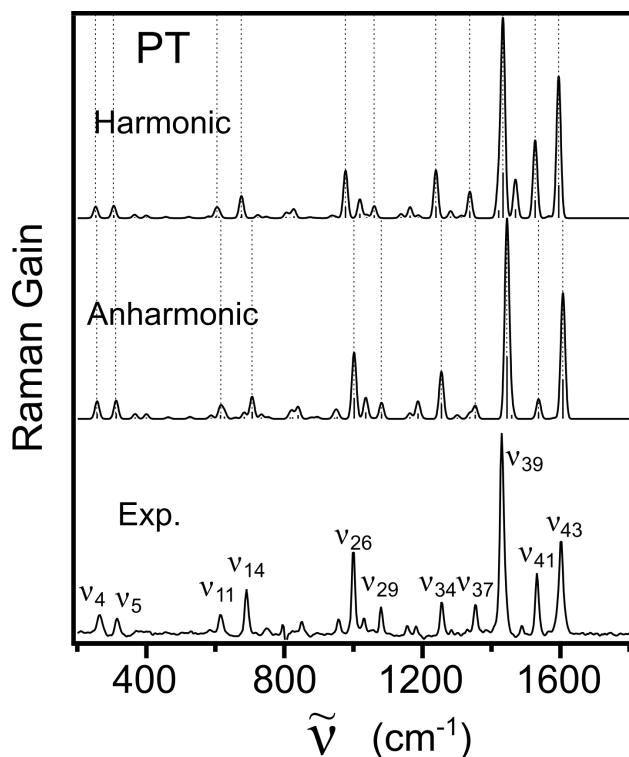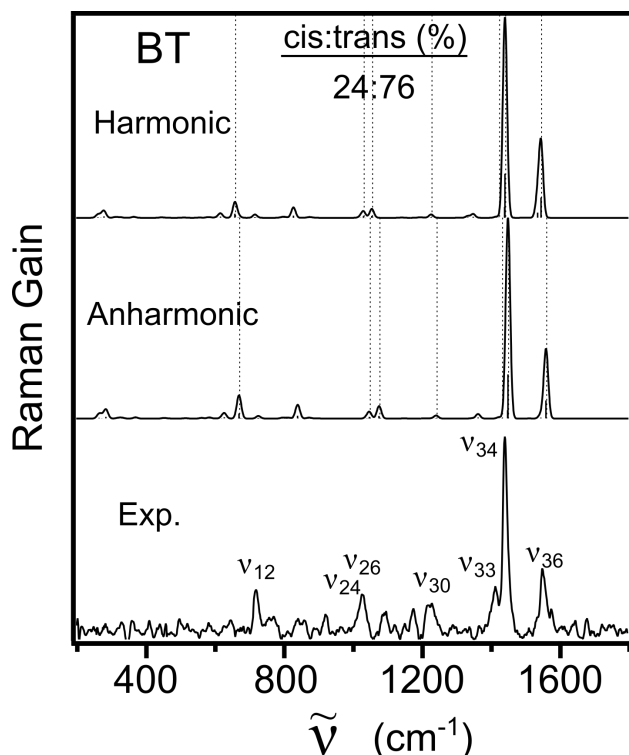
Figure 8.3: Ground-state Raman spectra of BT. The Raman transitions calculated with harmonic potentials (top) and anharmonic corrections (middle) are shown with the experimental spectrum (bottom). Experimental band assignments are indicated in the calculated spectra (dotted lines). All results are normalized to the strongest band in each spectrum.

on analogous vibrations of the thienyl substituent that are observed in PT. For example, the 706 cm^{-1} band is assigned to the symmetric $C-S-C$ bending motion, ν_{12}, which has the strongest calculated intensity in the BT spectrum within 100 cm^{-1}, and is also analogous to the ν_{11} mode in PT. Additionally, the band at 1019 cm^{-1} has been tentatively assigned to both ν_{24} and ν_{26}, as these thienyl $C-H$ bending vibrations are not only similar to each other and relatively isolated in the calculated spectra, but they are also analogous to the ν_{29} mode assigned in the spectrum of PT. The vibrational displacements of the assigned bands are shown in Figure S7 of the SI for the *trans* conformer. The assignments are identical for the *cis* conformer, and the displacement vectors are included in Figure S8. Table 8.3 lists the Boltzmann averages of the fractional intensities of these bands.

The overall errors in $\bar{I}_n$ between the experiment and the harmonic calculations are larger in BT than in BP or PT, based on the MUE of 0.096. All bands in Table 8.3 have between 44 and

Table 8.3: Assignment of BT Raman Transitions

Vibration	Harm.[a] $\tilde{\nu}_n$ (cm^{-1})	$\bar{I}_n$	Anharm. $\tilde{\nu}_n$ (cm^{-1})	$\bar{I}_n$	Exp. $\tilde{\nu}_n$ (cm^{-1})	$\bar{I}_n$	Motion
ν_{12}	662	0.051	671	0.073	706	0.092	sym. C−S−C bend
$\nu_{24} + \nu_{26}$	1043	0.049	1063	0.062	1019	0.109	in-plane C−H bend
ν_{30}	1228	0.011	1243	0.010	1219	0.099	sym. C−H bend and bridging C−C stretch
ν_{33}	1428	0.004	1429	0.005	1410	0.103	antisym. thienyl C=C stretch
ν_{34}	1442	0.602	1451	0.622	1441	0.413	bridging C−C stretch and out-of-phase thienyl C=C stretch
ν_{36}	1526	0.284	1561	0.228	1549	0.185	bridging C−C stretch and in-phase thienyl C=C stretch

[a] B3LYP with empirical scaling factor of 0.970.[116]

97% error with experiment, where the fractional intensities of ν_{34} and ν_{36} are overestimated by the calculations and all other bands are underestimated. Due to the fewer band assignments, it is difficult to confirm the trend observed in BP and PT, where agreement in $\bar{I}_n$ was substantially better for most bands <1100 cm^{-1}. Nevertheless, the corrections to the intensities of the ν_{12} and $\nu_{24} + \nu_{26}$ bands reduced the error by 24% and 12%, respectively. Similar to BP and PT, the anharmonic corrections decreased the MUE by 12%.

The anharmonic corrections generally increase the agreement between experimental and calculated fractional intensities. Relatively significant reductions of error of roughly 10% to 30%) occur in the majority of bands <1100 cm^{-1}, and the anharmonic corrections provide an overall decrease in the MUE of $\bar{I}_n$ by 12% to 15%. Nevertheless, the calculated Raman spectra with perturbative anharmonic corrections still overestimate the relative intensities of the higher-frequency vibrations and underestimate those of lower-frequency bands.

8.3.2 Torsion Angle Analysis

We explore the impact of the inter-ring torsion angle on the Raman intensities of these test molecules by performing a relaxed scan along this internal coordinate, from 0° to 90°. In each molecule, the internal coordinate is the dihedral angle between the planes of each of the rings. For BP, our calculations define each plane by the carbon atom that forms the bridging C−C bond and the carbon that is adjacent to it (Cα, relative to the inter-ring bond). Similarly, the dihedral angle in PT is that

between the planes formed by the C−S bond on the thiophene and the C=Cα bond on the phenyl ring. In BT, the global minimum along the torsion coordinate occurs in the *trans* isomer, therefore, the dihedral is also defined by the C−S bond on the thiophene and the C=Cα bond on the phenyl. The relaxed scan for BT is performed from $0°$ to $180°$ in order to explore the local minimum of the *cis* isomer. For brevity, we refer to the $90°$ to $180°$ structures along this torsion coordinate as the $90°$ to $0°$ geometries of the *cis* isomer, which are identical due to symmetry, defined along a dihedral angle between the planes formed by each thiophene ring's inner C−S bond.

The angle dependence of the Raman spectrum of BP is shown in Figure 8.4, which displays the Raman spectrum at each dihedral angle. As shown in the inset of the figure, which gives the I_{total} values at each angle, the overall Raman intensities decrease significantly as the aryl rings approach a perpendicular orientation. The largest change in intensity occurs in bands >1200 cm^{-1}, which are reduced by up to an order of magnitude, while the intensities of bands <1000 cm^{-1} are significantly less sensitive to the torsion. For comparison of relative intensities, the Raman spectra normalized by the corresponding I_{total} are included in Figures S9-S11 of the SI for BP, PT, and BT, respectively. Additionally, the ν_{48} shoulder band, which is observed in the experiment, is only visible at dihedral angles $>60°$.

The torsional dependence of ρ_n in BP is displayed in Figure 8.5(a), along with a dotted line at $\rho_n = 1$ to indicate perfect agreement between calculated and experimental intensities. Included in Figure 8.5(b) is the torsion potential energy surface, along with the value of kT at room temperature (thin green line). The calculated torsional energy barriers are roughly 1.46 and 2.15 kcal/mol for the planar and perpendicular orientations of the rings, respectively. As in Figure 8.4, we observe a significant torsion-dependent change in the Raman intensities of the assigned bands as the dihedral angle increases from $0°$ to $90°$ and the inter-ring conjugation breaks. Although the traces in Figure 8.5(a) are generally different for each Raman band, the best agreement, on average, is observed at a dihedral angle around $70°$, which is $\sim30°$ displaced from the energetic minimum. Relative to the equilibrium structure, the bands for which the error in ρ_n is reduced the most (by a factor of 3 to 10) are assigned to ν_{17}, ν_{28}, ν_{46}, and ν_{49}. Each of these vibrations (modes 6a, 12, 18a, and 9a

Figure 8.4: Dihedral angle dependence of Raman intensities in BP. Total integrated Raman intensities for the 200-1800 cm^{-1} region are shown in the inset, along with the Raman spectrum at each fixed angle. The experimental spectrum is shown at the bottom. Equilibrium geometry of BP has 38.8° dihedral angle. Dotted lines indicate band assignments.

in Wilson's notation) involves significant distortion of the phenyl rings and/or the bridging C−C bond.
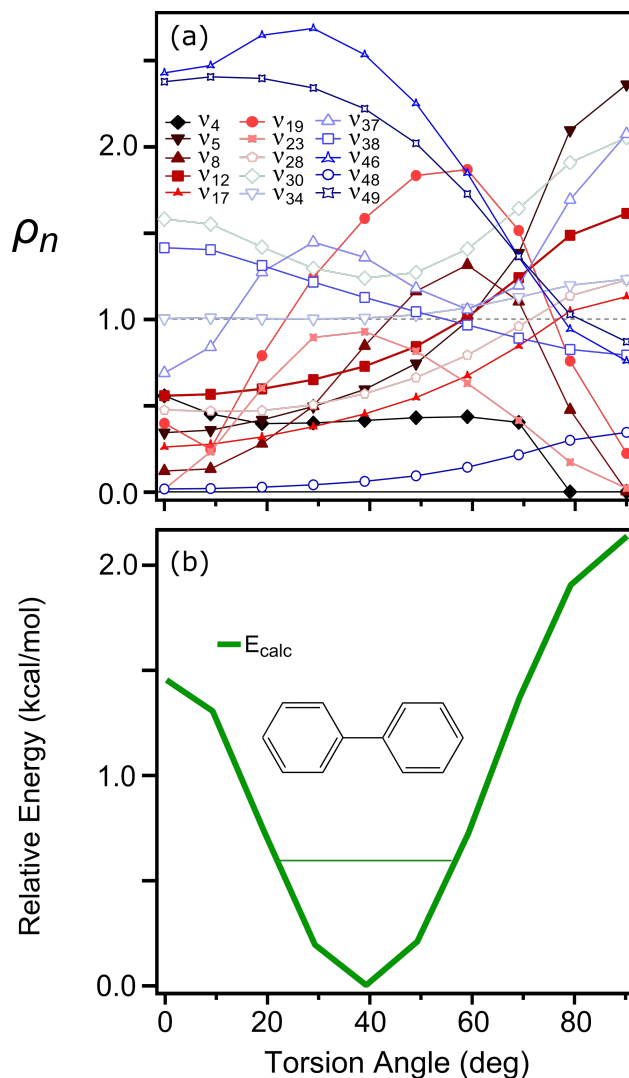
Figure 8.5: Torsion angle dependence in BP of (a) fractional intensity ratio and (b) the calculated energies. The potential energy surface is calculated with B3LYP, and shown with the ambient energy at room temperature (thin green).

The calculated Raman spectra of PT as a function of torsion angle are shown in Figure 8.6, along with the corresponding I_{total} values. Similar to BP, the overall Raman intensities generally decrease as the dihedral angle increases and the ring-ring conjugation breaks, with the largest changes occurring in the high-frequency bands >1400 cm^{-1}. The mode-specific ρ_n values and calculated torsional barrier are displayed in Figure 8.7. The potential energy surface in panel (b) shows that the torsional barrier at 90° (2.57 kcal/mol) is comparable to that of BP, but, due to the reduced steric strain in PT, the energy minimum occurs at a smaller torsion angle of 25°.
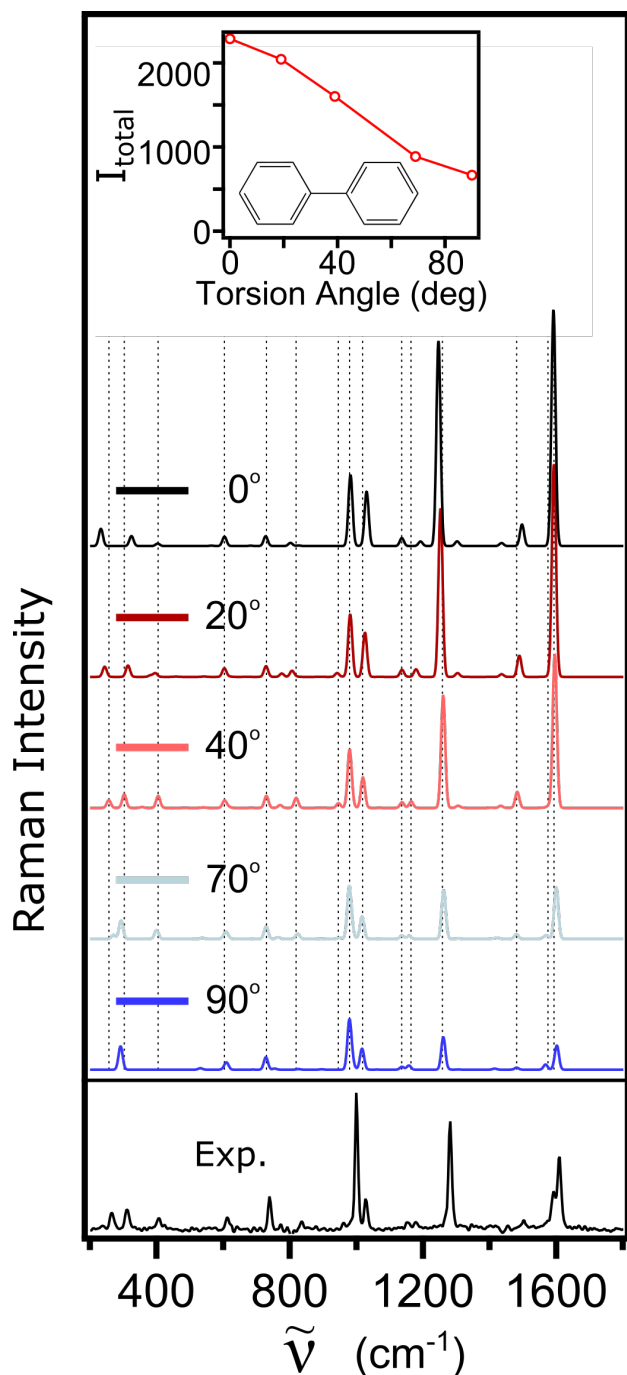
Figure 8.6: Dihedral angle dependence of Raman intensities in PT. Total integrated Raman intensities for the 200-1800 cm^{-1} region are shown in the inset, along with the Raman spectrum at each fixed angle. The experimental spectrum is shown at the bottom. Equilibrium geometry of PT has 25.4° dihedral angle. Dotted lines indicate band assignments.

Additionally, the ratios of fractional intensities in panel (a) generally follow more consistent trends than the ρ_n values in BP. Nevertheless, the best overall agreement in PT also occurs at a dihedral angle of 70°. The vibrations for which the error in ρ_n reduces the most (by a factor of between 3 and 11) are ν_{11}, ν_{14}, ν_{26}, and ν_{41}. With the exception of ν_{11} (mode 6b in Wilson's notation), the
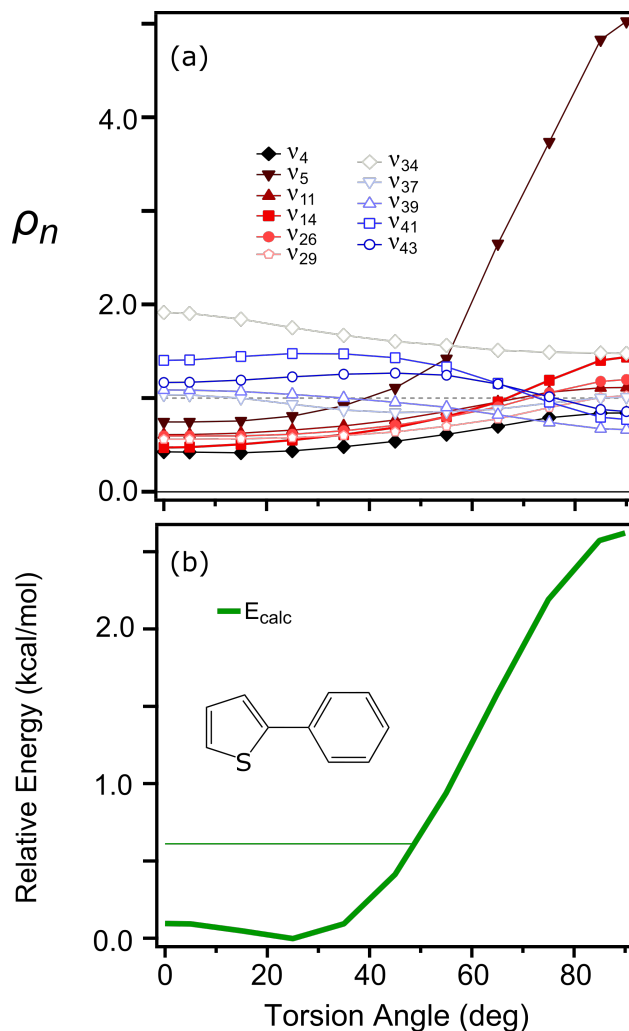
Figure 8.7: Torsion angle dependence in PT of (a) fractional intensity ratio and (b) the calculated energies. The potential energy surface is calculated with B3LYP, and shown with the ambient energy at room temperature (thin green).

remaining vibrations are analogous to those with the largest reduction in error in BP, where ν_{14}, ν_{26}, and ν_{41} correspond to the 6a, 12, and 18a modes in Wilson's notation, respectively.

Figures 8.8 and 8.9 display the calculated Raman spectra at the different torsion angles in the *trans* and *cis* conformers of BT, respectively. Similar to BP and PT, the I_{total} values in either conformer are significantly reduced as the angle approaches 90°. The calculated potential energy surface is plotted in Figure 8.10(b), and predicts torsional barriers of 2.56 and 1.87 kcal/mol for the *trans* and *cis* conformers, respectively. As in the two phenyl-substituted compounds, the optimal agreement with experiment occurs at around 75° and 105° along the dihedral coordinate. However,
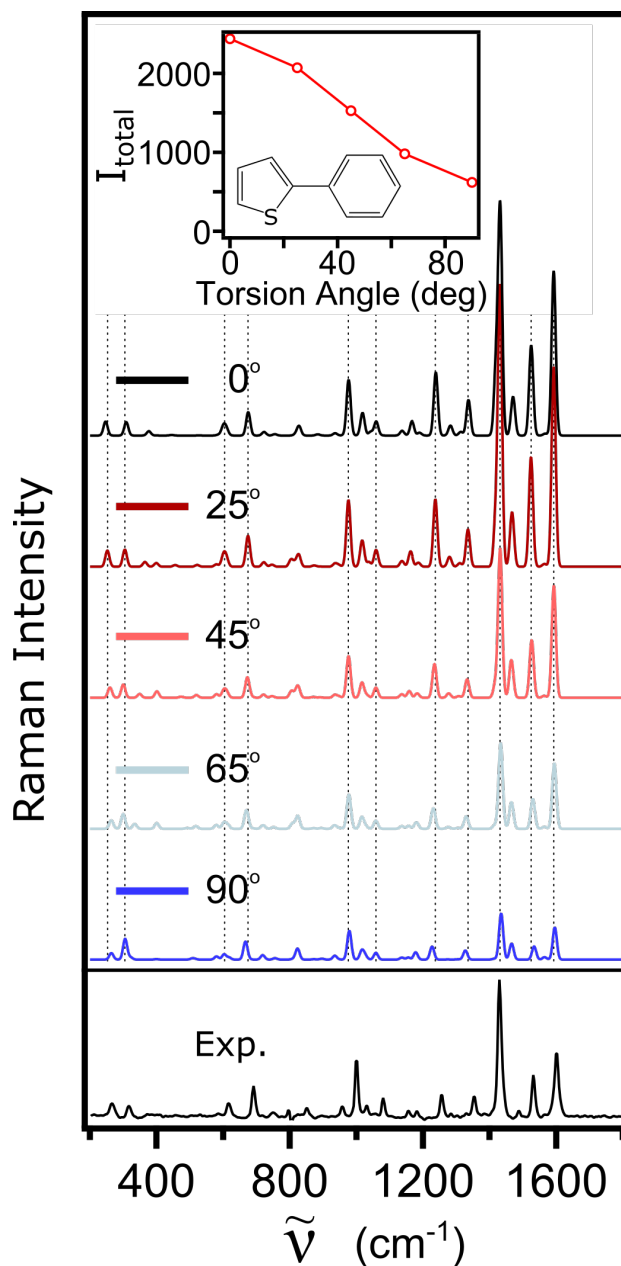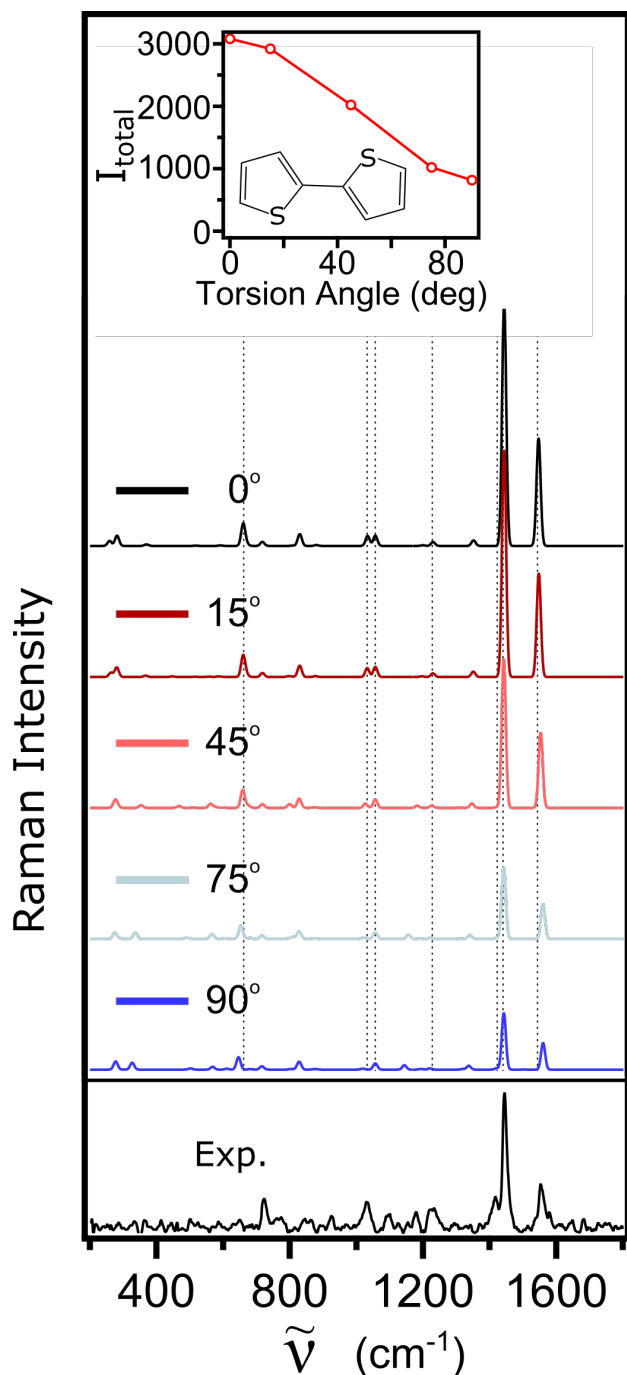
Figure 8.8: Dihedral angle dependence of Raman intensities in *trans*-BT. Total integrated Raman intensities for the 200-1800 cm^{-1} region are shown in the inset, along with the Raman spectrum at each fixed angle. The experimental spectrum is shown at the bottom. Equilibrium geometry of *trans*-BT has 20.7° dihedral angle. Dotted lines indicate band assignments.

unlike BP and PT, the angle dependence of ρ_n in Figure 8.10(a) displays a weaker trend for the assigned vibrations in BT. The vibrations with ρ_n values most sensitive to the torsion are ν_{12},
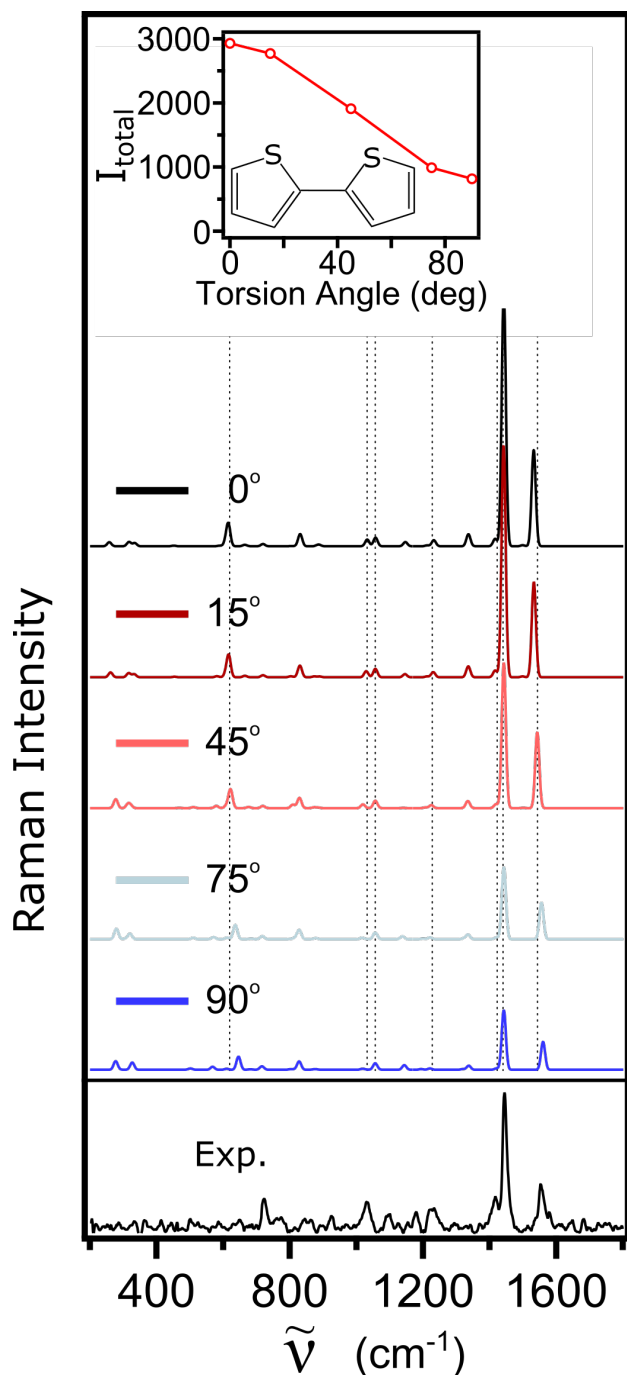
Figure 8.9: Dihedral angle dependence of Raman intensities in *cis*-BT. Total integrated Raman intensities for the 200-1800 cm^{-1} region are shown in the inset, along with the Raman spectrum at each fixed angle. The experimental spectrum is shown at the bottom. Equilibrium geometry of *cis*-BT has 31.6° dihedral angle. Dotted lines indicate band assignments.

$\nu_{24}+\nu_{26}$, and ν_{34}, each of which involve significant distortion of the C=C bonds in the thiophene rings.
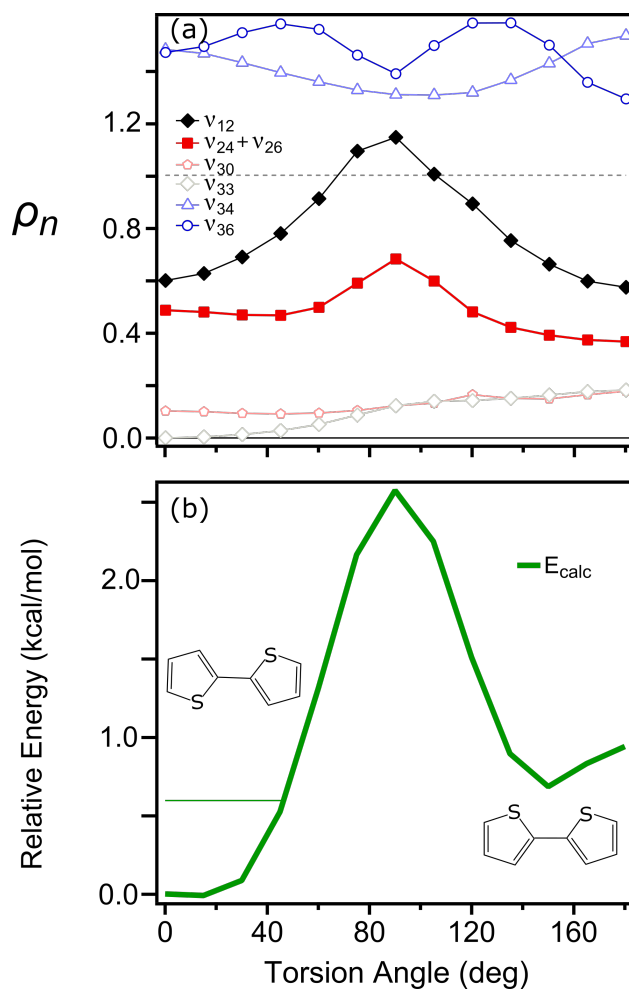
Figure 8.10: Torsion angle dependence in BT of (a) fractional intensity ratio and (b) the calculated energies. The potential energy surface is calculated with B3LYP, and shown with the ambient energy at room temperature (thin green).

The fractional intensity ratios for the bands in all three molecules generally tend toward better agreement with experiment at torsion angles that break conjugation. Thus, we use CCSD(T) calculations of the potential energy to obtain more accurate values of the torsional barrier, and of the range of angle values accessible at room temperature. The torsion potentials are shown in Figure 8.11, and are given relative to the energy minimum. In all three molecules, the CCSD(T) results reduce the energy barrier at $90°$ by >0.5 kcal/mol relative to the barrier computed with B3LYP. The higher-level calculations also consistently give larger energy barriers at planar orientations, which, together with the lower barrier at perpendicular orientations, predicts a slight shift of the energy minimum in the torsional potential to between $30°$ and $50°$ for each molecule.

137

Figure 8.11: Torsional energy barriers in (a) BP, (b) PT, and (c) BT.

The calculated torsional barriers are also in reasonably good agreement with results from the

literature. In the case of biphenyl, Johansson and Olsen performed a very similar calculation

using B3LYP/TZVPP to optimize the geometries, and then computed single-point energies using CCSD(T)/aug-cc-pVDZ.[198] The 0° and 90° barriers in Figure 8.11(a) are 2.22 and 1.56 kcal/mol, respectively, and are within 0.03 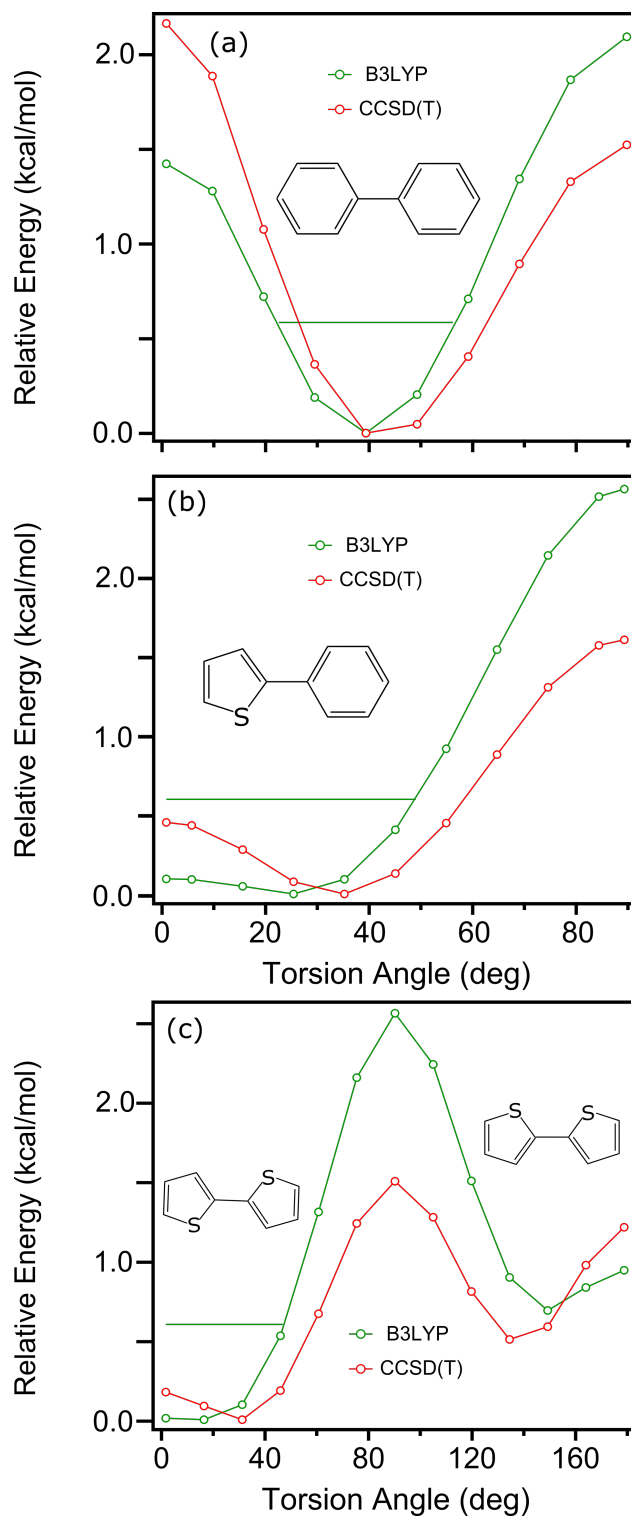kcal/mol of the results obtained from the literature. Additionally, a benchmark study by Bloom and Wheeler calculated the torsional barriers in BT with a variety of theoretical methods, using geometries optimized with MP2/aug-cc-pVTZ.[166] The energy barriers obtained with CCSD(T)/cc-pVTZ are still within 0.16-0.25 kcal/mol of the calculated barriers in Figure 8.11(c).

8.4   Discussion

The calculated harmonic Raman spectra for these conjugated aryl compounds consistently overestimate the high-frequency intensities relative to the lower frequency bands compared with experimental measurements. The inclusion of perturbative anharmonic corrections to the Raman intensities only reduces the error with experiment by about 12% to 15%, on average. On the other hand, the fractional intensities observed in the experiment are in significantly better agreement (on average, a factor of 2.2 in the errors in ρ_n values) with the majority of calculated vibrational bands as the torsion angle increases and the ring-ring conjugation breaks. In general, the agreement in $\bar{I}_n$ does not change appreciably until the torsion angle is at least $\pm 20°$ from the energy minimum, which suggests that the perturbative approach for the anharmonic corrections is not capturing a sufficient sample of the potential energy surface.

Although the DFT energy barriers along the inter-ring torsion degree of freedom indicate a small population at large angles at room temperature, the CCSD(T) data show that the DFT torsion angles at the minimum geometry are underestimated while the barriers are overestimated. Furthermore, the CCSD(T) barriers would be even lower if the relaxed scan had been fully performed at this level of theory (which is below our current computational capabilities). This points to an overestimation of the inter-ring conjugation in DFT, which leads to minimum geometries with angles that are too small, and is supported in the literature.[206]

As seen in the work of Ohno *et al.*, the low-frequency (<200 cm^{-1}) Raman bands of substituted

benzene compounds can be highly sensitive to ring-substituent orientation.[33,192] In particular, they observed a stereo-specific enhancement of Raman intensities of the ring-substituent torsion and out-of-plane bending modes in thioanisole compounds, resulting in roughly an order of magnitude increase in relative intensity of Raman bands when the substituent was oriented perpendicular to the phenyl ring. However, this strong enhancement is limited to the low-frequency torsional and bending motions, and the conformational change had negligible effect on the relative intensities of the higher-frequency bands of the thioanisoles.

On the other hand, in the conjugated systems studied in this work, the largest torsion-dependent effects are observed primarily in the high-frequency $C-C$ and $C=C$ stretching vibrations, in the 1200-1800 cm^{-1} region. At the same time, bending motions and other ring distortions that do not directly involve the inter-ring $C-C$ bond are much less sensitive to the torsion angle. Although many of these bending motions, which lie roughly between 600-1100 cm^{-1}, have a large reduction of error in the relative Raman intensities in Figures 8.5(a), 8.7(a), and 8.10(a), the Raman spectra in Figures 8.4, 8.6, 8.8, and 8.9 show that the absolute intensities change by significantly less than those of the higher-frequency bands. Both types of motion have considerable Raman cross section, because they both affect the π cloud on the aromatic rings and, thus, the polarizability. However, the polarizability change with stretching motions is considerably larger at small torsion angles, because the electron density is conjugated across both rings. Once the conjugation is broken at large torsion angles, the change in polarizability decreases and so do the intensities of these bands, see bands v_{38}, v_{46}, and v_{49} in Figure 8.4, v_{34}-v_{43} in Figure 8.6, and v_{34} and v_{36} in Figures 8.8 and 8.9. Conversely, bending motions and other ring distortion modes where the $C-C$ bond is not involved are localized on the individual rings, and the change in torsion angle affects them considerably less, see bands v_{12}-v_{28} in Figure 8.4, v_{11}-v_{29} in Figure 8.6, and v_{12} and v_{24}+v_{26} in Figures 8.8 and 8.9. A noticeable effect is observed for high-frequency $C=C$ stretching vibrations, for which the normal mode is the anti-symmetric combination of two local modes in the benzene or thiophene rings, as exemplified by v_{48} in BP (the anti-symmetric combination of the 9b mode in Wilson's notation) and v_{33} in BT. Contrary to v_{46} and v_{49} in BP (symmetric

combinations of the 18a and 9a local modes, respectively), ν_{48} increases in intensity as the torsion angle approaches $90°$ in Figure 8.4. The ν_{33} band of BT, however, increases in intensity as the dihedral coordinate approaches $180°$, and is only visible in the Raman spectra of the *cis* isomer in Figure 8.9. We note that we focused on the lowest-frequency internal coordinate that is most responsible for breaking conjugation between the rings, and whose energy profile is low enough that a large motion is allowed at room temperature. However, other low-energy modes, such as ν_2, ν_3, and ν_4 at 89, 122, and 256 cm^{-1} in BP (which are analogous to ν_2-ν_4 at 99, 134, and 252 cm^{-1} in PT and at 110, 124, and 269 cm^{-1} in BT), can also break conjugation, possibly in combination with the torsional motion due to anharmonic coupling. Therefore, these contributions to the change in relative intensities may need to be considered to further increase the agreement with the experimental spectra.

Direct solute-solvent interactions, beyond the electrostatic bulk effects recovered by PCM, may also affect the dynamics around the average geometry of these chromophores. These effects may be recovered through a combination of large-scale quantum and classical molecular dynamics simulations. Finally, pre-resonance effects at geometries away from equilibrium should also be investigated. However, all of these issues are beyond the scope of this work, and they will be addressed in future contributions.

8.5 Conclusions

In this chapter, we investigate the possible causes of the consistent overestimation of calculated high-frequency Raman intensities relative to lower-frequency transitions of conjugated molecules. Specifically, we examine the effects of anharmonic corrections and torsion angle. We show that perturbative anharmonic corrections provide better predictions of relative intensities, but that the experimental fractional intensities are almost perfectly reproduced only when the inter-ring torsion angle is $\sim70°$ and the ring-ring conjugation breaks. We explain this phenomenon in terms of Raman band intensities that are affected by inter-ring conjugation for certain vibrations (i.e., bond stretching), and those that are not affected by conjugation (i.e., bending and ring distortion that do

not involve the inter-ring C−C). The energy profile along the torsion coordinate shows that DFT overestimates the barriers compared to CCSD(T), and that the former method predicts minimum geometries that are too planar. This indicates a tendency of DFT to overemphasize conjugation across multiple rings, consistently with previous studies. Therefore, although DFT still represents the best compromise between cost and accuracy for the simulation of Raman spectra of conjugated polymers, caution must be exercised in the analysis of the relative intensities when comparing with experimental measurements.

Chapter 9

Identifying Low-Frequency Vibrational Coherences in the Excited-State Dynamics of 2,5-Diphenylthiophene

9.1 Introduction

The excited-state photophysics of substituted thiophene molecules are of great interest to researchers due to their optical and electronic applications, among which is their use as charge-transport devices in organic photovoltaics.[35,36,43–46] The conjugated organic structure of these compounds allows for efficient electrical conductivity across polymeric chains,[207,208] and the thiophene-based structures facilitate the formation of long-lived triplet states following photoexcitation.[36–38,42,54] Therefore, understanding the dynamical evolution of the electronic and nuclear properties of these molecules in the excited state is of key importance in constructing devices for the desired opto-electronic applications.

The majority of studies on the excited-state dynamics of these compounds use time-resolved electronic and vibrational spectroscopy techniques, such as transient absorption (TA),[41,47,209] femtosecond stimulated Raman spectroscopy (FSRS),[41,48–50,52–54] and vibrational coherence spectroscopy (VCS).[57–61] Whereas TA and FSRS provide direct measurements of the excited-state electronic absorption and vibrational Raman spectra, respectively, VCS is a pump-probe technique that utilizes ultrafast pulses on the order of 10-100 fs to impulsively excite the molecule and, by taking a Fourier transform of oscillations observed in the TA spectrum, indirectly obtain Raman transition intensities in the low-frequency region of the spectrum.[62–65] As a result, VCS is a unique method of observing excited-state structural dynamics immediately following photoexcitation, as

it involves simultaneous excitation to two different vibrational states, creating a vibrational coherence that is observed as an oscillation in the absorption/emission intensity at a frequency that is the difference between their excitation frequencies.[210–213] These coherent oscillations provide valuable insight into the structural evolution of the molecule along the excited-state potential energy surface (PES), as well as information on how the Franck-Condon (FC) overlap of the wavefunctions involved in the electronic excitation/emission changes due to the excited-state nuclear dynamics.

In this chapter, we study the excited-state dynamics of 2,5-diphenylthiophene (DPT) following $S_1 \leftarrow S_0$ excitation at 310 nm. The TA of DPT has been previously investigated, where it was observed that the initial dynamics in the S_1 state include structural relaxation into a planar conformation (as a result of π-π^* excitation) and vibrational cooling that occur on the order of $\sim$15 ps, followed by intersystem crossing (ISC) with a lifetime of 270 ± 7 ps into a long-lived triplet state.[52,53] The resonance-enhanced FSRS spectrum of the S_1 state of DPT has also been measured,[52] and the resonance condition was investigated in detail by observing the FSRS spectrum as a function of Raman excitation frequency across the main $S_N \leftarrow S_1$ excited-state absorption (ESA) band.[53] The Raman excitation profiles indicated strong resonance enhancement contributions from a single electronic transition at 566 nm, with possible contributions from a second, lower-energy electronic transition centered between 570-580 nm. In other words, the FSRS measurements suggested the presence of two electronic transitions within the singlet ESA band that had not been distinguished through TA measurements alone.

Additionally, a strong, characteristic quantum beating pattern of ~ 105 cm^{-1} was observed within the first few ps in the $S_N \leftarrow S_1$ absorption band of the TA spectrum that has not been explored in detail. Here, we present a more in-depth analysis of the initial excited-state dynamics of the S_1 state of DPT, where we observe multiple low-frequency (>700 cm^{-1}) vibrational coherences in the TA spectrum. The experimental observations are complemented with calculations of electronic-state energy gradients along vibrational displacement coordinates, and facilitate the assignment of the observed coherences to modes with motion along the torsion coordinate as well

as the C−S bonds in the thiophene ring. This chapter is organized as follows. After introducing the experimental parameters of our setup and our computational methods in Section 9.2, we then present the observed oscillations in the TA spectrum in both the time and frequency domains in Section 9.3.1. In Section 9.3.2, we display calculated vibrational frequencies in the S_1 state, calculated PES gradients along the vibrational displacements, and electron density difference maps that provide a visual guide for the changes in the electronic structure as a result of $S_N \leftarrow S_1$ transitions. We discuss the assignments of the vibrational coherences in Section 9.4, and present our conclusions in Section 9.5.

9.2   Experimental and Computational Methods

The transient absorption measurements utilize the modified output of an amplified Ti:sapphire laser (Coherent, Legend Elite), which produces 35 fs pulses with 1 kHz repetition rate at 800 nm. The actinic pump pulse at 310 nm is generated by splitting the 800 nm output and passing it into a commercial optical parametric amplifier (OPA) with two stages of frequency conversion. The actinic pulse is then compressed via a fused-silica prism pair to 100 ± 10 fs pulse duration, estimated from the pump-probe cross-correlation signal. We generate broadband (340-750 nm) white-light continuum (WLC) fs probe pulses by focusing a small portion of the remaining 800 nm laser fundamental into a translating CaF_2 window. The pump and probe pulses overlap in the sample, a 0.5 mM solution of DPT (TCI America) in cyclohexane (spectroscopic grade, Fisher), which is flowed through a windowless liquid jet with pathlength of 300 μm. After the sample, the transmitted probe light is dispersed by a grating (300 line/mm) onto a 2068 pixel linear CCD array (Hamamatsu, S11156-2048). A synchronized optical chopper is used at 500 Hz to block every other pump pulse, allowing for time-resolved measurement of differential absorption, ΔA. To eliminate anisotropic effects, TA spectra are measured with the relative polarization of the pump and probe pulses set to "magic angle" (54.7°). Cross-phase modulation effects[85,86] are corrected for by plotting the peak intensity of the cross-correlation signal against probe wavelength, and fitting the signal to a fifth-order polynomial. The fit is then used to offset the time-dependence of

the ΔA signal measured at each wavelength.

The calculations are performed with both time-dependent density functional theory (TD-DFT) and equation of motion coupled cluster theory with single and double excitations (EOM-CCSD).[147] For comparison with results from our previous work,[52,53] the calculated equilibrium structures of the S_0 and S_1 states, as well as the S_1 normal modes, are obtained using TD-B3LYP/aug-cc-pVDZ.[110,111,113] Calculated vibrational frequencies are scaled by an appropriate empirical factor of 0.970.[116] This level of theory is then used to calculate gradients of the potential energy surface of the S_1 state, ∇_1,

$$\nabla_1 = \left(\frac{\partial V_1}{\partial q_k^{S_1}} \right) \tag{9.1}$$

where V_1 is the potential energy of the S_1 state, and $q_k^{S_1}$ are the mass-weighted displacement coordinates of the normal mode vibrations calculated for the S_1 state. Due to the steric strain between the thiophene and phenyl rings, there are two energetic minima in the S_0 state of DPT, corresponding to parallel (C_s symmetry) and anti-parallel (C_2) orientations of the phenyl rings relative to each other. Therefore, the TD-DFT gradients of the S_1 state are calculated at each of the $S_1 \leftarrow S_0$ Franck-Condon (FC) geometries.

However, it has been shown that, for $S_N \leftarrow S_1$ transitions, TD-DFT does not provide an accurate representation of the higher-lying S_N electronic states in DPT, which can have up to $\sim$25% double excitation character.[53] Instead, we calculate gradients of the PES of S_N states with EOM-CCSD and, due to computational cost, we use the 6-31G(d) basis set.[214,215] Our work in Chapter 5 showed that S_N gradients calculated with EOM-CCSD/6-31G(d) were more successful in reproducing $S_N \leftarrow S_1$ transition energies and electronic resonance effects in higher-lying states than gradients calculated with TD-B3LYP/aug-cc-pVDZ. Therefore, we also use EOM-CCSD/6-31G(d) to calculate the S_1 equilibrium geometry, normal mode displacements, the $S_N \leftarrow S_1$ oscillator strengths, and the gradients along S_N states, ∇_N,

$$\nabla_N = \left(\frac{\partial V_N}{\partial q_k^{S_1}} \right) \tag{9.2}$$

where V_N is the energy of the S_N state, and ∇_N is calculated at the $S_N \leftarrow S_1$ FC geometry. The main electronic transitions of the experimental ESA band have been assigned as excitations to the S_5 and, possibly, S_4 states.[53] We visualize the electron density difference maps for these two $S_N \leftarrow S_1$ transitions, which are reproduced from our work in Chapter 5, and include energy gradients calculated at the S_1 equilibrium geometry for selected vibrational displacements along the S_4 and S_5 potentials. All calculations were performed using a development version of the GAUSSIAN software package.[78]

9.3 Results and Analysis

9.3.1 Excited-State Dynamics

The evolution of the transient absorption spectrum of DPT is shown in Figure 9.1. At early time delays, the excited-state singlet absorption spectrum appears as an intense band centered at 566 nm, with a weaker stimulated emission band at 391 nm. The excited-state absorption (ESA) and stimulated emission (SE) bands decay with the same time constant of 270 ps as the molecule undergoes ISC to the triplet state, which appears as a relatively weak absorption band centered around 430 nm. For comparison with calculations, we include Figure 9.2, which has been reproduced
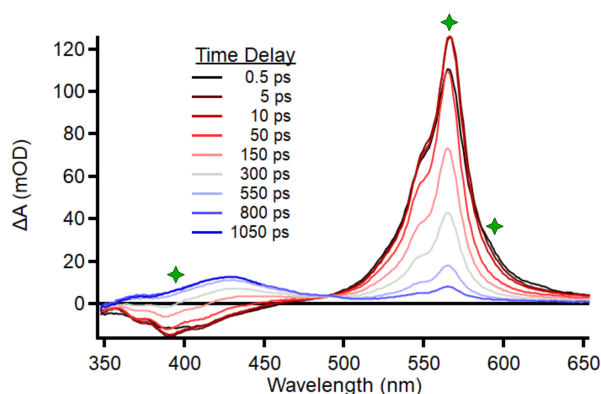

Figure 9.1: Transient absorption spectrum of DPT in cyclohexane at 310 nm excitation. Green markers at 396, 566, and 589 nm indicate the probe wavelengths at which the coherent oscillations are observed.

here from our work in Chapter 5 of this dissertation. Figure 9.2 displays the calculated oscillator

strengths for the $S_N \leftarrow S_1$ transitions with 0.25 eV Gaussian broadening. As determined through
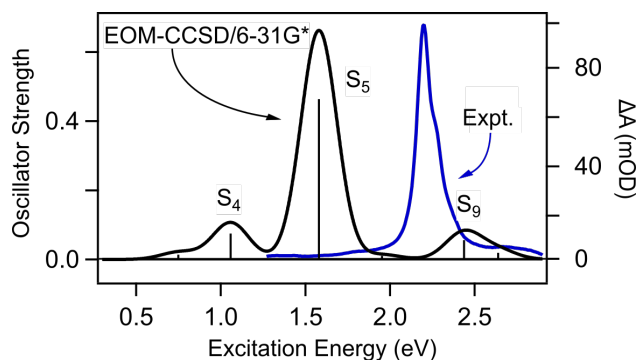

Figure 9.2: Calculated $S_N \leftarrow S_1$ absorption spectrum of DPT (black) and experimental TA spectrum (blue) at a time delay of 30 ps.

the electronic resonance contributions to the FSRS spectra in our previous study, the intense peak of the experimental ESA band is attributed as an excitation to the S_5 state, while the weak signal around ∼600 nm is possibly from the transition to S_4. Although the calculated transition energies are roughly ∼0.6 eV lower than those observed in the experiment, the spectrum simulated with EOM-CCSD gives a qualitatively accurate representation of the $S_N \leftarrow S_1$ transitions.

While not visible in Figure 9.1, there are time-dependent oscillations of the TA spectrum that are observed within the first few ps at multiple probe wavelengths. Figure 9.3(a) displays the transient absorption signal in the time domain for the peak absorbance wavelength in the ESA band. In order to analyze the quantum beating frequencies, we isolate the oscillations in ΔA by fitting the background absorption signal to a double exponential function, and subtract that fit from the differential absorption signal to obtain the residual beating pattern in Figure 9.3(b). The same procedure is applied to the TA spectrum at every probe wavelength, and the time-dependent oscillations are converted to the frequency domain using a Fast Fourier Transform (FFT). Figure 9.4 displays the Fourier-transformed TA spectrum as a two-dimensional plot of the frequency-domain oscillations at each probe wavelength. Other than the consistent, low-frequency fluctuations of 1-6 cm^{-1}, which are possibly an artifact of the baseline fit due to laser drift, Figure 9.4 shows that there are oscillations at multiple probe wavelengths which have relatively large amplitude compared to the rest of the transformed signal at that wavelength. The most distinguishable oscillations have
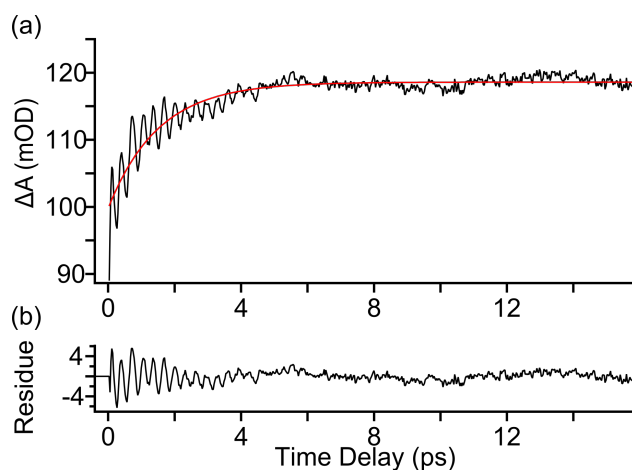
Figure 9.3: Coherent oscillations in the TA spectrum observed at 566 nm. The time-dependent ΔA signal (a) is fit to a double- exponential function (red), and the oscillations are isolated in panel (b) by subtracting the fit from the differential absorption signal.
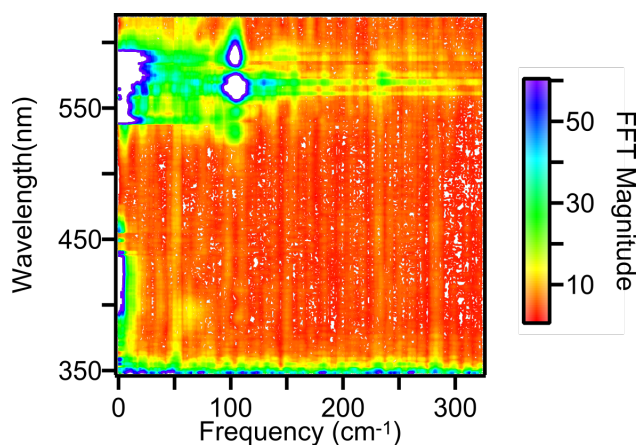
Figure 9.4: Time-dependent oscillations in the TA spectrum transformed into the frequency domain for each probe wavelength. The upper limit of the frequency domain is 324 cm^{-1}, based on the time-resolution of the actinic pump pulse.

peak amplitudes centered around 566 and 589 nm in the ESA band, and a third centered around 396 nm in the SE band.

These three oscillations are examined in more detail in Figure 9.5, which displays the time-dependent oscillations. As seen in Figure 9.4, the beating pattern in the SE band oscillation is of
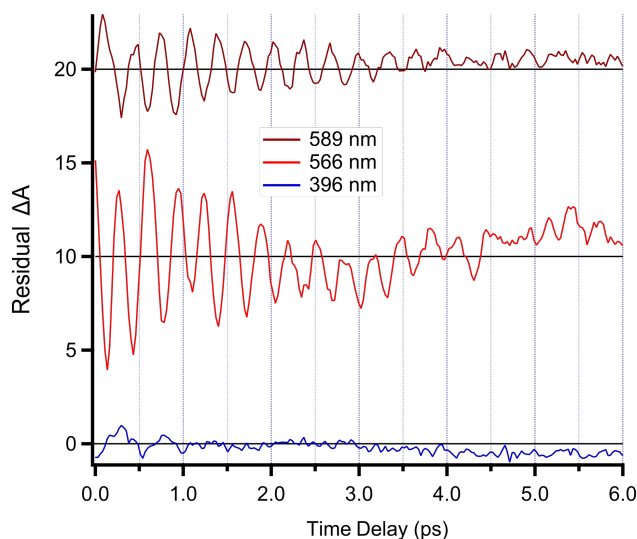
Figure 9.5: Time-dependent oscillations observed at each probe excitation wavelength. Dotted lines are included for visual comparison.

relatively low frequency compared to the others, and decays within ∼1 ps after excitation, while the two oscillations in the ESA band are of roughly twice the frequency of that in the SE band, and decay within ∼5 ps. The oscillations in the ESA band appear to be of the same frequency, however, they oscillate with opposite phase, where the peak amplitudes in the 566 nm trace coincide directly with the troughs in the 589 nm absorption. The frequencies of the oscillations in the ESA band are 104 and 105 cm$^{-1}$ for absorption at 589 and 566 nm, respectively, and, though the rapid decay of the SE band oscillation leads to a broad band in the frequency domain, the beating pattern at 396 nm is centered around 62 cm^{-1}.

9.3.2 Calculated Vibrational Mode Analysis

The three main time-dependent oscillations in Section 9.3.1 each decay within a few ps, therefore, it is possible that they are a result of vibrational coherences in the S_1 electronic state. The coherent
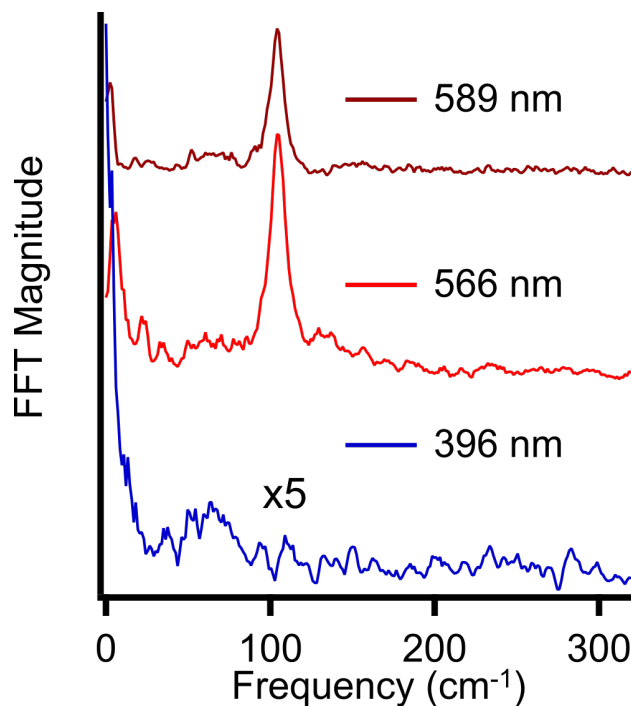
Figure 9.6: FFT of the oscillations in the TA spectrum of DPT. The peak FFT magnitude for each of the probe wavelengths of 589, 566, and 396 nm has a frequency of 104, 105, and 62 cm^{-1}.

oscillations are observed in the TA spectrum, therefore, the Franck-Condon (FC) overlaps for the electronic transitions are sensitive to the nuclear displacements that correspond to the vibrational coherences. Accordingly, we focus our analysis on the normal mode vibrations calculated for the S_1 state. Figure 9.7 displays the displacements for selected low-frequency vibrations calculated in S_1 with TD-DFT. The figure includes all vibrations with a frequency <200 cm^{-1} ($v_1 - v_7$), as well as two C$-$S stretching motions (v_{18} and v_{25}), which we have previously determined to have a large ∇_N for the higher-lying electronic states involved in the $S_N \leftarrow S_1$ transitions in DPT.[53] Thus, it is likely that vibrational displacements of these two modes will have a significant effect on the FC overlap between the S_1 and S_N states. Table 9.1 lists the vibrational motions, as well as the gradients of the S_1 state at the two $S_1 \leftarrow S_0$ FC geometries of DPT.

In order to determine the vibrational motions that have the most significant effect on the FC overlaps of the electronic transitions, it is important to examine the changes in the structure of the electronic state. The initial $S_1 \leftarrow S_0$ transition involves a $\pi - \pi^*$ transition that alters the electronic configuration to adopt a more quinoid-like character, which results in the planarization
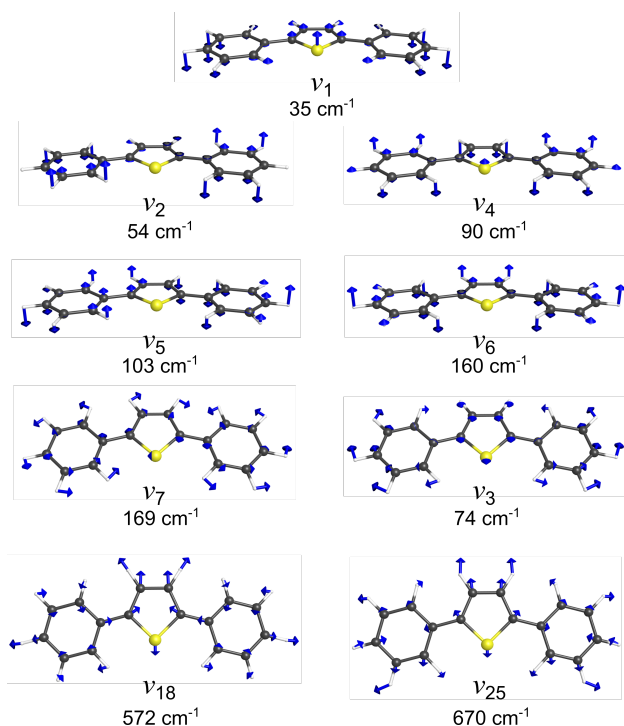
Figure 9.7: Normal mode displacements for low-frequency vibrations calculated for the S_1 state of DPT. The $v_2 - v_7$ vibrations are paired according to the anti-symmetric (left column) and symmetric (right column) combinations of specific local modes. Results are calculated with TD-B3LYP/aug-cc-pVDZ, and the frequencies have been scaled by a factor of 0.970.[116]

Table 9.1: Calculated Normal Modes (S_1) and Potential Energy Gradients

Mode	Symmetry	Freq.[a] (cm^{-1})	∇_1[b] C_s Geometry	C_2 Geometry	Motion
v_1	b_1	35	-0.29	-0.10	sym. out-of-plane inter-ring bending
v_2	a_2	54	0.38	2.11	anti-sym. inter-ring torsion
v_3	a_1	74	0.60	0.64	sym. in-plane Ph$-$C$-$S bending
v_4	b_1	90	1.37	-0.28	sym. inter-ring torsion
v_5	a_2	103	0.04	-0.05	anti-sym. inter-ring rocking
v_6	b_1	160	0.17	0.11	sym. inter-ring rocking
v_7	b_2	169	0.00	0.00	anti-sym. in-plane Ph$-$C$-$S bending
v_{18}	a_1	572	5.68	5.82	sym. C$-$S$-$C bend and phenyl distortion
v_{25}	a_1	670	4.72	4.75	sym. C$-$S$-$C stretching and phenyl distortion

[a] Frequencies are scaled by a factor of 0.970.[116]
[b] Potential energy gradients along mass-weighted displacement coordinates, reported in units of mHartree/Å·$\sqrt{amu}$.

of DPT after excitation to S_1.[47,53] However, the transitions to the S_4 and S_5 states (assigned to 589 and 566 nm excitation in the ESA band, respectively) are more complicated to determine. The electron difference density (EDD) maps in Figure 9.8 are reproduced from Chapter 5,[53] and show the change of electron density associated with the $S_N \leftarrow S_1$ transitions from the EOM-CCSD calculation. As a visual guide, the EDD maps indicate that both of the electronic transitions to
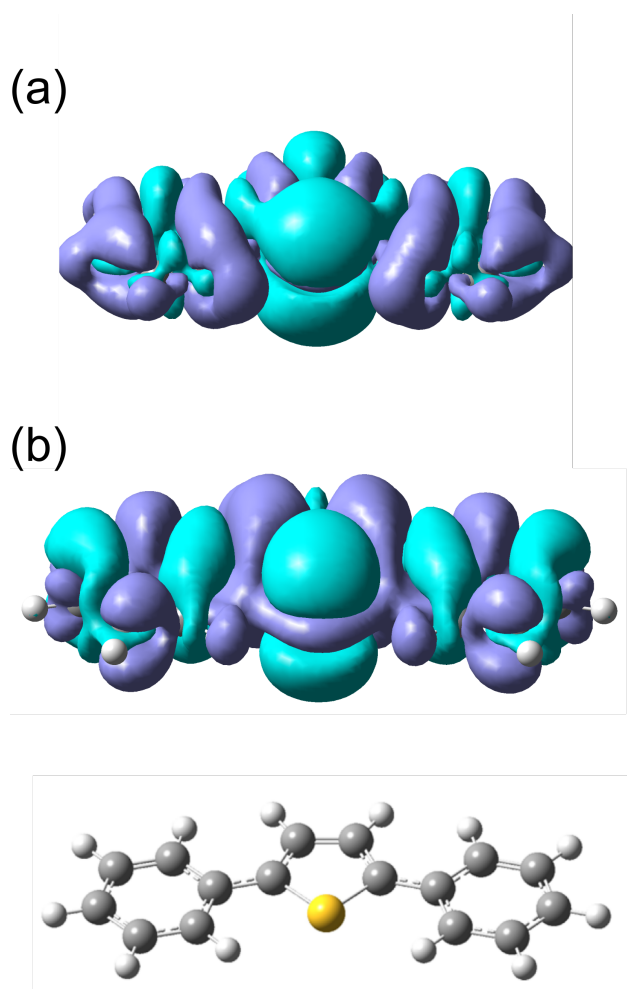
Figure 9.8: Reproduced from Chapter 5. Electron density difference maps for the (a) $S_4 \leftarrow S_1$ and (b) $S_5 \leftarrow S_1$ transitions calculated with EOM-CCSD/6-31G*. Blue indicates a decrease in density and purple indicates an increase. The ball-and-stick model shows the orientation of the molecule for visual reference.

higher-lying states involve a reduction of electron density in non-bonding sulfur orbitals and an alternation of the bonding pattern in the delocalized π electron distribution. However, the change in electron densities in the π bonding pattern is opposite for the two states, where an increase in

π electron density for a particular C atom via transition to S_4 is a reduction in the transition to S_5. The ∇_N values observed in Chapter 5[53] for the ν_{18} and ν_{25} vibrations in the S_4 and S_5 states are included in Table 9.2.

Table 9.2: Calculated S_N Potential Energy Gradients

Mode	∇_4 [a]	∇_5 [a]
ν_{18}	5.47	2.14
ν_{25}	0.48	-4.89

[a] Potential energy gradients along mass-weighted displacement coordinates, reported in units of mHartree/Å·$\sqrt{\text{amu}}$.

9.4 Discussion

The low-frequency oscillations observed in the SE and ESA bands of the TA spectrum decay within $\sim$1 and $\sim$5 ps, respectively. The decays occur on roughly the same timescale as the vibrational cooling in the absorption spectrum, and the experiment is measured at magic angle polarization conditions to eliminate anisotropy effects. Therefore, it is likely that the oscillations are indicative of vibrational coherences, rather than electronic coherence, for which the nearest electronic state transitions (to S_4 and S_5) differ in excitation energy by about 690 cm^{-1}.

The gradient values at the vertical excitation geometries provide insight into the vibrations that may be responsible for the observed coherences. The coherences decay soon after the actinic excitation, therefore, the initial excited-state nuclear dynamics along S_1 are expected to involve FC-active modes that have a large ∇_1 value at the FC geometries of the $S_1 \leftarrow S_0$ transition. Accordingly, a relatively large ∇_1 suggests a vibrationally excited population in the S_1 state for these modes, which indicates that they may be responsible for the observed vibrational coherences.

Additionally, the oscillations are observed in the TA signal, meaning that the change in absorption is most sensitive to the S_1 nuclear displacements that affect the FC overlap with the final electronic state (S_0 in the SE band, and S_4 or S_5 in the ESA band). Similarly, these FC-active vibrations will have relatively large gradients along the final state PES (∇_0, ∇_4, or ∇_5) at the $S_0 \leftarrow$

S_1 or $S_N \leftarrow S_1$ FC geometries, since displacement along these coordinates will produce significant changes to the FC overlap. The gradients along the S_0 state (∇_0) at the S_1 equilibrium geometry were not calculated directly, however, the ∇_1 values in Table 9.1 indicate that there is a large displacement along the coordinates of both torsional vibrations between the S_1 minimum geometry and either of the S_0 minima, which is supported by the fact that DPT planarizes after $S_1 \leftarrow S_0$ excitation.[47,216] Thus, the vibrational coherence that is observed in the stimulated emission band is relatively straightforward to assign as a torsional motion. Based on the calculated frequencies of the S_1 normal modes, as well as the fact that the ∇_1 value for ν_2 at the C_2 geometry of the S_0 state is slightly larger than the ∇_1 for ν_4 at the C_s geometry, the beating pattern observed in the SE band is tentatively identified as a vibrational coherence between excited vibrational energy levels of the anti-symmetric torsion mode. Although it is not immediately clear why nuclear displacement along ν_2 should be favored over ν_4, the broad frequency band in Figure 9.6 for the oscillation at 396 nm (which is a result of the relatively short dephasing time) may include contributions from both vibrations. Nevertheless, the ∇_1 values were only calculated at the S_0 minima, therefore, as the molecule evolves along S_1 and planarizes due to the quinoid-like C=C bonds between the aryl substituents, it is likely that there is more steric strain along the symmetric torsion coordinate that makes it less favorable than the anti-symmetric mode.

The ESA band coherences are less straightforward to identify, as the vibration that most closely matches the oscillation frequency is the anti-symmetric rocking motion, ν_5, which involves significant out-of-plane displacement and has a particularly small ∇_1. Given that vibrational coherences oscillate at the difference frequency between any two populated vibrational states,[210–213] the observed frequency could be a result of simultaneously populating vibrational levels in two separate modes. However, there are multiple pairs of vibrations in DPT with relatively large ∇_1 and frequencies that differ by $\sim$90-120 cm^{-1}. Thus, the ∇_N values can be used to further narrow the list of candidates. Furthermore, the EDD maps serve as a visual guide for identifying which motions are expected to have large ∇_4 and ∇_5. Accordingly, a coherence will most likely occur in vibrations that not only have large values for ∇_1 and ∇_N, but involve significant distortion of the electron den-

sity around the sulfur atom and in the π-conjugation of the phenyl rings. The two modes that fit all these criteria are ν_{18} and ν_{25}, which not only have relatively large ∇_N in Table 9.2, but the largest of these two gradients in S_4 has a slope that is in the opposite direction of the larger gradient in S_5. This relationship indicates that, as the molecule undergoes nuclear displacements that are a result of the combined excitation of ν_{18} and ν_{25}, the FC overlap for the $S_4 \leftarrow S_1$ transition will increase as the overlap for the $S_5 \leftarrow S_1$ transition decreases. Figures 9.7 and 9.8 are useful in visualizing this concept. Not only do ν_{18} and ν_{25} both have significant C$-$S stretching motions, but, as seen in Figure 9.7, the distortion of the phenyl rings in ν_{18} is in-phase with the C$-$S stretching while the same phenyl distortion in ν_{25} is out-of-phase with the thiophene motion. Therefore, the combined nuclear motion of ν_{18} and ν_{25}, which oscillates within the two-dimensional well of the S_1 potential at a frequency of $\sim$105 cm^{-1}, has the net effect of reducing the FC overlap with the wavefunction of one state while simultaneously increasing overlap with the other.

9.5   Conclusions

In this chapter, we have utilized calculations of vibrational frequencies and potential energy gradients along characteristic nuclear displacements in order to identify vibrational coherences that are present in the excited-state dynamics of DPT immediately following $S_1 \leftarrow S_0$ photoexcitation. Based on the Fourier-transforms of the time-dependent signals in the TA spectrum, the coherent oscillation observed in the SE band is directly attributed to a coherence between vibrational overtones of a torsional mode. This method of assignment is well-documented in VCS measurements, however, the low-frequency oscillations observed in the ESA band were instead assigned to a coherence between vibrational levels in two separate modes. Thus, the combination of experimental and computational methods to investigate the $S_N \leftarrow S_1$ electronic resonance condition in Chapter 5 provided invaluable information on the electronic transitions in DPT, allowing for a more complete physical interpretation of the excited-state dynamics. Future work will likely involve computational confirmation of these vibrational coherence assignments through simulations of wavepacket dynamics in the S_1 state of DPT.

Chapter 10

Summary and Future Directions

In this dissertation, we have used a combination of electronic structure calculations and experimental measurements to obtain a comprehensive understanding of Raman spectroscopic techniques and the information they provide on the physical properties of molecules. Focusing on excited-state vibrations observed through resonance-enhanced femtosecond stimulated Raman spectroscopy (FSRS) measurements, our goals have been to use calculations of excited-state polarizabilities and electronic state transitions to interpret the experiment, while also using the experimental results to help benchmark the computational methods and highlight limitations that are necessary to consider when comparing the two approaches. In addition to developing the analysis of transient Raman techniques, the combination of both experimental and theoretical approaches provides valuable insight into the dynamics of molecules in the excited state. Using conjugated thiophene derivatives as model systems, we have shown that studying the electronic resonance conditions and the effects of conjugation on the polarizability of these compounds provides a more complete understanding of the behavior of molecules following photoexcitation than can be obtained with either approach alone.

Our first step toward interpreting the resonance-enhanced FSRS spectra was the assignment of experimentally observed Raman bands to calculated vibrational modes in the electronically excited state. We utilized time-dependent density functional theory (TD-DFT) to calculate off-resonance excited-state Raman spectra for a series of aryl-substituted thiophene derivatives in both the singlet (S_1) and triplet (T_1) excited states.[52] The resonance enhancement is vibrational mode-specific, and Raman transitions with the largest enhancement have significant nuclear displacements along the potential energy surface (PES) of the resonant higher-lying electronic state. Based on this res-

157

onance condition, it was shown in Chapter 4 that relatively inexpensive calculations, which do not explicitly model the enhancements, can be used to assign the FSRS bands to specific vibrational modes on the basis of vibrational symmetry, as well as the consideration of the resonant electronic transition from the excited (π, π^*) state of the conjugated molecule to a higher-lying electronic state. Our vibrational assignments were supported by comparisons between molecules in the benchmark series with similar structure, which further highlighted the necessity of considering the resonance condition when assigning vibrations to resonance-enhanced Raman bands, as there can be significant mode-specific enhancement of Raman transitions that are relatively weak in the off-resonance calculations.

The excited-state vibrational assignments are further supported by simulations of the resonance-enhanced Raman spectra, in which we directly calculated the gradient of the PES of the resonant electronic state along the vibrational displacement coordinates. In Chapter 5, we explored the resonance enhancements for Raman transitions in the S_1 state of 2,5-diphenylthiophene (DPT) in more detail by measuring the FSRS spectrum at different Raman excitation wavelengths across the profile of the excited-state absorption (ESA) band, and compared the excitation profile with simulations of resonance Raman spectra for $S_N \leftarrow S_1$ transitions which may be resonant with the Raman excitation frequency.[53] Based on the Raman excitation profiles of the FSRS spectra and the resonance Raman spectra simulated using equation of motion coupled cluster theory with single and double excitations (EOM-CCSD), it was found that the strongest bands in the FSRS spectrum can be reproduced from the contributions of resonant electronic transitions to two S_N states: a strong transition to a state that mainly enhances low-frequency (500-700 cm^{-1}) C$-$S stretching vibrations, and a weaker transition to a neighboring state that mainly enhances high-frequency (1400-1600 cm^{-1}) C$=$C stretching vibrations. Therefore, the simulated Raman spectra are instrumental in the identification of the resonant electronic states, and provide valuable insight into the interpretation of the experimental FSRS spectrum of the S_1 state.

However, the resonance enhancements in the triplet electronic states of the aryl-substituted thiophenes are more complicated. In Chapter 6, we performed FSRS measurements at different

Raman excitation energies along the profile of the ESA band in the T_1 state of 2-phenylthiophene (PT), and compared the experimental spectra to simulated resonance Raman spectra using both TD-DFT and EOM-CCSD.[54] Although the simulated spectra have several features that agree well with the experiment, there are important discrepancies in the relative Raman intensities of both DFT and CCSD methods, and the FSRS spectra are consistently in better agreement with the calculated off-resonance spectra, which suggests a weaker mode-specific resonance enhancement than is observed in the S_1 state. Comparisons of the broadening in the triplet ESA spectrum relative to that of the S_1 state revealed that the presence of multiple nearby $T_N \leftarrow T_1$ transitions leads to significantly more homogeneous broadening, possibly due to vibronic coupling between higher-lying triplet states, which results in an overall reduction of mode-specific enhancements. Therefore, while the simulated Raman spectra still provide valuable insight for the interpretation of the FSRS measurements, the experiments also help benchmark the accuracy of the calculations.

On a more fundamental level, the delocalized π conjugation of aromatic thienyl- and phenyl-based compounds has a significant effect on the molecular polarizability,[28] and, hence, on the Raman spectra in general.[29,30] In Chapter 7, we compared calculations of ground-state Raman spectra for a series of benzene and thiophene compounds with aryl substituents. The calculations were performed using a set of DFT functionals and the second-order Møller-Plesset perturbation theory (MP2) method, and we benchmarked the accuracy of the calculated Raman intensities with experimental measurements of spontaneous Raman spectra. It was found that, although the simulated Raman spectra are generally in good agreement with experiment, the calculations tended to overestimate the relative Raman intensities of higher-frequency vibrations (1400-1600 cm^{-1}) compared to those of lower-frequency bands. This discrepancy between calculated and experimental relative Raman intensities is consistent for all methods, and especially noticeable in the Raman spectra of molecules with multiple aryl rings, such as biphenyl (BP), PT, 2-methyl-5-phenylthiophene (MPT), and DPT.[55] While the mean unsigned errors (MUE) in relative Raman intensities were roughly similar across methods, B3LYP and TPSSh had $\sim$11%-19% and $\sim$5%-14% smaller MUE values than the remaining methods.[55]

This overestimation of calculated Raman intensities in high-frequency bands was explored further by examining the effects of anharmonicity and inter-ring torsion on the Raman spectrum. Our work in Chapter 8 compared the ground-state experimental Raman spectra of BP, PT, and 2,2-bithiophene (BT) with anharmonic corrections to the calculated Raman intensities, as well as the calculated Raman spectra at different inter-ring dihedral angles.[56] Although the anharmonic corrections provide, on average, 12-15% better agreement with experimental intensities, the relative Raman intensities are still overestimated for higher-frequency (>1200 cm^{-1}) vibrations. However, the Raman spectra calculated at various dihedral angles showed that the absolute Raman intensities of the higher-frequency bands, which involve distortion of the bridging $C-C$ bond, were substantially reduced as the dihedral angle increases and breaks the ring-ring conjugation, whereas the lower-frequency (<1200 cm^{-1}) vibrations were generally less sensitive. This resulted in significantly better agreement between the experimental and calculated relative intensities for the majority of Raman bands at dihedral angles of $\sim70°$ in all three molecules. This provides valuable insight into the cause of the discrepancy between calculated relative intensities and experiment, and it was concluded that the DFT results are likely overestimating the strength of the inter-ring conjugation, predicting equilibrium structures that are too planar compared to what is observed in the experiment. Future efforts toward the accurate prediction of calculated Raman spectra for molecules with delocalized π conjugation would involve similar investigation of the Raman intensities along the internal coordinate of other low-frequency motions that break conjugation, such as the $Ph-C-C$ bending along the inter-ring bond. Given that the anharmonic corrections to the Raman intensities at the DFT level provided a noticeable increase in the agreement of the relative intensities, another future direction could include an optimization of the equilibrium structure using anharmonic force constants, which may obtain a more accurate minimum energy structure.

Our comparisons between calculated and experimental Raman spectra in both ground and excited states offered comprehensive insights into the potential energy gradients of the states involved in electronic transitions, which become very useful when interpreting excited-state dynamics. This was demonstrated in our work from Chapter 9, which studied the excited-state dynamics in DPT

immediately following $S_1 \leftarrow S_0$ photoexcitation. The TA spectrum of DPT shows two major quantum beating patterns in the differential absorption of the $S_N \leftarrow S_1$ ESA band, and a third located in the $S_0 \leftarrow S_1$ stimulated emission (SE) band. The oscillations were attributed to vibrational coherences in the S_1 state of DPT that alter the Franck-Condon overlap with the resonant electronic S_N or S_0 states. Using DFT calculations of the S_1 vibrations, the oscillation in the SE band was straightforward to assign as a coherence between vibrational overtones of the same torsional mode. However, based on our work from Chapter 5 characterizing the resonance-enhancement condition for the excited-state transitions in DPT, we were able to identify both of the beating patterns in the ESA band as a coherence between vibrational states of two different modes, which oscillates at a frequency that is the difference between the vibrational frequencies of the two modes. Thus, the comparisons between calculated and experimental excited-state Raman spectra provided invaluable information on the electronic transitions in DPT, allowing for a more complete physical interpretation of the excited-state dynamics of this molecule. Future work confirming the assignments of the vibrational coherences would involve modeling the structural evolution of the time-dependent wavepacket along the S_1 PES. Additionally, further determination of the initial dynamics of DPT may be obtained by reducing the pulsewidth of the actinic pump pulse toward the sub-10 fs level, increasing the time resolution of the transient absorption measurement and observing higher-frequency oscillations in the absorption spectrum.

In addition to giving specific insights into the behavior of the electronic and molecular structures of the molecules studied, our computational and experimental studies of Raman scattering provide significant contributions to the detailed analysis of excited-state resonance Raman spectra. While our work serves as a foundation on which researchers may utilize relatively inexpensive calculations to interpret the vibrational and electronic properties of molecules, additional efforts are necessary to accurately predict FSRS measurements. Although the simulations of resonance-enhanced Raman spectra appear to be successful in reproducing the mode-specific enhancements for low-frequency (500-800 cm^{-1}) and high-frequency Raman transitions (1400-1600 cm^{-1}), the simulated intensities for the intermediate frequency region between 800 and 1400 cm^{-1} still do

not reproduce the bands in the experiment. This may be due to the fact that the gradient approximation is most valid for A term scattering. Therefore, the calculated resonance Raman intensities are expected to be more accurate for vibrations with large gradients along the resonant state potential. For the thiophene derivatives, these are the C−S, C−C, and C=C stretching vibrations within the low- and high-frequency regions. On the other hand, the intensities are less accurate for vibrations like the C−H bending modes between 1100-1300 cm^{-1}. The gradient approximation also does not include vibronic coupling between electronic states, which can play a significant role in FSRS measurements, which typically involve resonant transitions to higher-lying states that are closely spaced and are more likely to have contributions from multiple states in the transient Raman spectrum. Thus, more accurate simulations of resonance-enhanced Raman intensities will require calculation of Herzberg-Teller vibronic coupling between electronic states, which will account for contributions from B and C term Raman scattering. However, the methods currently available for simulating Herzberg-Teller coupling effects on the resonance Raman spectrum rely on the overlap between harmonic vibrational wavefunctions at the equilibrium structure of the resonant electronic state, for which the harmonic approximation breaks down considerably when extrapolating to the Franck-Condon (FC) geometry.[54] Future work in detailing the effects of multiple state resonance on the FSRS spectrum would involve calculations of the vibronic coupling at the FC geometry for the vertical excitation to higher-lying states. In addition to a more accurate reproduction of the excited-state resonance Raman spectrum, these calculations would determine whether or not the coupling provides a substantial contribution to the homogeneous broadening of the TA spectrum, which ultimately provides a better understanding of the ways in which multiple electronic state transitions affect the dynamics observed for excited-state molecules.

It is also possible to measure the vibronic coupling between resonant transitions experimentally, using two-dimensional electronic-vibrational (2D EV) spectroscopy,[217] a coherent four-wave mixing technique that uses electronically resonant and vibrationally resonant transitions to elucidate couplings between electronic and vibrational degrees of freedom.[218] Comparisons between the 2D EV results and the calculated vibronic couplings will not only lead to a better understanding of

the advantages and limitations of the experimental and computational techniques, as we have seen in our work comparing FSRS with simulated Raman spectra, but the results will also provide a more detailed picture of the energy transfer dynamics observed for molecules in the excited state. Future developments in the measurement and analysis of FSRS and 2D EV spectra are expected to equip researchers with the tools necessary to map the topography of the multiple electronic state potential energy surfaces involved in complex photochemical reactions.

In addition to the vibrational dynamics along the initial excited state, our work will assist resonance-enhanced FSRS measurements in determining information about the nuclear dynamics along the PES of the resonant states involved in subsequent electronic transitions. The Raman bands with the strongest enhancements can identify the nuclear vibrations that will have the largest displacement along the potential energy surface of the resonant electronic state, and, therefore, allow for the tentative prediction of how the structure of the molecule will evolve, following a secondary excitation to that state. With complementary information on the coupling between electronic and vibrational transitions, obtained through both theoretical calculations and future 2D EV measurements, it may be possible to selectively induce nuclear motion along a desired reaction coordinate by exciting the molecule to an electronic state with a large gradient along that coordinate.[7] Therefore, utilizing both experimental and computational techniques to fully understand the potential energy surfaces and interactions of multiple electronic states will allow for more specific photochemical control of reaction yields, helping to guide the efficient formation of specific reaction products for use in material applications, and offering even more detailed information on the excited-state electronic and nuclear dynamics of molecules.

163

References

[1] Habibi, M. H.; Esfahani, M. N.; Egerton, T. A. Photochemical Characterization and Photocatalytic Properties of a Nanostructure CompositeTiO2Film. *Int. J. Photoenergy* **2007**, *2007*, 1–8.

[2] Martins, T. D.; Ribeiro, A. C. C.; de Souza, G. A.; de Sousa Cordeiro, D.; Silva, R. M.; Colmati, F.; de Lima, R. B.; Aguiar, L. F.; Carvalho, L. L.; dos Reis, R. G. C. S.; dos Santos, W. D. C. *Advanced Chemical Kinetics*; InTech, 2018.

[3] Crim, F. F. Bond-Selected Chemistry: Vibrational State Control of Photodissociation and Bimolecular Reaction. *J. Phys. Chem.* **1996**, *100*, 12725–12734.

[4] Elles, C. G.; Cox, M. J.; Crim, F. F. Vibrational Relaxation of CH$_3$I in the Gas Phase and in Solution. *J. Chem. Phys.* **2004**, *120*, 6973–6979.

[5] Crim, F. F. Chemical Dynamics of Vibrationally Excited Molecules: Controlling Reactions in Gases and on Surfaces. *P. Natl. Acad. Sci. USA* **2008**, *105*, 12654–12661.

[6] Feringa, B. L. The Art of Building Small: From Molecular Switches to Molecular Motors. *J. Org. Chem.* **2007**, *72*, 6635–6652.

[7] Ward, C. L.; Elles, C. G. Controlling the Excited-State Reaction Dynamics of a Photochromic Molecular Switch with Sequential Two-Photon Excitation. *J. Phys. Chem. Lett.* **2012**, *3*, 2995–3000.

[8] Ward, C. L.; Elles, C. G. Cycloreversion Dynamics of a Photochromic Molecular Switch via One-Photon and Sequential Two-Photon Excitation. *J. Phys. Chem. A* **2014**, *118*, 10011–10019.

[9] Huang, C.-W.; You, X.; Diemer, P. J.; Petty, A. J.; Anthony, J. E.; Jurchescu, O. D.; Atkin, J. M. Micro-Raman Imaging of Isomeric Segregation in Small-Molecule Organic Semiconductors. *Commun. Chem.* **2019**, *2*.

[10] Wood, S.; Hollis, J. R.; Kim, J.-S. Raman Spectroscopy as an Advanced Structural Nanoprobe for Conjugated Molecular Semiconductors. *J. Phys. D Appl. Phys.* **2017**, *50*, 073001.

[11] Castiglioni, C.; Tommasini, M.; Zerbi, G. Raman Spectroscopy of Polyconjugated Molecules and Materials: Confinement Effect in One and Two Dimensions. *Philos. T. Roy. Soc. A* **2004**, *362*, 2425–2459.

[12] Tao, S.; Yu, L.-J.; Pang, R.; Huang, Y.-F.; Wu, D.-Y.; Tian, Z.-Q. Binding Interaction and Raman Spectra of p-π Conjugated Molecules Containing CH2/NH2 Groups Adsorbed on Silver Surfaces: A DFT Study of Wagging Modes. *J. Phys. Chem. C* **2013**, *117*, 18891–18903.

[13] Palafox, M. A.; Rastogi, V. K.; Vats, J. K. 4-Aminobenzonitrile: ab initio calculations, FTIR and Raman spectra. *J. Raman Spectrosc.* **2006**, *37*, 85–99.

[14] Gorski, A.; Gawinkowski, S.; Herbich, J.; Krauss, O.; Brutschy, B.; Thummel, R. P.; Waluk, J. 1H-Pyrrolo[3,2-h]quinoline: A Benchmark Molecule for Reliable Calculations of Vibrational Frequencies, IR Intensities, and Raman Activities. *J. Phys. Chem. A* **2012**, *116*, 11973–11986.

[15] Halls, M. D.; Schlegel, H. B. Comparison study of the prediction of Raman intensities using electronic structure methods. *J. Chem. Phys.* **1999**, *111*, 8819.

[16] Neugebauer, J.; Reiher, M.; Hess, B. A. Coupled-cluster Raman intensities: Assessment and comparison with multiconfiguration and density functional methods. *J. Chem. Phys.* **2002**, *117*, 8623.

[17] Jiménez-Hoyos, C. A.; Janesko, B. G.; Scuseria, G. E. Evaluation of range-separated hybrid density functionals for the prediction of vibrational frequencies, infrared intensities, and Raman activities. *Phys. Chem. Chem. Phys.* **2008**, *10*, 6621.

[18] Rappoport, D.; Furche, F. Lagrangian approach to molecular vibrational Raman intensities using time-dependent hybrid density functional theory. *J. Chem. Phys.* **2007**, *126*, 201104.

[19] Cheeseman, J. R.; Frisch, M. J. Basis Set Dependence of Vibrational Raman and Raman Optical Activity Intensities. *J. Chem. Theory Comput.* **2011**, *7*, 3323.

[20] Zvereva, E. E.; Shagidullin, A. R.; Katsyuba, S. A. Ab Initio and DFT Predictions of Infrared Intensities and Raman Activities. *J. Phys. Chem. A* **2011**, *115*, 63–69.

[21] Bielecki, J.; Lipiec, E. Basis set dependence using DFT/B3LYP calculations to model the Raman spectrum of thymine. *J. Bioinform. Comput. Biol.* **2016**, *14*, 1650002.

[22] McCamant, D. W.; Kukura, P.; Mathies, R. A. Femtosecond Time-resolved Stimulated Raman Spectroscopy: Application to the Ultrafast Internal Conversion in β-Carotene. *J. Phys. Chem. A* **2003**, *107*, 8208–8214.

[23] Lee, S. Y.; Zhang, D. H.; McCamant, D. W.; Kukura, P.; Mathies, R. A. A Theory of Femtosecond Stimulated Raman Spectroscopy. *J. Chem. Phys.* **2004**, *121*, 3632–3642.

[24] Kukura, P.; McCamant, D. W.; Mathies, R. A. Femtosecond Stimulated Raman Spectroscopy. *Annu. Rev. Phys. Chem.* **2007**, *58*, 461–488.

[25] Lee, S. Y.; Heller, E. J. Time-dependent Theory of Raman Scattering. *J. Chem. Phys.* **1979**, *71*, 4777–4788.

[26] Shin, K. K.; Zink, J. I. Quantitative Evaluation of the Relationships Between Excited-state Geometry and the Intensities of Fundamentals, Overtones, and Combination Bands in Resonance Raman Spectra. *Inorg. Chem.* **1989**, *28*, 4358–4366.

[27] Myers, A. B. 'Time-dependent' Resonance Raman Theory. *J. Raman Spectrosc.* **1997**, *28*, 389–401.

[28] Rumi, M.; Zerbi, G. Conformational dependence of vibrational and molecular nonlinear optical properties in substituted benzenes: the role of π-electron conjugation and back-donation. *J. Mol. Struct.* **1999**, *509*, 11.

[29] Long, D. A. *The Raman Effect: A Unified Treatment of the Theory of Raman Scattering by Molecules*; Wiley: New York, 2002.

[30] Neugebauer, J.; Reiher, M.; Kind, C.; Hess, B. Quantum Chemical Calculation of Vibrational Spectra of Large Molecules - Raman and IR Spectra for Buckminsterfullerene. *J. Comp. Chem.* **2002**, *23*, 895–910.

[31] Baiardi, A.; Bloino, J.; Barone, V. A General Time-dependent Route to Resonance-Raman Spectroscopy Including Franck-Condon, Herzberg-Teller and Duschinsky Effects. *J. Chem. Phys.* **2014**, *141*, 114108.

[32] Ohno, K.; Kimura, J.; Yamakita, Y. Strong Raman activities of low frequency vibrational modes in alkylbenzenes: conformation specific – interactions between alkyl chain and benzene ring. *Chem. Phys. Lett.* **2001**, *342*, 207.

[33] Yamakita, Y.; Isogai, Y.; Ohno, K. Large Raman-scattering Activities for the Low-Frequency Modes of Substituted Benzenes: Induced Polarizability and Stereo-specific Ring-substituent Interactions. *J. Chem. Phys.* **2006**, *124*, 104301.

[34] Pontecorvo, E.; Ferrante, C.; Elles, C. G.; Scopigno, T. Structural Rearrangement Accompanying the Ultrafast Electrocyclization Reaction of a Photochromic Molecular Switch. *J. Phys. Chem. B* **2014**, *118*, 6915–6921.

[35] Tsivgoulis, G. M.; Lehn, J.-M. Multiplexing Optical Systems: Multicolor-bifluorescent-biredox Photochromic Mixtures. *Adv. Mater.* **1997**, *9*, 627–630.

[36] Shao, Y.; Yang, Y. Efficient Organic Heterojunction Photovoltaic Cells Based on Triplet Materials. *Adv. Mater.* **2005**, *17*, 2841–2844.

[37] Yost, S. R.; Hontz, E.; Yeganeh, S.; Voorhis, T. V. Triplet vs Singlet Energy Transfer in Organic Semiconductors: The Tortoise and the Hare. *J. Phys. Chem. C* **2012**, *116*, 17369–17377.

[38] Wang, C.; Angelella, M.; Doyle, S. J.; Lytwak, L. A.; Rossky, P. J.; Holliday, B. J.; Tauber, M. J. Resonance Raman Spectroscopy of the T_1 Triplet Excited State of Oligothiophenes. *J. Phys. Chem. Lett.* **2015**, *6*, 3521–3527.

[39] Gallaher, J. K.; Chen, K.; Huff, G. S.; Prasad, S. K. K.; Gordon, K. C.; Hodgkiss, J. M. Evolution of Nonmirror Image Fluorescence Spectra in Conjugated Polymers and Oligomers. *J. Phys. Chem. Lett.* **2016**, *7*, 3307–3312.

[40] Ohto, T.; Inoue, T.; Stewart, H.; Numai, Y.; Aso, Y.; Ie, Y.; Yamada, R.; Tada, H. Effects of cis–trans Conformation between Thiophene Rings on Conductance of Oligothiophenes. *J. Phys. Chem. Lett.* **2019**, 5292–5296.

[41] Yu, W. J.; Donohoo-Vallett, P. J.; Zhou, J. W.; Bragg, A. E. Ultrafast Photo-Induced Nuclear Relaxation of a Conformationally Disordered Conjugated Polymer Probed with Transient Absorption and Femtosecond Stimulated Raman Spectroscopies. *J. Chem. Phys.* **2014**, *141*.

[42] Thomas, A. K.; Brown, H. A.; Datko, B. D.; Garcia-Galvez, J. A.; Grey, J. K. Interchain Charge-Transfer States Mediate Triplet Formation in Purified Conjugated Polymer Aggregates. *J. Phys. Chem. C* **2016**, *120*, 23230–23238.

[43] Kolle, P.; Schnappinger, T.; de Vivie-Riedle, R. Deactivation Pathways of Thiophene and Oligothiophenes: Internal Conversion Versus Intersystem Crossing. *Phys. Chem. Chem. Phys.* **2016**, *18*, 7903–7915.

[44] Chosrovian, H.; Rentsch, S.; Grebner, D.; Dahm, D. U.; Birckner, E.; Naarmann, H. Time-resolved Fluorescence Studies on Thiophene Oligomers in Solution. *Synthetic Met.* **1993**, *60*, 23–26.

[45] Grebner, D.; Helbig, M.; Rentsch, S. Size-Dependent Properties of Oligothiophenes by Picosecond Time-Resolved Spectroscopy. *J. Phys. Chem.* **1995**, *99*, 16991–16998.

[46] Lap, D. V.; Grebner, D.; Rentsch, S. Femtosecond Time-Resolved Spectroscopic Studies on Thiophene Oligomers. *J. Phys. Chem. A* **1997**, *101*, 107–112.

[47] Zheldakov, I. L.; Wasylenko, J. M.; Elles, C. G. Excited-state Dynamics and Efficient Triplet Formation in Phenylthiophene Compounds. *Phys. Chem. Chem. Phys.* **2012**, *14*, 6211–6218.

[48] Zhou, J.; Yu, W.; Bragg, A. E. Structural Relaxation of Photoexcited Quaterthiophenes Probed with Vibrational Specificity. *J. Phys. Chem. Lett.* **2015**, *6*, 3496–3502.

[49] Yu, W.; Magnanelli, T. J.; Zhou, J.; Bragg, A. E. Structural Heterogeneity in the Localized Excited States of Poly(3- hexylthiophene). *J. Phys. Chem. B* **2016**, *120*, 5093–5102.

[50] Bragg, A. E.; Yu, W.; Zhou, J.; Magnanelli, T. Ultrafast Raman Spectroscopy as a Probe of Local Structure and Dynamics in Photoexcited Conjugated Materials. *J. Phys. Chem. Lett.* **2016**, *7*, 3990–4000.

[51] Batignani, G.; Pontecorvo, E.; Giovannetti, G.; Ferrante, C.; Fumero, G.; Scopigno, T. Electronic Resonances in Broadband Stimulated Raman Spectroscopy. *Sci. Rep.* **2016**, *6*, 18445.

[52] Barclay, M. S.; Quincy, T. J.; Williams-Young, D.; Caricato, M.; Elles, C. G. Assignment of Excited-State Vibrational Spectra from Resonance-Enhanced Femtosecond Stimulated Raman Scattering: Combining Experiment and Theory. *J. Phys. Chem. A* **2017**, *121*, 7937–7946.

[53] Quincy, T. J.; Barclay, M. S.; Caricato, M.; Elles, C. G. Probing Dynamics in Higher-Lying

Electronic States with Resonance-Enhanced Femtosecond Stimulated Raman Spectroscopy. *J. Phys. Chem. A* **2018**, *122*, 8308–8319.

[54] Barclay, M. S.; Caricato, M.; Elles, C. G. Femtosecond Stimulated Raman Scattering from Triplet Electronic States: Experimental and Theoretical Study of Resonance Enhancements. *J. Phys. Chem. A* **2019**, *123*, 7720–7732.

[55] Barclay, M. S.; Elles, C. G.; Caricato, M. A Benchmark Study of Ground State Raman Spectra in Conjugated Molecules. *J. Chem. Theory Comput.* **2019**, In Press. https://doi.org/10.1021/acs.jctc.9b00960.

[56] Barclay, M. S.; Elles, C. G.; Caricato, M. On the Discrepancy between Experimental and Simulated Ground-State Raman Intensities for Conjugated Phenyl and Thiophene Derivatives. *J. Phys. Chem. A* **2019**, To be submitted.

[57] Kumar, A. T. N.; Rosca, F.; Widom, A.; Champion, P. M. Investigations of amplitude and phase excitation profiles in femtosecond coherence spectroscopy. *J. Chem. Phys.* **2001**, *114*, 701.

[58] Kumar, A. T. N.; Rosca, F.; Widom, A.; Champion, P. M. Investigations of ultrafast nuclear response induced by resonant and nonresonant laser pulses. *J. Chem. Phys.* **2001**, *114*, 6795–6815.

[59] Gruia, F.; Ionascu, D.; Kubo, M.; Ye, X.; Dawson, J.; Osborne, R. L.; Sligar, S. G.; Denisov, I.; Das, A.; Poulos, T. L.; Terner, J.; Champion, P. M. Low-Frequency Dynamics ofCaldariomyces fumagoChloroperoxidase Probed by Femtosecond Coherence Spectroscopy†. *Biochemistry* **2008**, *47*, 5156–5167.

[60] Karunakaran, V.; Benabbas, A.; Youn, H.; Champion, P. M. Vibrational Coherence Spectroscopy of the Heme Domain in the CO-Sensing Transcriptional Activator CooA. *J. Am. Chem. Soc.* **2011**, *133*, 18816–18827.

[61] Buckup, T.; Motzkus, M. Multidimensional Time-Resolved Spectroscopy of Vibrational Coherence in Biopolyenes. *Annu. Rev. Phys. Chem.* **2014**, *65*, 39–57.

[62] Fujiyoshi, S.; Takeuchi, S.; Tahara, T. Time-Resolved Impulsive Stimulated Raman Scattering from Excited-State Polyatomic Molecules in Solution. *J. Phys. Chem. A* **2003**, *107*, 494–500.

[63] Cerullo, G.; Lüer, L.; Manzoni, C.; Silvestri, S. D.; Shoshana, O.; Ruhman, S. Time Domain Investigation of Excited-State Vibrational Motion in Organic Molecules by Stimulated Emission Pumping. *J. Phys. Chem. A* **2003**, *107*, 8339–8344.

[64] Turner, D. B.; Wilk, K. E.; Curmi, P. M. G.; Scholes, G. D. Comparison of Electronic and Vibrational Coherence Measured by Two-Dimensional Electronic Spectroscopy. *J. Phys. Chem. Lett.* **2011**, *2*, 1904–1911.

[65] Kuramochi, H.; Takeuchi, S.; Tahara, T. Femtosecond Time-Resolved Impulsive Stimulated Raman Spectroscopy using sub-7-fs Pulses: Apparatus and Applications. *Rev. Sci. Instrum.* **2016**, *87*, 043107.

[66] Raman, C. V. *A New Radiation*; Indian Association for the Cultivation of Science, 1927.

[67] Placzek, G. Handbuch der Radiologie VI. *Marx E.* **1934**, *2*, 290–374.

[68] Dirac, P. A. M.; Fowler, R. H. The Quantum Theory of Dispersion. *Proc. R. Soc. London* **1927**, *114*, 710.

[69] Craig, D. P.; Thirunamachandran, T. *Molecular Quantum Electrodynamics*; Dover: New York, 1998.

[70] Albrecht, A. C. On the Theory of Raman Intensities. *J. Chem. Phys.* **1961**, *34*, 1476.

[71] Heller, E. J. Wavepacket Path Integral Formulation of Semiclassical Dynamics. *Chem. Phys. Lett.* **1975**, *34*, 321–325.

[72] Heller, E. J.; Sundberg, R. L.; Tannor, D. Simple Aspects of Raman Scattering. *J. Phys. Chem.* **1982**, *86*, 1822–1833.

[73] Myers, A. B.; Mathies, R. A.; Tannor, D. J.; Heller, E. J. Excited State Geometry Changes from Preresonance Raman Intensities: Isoprene and Hexatriene. *J. Chem. Phys.* **1982**, *77*, 3857–3866.

[74] Albrecht, A. C. Theory of Raman Intensities. *J. Chem. Phys.* **1961**, *34*, 1476.

[75] Silverstein, D. W.; Jensen, L. Vibronic Coupling Simulations for Linear and Nonlinear Optical Processes: Simulation Results. *J. Chem. Phys.* **2012**, *136*, 064110.

[76] Guthmuller, J. The Role of Herzberg-Teller Effects on the Resonance Raman Spectrum of trans-Porphycene Investigated by Time Dependent Density Functional Theory. *J. Chem. Phys.* **2018**, *148*, 124107.

[77] Albrecht, A. C.; Hutley, M. C. On the Dependence of Vibrational Raman Intensity on the Wavelength of Incident Light. *J. Chem. Phys.* **1971**, *55*, 4438–4443.

[78] Frisch, M. J. et al. *Gaussian Development Version*, revision j.02 ed.; Gaussian, Inc.: Wallingford, CT, 2019.

[79] Baiardi, A.; Bloino, J.; Barone, V. Time-dependent Formulation of Resonance Raman Optical Activity Spectroscopy. *J. Chem. Theory Comput.* **2018**, *14*, 6370–6390.

[80] Vahtras, O.; Ågren, H.; Jørgensen, P.; Jensen, H. J. A.; Helgaker, T.; Olsen, J. Multiconfigurational quadratic response functions for singlet and triplet perturbations: The phosphorescence lifetime of formaldehyde. *J. Chem. Phys.* **1992**, *97*, 9178–9187.

[81] Hettema, H.; Jensen, H. J. A.; Jørgensen, P.; Olsen, J. Quadratic response functions for a multiconfigurational self-consistent field wave function. *J. Chem. Phys.* **1992**, *97*, 1174–1190.

[82] Ågren, H.; Vahtras, O.; Koch, H.; Jørgensen, P.; Helgaker, T. Direct atomic orbital based self-consistent-field calculations of nonlinear molecular properties. Application to the frequency dependent hyperpolarizability of para-nitroaniline. *J. Chem. Phys.* **1993**, *98*, 6417–6423.

[83] Aidas, K. et al. The Dalton quantum chemistry program system. *WIREs Comput. Mol. Sci.* **2014**, *4*, 269–284.

[84] Dietze, D. R.; Mathies, R. A. Femtosecond Stimulated Raman Spectroscopy. *ChemPhysChem* **2016**, *17*, 1224–1251.

[85] Kovalenko, S. A.; Dobryakov, A. L.; Ruthmann, J.; Ernsting, N. P. Femtosecond Spectroscopy of Condensed Phases with Chirped Supercontinuum Probing. *Phys. Rev. A* **1999**, *59*, 2369–2384.

[86] Ekvall, K.; van der Meulen, P.; Dhollande, C.; Berg, L.-E.; Pommeret, S.; Naskrecki, R.; Mialocq, J.-C. Cross Phase Modulation Artifact in Liquid Phase Transient Absorption Spectroscopy. *J. Appl. Phys.* **2000**, *87*, 2340–2352.

[87] Pontecorvo, E.; Ferrante, C.; Elles, C. G.; Scopigno, T. Spectrally Tailored Narrowband Pulses for Femtosecond Stimulated Raman Spectroscopy in the Range 330-750 nm. *Opt. Express* **2013**, *21*, 6866–6872.

[88] Marangoni, M. A.; Brida, D.; Quintaville, M.; Cirmi, G.; Pigozzo, F. M.; Manzoni, C.; Baronio, F.; Capobianco, A. D.; Cerullo, G. Narrow-bandwidth Picosecond Pulses by Spectral Compression of Femtosecond Pulses in Second-order Nonlinear Crystals. *Opt. Express* **2007**, *15*, 8884–8891.

[89] Marangoni, M. A.; Brida, D.; Conforti, M.; Capobianco, A. D.; Manzoni, C.; Baronio, F.; Nalesso, G. F.; De Angelis, C.; Ramponi, R.; Cerullo, G. Synthesis of Picosecond Pulses by Spectral Compression and Shaping of Femtosecond Pulses in Engineered Quadratic Nonlinear Media. *Opt. Lett.* **2009**, *34*, 241–243.

[90] Quincy, T. J. Direct and Indirect Probing of Higher-Lying Excited-States of Photoactive Molecules. Ph.D. thesis, University of Kansas, 2018.

[91] Kukura, P.; McCamant, D. W.; Davis, P. H.; Mathies, R. A. Vibrational Structure of the S_2 (1B$_u$) Excited State of Diphenyloctatetraene Observed by Femtosecond Stimulated Raman Spectroscopy. *Chem. Phys. Lett.* **2003**, *382*, 81 – 86.

[92] Myers Kelley, A. Resonance Raman and Resonance Hyper-Raman Intensities: Structure and Dynamics of Molecular Excited States in Solution. *J. Phys. Chem. A* **2008**, *112*, 11975– 11991.

[93] Wu, Y. C.; Zhao, B.; Lee, S. Y. Wave Packet Theory of Dynamic Stimulated Raman Spectra in Femtosecond Pump-Probe Spectroscopy. *J. Chem. Phys.* **2007**, *126*, 174104.

[94] Wu, Y. C.; Zhao, B.; Lee, S. Y. Time-Dependent Wave Packet Averaged Vibrational Frequencies from Femtosecond Stimulated Raman Spectra. *J. Chem. Phys.* **2016**, *144*, 05104.

[95] Sun, Z.; Qiu, X. Q.; Lu, J.; Zhang, D. H.; Lee, S. Y. Three-State Model for Femtosecond Broadband Stimulated Raman Scattering. *J. Raman Spectrosc.* **2008**, *39*, 1568–1577.

[96] Dorfman, K. E.; Fingerhut, B. P.; Mukamel, S. Broadband infrared and Raman probes of excited-state vibrational molecular dynamics: simulation protocols based on loop diagrams. *Phys. Chem. Chem. Phys.* **2013**, *15*, 12348–12359.

[97] Dorfman, K. E.; Fingerhut, B. P.; Mukamel, S. Time-Resolved Broadband Raman Spectroscopies: A Unified Six-Wave-Mixing Representation. *J. Chem. Phys.* **2013**, *139*, 124113.

[98] Agarwalla, B. K.; Ando, H.; Dorfman, K. E.; Mukamel, S. Stochastic Liouville Equations for Femtosecond Stimulated Raman Spectroscopy. *J. Chem. Phys.* **2015**, *142*, 024115.

[99] Rao, B. J.; Gelin, M. F.; Domcke, W. Resonant Femtosecond Stimulated Raman Spectra: Theory and Simulations. *J. Phys. Chem. A* **2016**, *120*, 3286–3295.

[100] Liu, J.; Liang, W. Analytical Approach for the Excited-State Hessian in Time-Dependent Density Functional Theory: Formalism, Implementation, and Performance. *J. Chem. Phys.* **2011**, *135*, 184111.

[101] Petrone, A.; Lingerfelt, D.; Williams-Young, D.; Li, X. Ab Initio Transient Vibrational Spectral Analysis. *J. Phys. Chem. Lett.* **2016**, *7*, 4501–4508.

[102] Petrone, A.; Williams-Young, D. B.; Lingerfelt, D. B.; Li, X. Ab Initio Excited-State Transient Raman Analysis. *J. Phys. Chem. A* **2017**, *121*, 3958–3965.

[103] Egidi, F.; Williams-Young, D. B.; Baiardi, A.; Bloino, J.; Scalmani, G.; Frisch, M. J.; Li, X.; Barone, V. Effective Inclusion of Mechanical and Electrical Anharmonicity in Excited Electronic States: VPT2–TDDFT Route. *J. Chem. Theor. Comp.* **2017**, 2789–2803.

[104] Sakamoto, A.; Tanaka, F.; Tasumi, M.; Torii, H.; Kawato, K.; Furuya, K. Comparison of the Raman Spectrum of *trans*-Stilbene in the S$_1$ State Calculated by the CIS Method and the Spectra Observed under Resonant and Off-Resonant Conditions. *Vib. Spectrosc.* **2006**, *42*, 176–182.

[105] Tsumura, K.; Furuya, K.; Sakamoto, A.; Tasumi, M. Vibrational Analysis of trans-Stilbene in the Excited Singlet State by Time-dependent Density Functional Theory: Calculations of the Raman, Infrared, and Fluorescence Excitation Spectra. *J. Raman Spectrosc.* **2008**, *39*, 1584–1591.

[106] Dobryakov, A. L.; Ioffe, I.; Granovsky, A. A.; Ernsting, N. P.; Kovalenko, S. A. Femtosecond Raman Spectra of cis-Stilbene and trans-Stilbene with Isotopomers in Solution. *J. Chem. Phys.* **2012**, *137*, 244505–244516.

[107] Batignani, G.; Pontecorvo, E.; Ferrante, C.; Aschi, M.; Elles, C. G.; Scopigno, T. Visualizing Excited-State Dynamics of a Diaryl Thiophene: Femtosecond Stimulated Raman Scattering as a Probe of Conjugated Molecules. *J. Phys. Chem. Lett.* **2016**, *7*, 2981–2988.

[108] Pontecorvo, E.; Kapetanaki, S. M.; Badioli, M.; Brida, D.; Marangoni, M.; Cerullo, G.; Scopigno, T. Femtosecond Stimulated Raman Spectrometer in the 320-520nm Range. *Opt. Express* **2011**, *19*, 1107–1112.

[109] Challa, J. R.; Du, Y.; McCamant, D. W. Femtosecond Stimulated Raman Spectroscopy Using a Scanning Multichannel Technique. *Appl. Spectrosc.* **2012**, *66*, 227–232.

[110] Becke, A. D. Density-functional Thermochemistry. III. The Role of Exact Exchange. *J. Chem. Phys.* **1993**, *98*, 5648.

[111] Becke, A. D. A New Mixing of Hartree-Fock and Local Density-functional Theories. *J. Chem. Phys.* **1993**, *98*, 1372.

[112] Lee, C. T.; Yang, W. T.; Parr, R. G. Development of the Colle-Salvetti Correlation-Energy Formula into a Functional of the Electron-Density. *Phys. Rev. B* **1988**, *37*, 785–789.

[113] Dunning, T. H. Gaussian basis sets for use in correlated molecular calculations. I. The atoms boron through neon and hydrogen. *J. Chem. Phys.* **1989**, *90*, 1007.

[114] Staniszewska, M.; Kupfer, S.; Labuda, M.; Guthmuller, J. Theoretical Assessment of Excited State Gradients and Resonance Raman Intensities for the Azobenzene Molecule. *J. Chem. Theory Comput.* **2017**, *13*, 1263–1274.

[115] Lanzani, G.; Nisoli, M.; Silvestri, S. D.; Tubino, R. Femtosecond Vibrational and Torsional Energy Redistribution in Photoexcited Oligothiophenes. *Chem. Phys. Lett.* **1996**, *251*, 339–345.

[116] NIST Computational Chemistry Comparison and Benchmark Database, NIST Standard Reference Database Number 101. 2016; `http://cccbdb.nist.gov/`, (accessed June 20, 2019).

[117] Scott, A.; Radom, L. Harmonic vibrational frequencies: An evaluation of Hartree-Fock,

Moller-Plesset, quadratic configuration interaction, density functional theory, and semiempirical scale factors. *J. Phys. Chem.* **1996**, *100*, 16502–16513.

[118] Castro, C. M.; Delgado, M. C. R.; Hernandez, V.; Hotta, S.; Casado, J.; Navarrete, J. T. L. Efficiency of the π Conjugation in a Novel Family of α,α '-Bisphenyl End-capped Oligothiophenes by Means of Raman Spectroscopy. *J. Chem. Phys.* **2002**, *116*, 10419–10427.

[119] Gardner, A. M.; Wright, T. G. Consistent Assignment of the Vibrations of Monosubstituted Benzenes. *J. Chem. Phys.* **2011**, *135*, 114305.

[120] McCamant, D. W.; Kukura, P.; Mathies, R. A. Femtosecond Broadband Stimulated Raman: A New Approach for High-Performance Vibrational Spectroscopy. *Appl. Spectrosc.* **2003**, *57*, 1317–1323.

[121] McCamant, D. W.; Kukura, P.; Yoon, S.; Mathies, R. A. Femtosecond Broadband Stimulated Raman Spectroscopy: Apparatus and Methods. *Rev. Sci. Instrum.* **2004**, *75*, 4971–4980.

[122] Tang, L. T.; Liu, W. M.; Wang, Y. L.; Zhao, Y. X.; Oscar, B. G.; Campbell, R. E.; Fang, C. Unraveling Ultrafast Photoinduced Proton Transfer Dynamics in a Fluorescent Protein Biosensor for Ca2+ Imaging. *Chem-Eur. J.* **2015**, *21*, 6481–6490.

[123] Valley, D. T.; Hoffman, D. P.; Mathies, R. A. Reactive and Unreactive Pathways in a Photochemical Ring Opening Reaction from 2D Femtosecond Stimulated Raman. *Phys. Chem. Chem. Phys.* **2015**, *17*, 9231–9240.

[124] Cen, Q. Y.; He, Y. H.; Xu, M.; Wang, J. J.; Wang, Z. H. Wavelength Dependent Resonance Raman Band Intensity of Broadband Stimulated Raman Spectroscopy of Malachite Green in Ethanol. *J. Chem. Phys.* **2015**, *142*.

[125] Fujisawa, T.; Kuramochi, H.; Hosoi, H.; Takeuchi, S.; Tahara, T. Role of Coherent Low-Frequency Motion in Excited-state Proton Transfer of Green Fluorescent Protein Studied

by Time-resolved Impulsive Stimulated Raman Spectroscopy. *J. Am. Chem. Soc.* **2016**, *138*, 3942–3945.

[126] Weigel, A.; Dobryakov, A.; Klaumunzer, B.; Sajadi, M.; Saalfrank, P.; Ernsting, N. P. Femtosecond Stimulated Raman Spectroscopy of Flavin After Optical Excitation. *J. Phys. Chem. B* **2011**, *115*, 3656–3680.

[127] Johnson, A. E.; Myers, A. B. Solvent Effects in the Raman Spectra of the Triiodide Ion: Observation of Dynamic Symmetry Breaking and Solvent Degrees of Freedom. *J. Phys. Chem.* **1996**, *100*, 7778–7788.

[128] Ma, H.; Liu, J.; Liang, W. Time-dependent Approach to Resonance Raman Spectra Including Duschinsky Rotation and Herzberg–Teller Effects: Formalism and Its Realistic Applications. *J. Chem. Theory Comput.* **2012**, *8*, 4474–4482.

[129] Stanton, J. F.; Gauss, J.; Ishikawa, N.; Headgordon, M. A Comparison of Single Reference Methods for Characterizing Stationary-points of Excited-state Potential-energy Surfaces. *J. Chem. Phys.* **1995**, *103*, 4160–4174.

[130] Caricato, M.; Trucks, G. W.; Frisch, M. J.; Wiberg, K. B. Electronic Transition Energies: A Study of the Performance of a Large Range of Single Reference Density Functional and Wave Function Methods on Valence and Rydberg States Compared to Experiment. *J. Chem. Theory Comput.* **2010**, *6*, 370–383.

[131] Oscar, B. G.; Chen, C.; Liu, W. M.; Zhu, L. D.; Fang, C. Dynamic Raman Line Shapes on an Evolving Excited-State Landscape: Insights from Tunable Femtosecond Stimulated Raman Spectroscopy. *J. Phys. Chem. A* **2017**, *121*, 5428–5441.

[132] Phillips, D. L.; Zgierski, M. Z.; Myers, A. B. Resonance Raman Excitation Profiles of 1,3-Butadiene in Vapor and Solution Phases. *J. Phys. Chem.* **1993**, *97*, 1800–1809.

[133] Cave, R. J.; Zhang, F.; Maitra, N. T.; Burke, K. A Dressed TD-DFT Treatment of the $2A_g$ States of Butadiene and Hexatriene. *Chem. Phys. Lett.* **2004**, *389*, 39–42.

[134] Roseli, R. B.; Tapping, P. C.; Kee, T. W. Origin of the Excited-state Absorption Spectrum of Polythiophene. *J. Phys. Chem. Lett.* **2017**, *8*, 2806–2811.

[135] Liu, W. M.; Tang, L. T.; Oscar, B. G.; Wang, Y. L.; Chen, C.; Fang, C. Tracking Ultrafast Vibrational Cooling during Excited-State Proton Transfer Reaction with Anti-Stokes and Stokes Femtosecond Stimulated Raman Spectroscopy. *J. Phys. Chem. Lett.* **2017**, *8*, 997–1003.

[136] Hoffman, D. P.; Mathies, R. A. Photoexcited Structural Dynamics of an Azobenzene Analog 4-nitro-4'-dimethylamino-azobenzene from Femtosecond Stimulated Raman. *Phys. Chem. Chem. Phys.* **2012**, *14*, 6298–6306.

[137] Kasha, M. Characterization of Electronic Transitions in Complex Molecules. *Discuss. Faraday Soc.* **1950**, *9*, 14–19.

[138] Houk, A. L.; Zheldakov, I. L.; Tommey, T. A.; Elles, C. G. Two-Photon Excitation of trans-Stilbene: Spectroscopy and Dynamics of Electronically Excited States above S_1. *J. Phys. Chem. B* **2015**, *119*, 9335–9344.

[139] Sun, Z.; Lu, J.; Zhang, D. H.; Lee, S.-Y. Quantum Theory of (Femtosecond) Time-resolved Stimulated Raman Scattering. *J. Chem. Phys.* **2008**, *128*, 144114.

[140] Wang, X. H.; Valverde-Aguilar, G.; Weaver, M. N.; Nelsen, S. F.; Zink, J. I. Resonance Raman De-enhancement Caused by Excited State Mixed Valence. *J. Phys. Chem. A* **2007**, *111*, 5441–5447.

[141] Wu, M.; Ray, M.; Sedlacek, A. J. Raman Resonance De-enhancement in the Excitation Profile of CS_2. *J. Chem. Phys.* **1998**, *109*, 1352–1358.

[142] Batignani, G.; Fumero, G.; Pontecorvo, E.; Ferrante, C.; Mukamel, S.; Scopigno, T. Genuine Dynamics vs Cross Phase Modulation Artifacts in Femtosecond Stimulated Raman Spectroscopy. *ACS Photonics* **2019**, *6*, 492–500.

[143] Wolde, A.; Jacobs, H. J. C.; Langkilde, F. W.; Bajdor, K.; Wilbrandt, R.; Negri, F.; Zerbetto, F.; Orlandi, G. Triplet State Resonance Raman and Absorption Spectroscopy of a Configurationally Locked (Z)-Hexatriene: 1,2-Divinylcyclopentene. *J. Phys. Chem.* **1994**, *98*, 9437–9445.

[144] Zuo, P.; Ma, C.; Kwok, W. M.; Chan, W. S.; Phillips, D. L. Time-resolved Resonance Raman and Density Functional Theory Study of the Deprotonation Reaction of the Triplet State of p-Hydroxyacetophenone in Water Solution. *J. Org. Chem.* **2005**, *70*, 8661–8675.

[145] Lee, J.; Challa, J. R.; McCamant, D. W. Pump Power Dependence in Resonance Femtosecond Stimulated Raman Spectroscopy. *J. Raman Spectrosc.* **2013**, *44*, 1263–1272.

[146] Koch, H.; Jørgensen, P. Coupled Cluster Response Functions. *J. Chem. Phys.* **1990**, *93*, 3333–3344.

[147] Stanton, J. F.; Bartlett, R. J. The Equation of Motion Coupled-cluster Method. A Systematic Biorthogonal Approach to Molecular Excitation Energies, Transition Probabilities, and Excited State Properties. *J. Chem. Phys.* **1993**, *98*, 7029–7039.

[148] Koch, H.; Kobayashi, R.; de Merás, A. S.; Jørgensen, P. Calculation of Size-intensive Transition Moments from the Coupled Cluster Singles and Doubles Linear Response Function. *J. Chem. Phys.* **1994**, *100*, 4393–4400.

[149] Piontkowski, Z.; McCamant, D. W. Excited-state Planarization in Donor-bridge Dye Sensitizers: Phenylene Versus Thiophene Bridges. *J. Am. Chem. Soc.* **2018**, *140*, 11046–11057.

[150] Čížek, J. *Advances in Chemical Physics*; John Wiley & Sons, Inc., 2007; pp 35–89.

[151] Purvis, G. D.; Bartlett, R. J. A Full Coupled-cluster Singles and Doubles Model: The Inclusion of Disconnected Triples. *J. Chem. Phys.* **1982**, *76*, 1910–1918.

[152] Scuseria, G. E.; Janssen, C. L.; Schaefer, H. F. An Efficient Reformulation of the Closed-shell Coupled Cluster Single and Double Excitation (CCSD) Equations. *J. Chem. Phys.* **1988**, *89*, 7382–7387.

[153] Scuseria, G. E.; Schaefer, H. F. Is Coupled Cluster Singles and Doubles (CCSD) More Computationally Intensive than Quadratic Configuration Interaction (QCISD)? *J. Chem. Phys.* **1989**, *90*, 3700–3703.

[154] Merrick, J. P.; Moran, D.; Radom, L. An Evaluation of Harmonic Vibrational Frequency Scale Factors. *J. Phys. Chem. A* **2007**, *111*, 11683–11700.

[155] Xue, J.; Vyas, S.; Du, Y.; Luk, H. L.; Chuang, Y. P.; But, T. Y. S.; Toy, P. H.; Wang, J.; Winter, A. H.; Phillips, D. L.; Hadad, C. M.; Platz, M. S. Time-resolved Resonance Raman and Computational Investigation of the Influence of 4-Acetamido and 4-N-Methylacetamido Substituents on the Chemistry of Phenylnitrene. *J. Phys. Chem. A* **2011**, *115*, 7521–7530.

[156] Langkilde, F. W.; Wilbrandt, R.; Brouwer, A. M.; Negri, F.; Zerbetto, F.; Orlandi, G. Molecular Structure of Stilbene in the T_1 State. Transient Resonance Raman Spectra of Stilbene Isotopomers and Quantum Chemical Calculations. *J. Phys. Chem.* **1994**, *98*, 2254–2265.

[157] Heather, R.; Metiu, H. Time-dependent Theory of Raman Scattering for Systems with Several Excited Electronic States: Application to a H3 Model System. *J. Chem. Phys.* **1989**, *90*, 6903–6915.

[158] Reber, C.; Zink, J. I. Resonance Raman Deenhancement Caused by Excited-state Potential Surface Crossing. *J. Phys. Chem.* **1992**, *96*, 571–576.

[159] Myers, A. B.; Harris, R. A.; Mathies, R. A. Resonance Raman Excitation Profiles of Bacteriorhodopsin. *J. Chem. Phys.* **1983**, *79*, 603.

[160] Myers, A. B.; Trulson, M. O.; Mathies, R. A. Quantitation of Homogeneous and Inhomogeneous Broadening Mechanisms in trans-Stilbene Using Absolute Resonance Raman Intensities. *J. Chem. Phys.* **1985**, *83*, 5000.

[161] Myers, A. B.; Trulson, M. O.; Pardoen, J. A.; Heeremans, C.; Lugtenburg, J.; Mathies, R. A. Absolute Resonance Raman Intensities Demonstrate that the Spectral Broadening Influence by the β-Ionone Ring in Retinal is Homogeneous. *J. Chem. Phys.* **1986**, *84*, 633.

[162] Lin, J. B.; Darzi, E. R.; Jasti, R.; Yavuz, I.; Houk, K. N. Solid-State Order and Charge Mobility in [5]- to [12]Cycloparaphenylenes. *J. Am. Chem. Soc.* **2019**, *141*, 952.

[163] Wang, J.; Cooper, G.; Tulumello, D.; Hitchcock, A. P. Inner Shell Excitation Spectroscopy of Biphenyl and Substituted Biphenyls: Probing RingRing Delocalization. *J. Phys. Chem. A* **2005**, *109*, 10886–10896.

[164] Sinnokrot, M. O.; Sherrill, C. D. Substituent Effects in π-π Interactions: Sandwich and T-Shaped Configurations. *J. Am. Chem. Soc.* **2004**, *126*, 7690–7697.

[165] Heckel, J. C.; Weisman, A. L.; Schneebeli, S. T.; Hall, M. L.; Sherry, L. J.; Stranahan, S. M.; DuBay, K. H.; Friesner, R. A.; Willets, K. A. Polarized Raman Spectroscopy of Oligothiophene Crystals To Determine Unit Cell Orientation. *J. Phys. Chem. A* **2012**, *116*, 6804–6816.

[166] Bloom, J. W. G.; Wheeler, S. E. Benchmark Torsional Potentials of Building Blocks for Conjugated Materials: Bifuran, Bithiophene, and Biselenophene. *J. Chem. Theory Comput.* **2014**, *10*, 3647–3655.

[167] Karabacak, M.; Cinar, M.; Ermec, S.; Kurt, M. Experimental Vibrational Spectra (Raman, Infrared) and DFT Calculations on Monomeric and Dimeric Structures of 2- and 6-Bromonicotinic Acid. *J. Raman Spectrosc.* **2010**, *41*, 98–105.

[168] Zhang, F.; Wu, D.; Xu, Y.; Feng, X. Thiophene-Based Conjugated Oligomers for Organic Solar Cells. *J. Mater. Chem.* **2011**, *21*, 17590.

[169] Kapitán, J.; Hecht, L.; Bouř, P. Raman spectral evidence of methyl rotation in liquid toluene. *Phys. Chem. Chem. Phys.* **2008**, *10*, 1003–1008.

[170] Perdew, J. P.; Ruzsinszky, A.; Tao, J.; Staroverov, V. N.; Scuseria, G. E.; Csonka, G. I. Prescription for the Design and Selection of Density Functional Approximations: More Constraint Satisfaction with Fewer Fits. *J. Chem. Phys.* **2005**, *123*, 062201.

[171] Perdew, J. P.; Burke, K.; Ernzerhof, M. Generalized Gradient Approximation Made Simple. *Phys. Rev. Lett.* **1996**, *77*, 3865–3868.

[172] Zhao, Y.; Truhlar, D. G. A new local density functional for main-group thermochemistry, transition metal bonding, thermochemical kinetics, and noncovalent interactions. *J. Chem. Phys.* **2006**, *125*, 194101.

[173] Tao, J.; Perdew, J. P.; Staroverov, V. N.; Scuseria, G. E. Climbing the Density Functional Ladder: Nonempirical Meta–Generalized Gradient Approximation Designed for Molecules and Solids. *Phys. Rev. Lett.* **2003**, *91*, 146401.

[174] Staroverov, V. N.; Scuseria, G. E.; Tao, J.; Perdew, J. P. Comparative assessment of a new nonempirical density functional: Molecules and hydrogen-bonded complexes. *J. Chem. Phys.* **2003**, *119*, 12129–12137.

[175] Zhao, Y.; Truhlar, D. G. Density Functional for Spectroscopy: No Long-Range Self-Interaction Error, Good Performance for Rydberg and Charge-Transfer States, and Better Performance on Average than B3LYP for Ground States. *J. Phys. Chem. A* **2006**, *110*, 13126–13130.

[176] Yanai, T.; Tew, D. P.; Handy, N. C. A new hybrid exchange–correlation functional using the Coulomb-attenuating method (CAM-B3LYP). *Chem. Phys. Lett.* **2004**, *393*, 51–57.

[177] Grimme, S. Semiempirical hybrid density functional with perturbative second-order correlation. *J. Chem. Phys.* **2006**, *124*, 034108.

[178] Head-Gordon, M.; Pople, J. A.; Frisch, M. J. MP2 energy evaluation by direct methods. *Chem. Phys. Lett.* **1988**, *153*, 281–289.

[179] Frisch, M. J.; Head-Gordon, M.; Pople, J. A. A direct MP2 gradient method. *Chem. Phys. Lett.* **1990**, *166*, 275–280.

[180] Frisch, M. J.; Head-Gordon, M.; Pople, J. A. Semi-direct algorithms for the MP2 energy and gradient. *Chem. Phys. Lett.* **1990**, *166*, 281–289.

[181] Head-Gordon, M.; Head-Gordon, T. Analytic MP2 frequencies without fifth-order storage. Theory and application to bifurcated hydrogen bonds in the water hexamer. *Chem. Phys. Lett.* **1994**, *220*, 122–128.

[182] Kesharwani, M. K.; Brauer, B.; Martin, J. M. L. Frequency and Zero-Point Vibrational Energy Scale Factors for Double-Hybrid Density Functionals (and Other Selected Methods): Can Anharmonic Force Fields be Avoided? *J. Phys. Chem. A* **2015**, *119*, 1701–1714.

[183] Kashinski, D. O.; Chase, G. M.; Nelson, R. G.; Di Nallo, O. E.; Scales, A. N.; Vander-Ley, D. L.; Byrd, E. F. C. Harmonic Vibration Frequencies: Approximate Global Scaling Factors for TPSS, M06, and M11 Functional Families Using Several Common Basis Sets. *J. Phys. Chem. A* **2017**, *121*, 2265–2273.

[184] Kendall, R. A.; Dunning, T. H.; Harrison, R. J. Electron affinities of the first-row atoms revisited. Systematic basis sets and wave functions. *J. Chem. Phys.* **1992**, *96*, 6796–6806.

[185] Schomacker, K. T.; Delaney, J. K.; Champion, P. M. Measurements of the Absolute Raman Cross Sections of Benzene. *J. Chem. Phys.* **1986**, *85*, 4240–4247.

[186] Fernández-Sánchez, J. M.; Montero, S. Gas Phase Raman Scattering Cross Sections of Benzene and Perdeuterated Benzene. *J. Chem. Phys.* **1989**, *90*, 2909–2914.

[187] Wilmshurst, J. K.; Bernstein, H. J. The Infrared and Raman Spectra of Toluene, Toluene--d3, m-Xylene, and m-Xylene-*t*-d6. *Can. J. Chem.* **1957**, *35*, 911–925.

[188] Carreira, L.; Towns, T. Raman Spectra and Barriers to Internal Rotation: Biphenyl and Nitrobenzene. *J. Mol. Struct.* **1977**, *41*, 1–9.

[189] Tomasi, J.; Mennucci, B.; Cammi, R. Quantum Mechanical Continuum Solvation Models. *Chem. Rev.* **2005**, *105*, 2999–3094.

[190] Wilson, E. B. The Normal Modes and Frequencies of Vibration of the Regular Plane Hexagon Model of the Benzene Molecule. *Phys. Rev.* **1934**, *45*, 706–714.

[191] Gardner, A. M.; Wright, T. G. Consistent Assignment of the Vibrations of Monosubstituted Benzenes. *J. Chem. Phys.* **2011**, *135*, 114305.

[192] Yamakita, Y.; Okazaki, T.; Ohno, K. Conformation-Specific Raman Bands and Electronic Conjugation in Substituted Thioanisoles. *J. Phys. Chem. A* **2008**, *112*, 12220–12227.

[193] Rogers, D. M.; Hirst, J. D.; Lee, E. P.; Wright, T. G. Ab initio Study of the Toluene Dimer. *Chem. Phys. Lett.* **2006**, *427*, 410–413.

[194] Mani, T.; Miller, J. R. Role of Bad Dihedral Angles: Methylfluorenes Act as Energy Barriers for Excitons and Polarons of Oligofluorenes. *J. Phys. Chem. A* **2014**, *118*, 9451–9459.

[195] Newby, J. J.; Müller, C. W.; Liu, C.-P.; Zwier, T. S. Jet-cooled Vibronic Spectroscopy and Asymmetric Torsional Potentials of Phenylcyclopentene. *Phys. Chem. Chem. Phys.* **2009**, *11*, 8330.

[196] Lin, J. B.; Jin, Y.; Lopez, S. A.; Druckerman, N.; Wheeler, S. E.; Houk, K. N. Torsional Barriers to Rotation and Planarization in Heterocyclic Oligomers of Value in Organic Electronics. *J. Chem. Theory Comput.* **2017**, *13*, 5624–5638.

[197] Grein, F. Twist Angles and Rotational Energy Barriers of Biphenyl and Substituted Biphenyls. *J. Phys. Chem. A* **2002**, *106*, 3823–3827.

[198] Johansson, M. P.; Olsen, J. Torsional Barriers and Equilibrium Angle of Biphenyl: Reconciling Theory with Experiment. *J. Chem. Theory Comput.* **2008**, *4*, 1460–1471.

[199] Dahlgren, M. K.; Schyman, P.; Tirado-Rives, J.; Jorgensen, W. L. Characterization of Biaryl Torsional Energetics and its Treatment in OPLS All-Atom Force Fields. *J. Chem. Inf. Model.* **2013**, *53*, 1191–1199.

[200] Masson, E. Torsional Barriers of Substituted Biphenyls Calculated using Density Functional Theory: A Benchmarking Study. *Org. Biomol. Chem.* **2013**, *11*, 2859.

[201] Popelier, P. L. A.; Maxwell, P. I.; Thacker, J. C. R.; Alkorta, I. A Relative Energy Gradient (REG) Study of the Planar and Perpendicular Torsional Energy Barriers in Biphenyl. *Theor. Chem. Acc.* **2018**, *138*.

[202] Tuttle, W. D.; Gardner, A. M.; Whalley, L. E.; Wright, T. G. Vibration and Vibration-torsion Levels of the S1 state of Para-fluorotoluene in the 580–830 cm-1 Range: Interactions and Coincidences. *J. Chem. Phys.* **2017**, *146*, 244310.

[203] Gardner, A. M.; Tuttle, W. D.; Groner, P.; Wright, T. G. Molecular Symmetry Group Analysis of the Low-wavenumber Torsions and Vibration-torsions in the S1 State and Ground State Cation of p-Xylene: An Investigation Using Resonance-enhanced Multiphoton Ionization (REMPI) and Zero-kinetic-energy (ZEKE) Spectroscopy. *J. Chem. Phys.* **2017**, *146*, 124308.

[204] Clabo, D.; Allen, W. D.; Remington, R. B.; Yamaguchi, Y.; Schaefer, H. F. A Systematic Study of Molecular Vibrational Anharmonicity and Vibration—Rotation Interaction by Self-consistent-field Higher-derivative Methods. Asymmetric Top Molecules. *Chem. Phys.* **1988**, *123*, 187–239.

[205] Barone, V. Anharmonic Vibrational Properties by a Fully Automated Second-order Perturbative Approach. *J. Chem. Phys.* **2005**, *122*, 014108.

[206] Donohoo-Vallett, P. J.; Bragg, A. E. π-Delocalization and the Vibrational Spectroscopy of Conjugated Materials: Computational Insights on Raman Frequency Dispersion in Thiophene, Furan, and Pyrrole Oligomers. *J. Phys. Chem. B* **2015**, *119*, 3583–3594.

[207] Irie, M. Photochromism: Memories and Switches - Introduction. *Chem. Rev.* **2000**, *100*, 1683–1684.

[208] Lucas, L. N.; de Jong, J. J.; Esch, J. H.; Kellogg, R. M.; Feringa, B. L. Syntheses of Dithienylcyclopentene Optical Molecular Switches. *Eur. J. Org. Chem.* **2003**, *2003*, 155–166.

[209] Paa, W.; Yang, J.-P.; Rentsch, S. Intersystem Crossing in Oligothiophenes Studied by fs Time-Resolved Spectroscopy. *Appl. Phys. B: Lasers Opt.* **2000**, *71*, 443–449.

[210] Letokhov, V. S.; Chebotayev, V. P. *Nonlinear Laser Spectroscopy*; Springer-Verlag: New York, 1977.

[211] Shen, Y. R. *The Principles of Nonlinear Optics*; Wiley-Interscience: New York, 1984.

[212] Jonas, D. M. Vibrational and Nonadiabatic Coherence in 2D Electronic Spectroscopy, the Jahn-Teller Effect, and Energy Transfer. *Annu. Rev. Phys. Chem.* **2018**, *69*, 327–352.

[213] Wright, J. C. Fundamental Studies of Relationships between Experimental Nonlinear Coherent Vibrational Spectroscopies. *J. Phys. Chem. Lett.* **2019**, *10*, 2767–2774.

[214] Petersson, G. A.; Bennett, A.; Tensfeldt, T. G.; Al-Laham, M. A.; Shirley, W. A.; Mantzaris, J. A Complete Basis Set Model Chemistry. I. The Total Energies of Closed-Shell Atoms and Hydrides of the First-Row Elements. *J. Chem. Phys.* **1988**, *89*, 2193–2218.

[215] Petersson, G. A.; Al-Laham, M. A. A Complete Basis Set Model Chemistry. II. Open-Shell Systems and the Total Energies of the First-Row Atoms. *J. Chem. Phys.* **1991**, *94*, 6081–6090.

[216] Cirmi, G.; Brida, D.; Gambetta, A.; Piacenza, M.; Sala, F. D.; Favaretto, L.; Cerullo, G.; Lanzani, G. Observation and Control of Coherent Torsional Dynamics in a Quinquethiophene Molecule. *Phys. Chem. Chem. Phys.* **2010**, *12*, 7917.

[217] Oliver, T. A. A.; Lewis, N. H. C.; Fleming, G. R. Correlating the Motion of Electrons and Nuclei with Two-Dimensional Electronic-Vibrational Spectroscopy. *P. Natl. Acad. Sci. USA* **2014**, *111*, 10061–10066.

[218] Gaynor, J. D.; Khalil, M. Signatures of Vibronic Coupling in Two-Dimensional Electronic-Vibrational and Vibrational-Electronic Spectroscopies. *J. Chem. Phys.* **2017**, *147*, 094202.